University of Nottingham
UK | CHINA | MALAYSIA

Vibrational response of complex structures to high-frequency correlated loads

Joshua Finn

Thesis submitted to the University of Nottingham
for the degree of Doctor of Philosophy

January 2025

Abstract

Distributed Electric Propulsion (DEP) is an innovative aircraft concept where thrust is generated by an array of electrically powered propellers. The application of electric propulsion systems ensures that a significant proportion of the cabin noise within DEP aircraft is the result of structural vibrations driven by Turbulent Boundary Layer (TBL) effects. The purpose of this thesis is thus to extend the Dynamical Energy Analysis (DEA) approach to consider excitations by high frequency correlated pressure fields, such as the TBL pressure field.

In Chapter 1 of this thesis, the rationale of the project is expressed and the necessity for a high-frequency vibrational modelling approach is explored.

In Chapter 2, several high-frequency modelling approaches are evaluated, and the advantages of the DEA approach are highlighted. A detailed review of the DEA methodology then follows. Several TBL pressure field models are then evaluated, based upon their suitability for implementation within DEA.

In Chapter 3, the approach for modelling correlated pressure fields within DEA is developed. This is first applied to model the excitation of small structural regions by homogeneous pressure fields, before being extended to consider full body excitations. Following this, the vibrational behaviour of flat plates is considered under TBL pressure fields for various material, boundary, and flow conditions. Here, the plate response is found to be highly spatially variant and extremely dependent on the system conditions, which has received minimal attention in prior studies.

In Chapter 4 the implementation of correlated point-forces, representing vibrations originating from the DEP propeller array, within DEA is explored. Here, the observed vibrational response is found to be the sum of the individual contributions plus a spatially oscillating interference term. This results in complex interference patterns, which are highly variable under different source arrange-

ments. It is also demonstrated that in some situations these interference effects generate steerable beams of vibrational energy, which may be beneficial for sound and wear reduction. The implemented approach however leads to non-physical negative phase-space densities, and an approach to rectify this using the Husimi Density Function (HDF) is discussed.

Declaration

The work presented in this thesis is the result of the research conducted during my PhD study at the University of Nottingham between October 2020 and July 2024. I declare that this work is my own, and has not been submitted, in whole or in part, for any other degree qualification here or elsewhere.

Acknowledgements

This work has been supported by the European Union funded SilentProp project under the Horizon 2020 research and innovation program (grant agreement number 882842) along with the Faculty of Engineering and the School of Mathematical Sciences within the University of Nottingham.

I would firstly like to express my eternal gratitude to my supervisors, Prof. Gregor Tanner and Dr. Martin Richter. Their extreme generosity and support has guided me through the many difficulties that I have faced during this project, and pushed me to achieve more than I ever thought was possible. I hope that they can find good ways to pass the time previously taken up by replying to all of my emails. I would also like to thank Prof. Richard Jefferson-Loveday and Dr. Dimitrios Chronopoulos for their support during their time in Nottingham, I hope I didn't scare you away. In addition, I wish to thank my SilentProp colleagues for many interesting discussions, in particular François-Xavier Bécot and Dr. Nurkanat Aimakov. I am also very grateful to Dr. Benjamin Rothwell, Dr. Nabil Fadai, Dr. Jamie Walton (and Gregor again!) for allowing me to support their taught classes. I had a lot of fun in these sessions and learnt a great deal from them, I just hope that the students can say the same. I am also extremely thankful to the University of Nottingham for their support, particularly around facilitating and funding the extension of my study. Most importantly, I wish to thank Jess for her enduring love and support throughout this time, especially during my many incoherent rambles about this work. I am sure that you are looking forward to me talking about something else from now on.

Finally, I would like to thank you for reading and I can only apologise for what is to come.

List of Publications

1. Finn, JS. Tanner, G. Richter, M. Using Dynamical Energy Analysis to model the vibrational response of complex structures to high-frequency TBL pressure fields. *Journal of Sound and Vibration, submitted.*

2. Finn, JS. Tanner, G. Richter, M. Aimakov, N. Directional excitation of structural vibrations due to correlated sources. *2024. Proceedings of Inter-Noise 2024.*

3. Finn, JS. Jefferson-Loveday, R. Richter, M. and Tanner, G. Using dynamical energy analysis to model the vibrational response of real-world structures to correlated excitation fields. *2022. Proceedings of ISMA-USA 2022 Page 1942-1949.*

Contents

List of Figures

Chapter 1

1 Introduction

In this chapter the motivation behind the work presented within this thesis will be discussed. In addition, experiment-based studies on the topic will be reviewed and the need for an appropriate computational modelling approach will be discussed. Following this, the key aims and objectives of the project will be outlined and the remaining chapters of the thesis will be summarised, highlighting the key results from each.

1.1 Motivation

Currently, aviation represents a significant contribution to climate change, accounting for around 2.5% of all CO_2 emissions globally [1]. Due to increasing demand and improvements in sustainability in other industries, this may reach around 11% [2, 3]. To attempt to prevent this, a significant amount of research is being performed to develop feasible alternatives to fossil fuel-powered aircraft. One potential alternative is to replace traditional jet engines with electric propulsion systems. A particularly exciting example of this is Distributed Electric Propulsion (DEP), where thrust is produced by an array of small electric propulsion systems (EPSs) spread across the airframe. In this thesis, the term "EPS" refers to the full configuration, including an electric motor and propeller, which is employed to generate thrust for DEP aircraft. A "propeller" is then the aerodynamic device which is rotated to generate the thrust itself.

This approach leads to increased low-speed lift generation as the propellers force air across the wings [4–7], along with increased stability and steering control through differential thrust [8]. These factors enable the reduction in the size

of key aerodynamic and control devices, greatly reducing drag and improving aerodynamic efficiency over traditional configurations [8–10].

In addition to the obvious climate benefits of these aircraft, electric propulsion systems also generate much less noise than their jet-engine counterparts [11, 12]. Currently, cabin noise experienced aboard aircraft is dominated by a combination of engine noise and turbulent boundary layer (TBL) effects [13]. The switch to electric propulsion would thus dramatically increase the influence of these TBL effects. This is especially important at frequencies $> 500\,Hz$, where TBL contributions already dominate the experienced cabin noise [14, 15]. When attempting to reduce the noise experienced aboard electric aircraft, a strong understanding of the influence of the TBL on the aircraft in flight is thus required.

However, direct evaluation of the vibrational response of aircraft structures under TBL pressure fields via wind tunnel or in-situ testing is extremely expensive and time consuming [16–18]. As a result, little research has been performed in this area, with direct vibrational studies of aircraft structures limited to point-force excitations [19–21]. In these experiments, shakers were utilised to excite vibrations in full size fuselage models. The vibrational response across the structure was then measured by accelerometers or scanning laser vibrometers on a grid of points across the structure. These results were then combined to define the distributed vibrational response of the fuselage under the applied excitation [20, 21]. Due to physical constraints, these measurements could only be performed on small regions of the fuselage, and were limited to the low-frequency range. The number of measurements required to perform this analysis also meant that these studies were extremely time consuming, taking several days to complete [21]. Housing the aircraft structures in environments of sufficient size without external influence also requires dedicated facilities [20], which may not be available in many cases. The impracticality of these direct experimental approaches means that alternative methods are necessary to compute the response of aircraft to high-frequency

TBL effects.

Due to the impracticality of these direct experimental approaches, numerous approximate methods have been developed to examine the vibrational behaviour of systems under TBL pressure fields. Amongst these are methods which attempt to synthetically recreate the pressure field applied by the TBL using an array of loudspeakers [22, 23]. By careful management of the location and amplitude of the sources, the loudspeaker array is able to produce a fluctuating pressure field across the plate which is equivalent to the TBL pressure field. Thus a real TBL pressure field, produced within a wind tunnel or in situ, is unnecessary, making this approach far more accessible than a direct experimental evaluation. This approach has been found to work well for low-frequency sources [22], but requires an unfeasibly dense loudspeaker array for high-frequency applications [23]. To rectify this issue, the Source Scanning Technique (SST) has been developed, which aims to accurately recreate the TBL using a single acoustic source [24, 25]. To do this, measurements are made of the response of the plate to the acoustic source when applied at various locations and amplitudes. If defined correctly, the linear combination of these responses is approximately equivalent to the response at this location under a full TBL pressure field excitation [24]. Cross-spectral results for this approach show close agreement with experimental results. However, this procedure can only define the response of the plate at a single location and the whole process must be repeated to define the response at further locations. The generation of a distributed representation of the structural response using this approach would thus be extremely time consuming.

Due to the discussed limitations in experimental evaluations of this phenomena, numerical procedures must be investigated. Amongst these are approaches which simplify the problem by considering the properties of the TBL pressure field and the vibrational behaviour of the plate independent of one another [26–28]. In these studies, the TBL pressure field is represented by an appropriate Cross-

Spectral Density (CSD) function, which describes the correlation in the pressure applied by the field at two distinct locations, based upon their separation. A review of several CSD models for TBL pressure fields is presented in Section 2.3. Appropriate parametric values for these models may be defined from wind-tunnel measurements [26, 28], or from recommendations in the literature such as the popular study by Graham [29]. The vibrational properties of the plate are then defined by a sensitivity function, which describes the vibrational response of the plate at some point $\boldsymbol{x}$ due to the application of a a point-force at location $\tilde{\boldsymbol{x}}$ [26, 27]. The integral of the product of the CSD and sensitivity function across wavenumber space then defines the response of the structure at $\boldsymbol{x}$ as a function of the excitation frequency [26, 27, 30]. This approach has been validated against experimental measurements of small, thin, plates under low-speed TBL fields across a range of frequencies, showing good agreement. However, this method can also only define the response at a single location and so is similarly unsuitable when considering a distributed description of the response.

As shown, existing experiment-based evaluations of the vibrational response of structures under TBL pressure fields are practical only for single point evaluation. To produce a distributed prediction of the response across the structure, a high-frequency modelling approach is required.

Another important source of structure-borne vibration in DEP aircraft is the propeller array [31–33]. Here, disturbances in the aerodynamic forces acting on the propellers during operation cause vibrations which spread across the aircraft [34–36]. This effect is likely to be particularly influential in DEP aircraft, due to the large number of propulsors applied in these configurations [37]. Given the close proximity of the propulsors within DEP configurations, it is likely that the vibrational waves generated by each propulsor could meet and interfere with one another. For many closely-packed propulsors, these interactions could generate a complex vibrational response across the aircraft. To properly compute the

vibrational behaviour of DEP aircraft, the chosen approach must also be able to quantify the response of structures to multiple correlated point-forces and their interference effects.

1.2 Aims and objectives

The purpose of this thesis is thus to develop a high-frequency approach for modelling the vibrational response of structures to correlated pressure fields (such as the TBL) and correlated point-force excitations (representing excitations from the propeller arrays of DEP aircraft). To achieve this, the following steps must be completed:

- Review existing high-frequency modelling approaches and identify the most appropriate for calculating a distributed representation of the response of structures to correlated pressure fields and correlated point-force excitations.
- Develop the chosen high-frequency modelling approach to evaluate the response of structures to generic correlated pressure fields.
- Derive an appropriate source term to model the TBL pressure field within this approach.
- Produce a spatially distributed representation of the response of plates to TBL pressure fields with different material, boundary, and flow conditions.
- Develop the chosen high-frequency modelling approach to evaluate the response of structures to correlated point-force excitations.
- Calculate the vibrational response of plates to two, or more, correlated point-forces, including interference effects.

1.3 Thesis outline

The following is a brief summary of the remainder of this thesis:

In Chapter 2, the range of models developed for simulating the high-frequency behaviour of complex systems will be discussed. Here, the Dynamical Energy Analysis (DEA) is highlighted as the preferred approach, and the theory behind this method is examined in more detail. The properties of the TBL pressure field are also examined, and the models used to represent this field in prior studies are evaluated. Finally, vibrational interference effects are discussed, along with numerous real-world applications of this effect. In Chapter 3, the implementation of correlated pressure fields within DEA is discussed. This is initially demonstrated for a generic, homogeneous, pressure field, and an appropriate implementation for a TBL pressure field is then derived. This is then applied to model the excitation of a flat plate by a TBL pressure field under different material, boundary, and flow conditions. These results display a spatial variation in the Vibrational response, and the significance of this outcome is discussed in the context of prior studies. In Chapter 4, the vibrational response of flat plates to correlated point-force excitations is considered. Results for varying sources, locations, and phases are presented here. This includes a discussion of how the vibrational energy from the sources may be channelled in desirable ways based upon a careful tuning of the relative phase of each source. Following this, a demonstration of the implementation of these sources into DEA is presented. This includes the introduction of a simple algorithm that is used to define an appropriate initial boundary for these sources. Here, it is demonstrated that non-physical energy density solutions can arise from correlated point-force excitations, and the Husimi Density Function (HDF) is introduced as an approach to prevent this. Finally, in Chapter 5 the key outcomes of this work are summarised and potential opportunities for further study are outlined.

1.4 Author's Contribution

The following is a list of contributions made by the author in the remainder of this work.

- Generalisation of the existing DEA approach to consider generic correlated pressure-field excitations, as discussed in Section 3.2.
- Identification of the Corcos and Mellen models as valuable representations of the TBL pressure field, as discussed in Section 2.3, and derivation of appropriate phase-space representations of the Corcos and Mellen model for implementation within DEA, as dicussed in Section 3.4.
- Implementation of the discussed DEA extensions for correlated pressure fields within an existing DEA software for both small-patch and full body excitations.
- All results and discussion presented in Section 3.
- Definition of appropriate source correlation functions for multiple correlated point-force excitations and resulting free-space phase-space density distribution, as discussed in Section 4.1.
- Generalisation of this approach to N correlated point forces of arbitrary phase, as discussed in Section 4.2.
- Development of python code to plot the direct phase-space energy density due to N correlated point-forces, presented throughout Section 4.
- Implementation of correlated point-force excitations within the existing DEA software, including investigations into appropriate definitions of the initially excited region, as discussed in Section 4.3.

- Discussion of possible negative phase-space energy density values and development of the HDF representation of the phase-space energy density, as discussed in Section 4.4.

- All discussions of limitations of the

Chapter 2

2 Background and Literature Review

This chapter presents a summary of the prior literature and background knowledge necessary to appreciate the work performed and results presented in the remainder of this thesis. In Section 2.1, the range of high-frequency vibration modelling approaches will be discussed, with the DEA method highlighted as the preferred method. In Section 2.2, the application of this approach to define the vibrational response of structures to high-frequency point-force excitations is then introduced. To implement TBL excitations within DEA, an appropriate representation of the applied pressure field is required. By discussing the formation and behaviour of the TBL, in Section 2.3, the formation and properties of the TBL will be discussed, and the CSD will be introduced as an accurate representation of the TBL pressure field. Here, the range of available TBL CSD models will be evaluated, focusing particularly on their suitability for implementation within DEA. Finally, in Section 2.4, the result of interference effects between waves will be examined, along with some real-world applications of this phenomena.

2.1 Review of high-frequency vibration modelling approaches

Developed in the 1950s, based upon the earlier work of Hrennikoff [38] and Courant [39], the Finite Element Method (FEM) is by far the most popular approach for solving complex vibro-acoustic problems [40]. In FEM, the vibrational behaviour of the system is described by a set of wave equations defined acros the structural surface [40–42]. Given the continuous nature of the structures to be modelled, it is impossible to solve these equation directly. Instead, in FEM the structure is reproduced using a set of small, non-overlapping, elements [40, 43, 44]. Approximate solutions to the wave equations are then defined within each element by fitting a set of basis functions to the solutions to the overall wave equations found at a set of nodal points within the element [43–45]. This is typically performed using a weighted residual approach such as the Galerkin or Least Squares residual minimisation methods [44, 45]. A detailed description of the vibrational response across the structure is then found by connecting all of these elements to re-assemble the original structure. FEM has been applied to accurately predict the vibrational response of structures to external loads in numerous prior studies [46–48], including in aviation [49, 50]. The quality of the results produced is however dependent on the size of the mesh elements and the chosen basis functions. For example, increasing the number of mesh elements and choosing more suitable basis functions will enable FEM to resolve finer details in the structural response [40, 41]. When considering vibrational problems using FEM, the number of cells required to resolve the behaviour of the structure typically scales with the wavelength of the vibrations. For example, when applying a piecewise constant basis, typically six mesh cells per wavelength must be employed [51, 52]. Thus, as the excitation frequency increases the mesh must be increasingly refined to properly capture the vibrational response. At higher

frequencies the computational demand of this approach is thus extremely high and quickly beomes unfeasible due to technological constraints [53–55]. Besides these computational difficulties, there are also fundamental issues in applying FEM for recreating real-world high-frequency vibrational problems. In the high-frequency regime, the vibrational behaviour of structures is extremely sensitive to fine details in the structural properties [54,56]. This is important, as there are inevitable small variations in all structures due to manufacturing imperfections or differing environmental influences such as temperature or static load [55, 57, 58]. As such, seemingly identical structures can produce greatly differing vibrational responses under the same applied load. This problem could be accounted for by performing an ensemble of FEM calculations covering the range of possible structural imperfections, though this solution is unfeasible in practise. Thus FEM is unsuitable for solving high-frequency vibrational problems and a statistical treatment is required.

The most widely known of these statistical methods is Statistical Energy Analysis (SEA). Developed in the early 1960s to predict the vibrational behaviour of aerospace structures in a cost effective manner [59, 60], SEA has since been employed to solve a wide array of vibro-acoustic problems across automation, aviation, and architecture [61–65]. This approach aims to predict the ensemble-average vibrational behaviour, using calculations based upon the fewest possible details of the system [55]. When applying SEA, the structure is split into several subsystems either along natural structural boundaries or to separate regions with significantly different bulk properties [66, 67]. Within each subsystem, the structural properties are presumed to be approximately constant [55]. In addition, it is assumed that the damping within individual subsystems and the coupling between subsystems are sufficiently weak to accommodate diffuse vibrational fields within each subsystem [68]. These assumptions ensure that the vibrational behaviour within each subsystem is homogeneous and isotropic, and can be de-

scribed by a single mean vibrational energy value [52, 55, 69]. The weak coupling of internally uniform subsystems then facilitates a thermodynamic description of the flow of vibrational energy between subsystems. Here, the time-averaged power flow between two coupled subsystems i and j is given by

$$P_{ij} = \omega \left[\eta_{ij} E_i - \eta_{ji} E_j\right], \tag{2.1}$$

where E_i is the time-averaged mean vibrational energy in the i^{th} subsystem and η_{ij} is the coupling loss factor for energy flowing from subsystem i to subsystem j [55]. These coupling loss factors encompass all of the necessary details of the subsystems and are given by

$$\eta_{ij} = \frac{L_{ij} c_{g_i}}{\pi S_i \omega} \tau_{ij}, \tag{2.2}$$

where L_{ij} is the length of the boundary which couples the two subsystems and τ_{ij} is the mean transmission efficiency. S_i is then the area of subsystem i and c_{g_i} is the group velocity within this subsystem [67]. The power flow between subsystems i and j in SEA is illustrated by Figure 1.

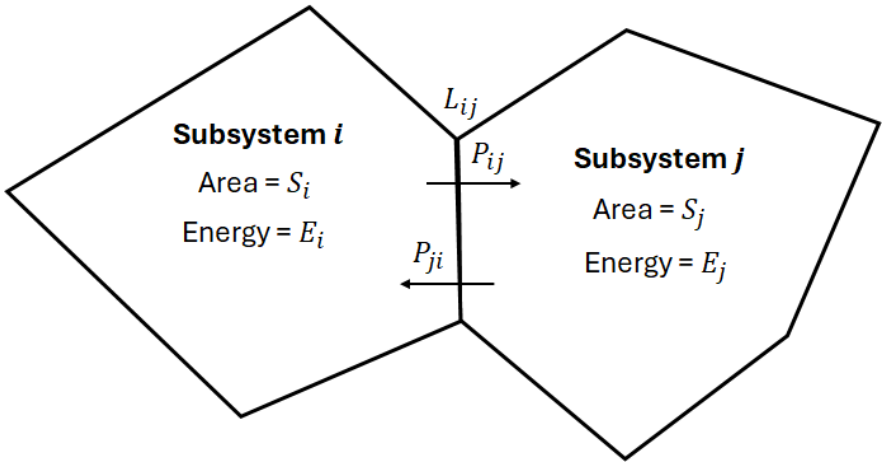

Figure 1: Demonstration of the power flow between subsystems i and j in SEA.

One may then produce a set of simultaneous equations encompassing the energy

flow between all subsystem pairs. By considering the boundary conditions of the system and conservation of energy, these may be solved to define the time-averaged equilibrium energy within each subsystem [55, 67].

The simplicity of this approach allows one to perform calculations very quickly at low computational cost, with only a limited knowledge of the system being modelled [55,70]. As a result, SEA is extremely useful in the early design phase of projects, where the full details of the structure are unknown [55]. By considering the individual power flow equations, the results of SEA calculations can also be useful to provide a rough estimate of the flow of energy around the system. In addition the usage of SEA to model the vibrational response of structures to TBL pressure fields is already being considered [71]. In this study, it is suggested that the power injected into each subsystem could be defined using an appropriate CSD for the TBL pressure field over wavenumber space. The overall vibrational response of the structure is then simply the solution to a set of simultaneous equations including these power terms. The SEA approach would then be capable of defining the vibrational behaviour of complex structures under TBL pressure fields in a simple and cost-effective manner. However, the vast simplification of the system employed by SEA brings numerous drawbacks. For example, the diffuse field approximation employed by SEA is often difficult to justify in real-world situations. This is especially true for large structures [72], or where passive damping treatments have been applied [73], such as aircraft fuselages [55]. This issue can somewhat be overcome however by applying Wave Intensity Analysis (WIA) [74]. Developed by Langley in 1992, this enhancement to SEA employs a Fourier series to approximate the directional dependence of the vibrational energy. This facilitates the relaxation of the diffuse field approximation within SEA, and provides enhanced accuracy when dealing with highly directional energy flows between subsystems [74]. Despite providing an improved description of the flow of vibrational energy between subsystems, under WIA the energy within each

subsystem is still required to be homogeneous. This is problematic, as it limits SEA solutions to a coarse description of the vibrational response of the structure. As such, SEA is unable to provide a detailed distribution of the vibrational energy within the system, or account for localised intense vibrations. This is important, as these focused points of vibrational energy are the main reason for failures in complex machinery [55]. In addition, the approach for defining an appropriate sub-division scheme for SEA calculations is highly challenging, requiring an expert knowledge of SEA sub-structuring techniques and of the system itself [52]. This is important, as the accuracy of the solutions produced using SEA is often highly dependent on the chosen subdivision configuration [66]. Thus, despite the speed and efficiency of the SEA method, the fragility of its assumptions in real-world situations and limited solution quality mean that an alternative high-frequency approach is often required.

One method which aims to combine the strengths of FEM and SEA is the Energy Flow Finite Element Analysis (EFEA) method. EFEA aims to apply an energy balance approach similar to an SEA subsystem treatment to finite element meshes [75]. EFEA begins by defining an appropriate equation of motion for the system and breaking down the structure into a finite element mesh. It is then assumed that the damping is sufficiently small to allow for a reverberant vibrational field to form within the structure, thus ignoring the direct contribution from the applied source [76]. The solution to the chosen equation of motion is then described as the sum of plane waves [77, 78]. The second approximation of this approach states that the energy flow is proportional to the gradient in the energy density [75]. By considering the conservation of energy within each mesh element, one can relate this energy flow to the balance between the external power entering the element and the power dissipated through damping [78, 79]. Applying this approximation, one can then form a 2^{nd} order differential equation for the energy density within the element. The boundary conditions for this formula

are then defined by evaluating the mean power flow across each of the element boundaries [77]. Han et al [80], have applied EFEA to predict the structural vibration of a flat plate excited by a TBL. In this study, the power injected into each cell is given in the same form as discussed by Maxit et al [71] for an SEA formulation. Here however, the simplicity of the structure ensures that the field is approximately homogeneous across the plate. The response of the plate is then considered by a single, averaged, energy density value and compared against an equivalent experimental study involving the measurement of the plate response using a scanning laser vibrometer. This comparison demonstrated that EFEA could produce a reasonable, though over-estimated, prediction of the vibrational behaviour of the plate at different frequencies. In a later study [81], the vibrational response of a ship's hull to a TBL pressure field was investigated using EFEA. Here, the injected power was defined based upon CFD calculations of the variance in the TBL properties across the structure. Unlike for SEA, the quality of the finite element mesh ensured that no further sub-structuring was necessary to capture the variance in the TBL parameters across the structure. The result of this calculation was then a distributed description of the vibrational response of the hull under the TBL. By repeating this process for different hull structures, EFEA was able to demonstrate how changes to the hull structure could effectively mitigate vibrations in the ship. These results are replicated here in Figure 2.

As shown by this study, the usage of finite element meshes enables EFEA to provide a far greater indication of the spatial variation in the vibrational energy compared to the subsystem-averaged results generated by SEA. In addition, the usage of finite element meshes enables the inclusion of local variations in the flow or structural properties [76, 82, 83]. The applied approximations however ensure that low-frequency finite element meshes are sufficient for EFEA calculations. Thus, the computational cost of EFEA is far smaller than an FEM evaluation of the same problem [75]. The applied reverberant wave assumption and associated

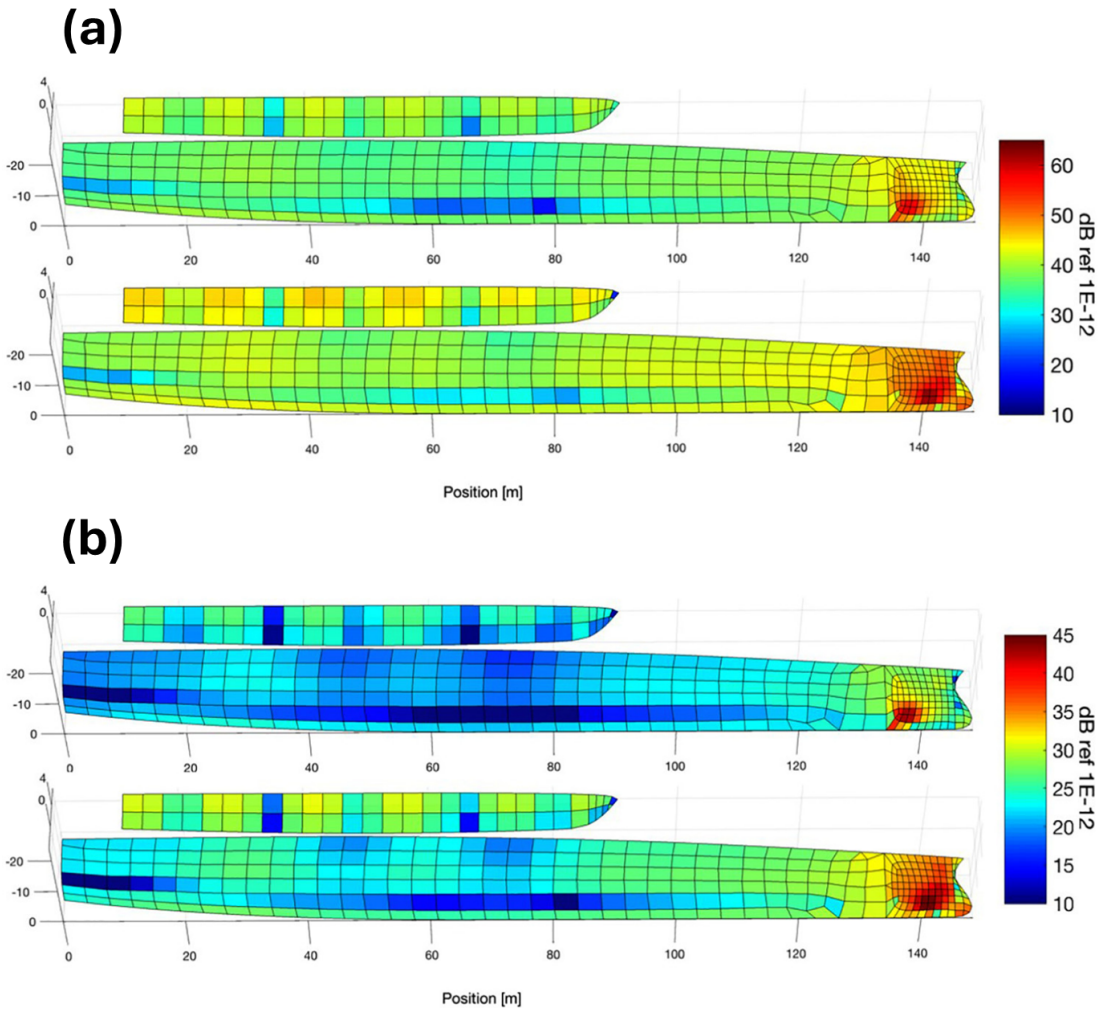

Figure 2: Vibrational response at 250 Hz (a) and 1 kHz (b) of the ship travelling at 20 knots (top of each plot) and 30 knots (bottom of each plot) calculated using EFEA [81].

neglect of the direct field contribution does however limit the effectiveness of this approach. In particular, EFEA underestimates the response close to the source point and significantly overestimates the result far from the excitation [76]. In addition, the assumed reverberant field breaks down in heavy damped cases, limiting the applicability of EFEA to minimally damped systems [77]. Even in these low damping cases the effectiveness of EFEA is questionable, as the minimal dissipation of energy ensures that the spatial variation in the energy density is effectively flat [76]. In such a case, the result produced is effectively equivalent to an SEA solution, which would be preferred due to its smaller computational cost.

Despite the improvements of this approach over FEM and SEA, these difficulties make EFEA impractical for these studies.

A very different approach for high-frequency vibro-acoustic modelling is the raytracing method. Initially developed in the late 1960s for room acoustic modelling and computer image generation [84–86], raytracing has more recently been applied to vibro-acoustic modelling. In this approach, the vibrational energy distribution is calculated by modelling the motion of rays which "carry" vibrational energy from the source across the domain. To begin, identical rays are emitted isotropically from the source point [72]. These rays follow classical ray behaviour, propagating in straight lines, reflecting specularly at structural boundaries, and losing energy over time due to damping and scattering effects [73, 84]. The total energy found at some location $\boldsymbol{r} \in \Omega$ within the structure is then the sum of contributions from all rays that have passed through this point in their lifetime [66,72,87]. Thus, with sufficient rays, the raytracing approach can construct a complete map of the vibrational response to the applied load. Figure 3 provides a visual demonstration of the raytracing procedure.

Unlike SEA, raytracing incorporates a great amount of detail of the structure being modelled [52]. This allows raytracing to accurately model the vibrational response of detailed structures with complex transmission properties [66, 72, 88]. This is particularly true for highly damped structures, where the assumptions of the SEA approach break down [72]. By considering the motion of the rays as they pass each point, raytracing can also accurately describe the directionality of the wave energy at each point. The effectiveness of the raytracing approach for vibrational behaviour of structures has been demonstrated by Chae and Ih [72]. Here, raytracing is applied to model the vibrational response of a single flat plate, as well as a coupled pair of plates, to point-force excitations. These results were compared against equivalent SEA and EFEA calculations, along with an analytical solution. For each case, the SEA result gives a uniform response

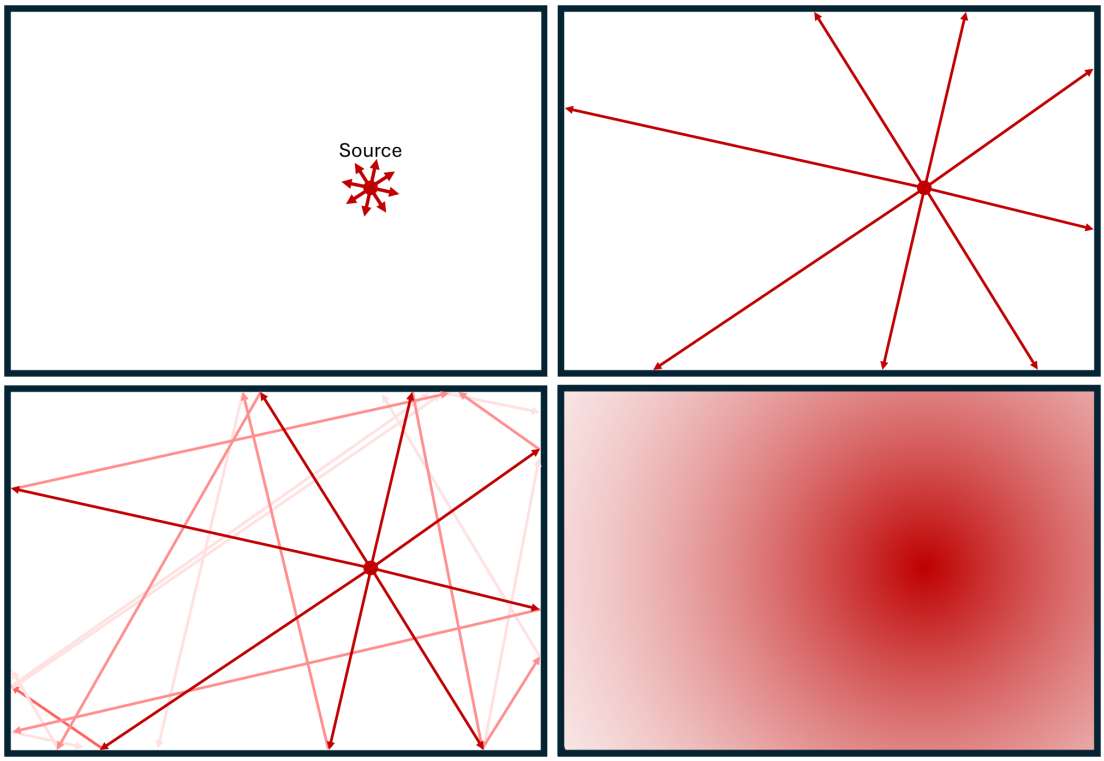

Figure 3: Visual demonstration of the raytracing procedure.

across each plate and the EFEA demonstrates characteristic accuracy issues. The raytracing result however shows an excellent match to the analytical solution, particularly for higher damped cases. The procedure for tracking the motion of the rays is however rather cumbersome. This is especially problematic in low damped cases, where the ray lifetime is rather long, or in complex geometries where a vast number of rays are required to fully resolve the structural surface [52, 69]. Thus, despite the excellent accuracy of this approach, these computational costs limit its practicality for more complex systems.

The final approach discussed here aims to combine the advantages of the raytracing and SEA methods. Introduced by Tanner in 2009, Dynamical Energy Analysis (DEA) is a raytracing-like approach applied on low-frequency finite element meshes [66]. Unlike other raytracing approaches, in DEA the motion of the rays is formulated on a boundary coordinate scheme. This ray motion is considered iteratively, with each iteration covering the motion of the rays between

successive encounters with the boundary. To compute how the rays travel across iterations, a linear transfer operator is applied [52, 66]. To properly model the motion of the rays, the transfer operator incorporates details such as changes in material properties and boundary conditions. A representation of the application of the transfer operator on a single ray propagation is demonstrated in Figure 4.

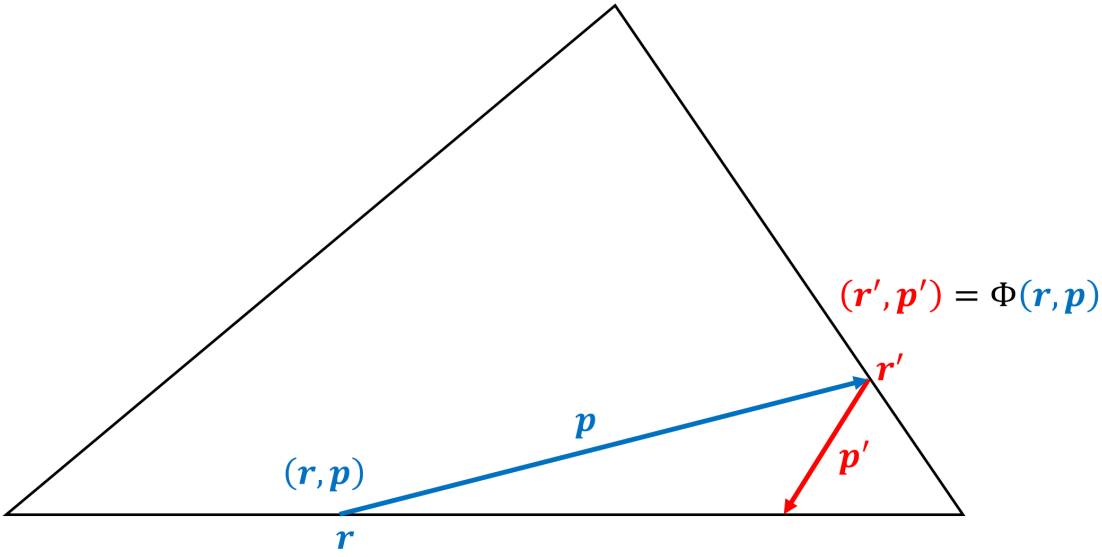

Figure 4: Application of the transfer operator Φ to define the new position and propagation of a ray due to a reflection at a structural boundary.

This transfer operator approach is far less computationally taxing than generating a continuous description of the motion of the rays across the structure. For computational purposes, this transfer operator is expressed as a matrix equation using a set of basis functions. The lowest order representation of this operator is similar to an SEA/EFEA implementation, with energy flowing between adjacent elements dependent on their relative energy balance [54, 66]. Higher order implementations then enhance the transfer operator to enable more detailed energy flows. This greatly improves the quality of the solutions produced, and enables DEA to properly account for complex geometric features, source directionality, and varying material properties in the structures studied [66]. This enhanced solution also facilitates the relaxation of the requirement for a homogeneous and

diffuse wave field within subsystems [56]. As a result, DEA is able to handle problems with high damping or strong directionality, where these approximations fail. This also ensures that the choice of sub-structuring approach is no longer critical to the quality of the solution, enabling a great deal more freedom when subdividing the structure for DEA calculations compared to SEA [54, 89]. For an increasing number of basis functions, the DEA solution demonstrates pointwise convergence to a full raytracing solution, meaning that DEA is effectively an interpolation between SEA and raytracing approaches [89]. In general, these computations require a very small number of basis functions, meaning that DEA can produce results of comparable accuracy to raytracing with a far smaller computational cost [66].

DEA has been employed to model the vibrational behaviour of complex structures in several prior studies. In the first, the vibrational behaviour of a Range Rover's aluminium shock tower was evaluated using DEA and compared against a Nastran FEM solver [89]. Here, the DEA model showed strong agreement with the FEM result, and was able to demonstrate geometry dependent features in the response that approaches such as SEA would fail to resolve. In a similar study, both DEA and FEM were applied to predict the response of a car floor to an applied point-force [56]. Here, the DEA solution again showed strong agreement, with results within 6% of the FEM prediction for a low damped case and within 12% for a higher damped case. In another study, the convergence of the DEA approach was investigated based upon predictions of the vibrational response of a reduced car model due to a point-force excitation [52]. Here, a result generated using just four Legendre polynomials was able to match the closest fit to an equivalent FEM calculation, demonstrating the fast convergence of this method. DEA has also been applied to predict the vibrational response of numerous other complex structures, such as a tractor chassis [53] and a double hull structure [69]. The distributed vibrational response of several complex structures calculated using

DEA are demonstrated in Figure 5.

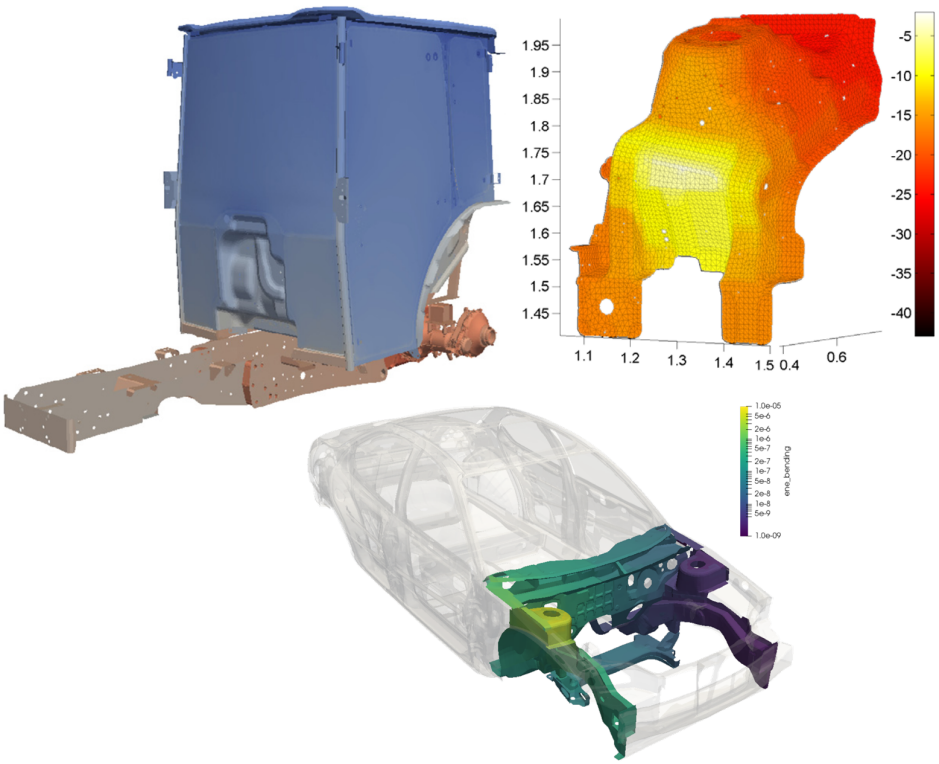

Figure 5: Previous DEA vibro-acoustic simulations of a tractor chassis (top-left) [53], a vehicle shock tower (top-right) [69], and a car chassis section (bottom) [52].

However, unlike SEA and EFEA, the DEA approach has currently only been applied to model the response of structures to individual point or monodirectional line sources. To be able to model the response of structures to TBL excitations, DEA must be extended to implement excitations by correlated pressure fields. To enable this, one must first understand how point-force excitations are modelled within this approach.

2.2 Point-Force Excitations in DEA

DEA was developed to consider the excitation of structures by high-frequency, continuous, monochromatic, point-force loads [66]. In this situation, the structure is excited by a point-force which oscillates periodically at a fixed driving frequency

ω without end. This ensures that the problem is stationary in time, enabling the description of the system in the frequency domain [90]. When attempting to define the vibrational response of the structure under the applied excitation, it is assumed that the behaviour of the system may be characterised by a linear wave operator $\hat{H}$, which describes the overall wave dynamics [66]. The form of $\hat{H}$ is chosen in each case to best capture the details of the structure, along with the type of vibrational waves being excited. In the general case, the response of a two-dimensional system to a point-force excitation of unit magnitude applied at $\boldsymbol{r}_0 \in \Omega$ is defined by solving

$$\left(\hat{H} + \omega^2\right) G\left(\boldsymbol{r}, \boldsymbol{r}_0, \omega\right) = -\delta(\boldsymbol{r} - \boldsymbol{r}_0). \tag{2.3}$$

Here, $G\left(\boldsymbol{r}, \boldsymbol{r}_0, \omega\right)$ is the Green function, which represents the vibration amplitude of the plate at a point $\boldsymbol{r} \in \Omega$ induced by the applied excitation at $\boldsymbol{r}_0 \in \Omega$. If one was to model the vibrational behaviour of a structure by considering the excitation of plane waves within a thin membrane, the appropriate form of the linear wave operator is given by $\hat{H} = c^2\Delta$, where c is the vibrational wave velocity [66]. In this case, the Green function is the solution to the Helmholtz equation

$$\left(\Delta + k^2\right) G_H\left(\boldsymbol{r}, \boldsymbol{r}_0, \omega\right) = -\frac{1}{c^2}\delta(\boldsymbol{r} - \boldsymbol{r}_0), \tag{2.4}$$

where $k = \omega/c$ is the vibrational wavenumber. However, in this study the excitation of bending waves within structures which may be represented by a set of thin, plate-like, elements is considered. In this case, the behaviour of the system is modelled using Kirchhoff-Love thin plate theory [90]. This theory assumes that the plate material is homogeneous and isotropic, the plate is initially flat, and the plate thickness does not vary due to deformation [91]. In addition, it is assumed that the out-of-plane displacement of the plate is negligible compared to the plate thickness [92]. When applying Kirchhoff-Love thin plate theory, the

linear wave operator is given by $\hat{H} = -\frac{D}{\varrho h}\Delta^2$, where ϱ is the density of the plate and h is its thickness. In addition, $D = \frac{Eh^3}{12(1-\nu^2)}$ is the bending stiffness, with E the Young's modulus and ν the Poisson ratio [93]. The Green function describing the response of the plate is then the solution to the bi-harmonic equation [66]

$$\left(\Delta^2 - k^4\right) G_B\left(\boldsymbol{r}, \boldsymbol{r}_0, \omega\right) = \frac{\varrho h}{D}\delta(\boldsymbol{r} - \boldsymbol{r}_0), \tag{2.5}$$

where $k = \left(\frac{\varrho h}{D}\omega^2\right)^{1/4}$ is now the bending wave vibrational wavenumber. To solve these equations, the Green function is split into two terms [90, 94]. The first is the free-space part of the Green function G_0, which captures the direct response at each location within the structure to the applied driving force. The second is the homogeneous part of the Green function G_h, which captures all indirect contributions to the response of the plate at each location to the applied driving force. This then encompasses the contributions made by vibrational waves which are scattered at the structural boundary and propagate back across the structure, providing additional vibrational energy contributions across the plate. The overall Green function may be written as the sum of these direct and homogeneous parts by

$$G\left(\boldsymbol{r}, \boldsymbol{r}_0, \omega\right) = G_0\left(\boldsymbol{r}, \boldsymbol{r}_0, \omega\right) + G_h\left(\boldsymbol{r}, \boldsymbol{r}_0, \omega\right). \tag{2.6}$$

The approaches to determine these components are described in Sections 2.2.1 and 2.2.2 respectively.

2.2.1 The free-space solution

As discussed, the free-space part of the Green function is the solution to equation (2.3) in an unbounded domain [90]. Before solving this equation, it is useful to define the free-space solution to the Helmholtz equation

$$\left(\Delta + k^2\right) G_{0H}\left(\boldsymbol{r}, \boldsymbol{r}_0, \omega\right) = -\frac{1}{c^2}\delta(\boldsymbol{r} - \boldsymbol{r}_0). \tag{2.7}$$

The following is a summary of the approach detailed by Smith in [95] to solve equation (2.7). Firstly, by converting into polar coordinates, this equation can be rewritten as

$$\left(\frac{\partial^2}{\partial r^2} + \frac{1}{r}\frac{\partial}{\partial r} + \frac{1}{r^2}\frac{\partial^2}{\partial \theta^2} + k^2\right) G_{0H}\left(r, \omega\right) = -\frac{1}{c^2}\frac{1}{r}\delta(r)\delta(\theta - \theta') \tag{2.8}$$

where $r = |\boldsymbol{r} - \boldsymbol{r}_0|$. Assuming that the Green function has no angular dependence, $\frac{\partial^2 G_{0H}}{\partial \theta^2} = 0$, removing the θ dependence from the left-hand side. The θ dependence on the right-hand side may then be removed by integrating both sides with respect to θ' across the range $\theta' \in [0, 2\pi]$. The result is then given by

$$\left(\frac{\partial^2}{\partial r^2} + \frac{1}{r}\frac{\partial}{\partial r} + k^2\right) G_{0H}\left(r, \omega\right) = -\frac{1}{c^2}\frac{\delta(r)}{2\pi r}. \tag{2.9}$$

Outside of $\boldsymbol{r} = \boldsymbol{r}_0$ the above is Bessel's equation, which has solutions of the form

$$G_{0H}\left(r, \omega\right) = AH_0^{(1)}(kr) + BH_0^{(2)}(kr) \tag{2.10}$$

where $H_0^{(1)}$ and $H_0^{(2)}$ are the zeroth order Hankel functions of the first and second kind respectively. To define appropriate terms for A and B, the Sommerfeld radiation condition is used [96], which states

$$\lim_{r\to\infty} \sqrt{r}\left(\frac{\partial}{\partial r} - ik\right) G_{0H}(r, \omega) = 0. \tag{2.11}$$

This condition ensures that for a scalar field to satisfy the Helmholtz equation, the energy which is radiated from the source must scatter to infinity in $\mathbb{R}^2$, with no energy radiated back into the field [97]. One can demonstrate that the result of substituting the zeroth order Hankel function of second kind into equation (2.11) is a function which is unbounded as $r \to \infty$. Thus, for equation (2.10)

to follow the Sommerfeld radiation condition, it is necessary that $B = 0$. Upon examination of the remaining term as $r \to 0$, one can deduce that $A = -i/4$ [95]. The free-space part of the Green function for the Helmholtz equation is then given by

$$G_{0H}(\boldsymbol{r}, \boldsymbol{r}_0, \omega) = -\frac{i}{4} H_0^{(1)}(k\,|\boldsymbol{r} - \boldsymbol{r}_0|). \tag{2.12}$$

The zeroth order Hankel function of the first kind is itself given by $H_0^{(1)}(z) = J_0(z) + iY_0(z)$ where J_0 and Y_0 are the zeroth order Bessel functions of the first and second kind respectively [98]. These are given by [99] as

$$\begin{aligned} J_n(z) &= \sum_{s=0}^{\infty} \frac{(-1)^s}{s!(n+s)!} \left(\frac{z}{2}\right)^{n+2s} \\ Y_n(z) &= \frac{J_n(z)\cos(n\pi) - J_{-n}(z)}{\sin(n\pi)}. \end{aligned} \tag{2.13}$$

To simplify future formulas, an approximated form of these functions is desired. As DEA is applied to high-frequency problems, it is appropriate to assume that the wavelength of the excitation is infinitesimal compared to the separation between the source and receiver locations in the majority of cases. As such, the far-field approximation is applied to equation (2.12), where $k\,|\boldsymbol{r} - \boldsymbol{r}_0| \to \infty$, leaving

$$G_{0H}(\boldsymbol{r}, \boldsymbol{r}_0, \omega) \approx -\frac{1}{4}\sqrt{\frac{2}{\pi k\,|\boldsymbol{r} - \boldsymbol{r}_0|}}\, e^{i\left(k|\boldsymbol{r}-\boldsymbol{r}_0| - \frac{\pi}{4}\right)}. \tag{2.14}$$

Returning to the biharmonic equation, equation (2.5), factorising the left-hand side gives

$$\left(\Delta - k^2\right)\left(\Delta + k^2\right) G_{0B}(\boldsymbol{r}, \boldsymbol{r}_0, \omega) = \frac{\varrho h}{D}\delta(\boldsymbol{r} - \boldsymbol{r}_0). \tag{2.15}$$

The Green function solution to this equation may be written as

$$G_{0B} = \alpha G_{0H} + \beta G_{0M} \tag{2.16}$$

where G_{0M} is the Green function of the modified Helmholtz equation [90, 95],

$$\left(\Delta - k^2\right) G_{0M}(\boldsymbol{r}, \boldsymbol{r}_0, \omega) = \frac{1}{c^2}\delta(\boldsymbol{r} - \boldsymbol{r_0}) \tag{2.17}$$

which is given by

$$G_{0M}(\boldsymbol{r}, \boldsymbol{r}_0, \omega) = -\frac{1}{2\pi} K_0(k\,|\boldsymbol{r} - \boldsymbol{r}_0|), \tag{2.18}$$

where K_0 is the zeroth-order modified Bessel function. By substituting equation (2.16) into equation (2.15) and forming simultaneous equations for terms with different orders of k^2, it can be shown that $\alpha = -\beta = 1/(2k^2)$ [95], leaving

$$G_{0B}(\boldsymbol{r}, \boldsymbol{r}_0, \omega) = \frac{\varrho h}{2Dk^2}\left(\frac{i}{4} H_0^{(1)}(k\,|\boldsymbol{r} - \boldsymbol{r}_0|) - \frac{1}{2\pi} K_0(k\,|\boldsymbol{r} - \boldsymbol{r}_0|)\right). \tag{2.19}$$

The second term decays exponentially with k and so disappears in the high-frequency limit [100]. Under the far-field approximation, the free-space part of the Green function for the biharmonic equation is thus given by

$$G_{0B}(\boldsymbol{r}, \boldsymbol{r}_0, \omega) \approx \frac{\varrho h}{8Dk^2}\sqrt{\frac{2}{\pi k\,|\boldsymbol{r} - \boldsymbol{r}_0|}}\, e^{i\left(k|\boldsymbol{r}-\boldsymbol{r}_0| - \frac{\pi}{4}\right)}. \tag{2.20}$$

As described in Section 2.1, interpreting the vibrational response of structures to applied loads using DEA involves describing the flow of energy induced by the source across the structure. As such, it is necessary that the solution produces a measure of both the spatial distribution and the flow of the vibrational energy throughout the system [101]. To simultaneously express both the spatial distribution and flow of energy across the system, a phase-space representation of the vibrational energy distribution is required. The phase-space corresponding to a two-dimensional system is four-dimensional, consisting of two position

coordinates $\boldsymbol{r} = (x, z)$ and two momentum coordinates $\boldsymbol{p} = (p_x, p_z)$ [53, 102]. To produce a phase-space representation of the vibrational energy, the Wigner Distribution Function (WDF) of the plate response must be defined [103]. Developed to describe the dynamics of quantum systems in phase-space [104], the WDF has since found widespread application in modelling light propagation in optical signals [105]. In the present case, the WDF is calculated from the correlation function of the vibrational response [102] which describes the level of coherence in the vibrational response of the structure at two separate locations $\boldsymbol{r}_1, \boldsymbol{r}_2 \in \Omega$. This correlation function can be defined from the Green function of the vibrational response by [106]

$$\Gamma_0\left(\boldsymbol{r}_1, \boldsymbol{r}_2, \omega\right) = \int\int G_0\left(\boldsymbol{r}_1, \boldsymbol{r}_1', \omega\right) \Gamma_f(\boldsymbol{r}_1', \boldsymbol{r}_2') G_0^*\left(\boldsymbol{r}_2, \boldsymbol{r}_2', \omega\right)\, d\boldsymbol{r}_1'\, d\boldsymbol{r}_2', \tag{2.21}$$

where the superscript $*$ denotes the complex conjugate. In this equation, $\Gamma_f(\boldsymbol{r}_1', \boldsymbol{r}_2')$ is the correlation in the force applied to the plate at positions $\boldsymbol{r}_1', \boldsymbol{r}_2' \in \Omega$. Typically, this describes a distributed pressure field, which applies force across a wide region of the structure. A point source excitation is thus a special case in which the force is applied at a single location, and has a magnitude of zero elsewhere. The correlation function relating the forces applied at positions $\boldsymbol{r}_1'$ and $\boldsymbol{r}_2'$ when considering a point-force applied at some position $\boldsymbol{r}_0 \in \Omega$, this is simply given by

$$\Gamma_f(\boldsymbol{r}_1', \boldsymbol{r}_2') = \delta(\boldsymbol{r}_1' - \boldsymbol{r}_0)\delta(\boldsymbol{r}_2' - \boldsymbol{r}_0). \tag{2.22}$$

As the force applied is zero at all locations except $\boldsymbol{r}_0$, then there is a non-zero correlation only where both $\boldsymbol{r}_1'$ and $\boldsymbol{r}_2'$ are found at this location. The WDF is then derived by taking the Wigner transform of equation (2.21) [107]. The Wigner transform of a generic correlation function $F(\boldsymbol{r}_1, \boldsymbol{r}_2)$, is given by

$$W\left(\boldsymbol{r}, \boldsymbol{p}, \omega\right) = \int_{\mathbb{R}} F\left(\boldsymbol{r} + \frac{\boldsymbol{\xi}}{2}, \boldsymbol{r} - \frac{\boldsymbol{\xi}}{2}\right) e^{-i\boldsymbol{p}\cdot\boldsymbol{\xi}}\, d\boldsymbol{\xi}. \tag{2.23}$$

Here, the points $\boldsymbol{r}_1$ and $\boldsymbol{r}_2$ have been rewritten in terms of their mean position $\boldsymbol{r} = \frac{1}{2}(\boldsymbol{r}_1 + \boldsymbol{r}_2)$ and separation $\boldsymbol{\xi} = \boldsymbol{r}_1 - \boldsymbol{r}_2$. Taking the Wigner transform of both sides of equation (2.21) then gives

$$W_0(\boldsymbol{r}, \boldsymbol{p}) = \int\int \mathcal{G}(\boldsymbol{r}, \boldsymbol{p}; \boldsymbol{r'}, \boldsymbol{p'}) W_\Gamma(\boldsymbol{r'}, \boldsymbol{p'})\, d\boldsymbol{r'}\, d\boldsymbol{p'}. \tag{2.24}$$

Here, $\mathcal{G}$ is the phase-space propagator [108]

$$\begin{aligned} &\mathcal{G}(\boldsymbol{r}, \boldsymbol{p}; \boldsymbol{r'}, \boldsymbol{p'}) = \\ &\int\int e^{-i\boldsymbol{p}\cdot\boldsymbol{\xi} + i\boldsymbol{p'}\cdot\boldsymbol{\xi'}} G\left(\boldsymbol{r} + \frac{\boldsymbol{\xi}}{2}, \boldsymbol{r'} + \frac{\boldsymbol{\xi'}}{2}\right) G^*\left(\boldsymbol{r} - \frac{\boldsymbol{\xi'}}{2}, \boldsymbol{r'} - \frac{\boldsymbol{\xi}}{2}\right) d\boldsymbol{\xi}\, d\boldsymbol{\xi'}. \end{aligned} \tag{2.25}$$

Assuming homogeneity and isotropy in the properties of the structure, the response at a point $\boldsymbol{r}$ to some excitation applied at $\boldsymbol{r'}$ will depend only on the separation of the points $|\boldsymbol{r} - \boldsymbol{r'}|$, rather than their actual positions. In this case, we introduce the variable $K(\boldsymbol{r} - \boldsymbol{r'}) = G(\boldsymbol{r}, \boldsymbol{r'})$, and following [107] equation (2.25) becomes

$$\mathcal{G}(\boldsymbol{r}, \boldsymbol{p}; \boldsymbol{r'}, \boldsymbol{p'}) = \delta(\boldsymbol{p} - \boldsymbol{p'}) \int e^{-i\boldsymbol{p}\cdot\boldsymbol{\xi}} K\left(\boldsymbol{r} - \boldsymbol{r'} + \frac{\boldsymbol{\xi}}{2}\right) K^*\left(\boldsymbol{r} - \boldsymbol{r'} - \frac{\boldsymbol{\xi}}{2}\right) d\boldsymbol{\xi}. \tag{2.26}$$

The phase-space propagator for the excitation of a flat plate can be found by substituting equation (2.20) into this equation to give

$$\mathcal{G}(\boldsymbol{r}, \boldsymbol{p}; \boldsymbol{r'}, \boldsymbol{p'}) = \frac{\varrho^2 h^2}{32\pi D^2 k^5} \delta(\boldsymbol{p} - \boldsymbol{p'}) \int \frac{e^{ik\left(\left|\boldsymbol{r} - \boldsymbol{r'} + \frac{\boldsymbol{\xi}}{2}\right| - \left|\boldsymbol{r} - \boldsymbol{r'} - \frac{\boldsymbol{\xi}}{2}\right|\right) - i\boldsymbol{p}\cdot\boldsymbol{\xi}}}{\sqrt{\left|\boldsymbol{r} - \boldsymbol{r'} + \frac{\boldsymbol{\xi}}{2}\right| \left|\boldsymbol{r} - \boldsymbol{r'} - \frac{\boldsymbol{\xi}}{2}\right|}}\, d\boldsymbol{\xi} \tag{2.27}$$

Assuming that the correlation in the vibrational response decays quickly with increasing separation, contributions to the phase-space propagator will be made

chiefly by small values of $\boldsymbol{\xi}$. As such, parts of the integrand may be approximated as the leading terms of their corresponding Taylor expansions about $\boldsymbol{\xi} = 0$ up to first order [106], as higher order contributions will be negligible by comparison. As a result, it can be approximated that

$$\begin{aligned} \left|\boldsymbol{r} + \frac{\boldsymbol{\xi}}{2} - \boldsymbol{r}'\right| \left|\boldsymbol{r} - \frac{\boldsymbol{\xi}}{2} - \boldsymbol{r}'\right| &\approx |\boldsymbol{r} - \boldsymbol{r}'|^2 \\ \left|\boldsymbol{r} + \frac{\boldsymbol{\xi}}{2} - \boldsymbol{r}'\right| - \left|\boldsymbol{r} - \frac{\boldsymbol{\xi}}{2} - \boldsymbol{r}'\right| &\approx \frac{\boldsymbol{r} - \boldsymbol{r}'}{|\boldsymbol{r} - \boldsymbol{r}'|} \cdot \boldsymbol{\xi} \end{aligned} \tag{2.28}$$

Substituting these terms into equation (2.27) and solving then leaves

$$\mathcal{G}(\boldsymbol{r}, \boldsymbol{p}; \boldsymbol{r'}, \boldsymbol{p'}) = \frac{\varrho^2 h^2}{32\pi D^2 k^5} \frac{e^{-\mu|\boldsymbol{r}-\boldsymbol{r}'|}}{|\boldsymbol{r} - \boldsymbol{r}'|} \delta(\boldsymbol{p} - \boldsymbol{p}') \delta\left(\boldsymbol{p} - k\frac{\boldsymbol{r} - \boldsymbol{r}'}{|\boldsymbol{r} - \boldsymbol{r}'|}\right) \tag{2.29}$$

In this equation, $e^{-\mu|\boldsymbol{r}-\boldsymbol{r}'|}$ is added to account for damping losses, with μ the attenuation factor. In addition, the fraction within the delta function is a unit vector, thus ensuring that the phase-space propagator is non-zero only for $|\boldsymbol{p}| = k$. This is important, as when describing the vibrational response in terms of propagating rays, the energy of these rays is dependent on the magnitude of the momentum and the excitation frequency [53,90]. This property thus implies that the plate acts as a filter, ensuring that all vibrational waves generated by an external excitation applied at a fixed frequency will carry the same energy.

Returning to equation (2.24), W_Γ is the Wigner transform of the point-force correlation function Γ_f. This is found by substituting equation (2.22) into equation (2.23) to give

$$W_\Gamma(\boldsymbol{r}, \boldsymbol{p}, \omega) = \int \delta\left(\boldsymbol{r} + \frac{\boldsymbol{\xi}}{2} - \boldsymbol{r}_0\right) \delta\left(\boldsymbol{r} - \frac{\boldsymbol{\xi}}{2} - \boldsymbol{r}_0\right) e^{-i\boldsymbol{p}\cdot\boldsymbol{\xi}}\, d\boldsymbol{\xi}. \tag{2.30}$$

The delta functions in this integral are equivalent, besides the sign of the $\boldsymbol{\xi}$ term. Both delta functions can give non-zero values simultaneously only in the case

that $\boldsymbol{\xi} = 0$. In this case

$$W_\Gamma(\boldsymbol{r}, \boldsymbol{p}) = \delta(\boldsymbol{r} - \boldsymbol{r}_0). \tag{2.31}$$

Substituting this solution, along with equation (2.29) into equation (2.24) then gives

$$\begin{aligned} &W_0(\boldsymbol{r}, \boldsymbol{p}) = \\ &\frac{\varrho^2 h^2}{32\pi D^2 k^5} \int\int \frac{e^{-\mu|\boldsymbol{r}-\boldsymbol{r}'|}}{|\boldsymbol{r}-\boldsymbol{r}'|} \delta(\boldsymbol{p}-\boldsymbol{p}') \delta\left(\boldsymbol{p} - k\frac{\boldsymbol{r}-\boldsymbol{r}'}{|\boldsymbol{r}-\boldsymbol{r}'|}\right) \delta(\boldsymbol{r}'-\boldsymbol{r}_0)\, d\boldsymbol{r}'\, d\boldsymbol{p}'. \end{aligned} \tag{2.32}$$

Here, each integral can be solved by evaluating the relevant delta function. The resultant WDF for the response of a flat plate to a point-force excitation is given by

$$W_0(\boldsymbol{r}, \boldsymbol{p}) = \frac{\varrho^2 h^2}{32\pi D^2 k^5} \frac{e^{-\mu|\boldsymbol{r}-\boldsymbol{r}_0|}}{|\boldsymbol{r}-\boldsymbol{r}_0|} \delta\left(\boldsymbol{p} - k\frac{\boldsymbol{r}-\boldsymbol{r}_0}{|\boldsymbol{r}-\boldsymbol{r}_0|}\right). \tag{2.33}$$

In a ray description, the WDF effectively defines the probability that a ray will occupy a set location in phase-space [53]. For an ensemble of rays, the WDF is then the density of rays that occupy each phase-space location. The overall ray density may then be related to the distribution of vibrational energy at each phase-space location across the plate. For this, the phase-space density is considered, which is given by [90] as

$$\rho_0(\boldsymbol{r}, \boldsymbol{p}) = \frac{1}{2} \varrho h \omega^2 W_0(\boldsymbol{r}, \boldsymbol{p}). \tag{2.34}$$

The direct contribution to the phase-space density due to a point-force excitation is then given by

$$\rho_0(\boldsymbol{r}, \boldsymbol{p}, \omega) = \frac{1}{64\pi} \frac{\varrho^2 h^2}{Dk} \frac{e^{-\mu|\boldsymbol{r}-\boldsymbol{r}_0|}}{|\boldsymbol{r}-\boldsymbol{r}_0|} \delta\left(\boldsymbol{p} - k\frac{\boldsymbol{r}-\boldsymbol{r}_0}{|\boldsymbol{r}-\boldsymbol{r}_0|}\right). \tag{2.35}$$

Given that $|\boldsymbol{p}| = k$, the delta function also ensures that energy density contributions are only made to phase-space locations where $\hat{\boldsymbol{p}} = \frac{\boldsymbol{r}-\boldsymbol{r}_0}{|\boldsymbol{r}-\boldsymbol{r}_0|}$. This means that contributions to the phase-space density at $(\boldsymbol{r}, \boldsymbol{p})$ are made only if $\boldsymbol{p}$ points directly from the source to the receiver location. As prescribed, the free-space contribution thus only accounts for the direct influence of the source on the plate, without reflection or scattering contributions. The contributions of these terms are then captured by the homogeneous solution.

2.2.2 The homogeneous solution

Prior to any scattering at the structural boundary, the initial phase-space density distribution across the structure is given by the free-space contribution shown in equation (2.35). To determine the additional contributions from energy density scattered at the boundary Γ, a raytracing approach is applied. In this method, the flow of vibrational energy across the structure is captured by the motion of rays through phase-space. As discussed in Section 2.1, in DEA the structure Ω is represented using a finite element mesh made up of N sub-domains Ω_i with $i = 1, 2, ..., N$. When applying a raytracing approach to a mesh grid, the boundary Γ now covers the line segments of all mesh element boundaries [69]. This means that the boundary between two cells is actually made up of two segments pointing in opposite directions, each of which captures the energy density flowing into their constituent mesh element across this boundary. By comparison, the structural boundaries are made up of only a single element, representing the energy density that is reflected at the structural boundary back into the structure. A diagram of the DEA mesh of a simple structure, highlighting these features, is illustrated in Figure (6).

The phase-space density is then expressed only on Γ, using a boundary coordinate representation of phase-space. Here, each phase-space location is expressed in two dimensions $\boldsymbol{X_s} = (s, p_s)$ where s is the location on Γ and p_s denotes the ray

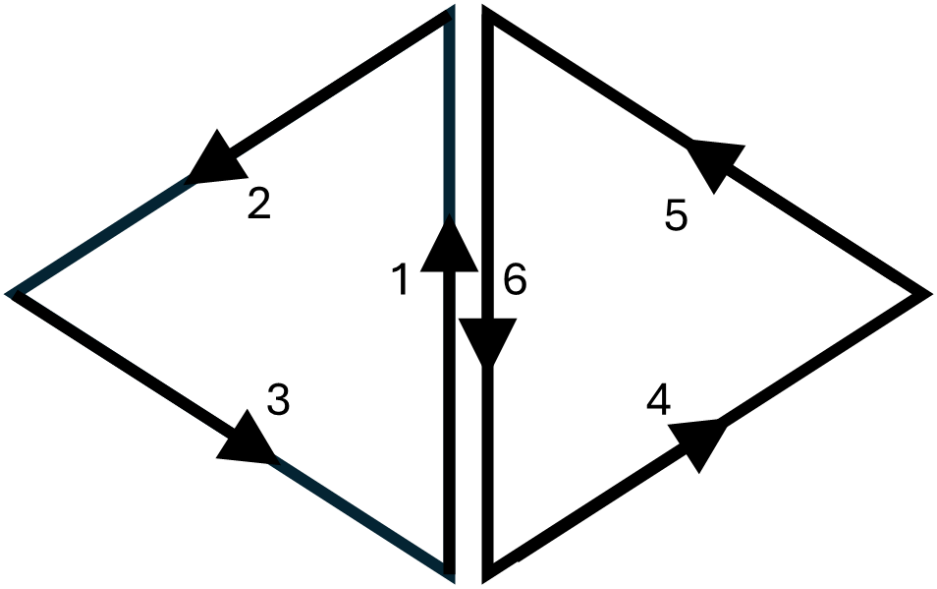

Figure 6: Labelled edges of two connected elements within the DEA mesh. Note that edges 1 and 6 refer to the same edge, representing the outward facing boundary segments for their constituent elements along this edge.

momentum component which is tangential to the local boundary [66]. The first step towards defining the homogeneous contribution to the phase-space density is thus to define an initial boundary density distribution.

To do this, firstly, an initially excited boundary region $\Gamma_{src} \subset \Gamma$, is selected. Here, Γ_{src} represents an appropriate subset of the overall boundary mesh which encapsulates the excitation. For a point-force excitation this is typically the outward-flowing boundary segments of the element containing the excitation. Appropriate boundaries for pressure fields and groups of correlated points are discussed in Chapters 3 and 4 respectively. Once this boundary is defined, the energy density distribution across Γ_{src} must be computed. This is given by the free-space energy density solution across the boundary. Based on equation (2.35), the energy density across the boundary of a cell containing a point-force excitation is given by

$$\rho\left(\boldsymbol{r}, \boldsymbol{p}, \omega\right) = \frac{1}{64\pi} \frac{\varrho^2 h^2}{Dk} \frac{e^{-\mu|\boldsymbol{r}-\boldsymbol{r}_0|}}{|\boldsymbol{r}-\boldsymbol{r}_0|} \delta\left(\boldsymbol{p} - k\frac{\boldsymbol{r}-\boldsymbol{r}_0}{|\boldsymbol{r}-\boldsymbol{r}_0|}\right). \tag{2.36}$$

Next, this energy density distribution must be converted into the boundary coordinate scheme. This is performed using the following relation

$$\rho(\boldsymbol{r}, \boldsymbol{p}, \omega) = \frac{k}{p_\perp}\tilde{\rho}(s, p_s, \omega)\delta(p_\perp - k_\perp), \tag{2.37}$$

where $p_\perp$ is the component of $\boldsymbol{p}$ normal to Γ at position s and $k_\perp = \sqrt{k^2 - p_s^2}$. [53]. By rearranging and substituting in equation (2.36), the initial boundary density on Γ_{src} due to a point-source excitation can be expressed as

$$\tilde{\rho}_0\left(s, p_s, \omega\right) = \frac{1}{64\pi}\frac{\varrho^2 h^2}{Dk}\frac{e^{-\mu|\boldsymbol{r}(s)-\boldsymbol{r}_0|}}{|\boldsymbol{r}(s)-\boldsymbol{r}_0|}\cos\left(\theta(p_s)\right)\delta\left(\boldsymbol{p}(p_s) - k\frac{\boldsymbol{r}(s)-\boldsymbol{r}_0}{|\boldsymbol{r}(s)-\boldsymbol{r}_0|}\right), \tag{2.38}$$

where $\cos(\theta) = p_\perp/k$ with θ representing the angle between $\hat{\boldsymbol{p}}$ and a vector orthogonal to the local boundary. Here, $\tilde{\rho}_0$ now represents the initial phase-space energy density. At this point, the raytracing methodology is applied to propagate this energy density across the structural domain. As mentioned in Section 2.1, this process is considered iteratively, with each iteration covering the motion of the rays between successive encounters with Γ. The energy density in one iteration $\tilde{\rho}(\boldsymbol{X_s})$ is mapped into the next $\tilde{\rho}'(\boldsymbol{X'_s})$ using the transfer operator $\mathcal{T}$, also called the Frobenius-Perron operator:

$$\tilde{\rho}'\left(\boldsymbol{X}'_s, \omega\right) = \{\mathcal{T}\tilde{\rho}\}(\boldsymbol{X}_s) = \int \lambda(\boldsymbol{X}'_s)e^{-\mu D(\boldsymbol{X}'_s, \boldsymbol{X}_s)}\delta\left(\boldsymbol{X}'_s - \Phi\left(\boldsymbol{X}_s\right)\right)\tilde{\rho}(\boldsymbol{X}_s, \omega)\, d\boldsymbol{X}_s. \tag{2.39}$$

Here, $D\left(\boldsymbol{X}'_s, \boldsymbol{X}_s\right)$ determines the distance travelled across the iteration. In addition, $\Phi(\boldsymbol{X}_s)$ is the boundary map, which is used to propagate rays from $\boldsymbol{X_s}$ to their next encounter with Γ. The delta function in this equation then ensures that contributions to the ray density at $\boldsymbol{X}'_s$ are only made if the rays propagating from $\boldsymbol{X}_s$ next encounter the boundary at $\boldsymbol{X}'_s$. Finally, $\lambda(\boldsymbol{X}'_s)$ is included to rep-

resent scattering events at the element boundary [53]. Scattering may be caused by differences in material parameters, boundary conditions, or curvature effects between elements [69]. An example of the scattering of the energy density at an element boundary is displayed in Figure (7).

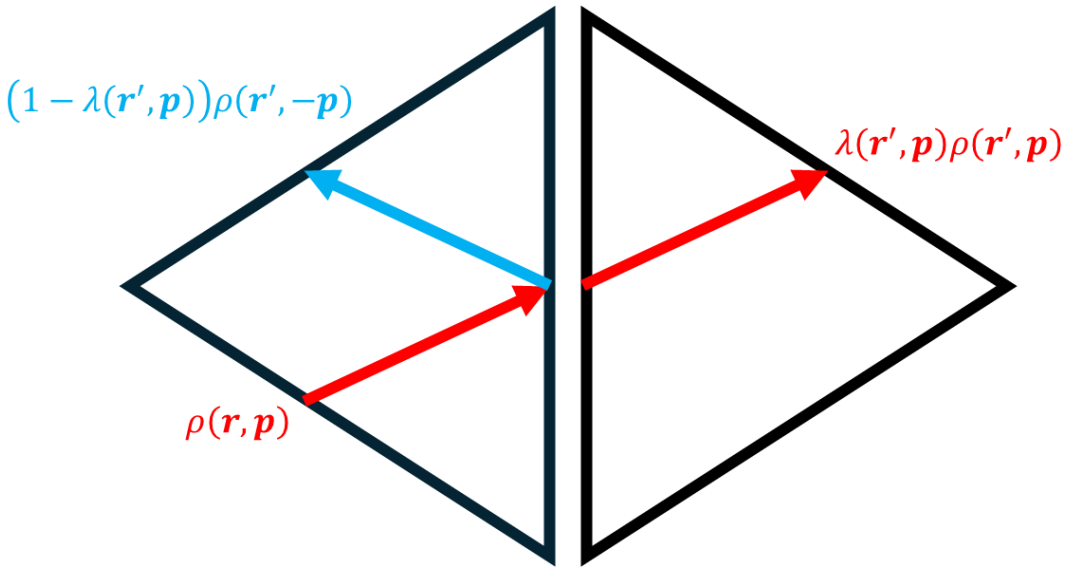

Figure 7: Resultant ray propagation following a scattering event at the cell boundary. Here, red refers to the propagation of the original ray and blue is used to represent the scattered ray density.

In this study the excitation of individual, homogeneous, flat plates is considered, meaning that $\lambda(\boldsymbol{r},\boldsymbol{p}) = 0$ across all boundaries between elements. All energy density reaching the external flowing boundary segment of one element will thus be directly transferred to the equivalent location on the internal flowing boundary of the coupled boundary segment. As a result, scattering may only occur at the external boundary. Since only cases of complete reflection or complete transmission, where $\lambda(\boldsymbol{r},\boldsymbol{p}) = 1$ or 0, will be considered in this study, this term will be omitted from future equations. A more complete consideration of the ray scattering effects is presented in [109]. The overall boundary phase-space density distribution may then be computed by repeating this process for $n \to \infty$ iterations, that is

$$\tilde{\rho}_\infty = \sum_{n=0}^{\infty} \mathcal{T}^n \tilde{\rho}_0 = (1 - \mathcal{T})^{-1} \tilde{\rho}_0, \tag{2.40}$$

which will converge for all cases involving non-zero scattering losses at the structural boundary or $\mu > 0$. The propagation of a single ray density across a simple domain over several iterations is highlighted in Figure (8).

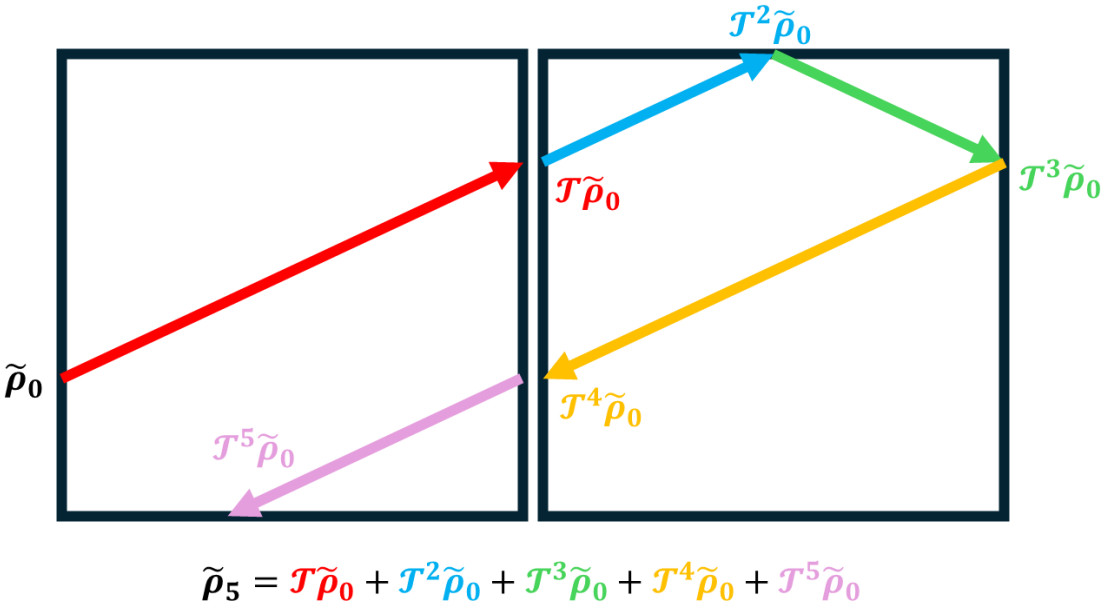

Figure 8: Propagation of a single ray across a simple domain over several iterations. In this figure, the energy density within each iteration and the final energy density distribution are highlighted.

The resulting boundary density distribution may then be mapped back into four-dimensional phase-space and propagated into the cell interiors to produce a distributed phase-space description of the vibrational response. For visualisation purposes, it is useful to integrate this solution over all $\boldsymbol{p}$, to define a spatial representation of the density. This is calculated as follows

$$\rho(\boldsymbol{r}, \omega) = \int \rho_\infty(\boldsymbol{r}, \boldsymbol{p}, \omega)\, d\boldsymbol{p} \tag{2.41}$$

where $\rho(\boldsymbol{r}, \omega)$ here is referred to as the spatial energy density in the remainder of this thesis.

2.2.3 Computational Implementation of DEA

When employing a raytracing methodology to compute the vibrational behaviour of structures, the number of rays required is dependent on the complexity and level of damping of the structure being modelled. When considering complex, minimally damped, structures, an extremely large number of rays is required to accurately capture the flow of vibrational energy across the system. Due to the large numbers of rays required for such cases, the process by which the dynamics of these rays are computed is extremely computationally expensive. To reduce this computational expense, within DEA these individual ray dynamics are replaced by a density of rays, the motion of which is considered across phase-space. As phase-space is a continuum, it is impossible to directly describe the phase-space density at all possible locations. Instead, it is useful to approximate the phase-space density by a suitable set of orthogonal basis functions, in both position and momentum space [66]. In position space, piecewise constant functions $\mathbb{1}_b(s)$ are used, with b the boundary segment. This function is defined by [90] as

$$\mathbb{1}_b(s) = \begin{cases} 1, & \text{if } s \text{ is within boundary segment } b \\ 0, & \text{otherwise.} \end{cases} \tag{2.42}$$

Initially, each boundary segment corresponds to a line segment of a mesh cell. These line segments may then be subdivided into several boundary segments, to enable variations in the energy density across each edge of each element. For momentum space Legendre polynomials $P_\beta\left(\frac{p_s}{k}\right)$ are applied due to their strong convergence properties [110]. Here β specifies the order of the Legendre Polynomial. When considering momentum and positional basis of 1, energy flows across cell boundaries in all directions with under the distribution $\frac{d\mathbf{p}}{d\theta} = k\cos(\theta)$, and the overall flow of energy between subsystems is dependent only on the energy difference across the boundary. This is then equivalent to an SEA/EFEA

evaluation, with each cell representing individual subsystems [66]. Higher order basis representations then enable a more detailed, and spatially variant, description of the flow of energy around the structure, converging to a full raytracing description [110]. The overall basis function is then given by

$$F_{\boldsymbol{n}}(\boldsymbol{X}_s) = \frac{1}{\sqrt{A_b k}} \mathbb{1}_b(s) P_\beta \left(\frac{p_s}{k} \right) \tag{2.43}$$

where $\boldsymbol{n} = (b, \beta)$ is the multi-index and A_b is the length of the current boundary segment. The energy density at some location on the boundary is then expressed in this basis as

$$\tilde{\rho}(\boldsymbol{X}_s, \omega) = \sum_{b=1}^{N_b} \sum_{\beta=1}^{N_\beta} f_{\boldsymbol{n}} F_{\boldsymbol{n}}(\boldsymbol{X}_s). \tag{2.44}$$

In this equation, N_b and N_β define the number of boundary segments within the mesh and the maximum degree of the Legendre polynomials respectively. In addition, $f_{\boldsymbol{n}}$ are the basis coefficients. The process to define and propagate these coefficients is discussed by Hartmann [53] and summarised here. Given an estimate of the initial boundary density distribution, the basis coefficients are given by

$$f_{0,\boldsymbol{n}} = \frac{(\tilde{\rho}_0, F_{\boldsymbol{n}}(\boldsymbol{X}_s))}{(F_{\boldsymbol{n}}(\boldsymbol{X}_s), F_{\boldsymbol{n}}(\boldsymbol{X}_s))} \tag{2.45}$$

with $(A, B) = \int_\Gamma A(x) B(x)\, dx$ denoting the inner product. The orthogonality of the chosen basis ensures that

$$(F_{\boldsymbol{n}}(\boldsymbol{X}_s), F_{\boldsymbol{n}'}(\boldsymbol{X}'_s)) = \frac{2}{2\beta + 1} \delta_{b,b'} \delta_{\beta,\beta'}. \tag{2.46}$$

For a point-force excitation, the initial basis coefficients are thus given by

$$f_{0,\boldsymbol{n}} = \frac{2\beta+1}{2\sqrt{A_b k}} \frac{1}{64\pi} \frac{\varrho^2 h^2}{Dk} \int_b \int_{-k}^{k} \frac{e^{-\mu D(s,\boldsymbol{r}_0)}}{D(s,\boldsymbol{r}_0)} \delta\left(\boldsymbol{p}(p_s) - k\frac{\boldsymbol{r}(s)-\boldsymbol{r}_0}{|\boldsymbol{r}(s)-\boldsymbol{r}_0|}\right) P_\beta(\sin(\theta(p_s))\cos(\theta(p_s))\, dp_s\, ds, \tag{2.47}$$

where the subscript b on the integral indicates that the integration takes place only on boundary segment b within Γ. The integral over p_s can be solved by evaluating the delta function, leaving

$$f_{0,\boldsymbol{n}} = \frac{2\beta+1}{2\sqrt{A_b k}} \frac{1}{64\pi} \frac{\varrho^2 h^2}{Dk} \int_b \frac{e^{-\mu D(s,\boldsymbol{r}_0)}}{D(s,\boldsymbol{r}_0)} P_\beta(\sin(\theta(p_s)))\cos(\theta(p_s))\, ds. \tag{2.48}$$

The complexity of the remaining integral ensures that this must be solved numerically. The basis coefficients in subsequent iterations are then found using the following

$$f_{\boldsymbol{n}'} = \sum_{b=0}^{N_b} \sum_{\beta=0}^{N_\beta} T_{\boldsymbol{n}',\boldsymbol{n}} f_{\boldsymbol{n}} \tag{2.49}$$

where $T_{\boldsymbol{n}',\boldsymbol{n}}$ are the matrix elements of the Frobenius-Perron operator [53]. These are derived as follows

$$T_{\boldsymbol{n}',\boldsymbol{n}} = \frac{(F_{\boldsymbol{n}'}(\boldsymbol{X}'_s), \mathcal{T} F_{\boldsymbol{n}}(\boldsymbol{X}_s))}{(F_{\boldsymbol{n}'}(\boldsymbol{X}'_s), F_{\boldsymbol{n}'}(\boldsymbol{X}'_s))}. \tag{2.50}$$

By exploiting the othogonality of the basis coefficients using equation (2.46) and substituting in the form of $\mathcal{T}$ from equation (2.39) then the entries of the matrix T are given in [90] as

$$T_{\boldsymbol{n}',\boldsymbol{n}} = \frac{2\beta'+1}{2} \int F_{\boldsymbol{n}'}(\boldsymbol{X}'_s) \int e^{-\mu D(\boldsymbol{X}'_s,\boldsymbol{X}_s)} \delta\left(\boldsymbol{X}'_s - \Phi(\boldsymbol{X}_s)\right) F_{\boldsymbol{n}}(\boldsymbol{X}_s)\, d\boldsymbol{X}_{s'}\, d\boldsymbol{X}_s. \tag{2.51}$$

The integral over $\boldsymbol{X}_{s'}$ is simplified by the delta function, which ensures that

contributions to the new boundary density are made only at phase space locations that are reached by $\boldsymbol{X}_s$ within a single iteration. Hence

$$T_{\boldsymbol{n}',\boldsymbol{n}} = \frac{2\beta' + 1}{2} \int e^{-\mu D(\Phi(\boldsymbol{X}_s),\boldsymbol{X}_s)} F_{\boldsymbol{n}'}(\Phi(\boldsymbol{X}_s)) F_{\boldsymbol{n}}(\boldsymbol{X}_s)\, d\boldsymbol{X}_s. \tag{2.52}$$

The fact that the transfer operator is given by an integral over the entire boundary phase-space coordinate system ensures that the basis coefficient for a particular multi index in the next iteration is the sum of rays propagating from elsewhere in the structure that contribute to the energy density within the specified multi-index. An example of the result of applying DEA to determine the response of a structure to a point-force excitation is shown in Figure 9.

Figure 9: Point-force excitation of a simple aircraft mesh simulated using DEA with $N_b = N_\beta = 5$, which corresponds to two boundary elements per edge of the triangular mesh elements. The colour scale shows the calculated energy density and runs from low energy (dark blue) to high energy (yellow).

2.3 Review of TBL CSD Models

To be able to implement TBL excitations into DEA, an appropriate model must be chosen to represent the pressure field applied by the TBL. To properly understand these models, the key properties of the TBL and its pressure field must be explored.

TBLs are formed across structures that are fully immersed within a fluid moving at some relative speed U_0. Here, frictional forces acting at the fluid-structure boundary slow the motion of fluid particles close to the structural surface [111]. This results in the formation of a thin layer of fluid particles that are stationary relative to the structure [112, 113]. Further interactions between this thin layer and passing fluid particles then leads to the build up of the boundary layer in the mean-stream direction of the fluid flow [111, 114, 115]. Close to the leading edge this boundary layer is considered laminar. Under laminar flow the fluid within the boundary tends to move across the structure in stacked layers, with minimal exchange of particles between layers [111, 116]. Some distance from the leading edge, the thickness of the boundary layer becomes too large to sustain laminar flow, and transitions into turbulent flow [117]. This transition is influenced by many factors including non-homogeneities in the fluid, the roughness of the plate, or external factors influencing the system [114]. These factors make it impossible to predict the exact location where the transition to turbulence will occur. However, an approximate location can be estimated using the Reynolds' number, which for a boundary layer is given by

$$Re = \frac{U_0 x}{\nu}. \tag{2.53}$$

Here x is the distance from the leading edge and ν is the kinematic viscosity of the fluid [111]. When the considered fluid is air, this transition typically occurs for Reynolds numbers $5 \times 10^5 \leq Re \leq 3 \times 10^6$ [113, 117]. Under turbulent flow

conditions the fluid motion becomes chaotic, with particles moving randomly in all directions [113]. A diagram of the development of the TBL with increasing distance from the leading edge is shown in Figure 10.

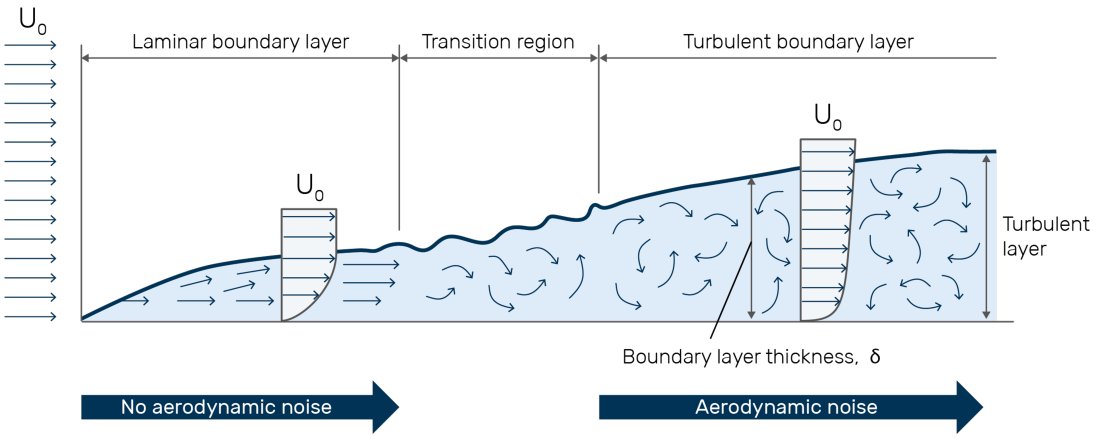

Figure 10: Formation of the TBL across a flat plate with increasing separation from the leading edge [118].

The chaotic motion of the particles leads to many of them striking the structure over time, generating a fluctuating pressure field across the surface [114, 119]. The random nature of these fluctuations means that it is impossible to accurately predict the pressure applied by the field at any specific location or time. When modelling the influence of the TBL, a statistical description of the applied pressure field must be used [119, 120].

This process can be demonstrated by considering the pressure field applied by a fully-formed TBL with zero pressure gradient flowing in the $+\hat{\boldsymbol{x}}$ direction, where $\hat{}$ represents a unit vector, over a flat plate in the $x - z$ plane. Treating the system in this manner allows us to consider the pressure field to be homogeneous in space and stationary in time [121]. The fluctuating pressure field is then best represented by a cross-correlation function, which describes the relationship in the pressure applied by the field at two separate locations on the plate surface [122]. The cross-correlation for the pressure applied by the field at arbitrary space-time positions (x_1, z_1, t_1) and (x_2, z_2, t_2) is given by the time-averaged product of the

pressures applied at each location

$$R_{pp}(\xi_x, \xi_z, \tau) = \langle p(x_1, z_1, t_1) p(x_2, z_2, t_2) \rangle \,. \tag{2.54}$$

Here $\xi_x = x_1 - x_2$ and $\xi_z = z_1 - z_2$ are the spatial separation of the points in x and z and $\tau = t_1 - t_2$ is the temporal separation [121,122]. As shown by equation (2.21), for implementation within DEA a frequency-dependent measure of the spatial-correlation in the applied pressure field is required. This can be found by taking the Fourier transform of R_{pp} to construct the CSD function [121]

$$\Psi_{pp}(\xi_x, \xi_z, \omega) = \frac{1}{2\pi} \int_{-\infty}^{+\infty} R_{pp}(\xi_x, \xi_z, \tau) e^{-i\omega\tau} \, d\tau. \tag{2.55}$$

Another interesting value is the wavenumber-frequency representation of the pressure field, which is given by the Fourier transform of $\Psi_{pp}(\xi_x, \xi_z, \omega)$ over the spatial separation

$$\tilde{\Psi}_{pp}(k_x, k_z, \omega) = \frac{1}{(2\pi)^2} \int_{-\infty}^{+\infty} \int_{-\infty}^{+\infty} \Psi_{pp}(\xi_x, \xi_z, \omega) e^{-i\omega \boldsymbol{\xi} \cdot \boldsymbol{k}} \, d\xi_x \, d\xi_z. \tag{2.56}$$

The most commonly applied CSD for a TBL pressure field is the Corcos model. This model was first published by GM Corcos in 1963, based upon a series of experimental studies performed in the late 1950s and early 1960s [123]. In this work, he postulated that the correlation in the stream-wise and cross-stream directions should be separable and represented by terms which exhibit exponential decay with increasing separation [27]. In addition, these terms should be multiplied by a complex exponential term, which captures the mean downstream convection of the TBL [13, 122]. For the case described previously, the resultant CSD for the Corcos model is given as

$$\Psi_{pp}(\xi_x, \xi_z, \omega) = \phi(\omega) e^{-\alpha_x k_c |\xi_x|} e^{-\alpha_z k_c |\xi_z|} e^{i k_c \xi_x}. \tag{2.57}$$

In this equation α_x and α_z are the longitudinal and latitudinal decay constants respectively, These terms typically have values of $\alpha_x = 0.10 - 0.12$ and $\alpha_z = 0.7 - 1.2$ [124], with Graham [29] choosing $\alpha_x = 0.1$ and $\alpha_z = 0.77$ in his high-frequency study of different CSD models. In addition, $k_c = \omega/U_c$ is the convective wavenumber of the TBL. Here, U_c is the convective velocity of the flow which is typically approximated by $U_c \approx 0.7\,U_0$ [121, 125, 126]. The $\phi(\omega)$ term is the single point wall-pressure spectrum, which defines the magnitude of the CSD as a function of the angular frequency ω [127]. By substituting equation (2.57) into equation (2.56), the wavenumber-frequency representation of the Corcos model CSD function is given as

$$\tilde{\Psi}_{pp}(k_x, k_z, \omega) = \phi(\omega) \frac{4\alpha_x \alpha_z k_c^2}{\left[\alpha_x^2 k_c^2 + (k_x - k_c)^2\right]\left[\alpha_z^2 k_c^2 + k_z^2\right]}. \tag{2.58}$$

The main advantage of the Corcos model is the separation of the correlation in the streamwise and cross-flow direction [121,127]. This is useful, as it ensures that the model can easily be converted between the wavenumber-frequency and space-time domains [121]. In addition, the model has only two empirical parameters, ensuring that minimal knowledge of the system is required when applying this model [120]. Finally, the Corcos model has been demonstrated to give an accurate representation of the wavevector-frequency spectrum at the convective peak, close to $|\boldsymbol{k}| = k_c$, where most of the TBL energy is contained [128, 129]. Outside of this range however, the Corcos model tends to overpredict the contribution, with predictions found to be around $20\,dB$ too high away from the convective peak [120,122]. In addition, at low wavenumbers the Corcos model fails to follow the Kraichnan-Phillips constraint, which states that the wavenumber-frequency representation of the CSD should be proportional to $|\boldsymbol{k}|^2$ and hence disappear as $|\boldsymbol{k}| \to 0$ [122,130].

Due to the limitations of the Corcos model, several alternative versions of this model have been developed. The first of these, presented by Efimtsov in 1982, was

developed based upon the belief that the correlation strength should be impacted by the boundary layer thickness δ [29,131]. For this, Efimtsov kept the correlation function in the same basic form as in equation (2.57), but replaced the exponents. These exponents are given by Graham [29] as follows

$$\begin{aligned}\alpha_x k_c &= \frac{1}{\delta}\sqrt{\left(\frac{a_1\omega\delta}{U_c}\right)^2 + \frac{a_2^2}{\left(\frac{\omega\delta}{U_\tau}\right)^2 + \left(\frac{a_2}{a_3}\right)^2}} \\ \alpha_z k_c &= \frac{1}{\delta}\sqrt{\left(\frac{a_4\omega\delta}{U_c}\right)^2 + \frac{a_5^2}{\left(\frac{\omega\delta}{U_\tau}\right)^2 + \left(\frac{a_5}{a_6}\right)^2}}.\end{aligned} \tag{2.59}$$

Where U_τ is the friction velocity of the TBL and $a_1 - a_6$ are empirical parameters [29]. This change enhances the Corcos model solution at low-frequencies [29], whilst at higher frequencies converges to the Corcos solution [131].

Another approach developed to improve the low-wavenumber accuracy of the Corcos model is the Smol'yakov-Tkachenko model, first presented in 1991 [132]. Much like for the Efsimov model, the Smol'yakov-Tkachenko model is derived based upon the belief that the correlation length should be inversely proportional to the thickness of the boundary layer [122]. Unlike the separated correlations presented by Corcos and Efimtsov, Smol'yakov and Tkachenko instead considered the correlation in terms of the overall separation of the points [29]. The spatial form of the initial Smol'yakov-Tkachenko model is presented by Hwang et al [122] as

$$\Psi_{pp}(\xi_x, \xi_z, \omega) = \phi(\omega) e^{-\bar{\alpha}(\omega)\sqrt{(k_c\xi_x)^2 + (m_0 k_c \xi_z)^2}} e^{ik_c\xi_x}, \tag{2.60}$$

where $m_0 = \alpha_z/\alpha_x$ and

$$\bar{\alpha}(\omega) = \alpha_x\sqrt{1 - \frac{0.2U_c}{\omega\delta_*} + \left(\frac{0.2U_c}{\omega\delta_*}\right)^2} \tag{2.61}$$

with δ_* the displacement thickness of the TBL, and α_x, α_z the correlation decay constants from the Corcos model [122]. When converting this model into the wavenumber-frequency domain, Smol'yakov and Tkachenko found that the low-wavenumber results were still higher than those found experimentally [29]. To fix this, a correction factor was added to the wavenumber-frequency solution. The full numerical form of the resultant function is presented by Graham in [29].

This change significantly improved the accuracy of this approach, with several studies demonstrating very good agreement with experimental data, particularly in the low-wavenumber range [121,125,128]. The added correction factor severely complicates the model however, and prevents its conversion back into a spatial representation of the CSD [121, 127]. Thus, the Smol'yakov-Tkachenko is innapropriate for implementation within DEA.

The final Corcos based model discussed here is the Mellen model [133]. Much like the Smol'yakov-Tkachenko model, this approach considers the correlation in terms of the overall separation. Unlike the Smol'yakov-Tkachenko model however, Mellen uses the exact same parameters as in Corcos' model. The spatial CSD for the Mellen model is then given by [133] as

$$\Psi_{pp}(\xi_x, \xi_z, \omega) = \phi(\omega) e^{-\sqrt{(\alpha_x k_c \xi_x)^2 + (\alpha_z k_c \xi_z)^2}} e^{i k_c \xi_x}. \tag{2.62}$$

The wavenumber-frequency representation of this field is given in [125] as

$$\tilde{\Psi}_{pp}(k_x, k_z, \omega) = \phi(\omega) \frac{\left(\alpha_x \alpha_z k_c^2\right)^2}{\left[\alpha_z^2 k_c^2 \left(k_x - k_c\right)^2 + \alpha_x^2 k_c^2 k_z^2 \left(\alpha_x \alpha_z k_c^2\right)^2\right]^{3/2}}. \tag{2.63}$$

As the Mellen model uses only Corcos' original parameters it too can be applied with minimal knowledge of the system. In addition, despite the lack of separation of spatial correlations it is relatively easy to transfer between spatial and wavenumber-frequency spectra. Despite these minimal changes, the Mellen model is also more accurate than the Corcos model in the low-wavenumber region, with

estimates around $8\,dB$ lower than those found using the Corcos model [26, 125]. The final CSD function discussed here is the Chase model [134]. Unlike the other Corcos-based models, the Chase model was developed to follow the Kraichnan-Phillips constraint, with the hope of addressing the limitations of the Corcos model away from the convective peak [122, 129]. The wavenumber-frequency spectrum for the Chase model is presented as follows [134]

$$\tilde{\Psi}_{pp}(k_x, k_z, \omega) = \frac{(2\pi)^3 \rho^2 \omega^2 U_\tau^2}{U_c^2 \phi(\omega)} \left[\frac{C_M k_x^2}{\left[K_+^2 + (b_M \delta)^{-2}\right]^{5/2}} + \frac{C_T \left|\boldsymbol{k}\right|^2}{\left[K_+^2 + (b_T \delta)^{-2}\right]^{5/2}} \right]. \tag{2.64}$$

The defined forms and numerical values for the unknowns within this equation are addressed by Graham in [29]. Much like the Smol'yakov-Tkachenko and Mellen models, the Chase spectrum is not explicitly separable between the streamline and cross-stream flow directions. This, in combination with the complexity of the model, makes transforming this function into the spatial form required for DEA highly challenging. An approach for completing this procedure has been presented by Josserand [135, 136]. The solution is given by

$$\begin{aligned} \Psi_{pp}\left(\xi_x, \xi_z, \omega\right) = {} & A_M(\omega) f_M(\xi_x, \xi_z, \omega) e^{-z_M} e^{ik_c \xi_x} \\ & + A_T(\omega) f_T(\xi_x, \xi_z, \omega) e^{-z_T} e^{ik_c \xi_x} \end{aligned} \tag{2.65}$$

where the A terms are relative magnitudes, defined in terms of the convective velocity and angular frequency and

$$\begin{aligned} f_M &= 1 + z_M + \alpha_M^2 \mu_M^2 \left(1 - \frac{z_{Mx}^2}{z_M}\right) + 2i\alpha_M \mu_M z_{Mx} \\ f_T &= 1 + z_T + \alpha_T^2 \left(1 - \frac{z_{Tz}^2}{z_T}\right) + \alpha_T^2 \mu_T^2 \left(1 - \frac{z_{Tx}^2}{z_T}\right) + 2i\alpha_T \mu_T z_{Tx}. \end{aligned} \tag{2.66}$$

Here, the z and α terms are functions of the separation, convective wavenumber, and empirical parameters [135]. The equations and appropriate numerical values for each of these terms are discussed by Finnveden in [135].

This approach has demonstrated excellent accuracy in comparison with numerical results in prior studies [127, 128], particularly in the low-frequency region where the Corcos model fails. However, the model is highly complex and requires a detailed understanding of both the structural properties and of the TBL itself [121]. In addition, the model contains six empirical parameters which have no universal values, and so must be individually calibrated for each problem [120, 131]. As a result, the Chase model is not preferred for representing TBL pressure fields in DEA.

Due to their simplicity and ease of transfer between spatial and wavenumber-frequency CSD functions, the Corcos and Mellen models are preferred for modelling TBL pressure fields in DEA.

2.4 Review of vibration interference effects

Another aim of this study is to consider vibrations originating from the propeller arrays employed by DEP aircraft. During operation, these propellers will rotate with a constant frequency ω. It is thus likely that the structural vibrations generated by interactions between the propellers and the air will oscillate at the same frequency. This is important, as when propagating waves of similar frequencies encounter one another they merge to form a new waves through interference [137, 138]. Under the superposition principle, the resultant wave is simply the sum of the interfering waves [139]. This effect may be demonstrated by considering the interference between two harmonic waves of equal magnitude, which are propagating in the $+\hat{\boldsymbol{x}}$ direction with identical wavenumber k, and are separated by a phase difference ϕ. These may be described by $\psi_1(x,t) = Ae^{i(kx-\omega t)}$ and $\psi_2(x,t) = Ae^{i(kx-\omega t+\phi)} = Ae^{i\phi}e^{i(kx-\omega t)}$ [139]. The combined wavefunction is

then the sum of the individual wavefunctions and is given by

$$\psi(x,t) = A(1 + e^{i\phi})e^{i(kx-\omega t)}. \tag{2.67}$$

The result is another wave propagating in the $+\hat{\boldsymbol{x}}$ direction, with frequency ω. To evaluate the amplitude of this wavefunction, $e^{i\phi}$ is expanded using Euler's formula [139], this leaves

$$\psi(x,t) = A((1 + \cos(\phi)) + i\sin(\phi))e^{i(kx-\omega t)}. \tag{2.68}$$

The term in the brackets is now a complex number of the form $z = a + ib$, the magnitude of which is given by $z = \sqrt{a^2 + b^2}$. After applying trigonometric identities, the resultant wavefunction is given by

$$\psi(x,t) = 2A\cos(\phi/2)e^{i(kx-\omega t)}. \tag{2.69}$$

The magnitude of the resultant wave is then defined based upon the phase-difference between the original waves. When this phase difference is given by $\phi = 2n\pi$ with $n = 0, 1, 2, ...$ the interfering waves are identical, and the magnitude of the resultant wave at each location is double the magnitudes of the original waves. This is known as constructive interference [137, 139]. When the phase difference $\phi = (2n + 1)\pi$ with $n = 0, 1, 2, ...$ the interfering waves are anti-aligned, meaning that the waves are exactly opposite at all points. In this case, the two waves cancel out and all wave propagation is lost. This is known as destructive interference [137, 139]. These interference effects are demonstrated in Figure 11.

For any ϕ outside of these cases, the waves are considered "out of phase" and the resultant wavefunction is more complex [139].

The opposite case of interfering waves propagating in opposite directions may also be considered. Here, ψ_1 is defined as before, with $\psi_2 = Ae^{-i(kx+\omega t)}$. By once

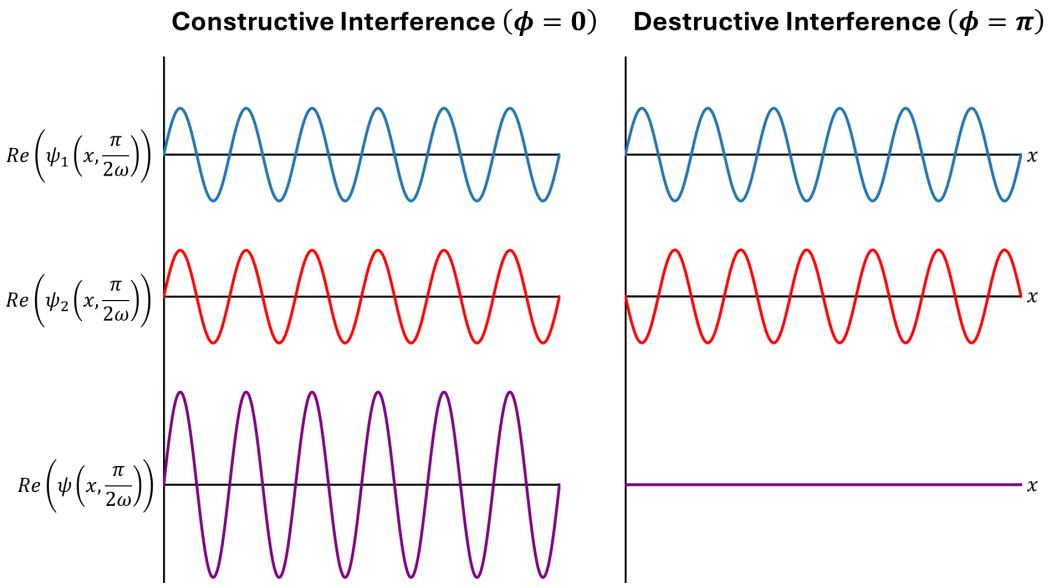

Figure 11: Constructive and destructive interference of two one-dimensional propagating in the same direction at time $t = \frac{\pi}{2\omega}$ [140].

again taking the sum of the waves, the resultant wavefunction is given by

$$\psi(x,t) = Ae^{-i\omega t}\left(e^{ikx} + e^{-ikx}\right). \tag{2.70}$$

By applying Euler's formula, the resultant wavefunction can be defined as

$$\psi(x,t) = 2A\cos(kx)e^{-i\omega t}. \tag{2.71}$$

Here, the spatial and temporal dependencies are separated, meaning that the time-dependence is equivalent at all locations along the wave [139]. The result is that changes in t no longer generate propagation of the wave in space, instead the value of ψ at all points simply oscillates with frequency ω. In this case, the wavefunction is known as a standing wave [139]. The constituent and resultant wavefunctions for this system for various t values are shown in Figure 12.

In this thesis, two-dimensional time-independent vibrational waves generated by point-force excitations are considered. In this case, the waves are generated at the source, and propagate radially across the structure. As discussed in Section

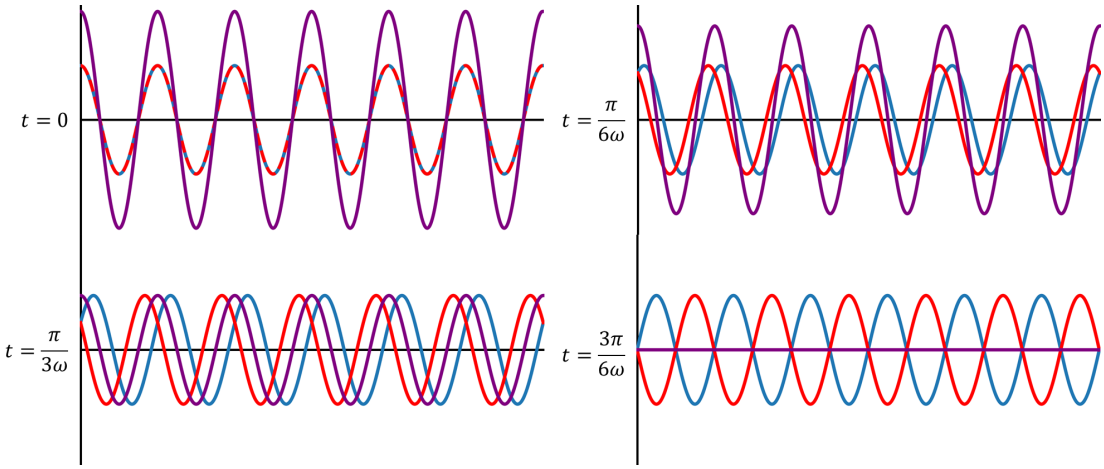

Figure 12: Plot of two one-dimensional waves ψ_1 (blue) and ψ_2 (red) propagating in opposite directions, along with their resultant standing wave ψ (purple) at various times t.

2.2, the response of the plate to a point-force at location $\boldsymbol{r}_1$ is given by the Green function $G_1(\boldsymbol{r}, \boldsymbol{r}_1, \omega) \propto \frac{A}{\sqrt{|\boldsymbol{r}-\boldsymbol{r}_1|}} e^{ik|\boldsymbol{r}-\boldsymbol{r}_1|}$. As shown in this equation, the radial propagation of the vibrational waves ensures that the magnitude of the response at any location $\boldsymbol{r}$ is dependent only on the distance from the source. Introducing a second point-force at some location $\boldsymbol{r}_2$ nearby, then induces additional vibrations within the structure, described by $G_2(\boldsymbol{r}, \boldsymbol{r}_2, \omega) \propto \frac{A}{\sqrt{|\boldsymbol{r}-\boldsymbol{r}_2|}} e^{ik|\boldsymbol{r}-\boldsymbol{r}_2|}$. As the vibrational waves generated by both sources propagate they will encounter one another at various locations across space, at different distances from each source. The relative phase of the waves will then differ at each meeting point, leading to large variation in the interference effects across space. The result is a highly complex wavefield, an example of which is demonstrated by Figure 13.

The dependence of each wavefunction on the distance from the source means that a convenient form for the wavefield is difficult to obtain in practise. An approximate solution may however be found at great distances from the sources, where the source separation is comparably negligible [139]. In this case, the amplitude of each Green function is approximated as equal to the amplitude of the Green function for a source positioned directly between the two sources. By

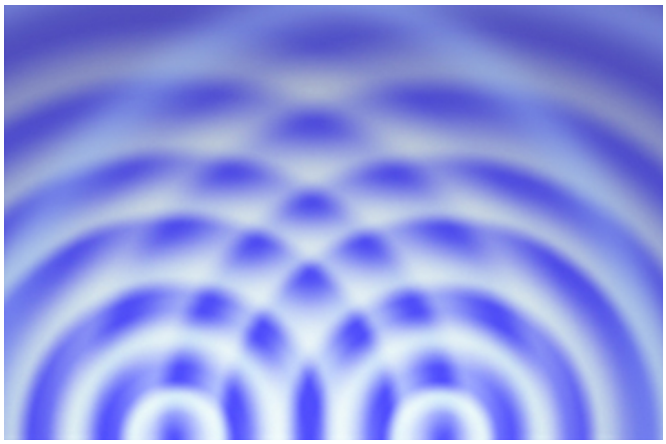

Figure 13: Two-dimensional interference pattern within a ripple tank formed through interference of circular waves formed from two point-forces [141].

rewriting each Green function in terms of this distance and adding them together, the resultant wavefunction at large distances from the sources is given by

$$G(\boldsymbol{r},\omega) = \frac{Ae^{\frac{1}{2}ik(|\boldsymbol{r}-\boldsymbol{r}_1|+|\boldsymbol{r}-\boldsymbol{r}_2|)}}{\left|\boldsymbol{r}-\frac{1}{2}(\boldsymbol{r}_1+\boldsymbol{r}_2)\right|}\cos\left(\frac{k(|\boldsymbol{r}-\boldsymbol{r}_1|-|\boldsymbol{r}-\boldsymbol{r}_2|)}{2}\right). \tag{2.72}$$

As in the one-dimensional case, the result is a wavefunction with an amplitude which oscillates across space. In this case however, it is the difference in the separation of the location from each point-force which defines this amplitude. Given that $\cos(n\pi) = (-1)^n$ for $n = 0, 1, 2, ...$, maxima in the magnitude of the amplitude are found where $|\boldsymbol{r}-\boldsymbol{r}_1| - |\boldsymbol{r}-\boldsymbol{r}_2| = \frac{2n\pi}{k}$. Given that $k = 2\pi/\lambda$, then this is equivalent to $|\boldsymbol{r}-\boldsymbol{r}_1| - |\boldsymbol{r}-\boldsymbol{r}_2| = n\pi$, where λ is the wavelength of the vibrational waves excited by each source. Thus, peaks are found where the vibrational waves propagating from each source are separated by $n\lambda$, meaning that they are in-phase and hence constructive interference will occur. Given that $\cos\left(\frac{n\pi}{2}\right) = 0$ for $n = 0, 1, 2, ...$, zero amplitude is found where the vibrational waves differ in path length by $\lambda/2$, which is where the sources are anti-phase and destructive interference occurs. These results thus match the one-dimensional result. Outside of these locations the vibrational waves from each source are out of phase, with a rapidly varying magnitude across space. The combination

of these interactions results in a complex interference wavefield, such as that demonstrated in Figure 13.

To the author's knowledge, no prior studies have considered the vibrational response of structures under multiple, coherent, point-force excitations. Vibrational interference is however a popular area of study, having found usage in a wide range of applications, as detailed below.

A key area of application of vibrational interference is as a means of Active Vibration Control (AVC). When subjected to vibrational disturbances, AVC systems drive actuators to generate a signal which is equal in magnitude and frequency to the disturbance, with a phase difference of $\phi = \pi$. As discussed, the interference of two coherent waves propagating in opposite directions generates a standing wave. The chosen phase difference is such that the interfering waves are anti-aligned, meaning that the waves cancel [142–144]. AVC systems are employed in numerous complex structures, including, motor vehicles [142], aircraft [145], wind turbines [146], and sensitive measuring equipment [147]. An equivalent adaptive approach has also been developed for the purpose of sound mitigation. Here, a reference sensor detects any incoming sound waves and a loudspeaker is employed to generate the appropriate inverted signal [148–150]. This procedure has been applied to prevent feedback in hearing aids [151], reduce the noise generated by MRI machines during operation [152], and to limit community noise in noise-cancelling headphones [153].

Another, more complex, application of vibrational interference is found in the function of phased array transducers. This is a device made up of an array of elements that independently emit vibrational or electromagnetic waves [154]. By sequentially firing the elements with some set time delay, the resulting interference pattern produces a propagating beam of plane waves in a specific direction [155, 156]. Adjustments to the time delay between adjacent elements then change the angle of the beam, enabling directional control of the beam propagation [154,156].

This is useful for radar applications, as it enables phased array transducers to scan across wide areas without any physical motion [156, 157]. This technique is also applied for broadcasting [158], satellite communications [159] (including deep space missions [160]), medical imaging and treatment [161–163] and fault detection in sensitive systems such as nuclear reactors [155, 164].

These applications of vibrational interference suggest that, with careful management of the phase relation between the propulsors, it may be possible to cancel out or otherwise favourably direct the vibrational energy generated by the propulsors in DEP aircraft. This concept is explored further in Chapter 4.

2.5 Conclusion

This chapter has provided the key background information required to understand the findings presented in the remainder of the thesis. Having discussed the need for a high-frequency approach for modelling the response of structures to TBL pressure fields, in Section 2.1 several possible methods for this have been evaluated. Here, DEA has been established as the preferred approach, and in Section 2.2 the background theory and computational implementation of this method have been detailed. As DEA is currently limited to point-force excitations, the implementation within DEA of appropriate correlation functions representing the TBL pressure field has also been discussed. In Section 2.3 several TBL correlation functions have been discussed, with the Corcos and Mellen models found to be the most suitable for a DEA implementation due to their favourable mathematical properties. The implementation of TBL pressure fields in DEA using these models will be explored in Chapter 3. Finally, in Section 2.4, the interference effects between monochromatic waves and the resultant wavefields have been investigated and some real-world applications of this effect have been discussed. This theory will be important when implementing correlated point-force excitations in DEA, as will be investigated in Chapter 4.

Chapter 3

3 Implementation of correlated pressure fields in DEA

3.1 Introduction

In Chapter 2, the DEA approach for modelling the vibrational response of complex structures to point-force excitations was introduced. There, it was demonstrated that the vibrational response of structures to any correlated pressure source can be defined using an appropriate correlation function representing the applied source. In addition, the range of correlation functions developed to capture the properties of the pressure field applied to structures by the TBL was discussed. In this chapter these concepts are combined, to produce an approach to determine the vibrational response of complex structures to correlated pressure field excitations, such as that applied by the TBL.

The chapter is presented as follows. In Section 3.2, the approach to model the excitation of structures by correlated pressure fields within DEA is introduced by considering the excitation of a small, convex, patch of a simple structure by an arbitrary pressure field. It is demonstrated here that the energy density at the boundary of a region excited by a homogeneous pressure field is dependent on the geometry of the excited region and a phase-space representation of the applied pressure field. The procedure to apply specific excitations is then demonstrated in Section 3.4, through the implementation of the TBL pressure field. This involves

defining the Wigner transform of an appropriate correlation function representing the applied pressure field. For a homogeneous source, it is demonstrated that the resultant Wigner transform term is also homogeneous. Following this, in Section 3.5 approaches to extend this approach to larger patches, including full-body excitations, are evaluated. In Section 3.6, the approach to model the response of structures to full-body correlated source excitations is demonstrated. Here, the vibrational response of a flat plate under a fully-formed, homogeneous, TBL pressure field is evaluated. The system configuration for this simulation is described in Section 3.6.1, and the results for a variety of flow, structural, and boundary conditions are presented in Sections 3.6.2 - 3.6.4. Finally, in Section 3.6.5, the applicability of this approach to more general situations is considered, and opportunities for future development are discussed.

3.2 Small patch excitations

In this section the approach for modelling the excitation of structures to correlated pressure fields within DEA is discussed. To introduce this topic, the excitation of a simple structure by a generic pressure field applied within a small, convex, patch on the structural surface Ω_{src} is considered. The structure to be studied, and its associated finite element mesh, are displayed in Figure 14.

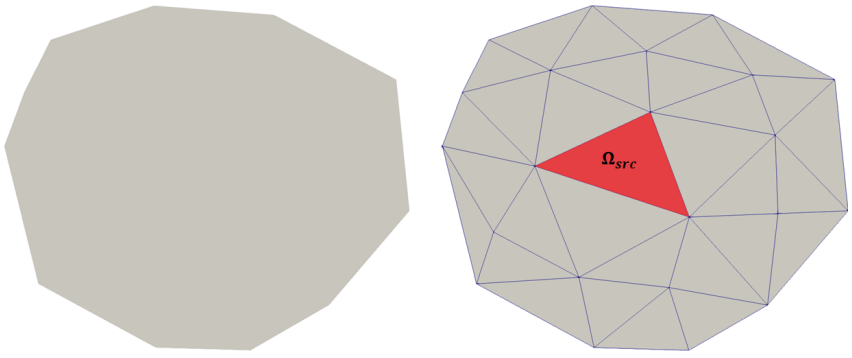

Figure 14: Left: Simple structure within which the small patch excitation is studied. Right: Finite element mesh applied to model this structure computationally, the red cell highlighted here indicates the patch excited by the correlated field.

The region highlighted in red indicates the patch excited by the correlated pressure field. As shown, the excitation is applied here to a single finite element mesh cell within the structure, defined in the plot by Ω_{src}. This is an un-physical situation, however it will act as a starting point to develop the theory behind modelling the influence of correlated fields far larger than individual cells, including full-body excitations.

Here, the aim is to compute the direct contribution from the excited patch to the phase-space density at some location on the boundary of Ω_{src}. As shown by equation (2.21) in Section 2.2.1, when defining the response of a structure to an applied pressure field, a correlation function defining the coherence in the force applied by the field at locations $\boldsymbol{r}_{01}$ and $\boldsymbol{r}_{02}$ within the excited region is required. At this stage it is assumed that the correlation in the force applied by the generic pressure field is homogeneous. The associated correlation function is then denoted by $\Gamma_F\left(\boldsymbol{r}_{01}-\boldsymbol{r}_{02}\right)$, indicating that the correlation between the force applied at the two locations is dependent only on their spatial separation. This is chosen here for simplicity, however it will be demonstrated in Section 3.4 that this is an appropriate representation for the TBL pressure field within individual finite elements. The correlation function describing the response of the structure to the applied excitation is then given by

$$\begin{aligned}&\Gamma_0\left(\boldsymbol{r}_1,\boldsymbol{r}_2,\omega\right)=\\&\int_{\Omega_{src}}\int_{\Omega_{src}} G_0\left(\boldsymbol{r}_1,\boldsymbol{r}_{01},\omega\right)\Gamma_F\left(\boldsymbol{r}_{01}-\boldsymbol{r}_{02}\right)G_0^*\left(\boldsymbol{r}_2,\boldsymbol{r}_{02},\omega\right)\,d\boldsymbol{r}_{01}\,d\boldsymbol{r}_{02},\end{aligned} \tag{3.1}$$

where $\boldsymbol{r}_{01},\boldsymbol{r}_{02}\in\Omega_{src}$. As described in Section 2.2.1, to define the WDF of the excitation the Wigner transform of this response correlation function must be found. As shall be demonstrated in Section 3.4, the Wigner transform of a spatially homogeneous function produces a function which is dependent only on the momentum $\boldsymbol{p}$. Based upon equation (2.32), the WDF at some phase-space

location $(\boldsymbol{r}, \boldsymbol{p})$ due to the applied homogeneous pressure field is thus given by

$$W_0(\boldsymbol{r}, \boldsymbol{p}) = R_0 \int_{\Omega_{src}} \int \frac{e^{-\mu|\boldsymbol{r}-\boldsymbol{r}'|}}{|\boldsymbol{r}-\boldsymbol{r}'|} \delta(\boldsymbol{p}-\boldsymbol{p}') \delta\left(\boldsymbol{p} - k\frac{\boldsymbol{r}-\boldsymbol{r}'}{|\boldsymbol{r}-\boldsymbol{r}'|}\right) W_\Gamma(\boldsymbol{p}')\, d\boldsymbol{p}'\, d\boldsymbol{r}'. \tag{3.2}$$

Here R_0 defines the magnitude of the response to the applied pressure field and is defined by $R_0 = \frac{\varrho^2 h^2}{32\pi D^2 k^5}$ in equation (2.33) [53]. Solving the integral over $\boldsymbol{p}'$ then leaves

$$W_0(\boldsymbol{r}, \boldsymbol{p}) = R_0 W_\Gamma(\boldsymbol{p}) \int_{\Omega_{src}} \frac{e^{-\mu|\boldsymbol{r}-\boldsymbol{r}'|}}{|\boldsymbol{r}-\boldsymbol{r}'|} \delta\left(\boldsymbol{p} - k\frac{\boldsymbol{r}-\boldsymbol{r}'}{|\boldsymbol{r}-\boldsymbol{r}'|}\right) d\boldsymbol{r}'. \tag{3.3}$$

To solve the resulting integral over $\boldsymbol{r}'$ a coordinate transform is performed, defining $\boldsymbol{r}'' = \boldsymbol{r}' - \boldsymbol{r}$. The resulting integral is given by

$$W_0(\boldsymbol{r}, \boldsymbol{p}) = R_0 W_\Gamma(\boldsymbol{p}) \int_{\Omega_{src}} \frac{e^{-\mu|\boldsymbol{r}''|}}{|\boldsymbol{r}''|} \delta\left(\boldsymbol{p} + k\frac{\boldsymbol{r}''}{|\boldsymbol{r}''|}\right) d\boldsymbol{r}'' \tag{3.4}$$

By writing $\boldsymbol{r}'' = (r_x'', r_z'')$ with $|\boldsymbol{r}''| = \sqrt{(r_x'')^2 + (r_z'')^2}$, the delta function in this equation can be split into the product of parallel and orthogonal terms with regards to $\hat{\boldsymbol{p}}$.

$$\begin{aligned} W_0(\boldsymbol{r}, \boldsymbol{p}) = R_0 W_\Gamma(\boldsymbol{p}) \int \int_{\Omega_{src}} \frac{e^{-\mu|\boldsymbol{r}''|}}{|\boldsymbol{r}''|} \delta\left(|\boldsymbol{p}| + k\frac{r_x'' \cos(\phi) + r_z'' \sin(\phi)}{|\boldsymbol{r}''|}\right) \\ \delta\left(k\frac{r_z'' \cos(\phi) - r_x'' \sin(\phi)}{|\boldsymbol{r}''|}\right) dr_x''\, dr_z''. \end{aligned} \tag{3.5}$$

Here ϕ defines the angle between the $\boldsymbol{p}$ vector and the $+\hat{\boldsymbol{x}}$ direction. The resultant integral is then converted into polar coordinates (R, φ). Here $|\boldsymbol{r}''| = R$, $r_x'' = R\cos(\varphi)$, and $r_z'' = R\sin(\varphi)$, with φ defining the angle between $\hat{\boldsymbol{r}''}$ and the $+\hat{\boldsymbol{x}}$ direction. Making this transform then gives

$$W_0(\boldsymbol{r},\boldsymbol{p}) = R_0 W_\Gamma(\boldsymbol{p}) \int\int_0^{2\pi} e^{-\mu R}\delta\left(|\boldsymbol{p}| + k\left(\cos(\varphi)\cos(\phi) + \sin(\varphi)\sin(\phi)\right)\right) \\ \delta\left(k\left(\sin(\varphi)\cos(\phi) - \cos(\varphi)\sin(\phi)\right)\right)\, d\varphi\, dR. \tag{3.6}$$

Employing trigonometric identities [165], this can be simplified to

$$W_0(\boldsymbol{r},\boldsymbol{p}) = R_0 W_\Gamma(\boldsymbol{p}) \int_{\Omega_{src}}\int_0^{2\pi} e^{-\mu R}\delta\left(|\boldsymbol{p}| + k\cos(\varphi-\phi)\right) \\ \delta\left(k\sin(\varphi-\phi)\right)\, d\varphi\, dR. \tag{3.7}$$

As k is positive and real, the second delta function can give a non-zero solution only if $\sin(\varphi-\phi)=0$. Given the constrained range of φ within the integral, this is only possible if $\varphi-\phi = 0, \pi, 2\pi$. By definition, $|\boldsymbol{p}|$ is also positive and real, meaning that for the first delta function to give non-zero solutions $\cos(\varphi-\phi) < 0$. The only solution which fits both constraints is then where $\varphi-\phi=\pi$. Given that ϕ describes the angle between $\hat{\boldsymbol{p}}$ and $\hat{\boldsymbol{x}}$ and φ describes the angle between $\hat{\boldsymbol{r''}}$ and $\hat{\boldsymbol{x}}$ then $\varphi-\phi$ must by definition describe the angle between $\hat{\boldsymbol{r''}}$ and $\hat{\boldsymbol{p}}$. Given that $\varphi-\phi=\pi$, then these vectors must be anti-parallel to each-other. This means that contributions to the energy density at the location $(\boldsymbol{r},\boldsymbol{p})$ can only come from source locations $\boldsymbol{r'}$ within the excited region which are located along a line pointing from $\boldsymbol{r}$ in the $-\hat{\boldsymbol{p}}$ direction. This result is logical, as these are the only points from which rays of momentum $\boldsymbol{p}$ can be emitted and pass through $(\boldsymbol{r},\boldsymbol{p})$ without prior scattering. The result of the integral over φ is then given by

$$W_0(\boldsymbol{r},\boldsymbol{p}) = R_0 W_\Gamma(\boldsymbol{p})\,\delta\left(|\boldsymbol{p}| - k\right)\int_0^{R_B} e^{-\mu R}\, dR, \tag{3.8}$$

where $R_B(\boldsymbol{r},\boldsymbol{p})$ describes the distance from the current location to the boundary

of Ω_{src} in the $-\hat{\boldsymbol{p}}$ direction. This is determined by finding the distance between $\boldsymbol{r}$ and the point at which a line drawn from this location in the $-\hat{\boldsymbol{p}}$ direction intercepts another boundary of the excited cell. This process is displayed in Figure 15.

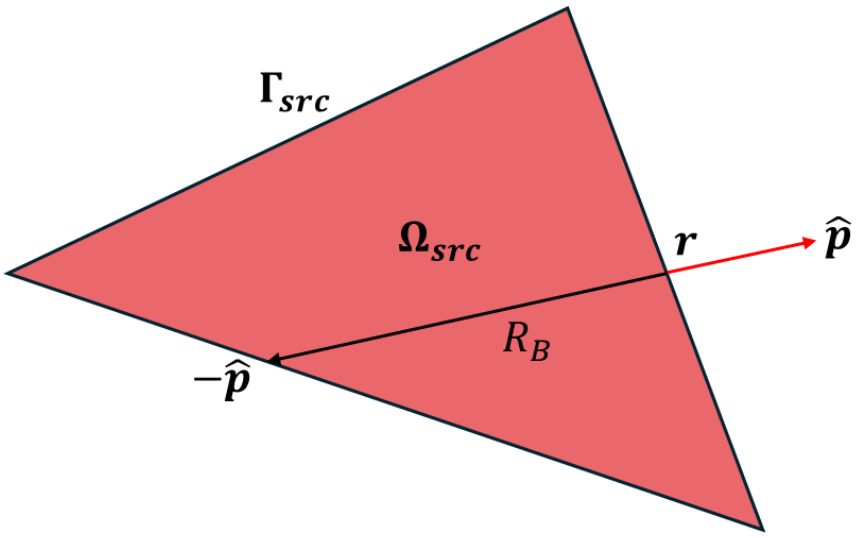

Figure 15: Demonstration of R_B for a particular phase-space location on the boundary of an excited cell.

Solving the integral along this line then gives the WDF for the arbitrary correlated field excitation as

$$W_0(\boldsymbol{r},\boldsymbol{p}) = \frac{1}{\mu} R_0 \left(1 - e^{-\mu R_B(\boldsymbol{r},\boldsymbol{p})}\right) W_\Gamma(\boldsymbol{p})\, \delta\left(|\boldsymbol{p}| - k\right). \tag{3.9}$$

Substituting into equation (2.34) then gives the direct contribution to the phase-space density as

$$\rho_0(\boldsymbol{r},\boldsymbol{p}) = \frac{1}{\mu} R' \left(1 - e^{-\mu R_B}\right) W_\Gamma(\boldsymbol{p})\, \delta\left(|\boldsymbol{p}| - k\right) \tag{3.10}$$

with $R' = \frac{1}{2}\varrho h\omega^2 R_0$. By definition, this solution is the energy density at the boundary of the excited cell. For a single-cell excitation, this boundary is defined as Γ_{src}, which is identical to that applied for a point-force excitation. Conversion into the boundary coordinate scheme is then performed by substituting this result

into equation (2.37), leaving

$$\tilde{\rho}_0(s, p_s, \omega) = \frac{1}{\mu} R' \left(1 - e^{-\mu R_B(s,p_s)}\right) W_\Gamma(p_s) \cos(\theta(p_s)) \delta(|\boldsymbol{p}| - k). \tag{3.11}$$

The initial basis coefficients are thus defined by substituting this solution into equation (2.45), giving

$$f_{0,\boldsymbol{n}} = \frac{2\beta + 1}{2\sqrt{A_b k}} \frac{R'}{\mu} \int_b \int_{-k}^{+k} \left(1 - e^{-\mu R_B(s,p_s)}\right) W_\Gamma(p_s) \delta(|\boldsymbol{p}| - k) \cos(\theta(p_s)) P_\beta(\sin(\theta(p_s)) \, dp_s \, ds. \tag{3.12}$$

The various dependencies of terms on s and p_s means that this is highly challenging to solve analytically, and numerical approaches are thus preferred. Solving this integral numerically also has difficulties, due to a gradient discontinuity in R_B observed in the integral over p_s. This occurs where the edge that is intercepted by the vector $-\hat{\boldsymbol{p}}$ swaps as p_s changes, which occurs at some value $p_{crit}(s)$. This phenomena is demonstrated by Figure 16.

To eliminate this issue, the integral across p_s at each location s is split into two separate integrals across $p_{crit}(s)$. These integrals are solved using quadpy C2 numerical integration schemes, adjusted to fit triangular domains [166].

3.3 Physical Parameters

In the following sections, the high-frequency vibrational behaviour of plate-like structures excited by correlated pressure fields will be studied. As demonstrated by equation (3.11), the response of the plate is dependent on parameters which describe the force applied by the TBL, along with the structural properties of the plate itself. In this section, appropriate values for these terms will be defined, for application in the remainder of this chapter.

DEA is a high-frequency approach, and so it is important that the vibrational

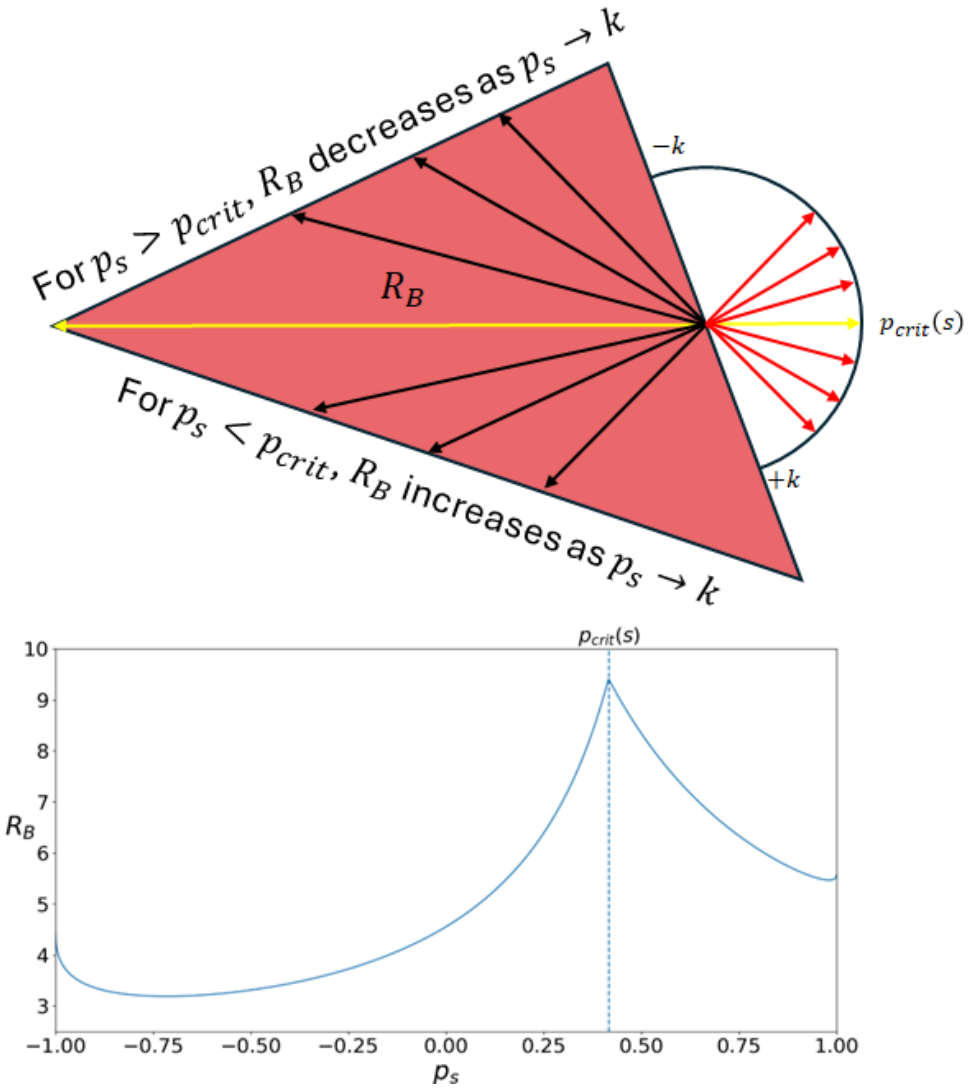

Figure 16: Demonstration of the gradient discontinuity in R_B for varying p_s at a particular boundary location s.

frequency f is carefully selected to ensure that this approach is applicable to the considered problem. In vibrational analysis, high-frequency typically refers to situations where the scale of variations of the structure are far greater than the wavelength of the excited vibrations [167]. However, as the structure is modelled using Kirchhoff-Love thin plate theory, it is essential that the chosen wavelength is much greater than the thickness of the plate [168, 169].

When modelling the vibrations of plates of lengths of order $0.1m - 1m$ using high-frequency methods such as SEA and DEA, frequencies in the range $2 - 10\,kHz$

are typically considered [56, 74, 110]. In this study, a value of $f = 5\,kHz$ is selected, giving a vibrational wavelength of $0.068\,m$. As discussed previously, the R' term in equation (3.11), which represents the strength of the applied source, varies depending on ω^2. The impact of changes to this quantity thus affects the magnitude of the response observed at each location by some scale factor. In this study however, only the spatial variation of the vibrational energy across the plate is of interest, rather than the magnitudes themselves. As such, this value is irrelevant to the conclusions of this study. For simplicity, a value of $R' = 1$ is thus chosen. The plate is considered to be constructed from aluminium alloy 6061. This material has density $\varrho = 2700kgm^{-3}$, Young's modulus $E = 68.9GNm^{-2}$, and poisson ratio $\nu = 0.33$ [170]. In addition, a thickness of $h = 3mm$ is chosen. This is far smaller than the vibrational wavelength of the system as defined above, and so Kirchhoff-Love thin plate theory is valid in this example. Using this thickness, the bending stiffness and vibrational wavenumber are given by $D = 173.97\,Nm$ and $k = 82.33\,m^{-1}$ respectively. Given that the speed of sound $c = 340ms^{-1}$ and $f = 5\,kHz$, the vibrational wavelength is given by $\lambda = 0.068\,m$ meaning $\lambda \gg h$. Thus, . In this thesis only bending waves are considered, and mode conversions at boundaries are neglected.

3.4 Implementation of the TBL pressure field

As demonstrated by equation (3.10), for a cell of known geometry the only unknown contribution to the phase-space density excited by a correlated field is W_Γ. Thus, to define the response of a structure to a specific correlated field, this function must provide an accurate representation of the applied pressure field. As demonstrated in Section 2.2.1, a useful choice for this term is the Wigner transform of an appropriate correlation function representing the applied pressure field, using equation (2.23).

In this study the excitation of flat plates by TBL pressure fields is considered.

As discussed in Section 2.3, the Corcos and Mellen models have been chosen to represent the TBL pressure fields in this study. Considering the excitation of plates orientated in the $x-z$ plane by TBL pressure fields formed due to a free-stream flow in the $+\hat{\boldsymbol{x}}$ direction, the correlation functions for these models are given by equations (2.57) and (2.62) respectively. The approach for defining W_Γ for each model is demonstrated in Sections 3.4.1 and 3.4.2.

3.4.1 Wigner transform of the Corcos model

The Wigner transform of the Corcos model, found by substituting equation (2.57) into equation (2.23), is given by equation (3.13)

$$W_\Gamma(\boldsymbol{r},\boldsymbol{p},\omega) = \int e^{-\alpha_x k_c|\xi_x|} e^{-\alpha_z k_c|\xi_z|} e^{ik_c\xi_x} e^{-i\boldsymbol{p}\cdot\boldsymbol{\xi}}\, d\boldsymbol{\xi}. \tag{3.13}$$

Here, the single point wall-pressure spectrum term $\phi(\omega)$ is omitted, as for a homogeneous TBL this is dependent only on the vibrational frequency ω. Much like R', this term thus impacts only the magnitude of the vibrational response observed rather than the distribution. As the Corcos model is already dependent only on the separation of the points, rewriting this function for the Wigner transform is unnecessary. To solve, the integral is separated into its streamwise and cross-stream components, leaving

$$W_\Gamma(\boldsymbol{r},\boldsymbol{p},\omega) = \left[\int_{-\infty}^{+\infty} e^{-\alpha_x k_c|\xi_x|} e^{ik_c\xi_x} e^{-ip_x\xi_x}\, d\xi_x\right] \times \left[\int_{-\infty}^{+\infty} e^{-\alpha_z k_c|\xi_z|} e^{-ip_z\xi_z}\, d\xi_z\right]. \tag{3.14}$$

Focusing first on the streamwise integral, this may be split into two integrals across $\xi_x = 0$ to give

$$\begin{aligned}\int_{-\infty}^{+\infty} e^{-\alpha_x k_c|\xi_x|} e^{ik_c\xi_x} e^{-ip_x\xi_x}\, d\xi_x \;&= \int_{-\infty}^{0} e^{(i(k_c-p_x)+\alpha_x k_c)\xi_x}\, d\xi_x \\ &\quad + \int_{0}^{+\infty} e^{(i(k_c-p_x)-\alpha_x k_c)\xi_x}\, d\xi_x.\end{aligned} \tag{3.15}$$

Solving the first integral

$$\int_{-\infty}^{0} e^{(i(k_c-p_x)+\alpha_x k_c)\xi_x}\, d\xi_x = \frac{\left[e^{(i(k_c-p_x)+\alpha_x k_c)\xi_x}\right]_{-\infty}^{0}}{\alpha_x k_c + i(k_c-p_x)}. \tag{3.16}$$

As discussed in Section 2.3, α_x is an empirical parameter of value $0.10-0.12$ and $k_c = \omega/U_c$ where ω is the excitation frequency and U_c is the convective flow speed. As each of these parameters are positive, $\alpha_x k_c > 0$, and the integral solution tends to 0 as $\xi_x \to -\infty$. The solution to this integral is thus given by

$$\int_{-\infty}^{0} e^{(i(k_c-p_x)+\alpha_x k_c)\xi_x}\, d\xi_x = \frac{1}{\alpha_x k_c + i(k_c-p_x)}. \tag{3.17}$$

Similarly,

$$\int_{0}^{+\infty} e^{(i(k_c-p_x)-\alpha_x k_c)\xi_x}\, d\xi_x = \frac{1}{\alpha_x k_c - i(k_c-p_x)}. \tag{3.18}$$

The solution to the streamwise component of equation (3.14) is then given by

$$\begin{aligned}\int_{-\infty}^{+\infty} e^{-\alpha_x k_c|\xi_x|} e^{ik_c\xi_x} e^{-ip_x\xi_x}\, d\xi_x &= \frac{1}{\alpha_x k_c + i(k_c-p_x)} + \frac{1}{\alpha_x k_c - i(k_c-p_x)} \\ &= \frac{2\alpha_x k_c}{\alpha_x^2 k_c^2 + (k_c-p_x)^2}.\end{aligned} \tag{3.19}$$

The cross-stream component of equation (3.14) may also be split across ξ_x, to give

$$\int_{-\infty}^{+\infty} e^{-\alpha_z k_c|\xi_z|} e^{-ip_z\xi_z}\, d\xi_z = \int_{-\infty}^{0} e^{(\alpha_z k_c - ip_z\xi_z)}\, d\xi_z + \int_{0}^{+\infty} e^{-(\alpha_z k_c + ip_z\xi_z)}\, d\xi_z. \tag{3.20}$$

As α_z is also a non-zero, positive, empirical parameter, the solutions of each integral are given by

$$\int_{-\infty}^{0} e^{(\alpha_z k_c - i p_z \xi_z)}\, d\xi_z = \frac{1}{\alpha_z k_c - i p_z}. \tag{3.21}$$

and

$$\int_{0}^{+\infty} e^{-(\alpha_z k_c + i p_z \xi_z)}\, d\xi_z = \frac{1}{\alpha_z k_c + i p_z}. \tag{3.22}$$

given that $\alpha_z k_c > 0$. The overall cross-stream component of equation (3.14) is given by

$$\int_{-\infty}^{+\infty} e^{-\alpha_z k_c |\xi_z|} e^{-i p_z \xi_z}\, d\xi_z = \frac{2\alpha_z k_c}{\alpha_z^2 k_c^2 + p_z^2}. \tag{3.23}$$

The overall Wigner transform of the Corcos model is thus given by

$$\begin{aligned} W_\Gamma(\boldsymbol{p}, \omega) &= \left[\frac{2\alpha_x k_c}{\alpha_x^2 k_c^2 + (k_c - p_x)^2} \times \frac{2\alpha_z k_c}{\alpha_z^2 k_c^2 + p_z^2} \right] \\ &= \frac{4\alpha_x \alpha_z k_c^2}{\left[\alpha_x^2 k_c^2 + (k_c - p_x)^2\right] \left[\alpha_z^2 k_c^2 + p_z^2\right]}. \end{aligned} \tag{3.24}$$

In this result the Wigner transform of the Corcos model varies only with the ray momentum $\boldsymbol{p}$. When studying equation (2.23), which is used to define this term, it can be shown that the Wigner transform procedure provides no additional spatial dependency. Thus, if the correlation function being considered is spatially homogeneous then the resulting Wigner transform will as well. As discussed in Section 2.3, the TBL pressure field models studied here were developed to represent the pressure field applied by fully formed, homogeneous, TBLs across flat plates. It is thus appropriate that the term used to capture the TBL pressure field is also spatially homogeneous. As demonstrated in equation (3.11), only rays with $|\boldsymbol{p}| = k$ can contribute to the energy density across the plate. Thus, $p_x^2 + p_z^2 =$

k, and if k is known, then $\boldsymbol{p}$ effectively defines the direction of propagation of the rays. The contribution to the energy density from the TBL represented by the Corcos model is then best represented by a radial plot. An example for several mean flow speeds is demonstrated by Figure 17.

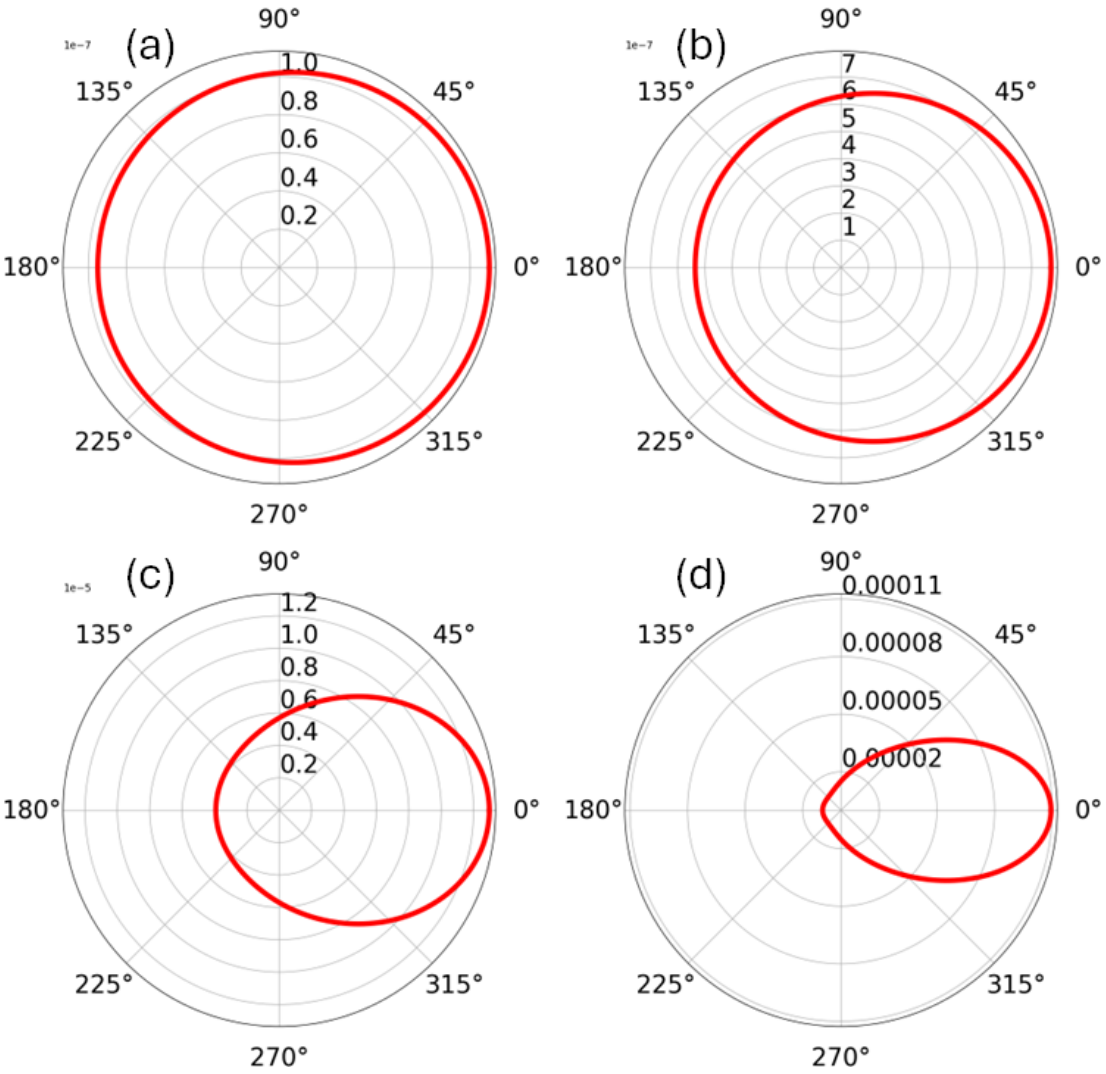

Figure 17: Radial plots of the energy density flowing from a point excited by a TBL represented by the Corcos model. The free-stream is flowing at 0^o at speeds (a) $19\,ms^{-1}$, (b) $50\,ms^{-1}$ (c) $160\,ms^{-1}$ and (d) $300\,ms^{-1}$. Here, $p_x = k\cos(\theta)$ and $p_z = k\sin(\theta)$ with the additional parameters as stated in Section 3.3.

Figure 17 shows that at low speeds the energy inserted by the field propagates near isotropically from the source location. For increasing flow speeds however, the ray density becomes progressively more directional, with the vast majority

of rays propagating in the flow direction for $U_0 = 300\,ms^{-1}$. Thus, despite the homogeneous nature of the applied pressure field, the observed directional dependence of the energy flow suggests that the response of the structure may vary with position. This is interesting, as in Section 2.1 it was discussed that prior studies of the vibrational response of plates under TBL excitations consider either a single-point or point-averaged response [26, 80, 120]. These results would thus fail to account for spatial variations in the vibrational behaviour of the plate. The overall response is however likely to depend on the properties of the plate, as the applied boundary conditions or damping may limit the importance of this directional effect. The influence of these effects on the vibrational energy distribution across the plate is explored in detail in Section 3.6.

3.4.2 Wigner transform of the Mellen model

The Wigner transform of the Mellen model, found by substituting equation (2.62) into equation (2.23), is given by

$$W_\Gamma = \int e^{-\sqrt{(\alpha_x k_c \xi_x)^2 + (\alpha_z k_c \xi_z)^2}} e^{ik_c \xi_x} e^{-i\boldsymbol{p}\cdot\boldsymbol{\xi}}\, d\boldsymbol{\xi}. \tag{3.25}$$

with $\phi(\omega)$ once again omitted. Unlike with the Corcos model, it is impossible to split this integral into its streamwise and cross-stream components. Instead, an approach similar to that employed previously in [125] to compute the Fourier transform of the Mellen model is applied. Here, the dot product is expanded and the resulting exponent is re-factorised to give

$$W_\Gamma(\boldsymbol{r}, \boldsymbol{p}, \omega) = \int\int e^{-\sqrt{(\alpha_x k_c \xi_x)^2 + (\alpha_z k_c \xi_z)^2}} e^{-i(p_x - k_c)\xi_x} e^{-ip_z \xi_z}\, d\xi_x\, d\xi_z. \tag{3.26}$$

The substitutions $\alpha_x k_c \xi_x = \xi_x'$ with $d\xi_x = \frac{1}{\alpha_x k_c} d\xi_x'$ and $\alpha_z k_c \xi_z = \xi_z'$ with $d\xi_z = \frac{1}{\alpha_z k_c} d\xi_z'$ are then made, leaving

$$W_\Gamma(\boldsymbol{r},\boldsymbol{p},\omega) = \frac{1}{\alpha_x\alpha_z k_c^2}\int\int e^{-\sqrt{(\xi_x')^2+(\xi_z')^2}} e^{-i\frac{1}{\alpha_x k_c}(p_x-k_c)\xi_x'} e^{-i\frac{1}{\alpha_z k_c}p_z\xi_z}\, d\xi_x'\, d\xi_z'. \tag{3.27}$$

Writing $\boldsymbol{\xi}' = (\xi_x', \xi_z')$ and $\boldsymbol{p}' = \left(\frac{1}{\alpha_x k_c}(p_x - k_c), \frac{1}{\alpha_z k_c}p_z\right)$, this can be re-formatted as

$$W_\Gamma(\boldsymbol{r},\boldsymbol{p},\omega) = \frac{1}{\alpha_x\alpha_z k_c^2}\int\int e^{-|\boldsymbol{\xi}'|} e^{-i\boldsymbol{\xi}'\cdot\boldsymbol{p}'}\, d\xi_x'\, d\xi_z'. \tag{3.28}$$

The integral is then converted into polar coordinates, with $\xi' = |\boldsymbol{\xi}'|$ and $d\xi_x' d\xi_z' = \xi' d\xi' d\theta$. In addition, the substitution $P = |\boldsymbol{p}'|$ is made. Hence,

$$W_\Gamma = \frac{2\pi}{\alpha_x\alpha_z k_c^2}\int_0^\infty \xi' e^{-\xi'}\left[\frac{1}{2\pi}\int_0^{2\pi} e^{-i\xi' P\cos(\theta)}\, d\theta\right] d\xi'. \tag{3.29}$$

The integral over θ is the definition of the zeroth order Bessel function of the first kind $J_0(RP)$ [171] and so

$$W_\Gamma = \frac{2\pi}{\alpha_x\alpha_z k_c^2}\int_0^\infty \xi' e^{-\xi'} J_0(\xi' P)\, d\xi'. \tag{3.30}$$

The resultant integral is the Hankel transform of $e^{-\xi'}$ [171] which has the solution

$$W_\Gamma = \frac{2\pi}{\alpha_x\alpha_z k_c^2}\frac{1}{(P^2+1)^{3/2}}. \tag{3.31}$$

Substituting back in for P,

$$W_\Gamma = \frac{2\pi}{\alpha_x\alpha_z k_c^2}\frac{1}{\left(\left(\frac{1}{\alpha_x k_c}(p_x-k_c)\right)^2 + \left(\frac{1}{\alpha_z k_c}p_z\right)^2 + 1\right)^{3/2}}, \tag{3.32}$$

which can be simplified to give

$$W_\Gamma = \frac{2\pi(\alpha_x\alpha_z k_c^2)^2}{((\alpha_z k_c)^2(p_x-k_c)^2 + (\alpha_x k_c)^2 p_z^2 + (\alpha_x\alpha_z k_c^2)^2)^{3/2}}. \tag{3.33}$$

Once again, the homogeneous nature of the original correlation function leads

to a homogeneous, radially dependent, representation of the TBL pressure field. Radial plots of this function for various mean stream flow speeds are shown in Figure 18.

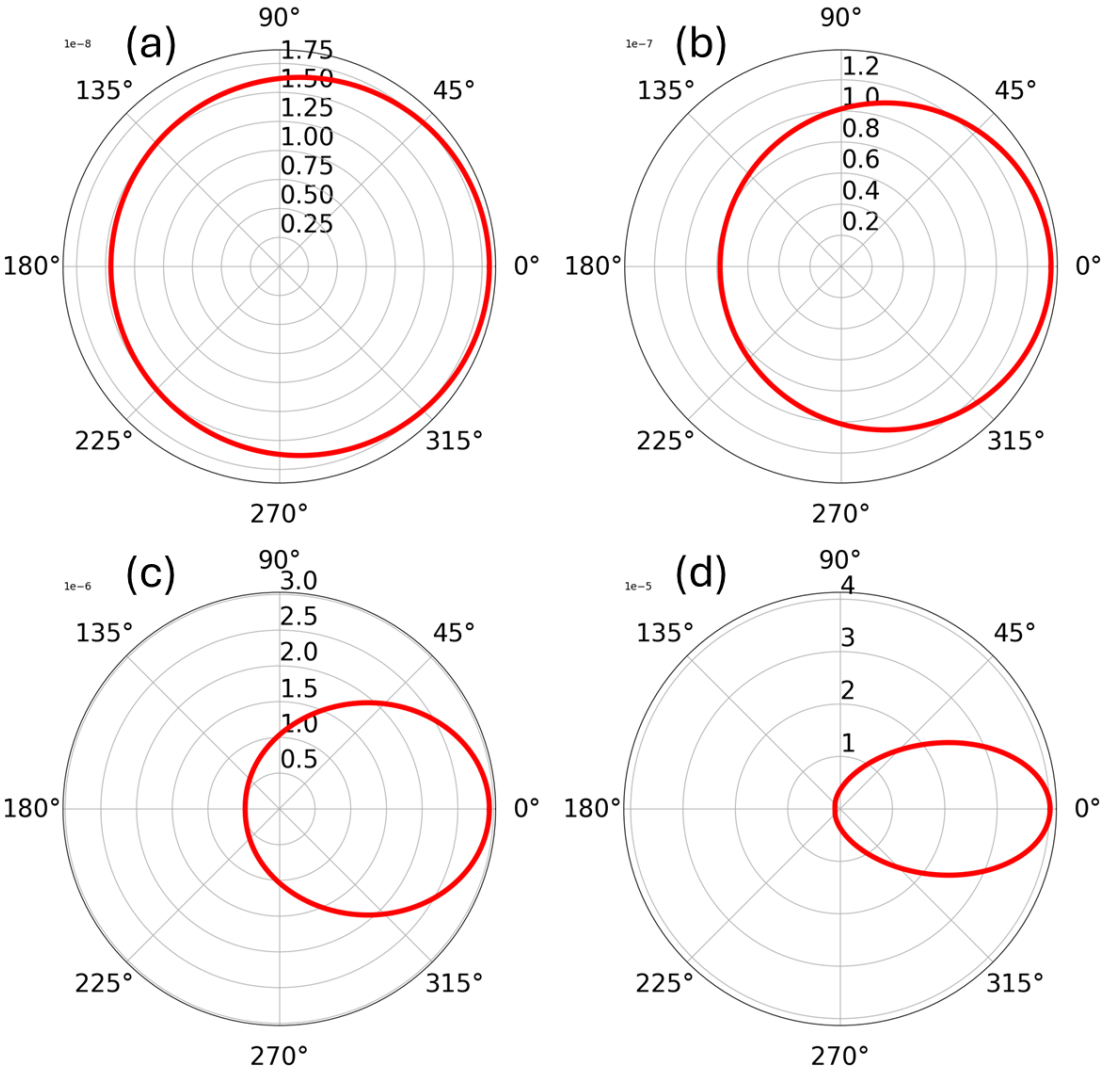

Figure 18: Radial plots of the energy density flowing from a point excited by a TBL represented by the Mellen model. The free-stream is flowing at 0^o at speeds (a) $19\,ms^{-1}$, (b) $50\,ms^{-1}$ (c) $160\,ms^{-1}$ and (d) $300\,ms^{-1}$. Here, $p_x = k\cos(\theta)$ and $p_z = k\sin(\theta)$ with the additional parameters as stated in Section 3.3.

These results are rather similar to those demonstrated when applying the Corcos model, as shown in Figure 17. The main difference being that the energy flow in the Mellen model shows a stronger preference towards the mean flow direction than the Corcos model at all flow speeds. This is most apparent when consid-

ering the higher speed cases, with the Mellen model demonstrating effectively zero energy flow anti-parallel to the mean flow at $300\,ms^{-1}$. The impact of this difference on the resultant vibrational behaviour will be studied in the following section.

3.4.3 TBL excitation of a single patch

To demonstrate the implementation of TBL pressure fields within DEA, the excitation of the simple structure shown in Figure 14 by a TBL pressure field applied within the highlighted region is considered. To isolate the influence of the flow on the vibrational response of the plate, absorbing boundary conditions are applied at the structural boundary. The resultant vibrational energy distribution for both the Corcos and Mellen models for a flow speed of $U_0 = 50\,ms^{-1}$ is shown by Figure 19.

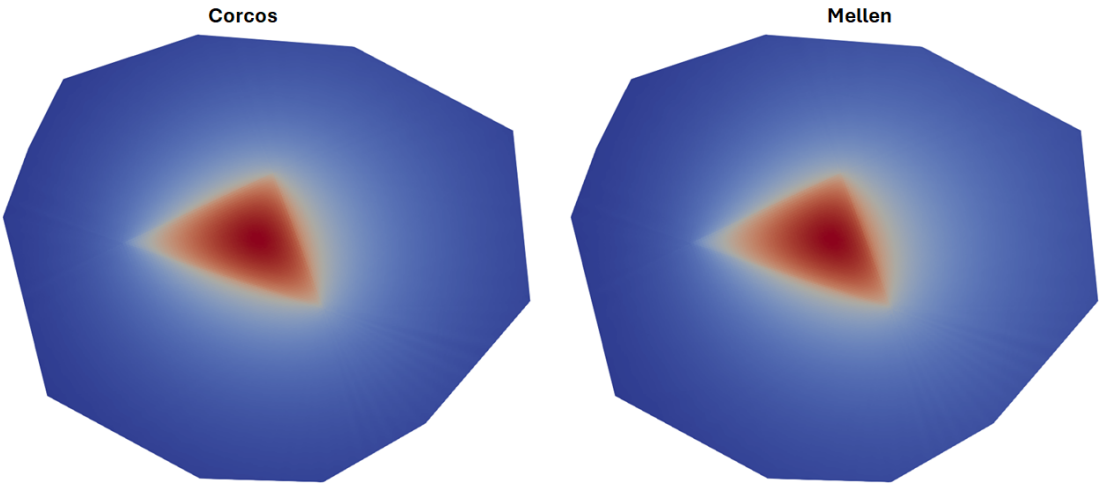

Figure 19: Vibrational response of the simple structure to a TBL of flow speed $U_0 = 50\,ms^{-1}$ applied within the indicated region. The colour scale shows the calculated energy density and runs from low energy (blue) to high energy (red).

In this plot, it can be observed that the energy density inserted by the field radiates near isotropically from the excited cell. This is unsurprising, as in Figures (17) and (18) at $50\,ms^{-1}$ both the Corcos and Mellen models show that there is

little preference in the direction of propagation of ther rays from the source at this speed. This is also why the peak of the vibrational energy is found close to the centre of the excited patch in each case. As the rays are emitted almost isotropically, the energy density at each location is effectively determined by the range of locations which emit rays that will intercept this point as they propagate across the domain. The actual peak is then found slightly downstream of this centre, indicating a slight preference for emission of rays in this direction. The vibrational response of the plate to a TBL pressure field applied with a flow speed of $U_0 = 300\,ms^{-1}$ is then shown by Figure 20.

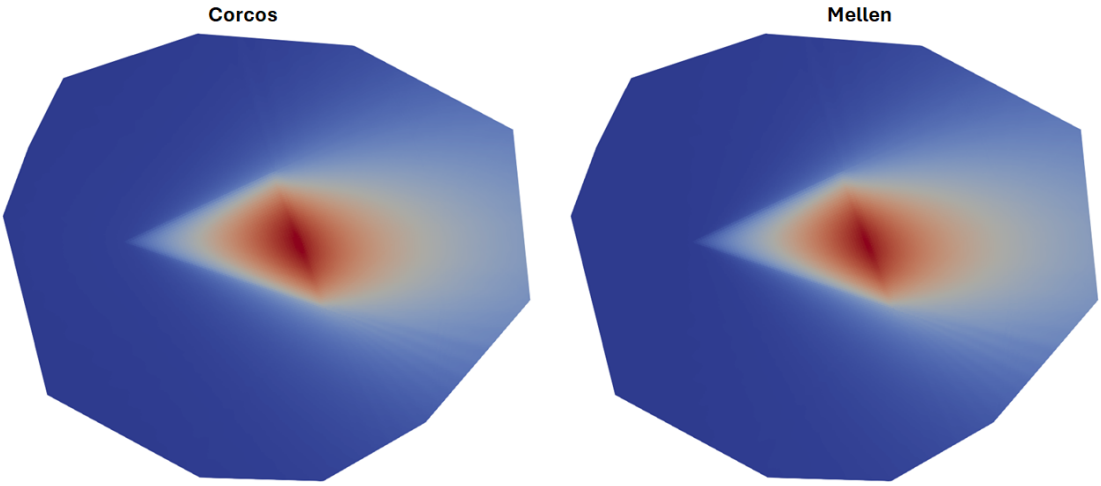

Figure 20: Vibrational response of the simple structure to a TBL of flow speed $U_0 = 300\,ms^{-1}$ applied within the indicated region.

As shown by Figures 17 and 18, at higher speeds the energy flow from the source is far more directional, demonstrating a strong preference for the emission of rays which propagate in the mean flow direction. This is demonstrated in Figure 20, with the bulk of the energy flowing close to parallel with the $+\hat{\boldsymbol{x}}$ direction. The result is a clear variation in the vibrational response of the plate based on the location relative to the original source. In comparison to the low-speed case, the peak in the energy density has also shifted to be further downstream. This is because, the further that one moves downstream within the excited cell, the

more rays which propagate close to the flow direction will intercept this location. As the fraction of rays propagating in the flow direction increases for increasing flow speeds, the peak in the energy density also shifts downstream.

3.5 Large patch and full-body excitations

The extension of this approach for more widespread source fields, spanning multiple mesh elements, is now considered. To introduce this idea, the excitation of a rectangular patch made up of two conjoined triangular cells is considered. When applying a correlated field to this patch, the constituent cells may be handled in one of two ways. The first is the "split-cell" approach, where each mesh element is treated as an individual patch excitation as in Section 3.2. The overall response of the plate is then the sum of the response to each excitation. The other method is the "super-cell" approach, where the elements which make up the excited patch are merged to form a single larger cell. To establish the merits of these approaches, the capability of each to provide an accurate measure of the energy density at the boundary of the excited patch must be considered. Considering the excitation of the patch by an arbitrary, homogeneous, excited field, the energy density at some location on the boundary can be expressed in terms of the shape of the patch by $\tilde{\rho}_0(s, p_s) \propto \left(1 - e^{-\mu R_B(s,p_s)}\right)$. The approach to define the energy density at an arbitrary point on the boundary of the rectangular patch using each approach is demonstrated in Figure 21.

As shown in this figure, the approaches give equivalent estimates for the energy density at the boundary of the excited patch. It can be demonstrated that this is true for any combination of numbers and shapes of cells. The preferred approach must thus be chosen based upon the suitability of each method for modelling large excitation regions. When applying the super-cell approach, the energy density is only calculated across the outer boundary of the excited patch. By comparison, for the split-cell method this calculation must instead be performed across the

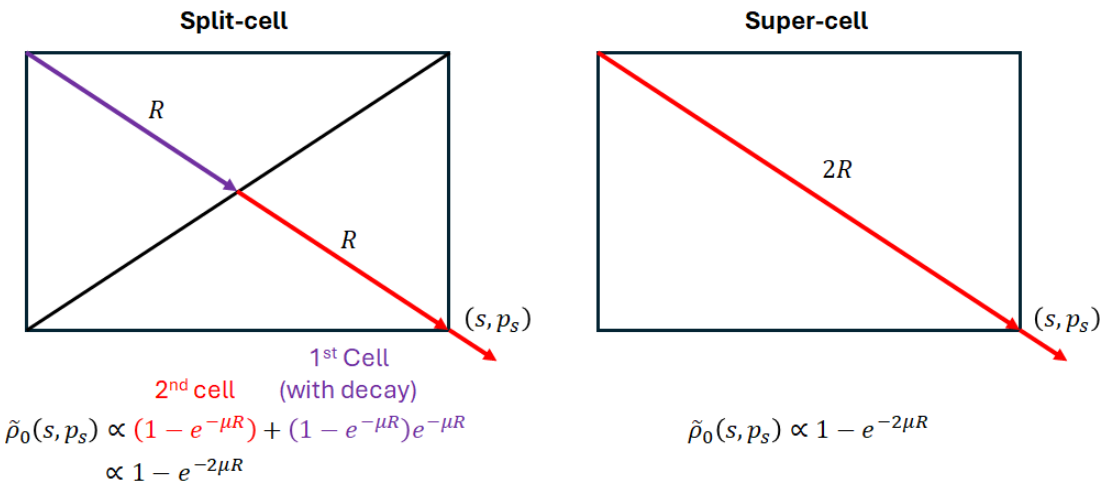

Figure 21: Calculation of the boundary density of a rectangular patch using the split-cell and super-cell approaches.

boundary segments of all mesh elements within the excited patch. The super-cell approach is thus likely to be far less computationally taxing than the split-cell approach, particularly for large excitations spanning many mesh elements. However, the region contained within the super-cell must be concave, and the approach for defining the super-cell boundary is cumbersome. These issues then limit the applicability of this approach in situations involving large pressure fields applied across complex structures. The greatest fault of the super-cell approach is however found when attempting to account for spatial variances in the source, structural, or material properties. To do so effectively would involve considering the contributions made at each boundary phase-space location individually, accounting for changes in these properties as the energy propagates through other mesh elements to the boundary, involving highly complex and time-consuming calculations. To mitigate this issue, it could be assumed the variance in the system properties is sufficiently small that the excited region could be treated as a single, flat, element with consistent properties. For cases involving spatially variant source fields applied to structures with complex geometries and varying material properties this may severely limit the accuracy of the approach. Thus,

despite its greater computational cost, the split-cell approach is preferred here due to its reduced complexity and ability to manage variations in structural properties. This approach is employed to define the response of plates to full-body excitations in Section 3.6.

3.6 TBL excitation of a flat plate

3.6.1 System configuration

Having extended the correlated field approach from single-cell to larger patch excitations, the response of structures to correlated fields spanning the structural surface may now be considered. To demonstrate this procedure, the excitation of a flat plate by a spatially homogeneous TBL applied across the plate surface is considered. The basis of this test is a common wind tunnel experiment performed to measure the vibrational response of plates under TBL pressure fields. In these experiments, the plate is positioned on the floor of a wind tunnel and is subjected to a grazing flow of air moving parallel to the plate surface [172–174]. As discussed in Section 2.3, this leads to the formation of a boundary layer across the floor. Within the wind tunnel, the plate is positioned far downstream of the inlet [175], and in many cases the flow is tripped by a piece of sandpaper or wire [176–178]. The purpose of these actions is to ensure that the TBL is fully-formed across the plate [27]. When modelling this system, it is thus appropriate to consider the TBL to be spatially homogeneous. As discussed in Section 2.3, this enables the modelling of the TBL pressure field using the Corcos or Mellen models [121]. Due to the similarity in the single-patch response observed for both models in Section 3.2, only the Corcos model results will be presented here. Results for TBL pressure fields represented by the Mellen model will be presented in Appendix A. The plate to be studied has dimensions $200 \times 150 \times 3\,mm$ and is constructed of aluminium alloy 6061, with material properties as described in Section 3.3. It

is represented computationally by a mesh grid of 36×28 quadrilateral elements, each of dimensions $5.56 \times 5.36\,mm$, as demonstrated in Figure 22.

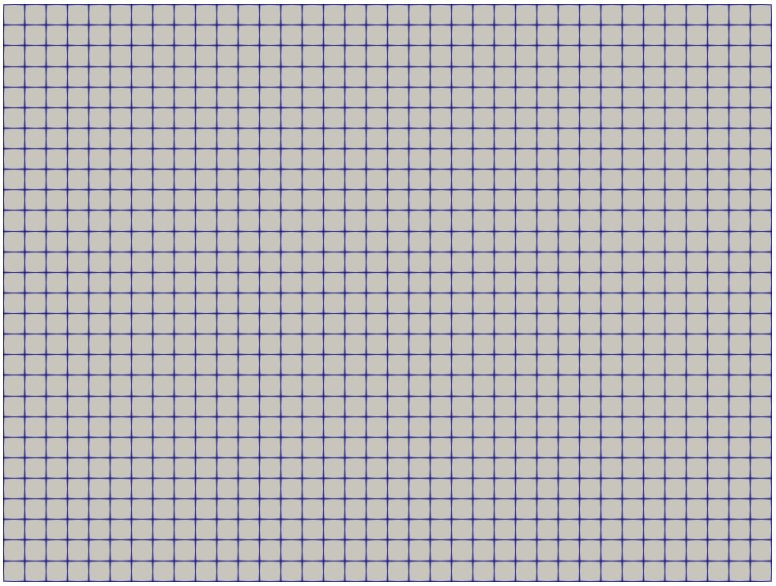

Figure 22: Mesh used to represent the flat plate for the results presented in this section.

The vibrational response of the plate will be considered under three different boundary conditions: (i) Absorbing boundary conditions, where all energy reaching the boundary is absorbed without any reflection (equivalent to $\lambda(\boldsymbol{r}, \boldsymbol{p}) = 0$ in equation (2.36)); (ii) Reflecting boundary conditions, where all energy reaching the boundary is fully reflected (equivalent to $\lambda(\boldsymbol{r}, \boldsymbol{p}) = 1$); (iii) Periodic boundary conditions, where absorbing boundary conditions are applied to the leading and trailing edges and periodic boundary conditions are applied to the flow-parallel edges. In this study, the effect of damping on the vibrational behaviour of the plate will also be investigated. As such, the damping coefficient will be varied between $\mu = 0.01$ and $\mu = 0.80$.

When modelling this system in DEA, the flow is captured by Legendre polynomials up to order $N_\beta = 25$, and each boundary segment is subdivided into $N_b = 15$ segments. The resultant energy density distributions for the chosen flow, structural, and boundary conditions are presented in sections 3.6.2 - 3.6.4.

3.6.2 Absorbing boundary conditions

The vibrational response of the plate with absorbing boundary conditions for various flow speeds is demonstrated by Figure 23.

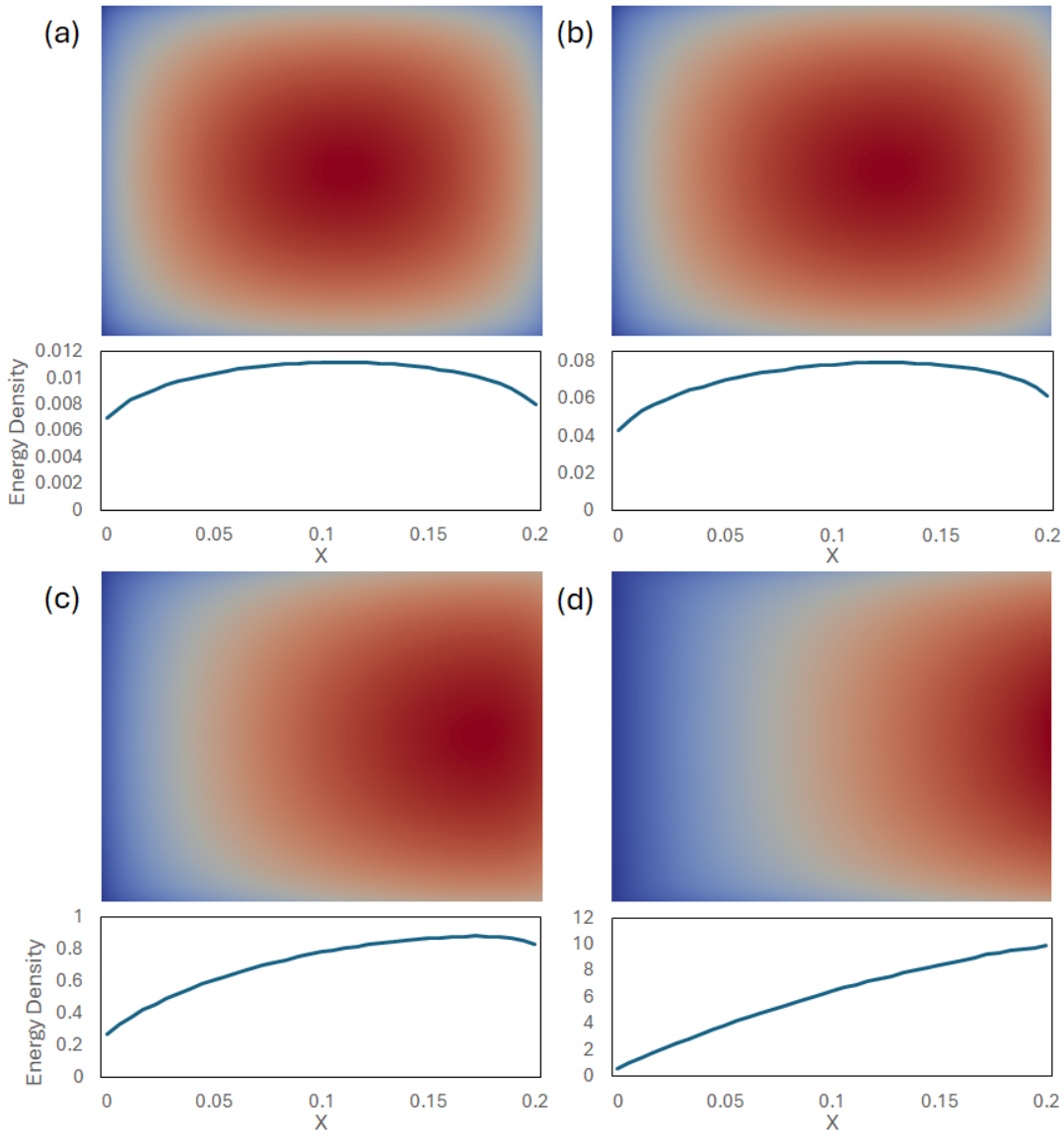

Figure 23: Vibrational response of a flat plate with absorbing boundary conditions and damping coefficient $\mu = 0.01$ under TBL pressure fields formed from free-stream flows with speeds (a) $19\,ms^{-1}$ (b) $50\,ms^{-1}$ (c) $150\,ms^{-1}$ (d) $300\,ms^{-1}$.

The results shown in this figure display a strong resemblance to the single-cell excitation case in subsection 3.4.3. In both cases, the absorbing condition applied to the boundary ensures that the rays generated by the sources may propagate

across the structural domain only once before they are lost. The peak in the energy density is then found at the location that the greatest number of rays generated by the field cross in a single journey across the plate. At low speeds, rays are emitted near-isotropically at each location, and the peak is thus found close to the centre of the plate. As U_0 is increased, the source field becomes progressively more directional, and a strong preference emerges for the generation of rays which propagate in the mean flow direction. The increased generation of rays in the flow direction then ensures that the peak in the energy density moves gradually downstream for increasing flow speeds. At $U_0 = 300\,ms^{-1}$, the preference for the propagation of rays in the flow direction is sufficiently strong that the peak in the energy density is found at the trailing edge of the plate, with a near-linear increase in energy density along the plate.

By repeating this study with various μ values, the effect of damping on the observed vibrational behaviour of the plate may be investigated. This is demonstrated in Figure 24, where the energy density distribution across the plate along the line $z = 0$ is displayed for various damping coefficients μ is demonstrated by.

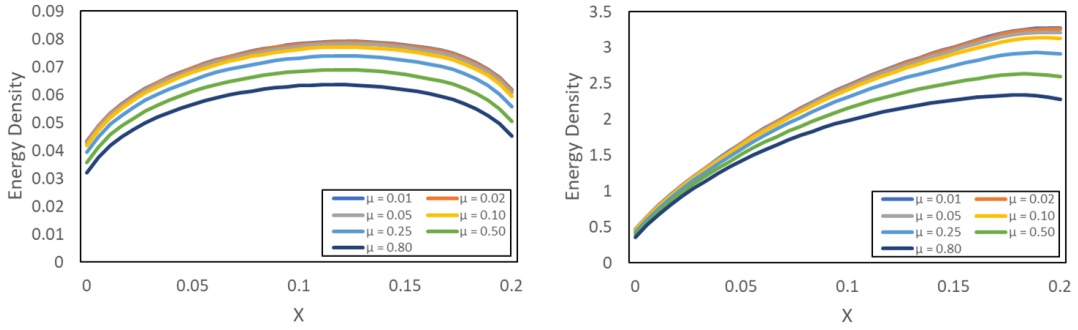

Figure 24: Energy density distribution along the line $z = 0$ for flow speeds $U_0 = 50\,ms^{-1}$ (left) and $U_0 = 300\,ms^{-1}$ (right) with absorbing boundary conditions.

In the lower speed case, the distribution of energy density across the plate appears approximately constant with increasing μ, with only a small reduction in the magnitudes observed. The reason for this is the absorbing condition applied to the structural boundary, and its effect to limit the rays to a single propagation

across the plate. Given that the plate has dimensions of $0.2 \times 0.15\,m$, these rays travel a ver short distance in their lifetimes, and very little ray density is lost due to damping. This is illustrated by Figure 25.

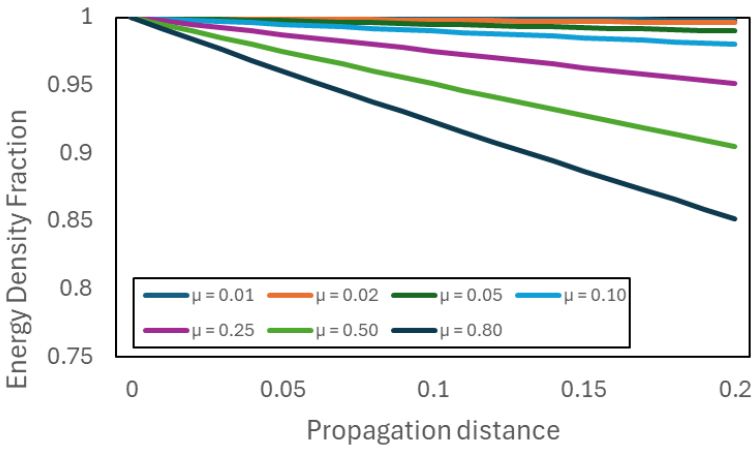

Figure 25: Decay of energy density for rays propagating across plates with different damping coefficients μ.

Here, even in the most highly damped cases, the short lifetime of the rays ensures that damping has a limited impact on the observed vibrational response.

In the higher speed case there is however some variation in the observed vibrational response, particularly at the trailing edge. As discussed previously, for large U_0 the majority of rays propagate in the mean-stream flow direction. Thus, contributions to the energy density at any arbitrary location on the plate will chiefly come from rays originating upstream of the considered point. Close to the leading edge, the distance travelled by these rays is minimal and so very few are lost due to damping. There is thus very little difference in the energy density observed for different μ values. Further downstream, the mean distance travelled by the rays increases, meaning that the damping will have a greater impact on the resulting energy density distribution. The increase in significance of this effect further downstream then leads to the "tailing off" of the energy density close to the trailing edge. Although most apparent in the highest speed case, this effect will occur at all flow speeds due to the inherent directionality of the source field.

This effect can be observed through comparison of the results for $\mu = 0.01$ in Figure 23 with the results presented in Figure 26 for $\mu = 0.80$.

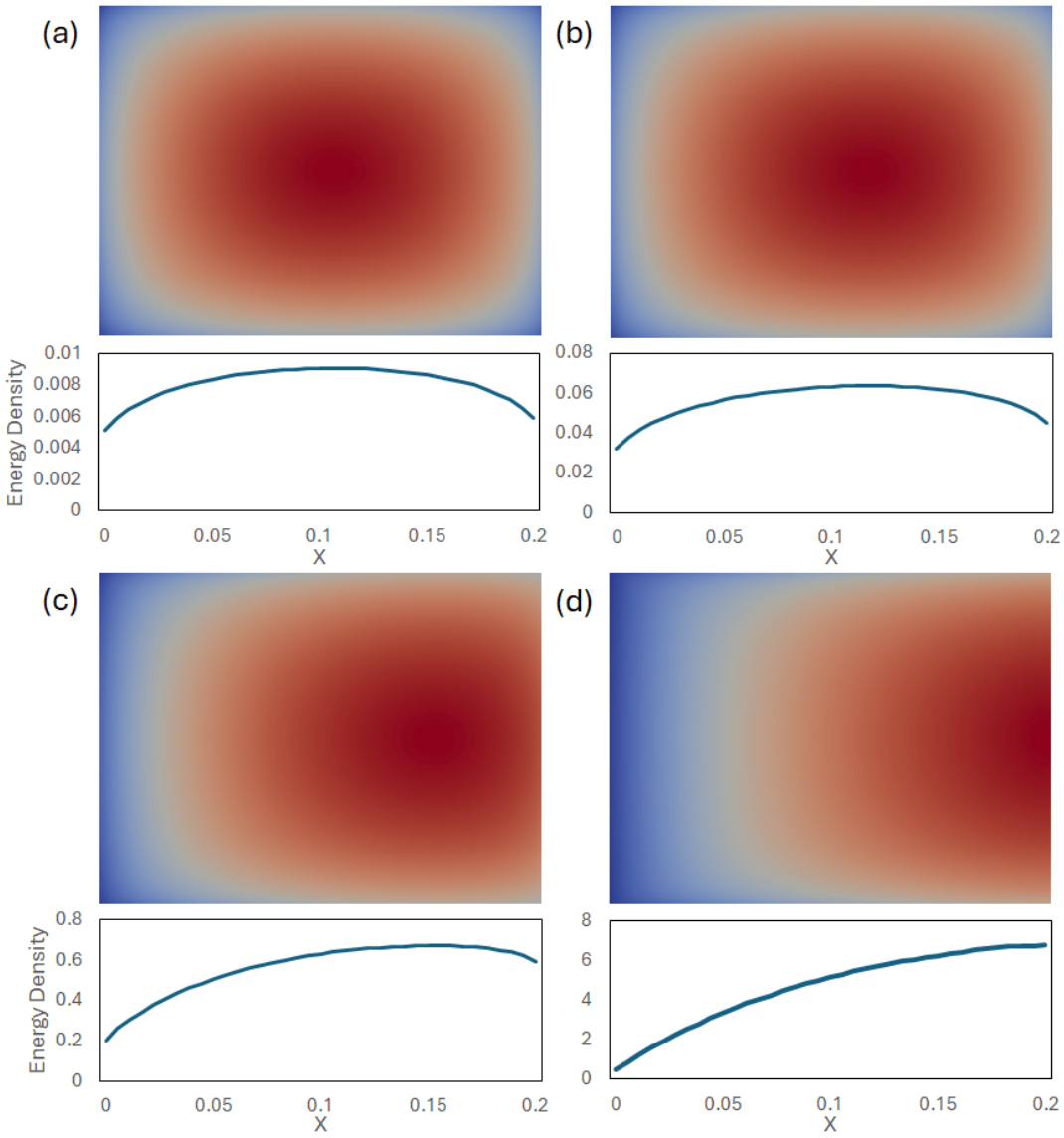

Figure 26: Vibrational response of a flat plate with absorbing boundary conditions and damping coefficient $\mu = 0.80$ under TBL pressure fields formed from free-stream flows with speeds (a) $19\,ms^{-1}$ (b) $50\,ms^{-1}$ (c) $150\,ms^{-1}$ (d) $300\,ms^{-1}$.

Here, the increased damping at the trailing edge leads to the broadening of the peak in the energy density compared to the low-damping case, as well as shifting this peak slightly upstream. This effect is more prominent for greater U_0.

3.6.3 Reflecting boundary conditions

The vibrational response of the plate under reflecting boundary conditions for various flow speeds is demonstrated in Figure 27.

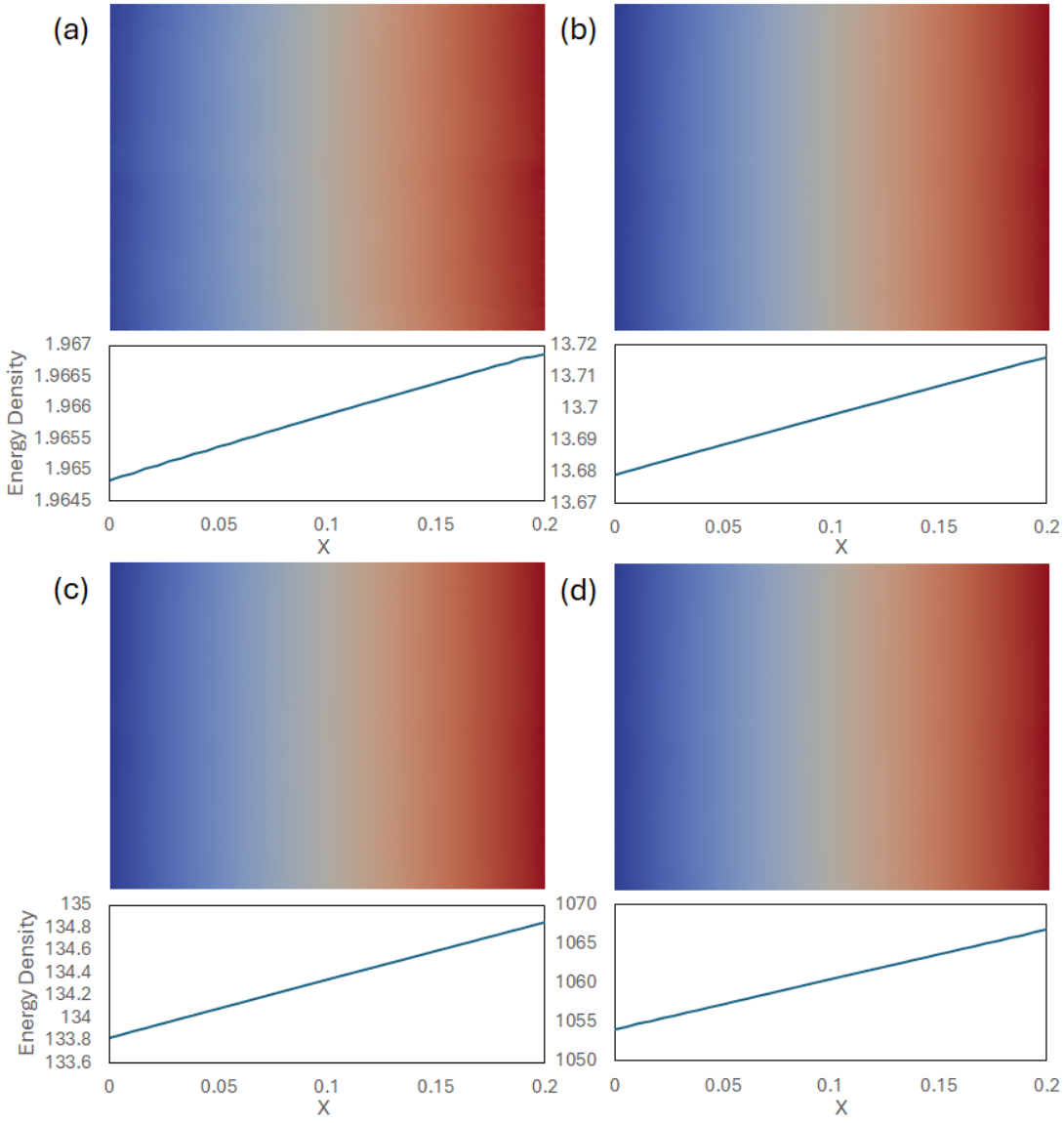

Figure 27: Vibrational response of a flat plate with reflecting boundary conditions and damping coefficient $\mu = 0.01$ under TBL pressure fields formed from free-stream flows with speeds (a) $19\,ms^{-1}$ (b) $50\,ms^{-1}$ (c) $150\,ms^{-1}$ (d) $300\,ms^{-1}$.

When applying reflecting boundary conditions, rays impinging on the structural boundary are reflected back into the structural domain, without scattering losses. In this situation, the density of rays can only decay due to damping losses. As

all of the energy density remains in the plate rather than being dissipated at the structural boundary, the vibrational energy excited within the plate is far greater than in the absorbing boundary case. Through comparison of Figures 23 and 27, one can observe that the energy densities are approximately two orders of magnitude greater here than in the equivalent absorbing boundary cases.

The application of reflecting boundary conditions has also impacted the distribution of the energy density across the plate. As discussed in subsection 3.6.2, the plate is sufficiently small that damping losses are minimal for individual journeys across the surface, even in the more highly damped cases. As such, the rays are able to propagate across the plate many times before being lost to damping. This is a key assumption of the SEA approach [55,68], which is employed to justify the assumed homogeneous energy distribution within each subsystem. In the cross-flow direction this result is true, as the energy density is equal in this direction for any distance from the leading edge. In the streamwise axis however, the directionality of the source field leads to the linear increase in the observed energy density with increasing distance from the leading edge. The result is that for all flow speeds, the resultant energy density distributions appear to be remarkably similar. Despite the visual similarity in each case, the distribution of the energy density varies substantially for different flow speeds. For the $U_0 = 19\,ms^{-1}$ case, the relative difference in the energy density between the leading and trailing edges is around 0.1 % of the leading edge energy density, whilst for the $U_0 = 300\,ms^{-1}$ case, this difference is 1.21 %. As discussed, higher flow speeds generate a greater proportion of rays which propagate initially in the mean flow direction. As such, despite the final energy density distribution being the sum of many ray journeys across the plate, the initial distribution of ray momenta is still highly influential on the observed vibrational response.

In this case the only source of decay of the ray density is damping within the plate, and so it is likely that adjustments to the damping coefficient μ will have a larger

impact on the distribution of energy density across the plate. The distribution of vibrational energy across the plate in the streamwise direction for different damping coefficients with reflecting boundary conditions is shown in Figure 28.

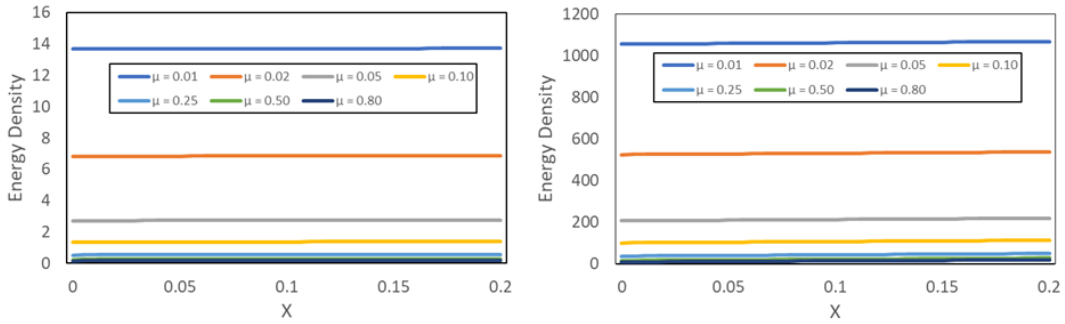

Figure 28: Energy density distribution along the line $z = 0$ for flow speeds $U_0 = 50\,ms^{-1}$ (left) and $U_0 = 300\,ms^{-1}$ (right) with reflecting boundary conditions.

As expected, the damping coefficient has a large impact on the resultant vibrational energy density within the plate. In each case the energy densities found for $\mu = 0.01$ are two orders of magnitude larger than in the $\mu = 0.80$ case. Interestingly however, the difference in energy across the plate seems to be very similar for all damping values. To study this in more detail, the absolute and percentage differences in energy density across the plate are considered for each μ value. These results are demonstrated in Figure 29.

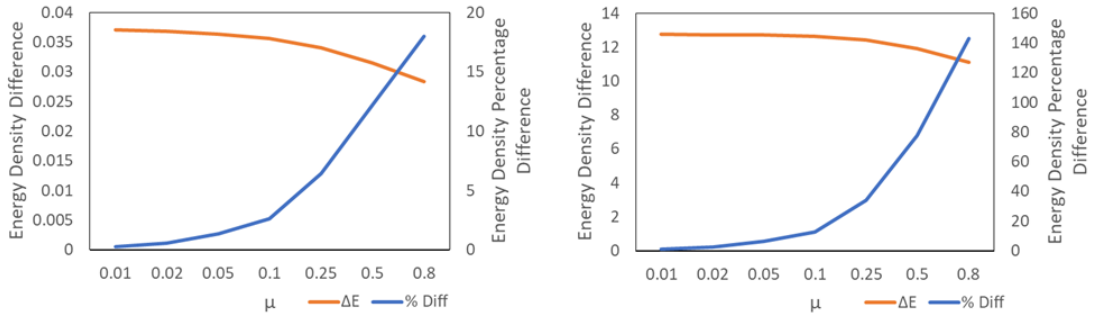

Figure 29: Absolute and relative energy difference in the energy between the leading and trailing edge of the plate for different μ values and flow speeds $U_0 = 50\,ms^{-1}$ (left) and $U_0 = 300\,ms^{-1}$ (right) with reflecting boundary conditions.

As shown in Figure 29, the difference in the energy density across the plate is

approximately constant for all μ in each case, despite the large difference in the energy density values observed for different damping values. This suggests that the observed energy difference across the plate is far more strongly linked to the properties of the source field than the material properties of the plate. Given the consistency in this energy density difference across all μ it is likely that this energy difference is generated in the initial propagation of the rays across the structural domain. This is because for many journeys across the plate the ray density will fall rapidly for large μ but, as shown in Figure 25, within a single propagation the damping loss is minor. This also accounts for the small decline in the energy difference across the plate for high μ, which closely matches the decay in energy density for a single journey across the plate. Given the difference in energy density for each μ, this almost constant energy difference across the plate means that the relative energy difference varies dramatically for different μ. As discussed the relative energy difference across the plate is around 0.27 % for the $U_0 = 50\,ms^{-1}$ case and around 1.21 % for the $U_0 = 300\,ms^{-1}$ case, whilst for $\mu = 0.80$, these values are now $\approx$ 20% and $\approx$ 150% respectively. Despite its small size, the vibrational behaviour is thus highly variable across the plate, particularly for highly damped cases.

3.6.4 Periodic boundary conditions

Finally, the vibrational response of a plate with absorbing boundary conditions on the leading and trailing edges and periodic boundary conditions on the flow-parallel edges is considered. Under periodic boundary conditions, any rays departing the plate through one periodic boundary re-enter at the equivalent location on the paired edge, with identical $\boldsymbol{p}$ [179–181]. The application of periodic boundary conditions here ensures that the plate behaves as a small section of an infinitely wide plate. The vibrational response of the plate with periodic boundary conditions is demonstrated by Figure 30.

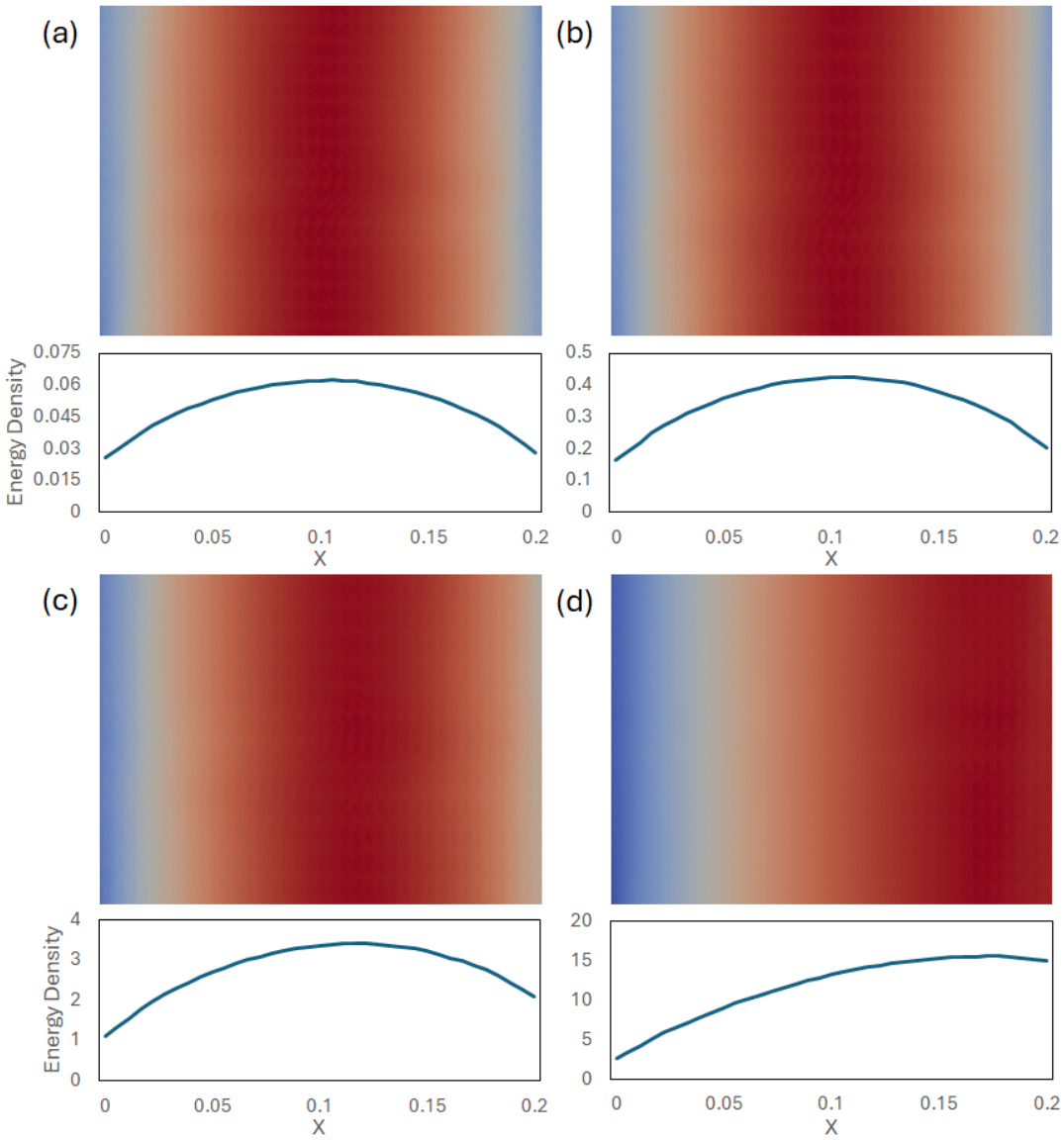

Figure 30: Vibrational response of a flat plate with periodic boundary conditions and damping coefficient $\mu = 0.01$ under TBL pressure fields formed from free-stream flows with speeds (a) $19\,ms^{-1}$ (b) $50\,ms^{-1}$ (c) $150\,ms^{-1}$ (d) $300\,ms^{-1}$.

Given the symmetry of the plate and the source field in the cross-flow direction, as shown in Figure 17, the ray density flowing through the top and bottom edges will be equal across all iterations. The result is that the periodic boundary conditions applied to these edges are equivalent to reflecting boundaries. This can be observed in the resultant vibrational energy distributions, as these share the constant energy density in the cross-flow direction associated with the reflecting

boundary condition results, as displayed in Figures 27. In addition, the action of these boundaries to return any rays leaving the system causes an increase in the energy density across the plate for all flow speeds when compared to the absorbing boundary case. This is particularly apparent for the lower flow speed cases, for example the peak energy density for $U_0 = 19$ is around 5.5 times greater than in the equivalent absorbing boundary case. As shown in Figure 17, at lower flow speeds a large proportion of the rays generated by the source propagate in the cross-stream direction. In this case, these rays remain trapped within the system by the periodic boundaries, propagating across the plate many times and contributing a significant proportion of their energy density to the plate via damping. At higher flow speeds an increasing proportion of the rays generated will propagate close to the streamwise direction and so will be dissipated by the absorbing boundary, contributing less of their energy density to the plate. There is thus a far smaller difference in the energy density as compared to the absorbing case. For example, for $U_0 = 300\,ms^{-1}$, the peak energy density here is only around 1.2 times the equivalent value for the absorbing boundary conditions.

The absorbing boundary conditions applied to the leading and trailing edges ensure that the energy density in the streamwise axis behave as in subsection 3.6.2. At low speeds the near isotropicity of the source ensures that the energy density peak is found close to the centre of the plate. For greater flow speeds the increasing directionality of the source field then leads to the downstream shift in this peak. Interestingly, the drift of the peak with increasing flows speeds is slower here than in the absorbing boundary case. This is likely due to the increased contributions made by rays that are trapped within the plate by the periodic boundaries. Rays which propagate close to the centre of the plate in the cross-stream axis are likely to be trapped within the plate for the greatest number of journeys across the plate. As such, these rays will contribute a larger proportion of their energy density to the plate as compared to rays which propagate closer

to the flow direction or are positioned further from the centre of the plate. The result is that the peak will be more closely aligned with the centre of the plate than in the absorbing boundary case, as is observed.

One may also consider the influence of the damping coefficient on the results observed. The distribution of vibrational energy across the plate in the streamwise direction for different damping coefficients μ is demonstrated by Figure 31.

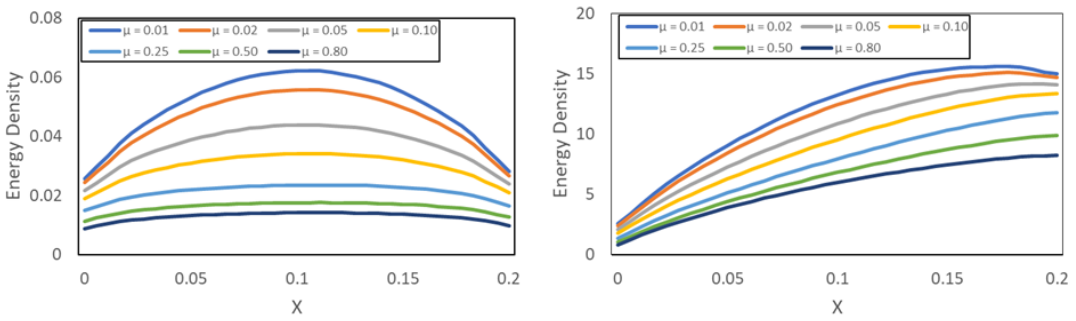

Figure 31: Energy density distribution along the line $z = 0$ for flow speeds $U_0 = 50\,ms^{-1}$ (left) and $U_0 = 300\,ms^{-1}$ (right) with periodic boundary conditions.

As shown in Figure 31, the damping coefficient has a large impact on the observed energy density results. In both cases, increasing μ leads to a large decrease in the peak energy density values. For $U_0 = 300\,ms^{-1}$ the peak energy density for $\mu = 0.01$ is around 1.9 times larger than the result for $\mu = 0.80$ whilst for $U_0 = 50\,ms^{-1}$ the $\mu = 0.01$ result is 4.3 times larger. This impact is due to the influence of the rays which are trapped within the plate by the periodic boundaries. Due to their extended lifetimes, these rays contribute a significant amount of energy density across the plate, and are also heavily impacted by changes to the damping coefficient μ. The high proportion of these rays generated for lower flow speeds is then the reason why this effect is more severe in the $U_0 = 50\,ms^{-1}$ case. The increased loss of these rays is also clearly visible in the shapes of the distributions in each case. In the $U_0 = 50\,ms^{-1}$ case, the strong peak in the centre caused by the trapped rays becomes flatter with increasing

μ, as the influence of these rays is reduced. In the $U_0 = 300\,ms^{-1}$ case the increased loss of these rays also reduces the energy density found at the centre of the plate in particular, leading to the energy density peak shifting downstream for increasing μ. The energy density distributions for all flow speeds with $\mu = 0.80$ are demonstrated in Figure 32.

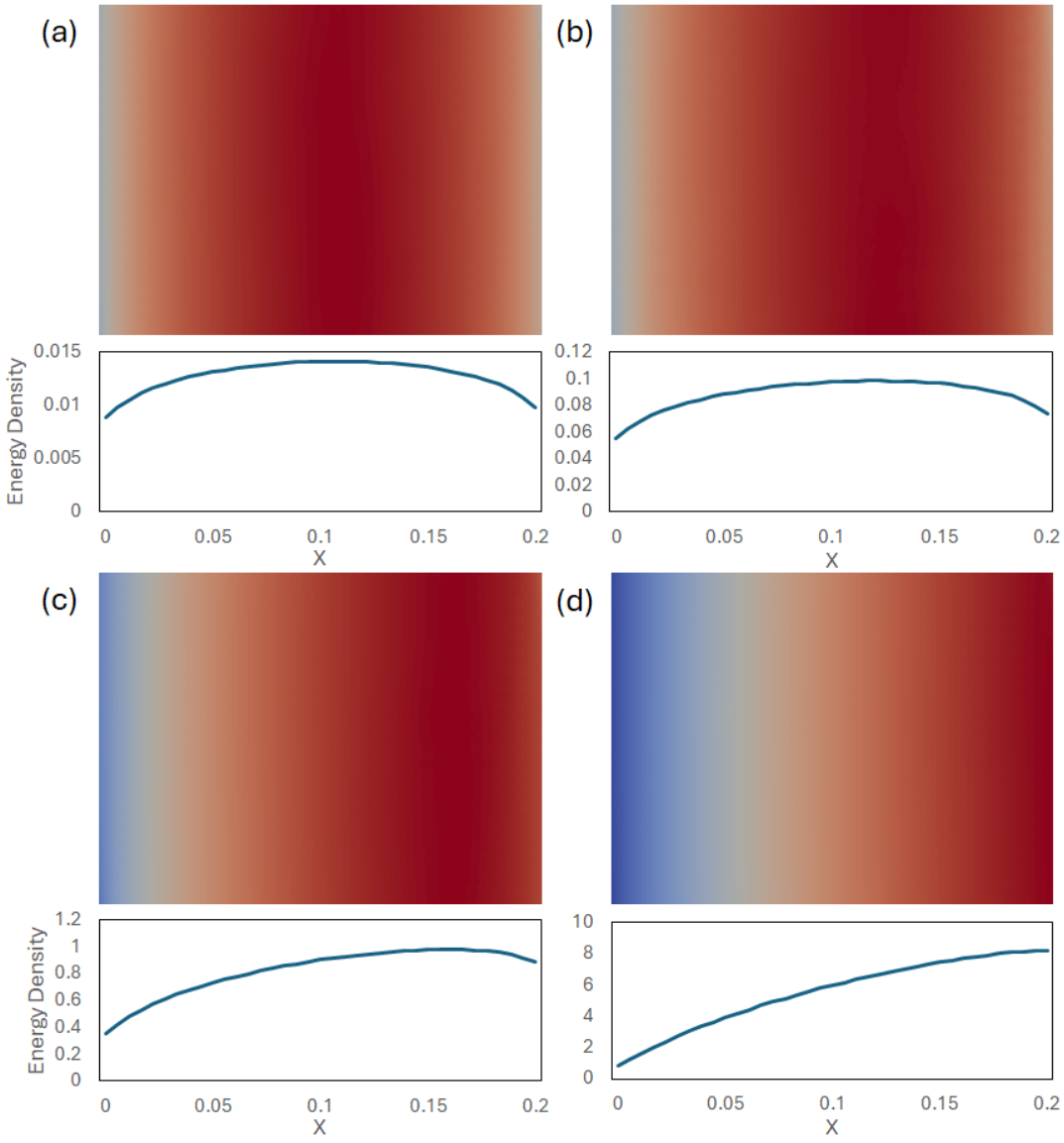

Figure 32: Vibrational response of a flat plate with periodic boundary conditions and damping coefficient $\mu = 0.80$ under TBL pressure fields formed from free-stream flows with speeds (a) $19\,ms^{-1}$ (b) $50\,ms^{-1}$ (c) $150\,ms^{-1}$ (d) $300\,ms^{-1}$.

As expected, the low-speed cases here show a clear broadening of the energy

density peak as compared to the $\mu = 0.01$ results. As an equivalent result is not observed when applying absorbing boundary conditions, it is clear that this is down to the increased damping of rays trapped by the periodic boundary conditions, as discussed previously. The higher speed cases are also changed dramatically by the increase in damping, with the peak in the energy density shifted further downstream as compared to the $\mu = 0.01$ case. As discussed, this result is also a consequence of the periodic boundary condition applied to the flow-parallel edges.

3.6.5 Discussion

In the previous subsections, the vibrational behaviour of flat plates with a variety of structural and boundary properties have been considered under TBL pressure fields with various flow speeds. Under absorbing boundary conditions, the vibrational response peaked at the centre of the plate for low flow speeds, gradually shifting downstream at greater flow speeds. For reflecting boundary conditions, the vibrational energy density increased linearly towards the trailing edge of the plate. In lightly damped cases, the variation in energy across the plate was limited, whilst for highly damped plates, particularly at high flow speeds, the observed energy variation was dramatic. Periodic boundary conditions then produced an effective interpolation of the prior results, with constant vibrational energy in the cross-flow direction and a centralised peak in the flow direction which drifted downstream with increasing flow speed. In this case, the damping had a large and varied impact on the energy density distribution, with increased damping producing a more even vibrational response at low speeds and greater variation in the vibrational response for higher flow speeds.

Thus, despite its small and simple shape, the vibrational behaviour of the plate has been shown to be highly complex and variable under different flow or structural conditions. The vibrational behaviour of real-world structures, such as air-

craft fuselage, are thus likely to be even more complex, due to the extreme scale and complexity of these systems as compared to the simple plate. Single-point or averaged vibrational responses are thus likely to be inefective when describing these systems. Thus, when considering the vibrational behaviour of these systems under correlated pressure fields, it is essential that a full spatial representation is generated, using approaches such as the one demonstrated here.

The results presented here however represent the excitation of a very simple structure by an idealised representation of the TBL pressure field, which is unlikely to be found in practical settings. When considering the vibrational behaviour of more complex structures in real-world situations, adjustments must be made to the applied methodology.

The first detail to consider is the assumed fully-formed and spatially homogeneous pressure field across the plate surface. As discussed in subsection 3.6.1, this is achieved experimentally through the presence of structures upstream of the plate which act to accelerate the formation of the TBL to ensure that it is fully formed and homogeneous across the plate surface. In real-world applications no such structures exist, and the TBL will only begin to form at the point of first contact with the structure. Close to the leading edge of the structure the TBL will thus not be fully formed and hence in-homogeneous. This is important, as when considering the pressure field applied by the TBL, the assumed homogeneity enabled the simplification of some key parameters in the applied pressure field. For example, the approximation of the convective velocity U_c as $U_c \approx 0.7\,U_0$. In reality, this is a complex variable which is dependent on local details of the TBL structure, which is defined by Bull [27, 182] as

$$U_c \approx U_0 \left(0.59 + 0.3e^{-\frac{0.89\omega\delta^*}{U_0}}\right). \tag{3.34}$$

Here δ^* is the boundary layer displacement thickness, which is dependent on the local thickness of the TBL [111]. Another term which is dependent on the local

properties of the TBL is the single point wall-pressure spectrum $\phi(\omega)$. Numerous models have been developed to represent this function, a comprehensive review of which has been performed by Miller [127]. In this study, the Goody model was highlighted [183] due to its numerical simplicity and excellent accuracy. The Goody approximation for the single point wall-pressure spectrum is given by

$$\phi(\omega) = \frac{3\left(\delta/U_0\right)^3\left(\omega\tau_w\right)^2}{\left[\left(\omega\delta/U_0\right)^{0.75}+0.5\right]^{3.7}+\left[\left(1.1R_T^{-0.57}\right)\left(\omega\delta/U_0\right)\right]^7}, \tag{3.35}$$

where $R_T = U_\tau^2\delta/U_0\nu$, with $U_\tau = \sqrt{\tau_w/\varrho_f}$ the friction velocity [111, 124]. In addition τ_w is the wall-shear stress, which is itself given by

$$\tau_w \approx \frac{0.0225\varrho U_0^2}{\left(8U_0\delta^*\nu^{-1}\right)^{1/4}} \tag{3.36}$$

where ν is the kinematic viscosity of the air. When considering the excitation of structures by non-homogeneous TBL pressure fields, these terms ensure that the source pressure field is defined based upon the local boundary layer thickness. It is possible to define the wall-shear stress value experimentally, either using hot wire measurements [80, 135], or by measuring the mean velocity profile within the TBL normal to the plate $U(y)$, and applying von Karmen's estimate of the boundary layer thickness [176, 177, 184]

$$\delta^* = \int_0^\infty \left(1-\frac{U(y)}{U_0}\right)\,dy. \tag{3.37}$$

Where experimental readings are unavailable, the boundary layer thickness may also be approximated using the work of Blasius [111, 185]. Here,

$$\delta^* \approx \frac{1.72x}{\sqrt{Re}} \tag{3.38}$$

where x is the separation from the leading edge. As discussed in subsection 3.2, modelling the response of structures to spatially variant pressure fields is highly

challenging. However, the choice to apply the split-cell approach to represent the applied pressure field, where the excitation is applied to each mesh element independently, may help to simplify this process somewhat. Given that DEA is typically performed on finite element meshes with $\approx 10^6$ elements [52, 53, 56], the size of each element is likely to be negligible compared to the overall structure. For even complex structures, it is thus likely that the variance in the TBL parameters is also negligible across individual mesh elements. In this case, it should be appropriate to represent the spatially variable pressure field as the sum of pressure fields applied within individual elements which are locally homogeneous. An accurate representation of the pressure field within each element may then be defined from averages of these parameters taken across each element. This approach has been employed by Guillon *et al*, to represent an in-homogeneous TBL pressure field in [120]. Here, the vibrational response of a flat plate under the subsystem averaged pressure field was found to provide close agreement to that under a fully variable pressure field. By implementing an approach to define appropriate parameter values across the structure, it will thus be possible to extend the presented approach to consider the in-homogeneous pressure fields found in real-world situations.

Alongside spatial variations in the TBL, geometric complexities in the structure being studied must also be considered. As discussed in Section 2.3, the TBL pressure correlation function models discussed in this thesis were developed to model the pressure field applied to a flat plate by a grazing TBL flow [123, 133]. This is thus an inappropriate representation of the highly complex and three-dimensional nature of aircraft structures. Further work is thus required to ensure that the representation of the TBL pressure field applied within DEA is appropriate for all structures.

Alongside considerations of spatial deviations in the pressure field applied by the TBL, one must also account for additional sources of vibrational excitation

which may be important during flight. One example of this is additional acoustic contributions to the pressure field from the air, which were suggested following an experimental study by Arguillat *et al* [186], aimed at determining the correlation in the pressure field applied by a TBL to a flat plate. As the Corcos and Mellen models show approximately exponential decay in the correlation with increasing point separation, one would expect a logarithmic plot of the observed correlation to decay linearly. The actual logarithmic plot of the decay observed in [186] is displayed in Figure 33.

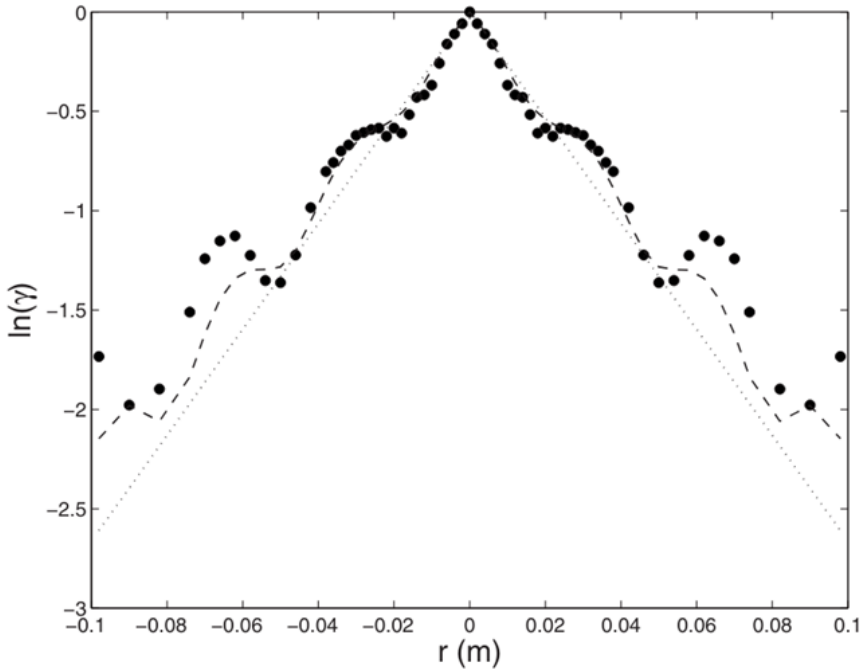

Figure 33: Correlation in the pressure field applied by the TBL for points with cross-flow separations r measured by Arguillat *et al* [186].

Here, the expected linear decay in the correlation is observed, but with additional oscillations around the expected result. When converted into a spectral representation of the field, these oscillations appear as a distinct contribution to the pressure field, associated with acoustic contributions generated at the exterior of the turbulent flow [187]. The cross-spectral density function representing this acoustic contribution is defined by [186, 188]

$$\Psi_{acc}(\xi_x, \xi_z, \omega) = S_{acc}(\omega)\frac{\sin\left(k_0\left|\boldsymbol{\xi}\right|\right)}{k_0\left|\boldsymbol{\xi}\right|}. \tag{3.39}$$

Here $k_0 = \omega/c$ is the acoustic wavenumber of the plate, with c the speed of sound and $S_{acc}(\omega)$ is the single point wall-pressure spectrum of the acoustic field. In a DEA context, the acoustic contribution to the applied pressure field is found by taking the Wigner transform of this function, giving

$$W_{\Gamma,acc} = \frac{S_{acc}(\omega)}{2\pi k_0^2}\frac{1}{\sqrt{1-\left(\frac{k}{k_0}\right)^2}} \tag{3.40}$$

for $k < k_0$. Based on the experimental data produced, Arguillat *et al* proposed an alternate TBL CSD function, which in a DEA context translates to

$$W_{\Gamma} = \frac{1}{1+A}(W_{\Gamma,TBL} + AW_{\Gamma,acc}) \tag{3.41}$$

where A describes the size of the acoustic contribution to the applied pressure field. In an automotive context, this is estimated to be around 0.05 in most cases. However, in high-frequency and resonant cases the acoustic contribution can rise to $A \approx 0.45$, representing a significant contribution to the overall pressure field [186]. As demonstrated by equation (3.40) however, the acoustic contribution to the overall pressure field is both homogeneous and isotropic. As a result, this term will only impact the magnitude of the pressure field applied at each point on the plate, without affecting the overall distribution of energy. This factor would thus not impact the results of the current study, though would be important when discussing the noise generated through the vibrations of the excited structure. This is important as the eventual aim of this work is to define the cabin noise experienced due to the excitation of aircraft by the TBL pressure field during flight. As such, it is also essential that further work is performed to ensure that the results of these DEA calculations can be coupled with sound

radiation techniques, such as those introduced in [93], to produce a detailed three-dimensional description of the sound field generated through these interactions. Finally, as discussed, no previous experimental or numerical study has generated a detailed distributed representation of the vibrational response of structures to TBL pressure fields. It is thus essential that an experimental recreation of the test case considered here is performed, in order to validate the assumptions applied and results generated in this study.

3.7 Conclusion

In this chapter, the approach for modelling the response of complex structures to correlated pressure fields using DEA has been introduced. To achieve this, the excitation of a small region of a structure by a homogeneous, continuous, pressure field has been considered. By solving the resultant equations, it has been found that the resultant vibrational response of the structure is dependent on the material properties of the plate, the geometry of the excited region, and a WDF representation of the applied source. For a TBL pressure field, the source WDF is the Wigner transform of an appropriate correlation function, the result of which is a homogeneous and directionally dependent pressure field. Using this approach, the vibrational response of a simple structure to a TBL excitation applied to a small patch was then modelled. Having extended the introduced approach to apply full structural excitations, the response of a flat plate with varying boundary conditions under a TBL excitation was then studied. When applying absorbing boundary conditions, the vibrational energy was found to peak at the centre of the plate at low flow speeds, before shifting gradually downstream as U_0 increased. For reflective boundaries, a linear increase in vibrational energy downstream was observed for all flow and damping conditions, changes to which only impacted energy difference across the plate. Periodic boundary conditions showed a combination of these results, with constant values in the

crossflow direction and a centrally located peak in the vibrational energy which steadily shifted downstream with increasing flow speed.

Opportunities for the future development of this approach have also been considered in this chapter. This included the consideration of spatially variant pressure fields, which could be represented by the sum of locally homogeneous patch excitations. The inclusion of acoustic contributions to the applied pressure field have also been discussed, although the homogeneous and isotropic nature of these fields would only impact the magnitude of the observed response. Finally, the need to determine the noise generated by these vibrations and to validate the implemented method was discussed.

Chapter 4

4 Implementation of correlated point-forces in DEA

Having developed an approach to model the vibrational behaviour of DEP aircraft under TBL pressure fields, in this chapter an additional vibration source originating from interactions between the propellers of the aircraft and the passing air is considered. As discussed in subsection 2.4, the equal rotational speed of these propellers should ensure that the vibrational waves generated through these interactions will have identical frequencies, and will thus interfere with one another. The resultant interference effects between vibrational waves generated by an array of closely arranged propellers will thus likely generate complex vibrational effects within the structure. In this chapter an approach is introduced to model the excitation of structures by multiple correlated sources, including all interference effects, using DEA. In this approach, the propellers are modelled by point-force excitations, and the vibrational response of structures under various numbers and configurations of point-forces is demonstrated.

The chapter is presented as follows. In Section 4.1, the approach for considering the response of structures to correlated point-forces, including interference effects, is introduced for the simple case of 2 point-force excitations. Here, results are presented for various point-separations and phase differences. This method is generalised in Section 4.2 to consider n phase-shifted sources and the complex interference effects of these configurations are studied. In addition, the opportu-

nity to generate preferable vibrational energy flow through careful phase selection is discussed. In Section 4.3, the implementation of this approach within DEA is demonstrated, including the definition of the initial excited boundary. These results demonstrate non-physical negative phase-space density values, and in Section 4.4 the Husimi Density Function (HDF) is introduced as a possible solution. In Section 4.5, the limitations of the current implementation are discussed, and opportunities for further development are explored.

4.1 Excitation of a plate by two phase-correlated point forces.

As discussed in subsection 2.2, the excitation of a plate by a point-force of driving frequency ω generates propagating vibrational waves within the structure. If a second point-force of equal frequency is then added to the system, the waves generated by each force will thus interfere. As discussed in Section 2.4, this interference produces a resultant interference wavefield, which is the sum of the vibrational wavefields generated individually by each source. In DEA, the vibrational response of structures to external sources is described by the response correlation function, which is calculated using equation (2.21). In this equation, the correlation function is defined based upon the response of the structure to individual point-force excitations, and a correlation function describing the source field applied to the system. In this case, the excitation of a plate by two-point force excitations of unit magnitude applied at locations $\boldsymbol{r}_{01}, \boldsymbol{r}_{02} \in \Omega$ is considered. The correlation function describing this excitation is defined here as

$$\begin{aligned}\Gamma_f(\boldsymbol{r}_1, \boldsymbol{r}_2) = &\left(\delta(\boldsymbol{r}_1 - \boldsymbol{r}_{01})\, e^{i\phi_1} + \delta(\boldsymbol{r}_1 - \boldsymbol{r}_{02})\, e^{i\phi_2}\right) \\ &\left(\delta(\boldsymbol{r}_2 - \boldsymbol{r}_{01})\, e^{-i\phi_1} + \delta(\boldsymbol{r}_2 - \boldsymbol{r}_{02})\, e^{-i\phi_2}\right),\end{aligned} \tag{4.1}$$

where ϕ_1 and ϕ_2 represent the phase of each point-force. By substituting this force correlation function into equation (2.21), the correlation function of the response of a plate to two point-force excitations is given by

$$\begin{aligned}
&\Gamma_0\left(\boldsymbol{r}_1, \boldsymbol{r}_2, \omega\right) = \\
&\int\int G(\boldsymbol{r}_1, \boldsymbol{r}'_{01})\delta\left(\boldsymbol{r}'_{01} - \boldsymbol{r}_{01}\right)\delta\left(\boldsymbol{r}'_{02} - \boldsymbol{r}_{01}\right) G^*\left(\boldsymbol{r}_2, \boldsymbol{r}'_{02}\right)\, d\boldsymbol{r}'_{01}\, d\boldsymbol{r}'_{02} \\
&+ \int\int G(\boldsymbol{r}_1, \boldsymbol{r}'_{01})\delta\left(\boldsymbol{r}'_{01} - \boldsymbol{r}_{02}\right)\delta\left(\boldsymbol{r}'_{02} - \boldsymbol{r}_{02}\right) G^*\left(\boldsymbol{r}_2, \boldsymbol{r}'_{02}\right)\, d\boldsymbol{r}'_{01}\, d\boldsymbol{r}'_{02} \\
&+ e^{i(\phi_1-\phi_2)} \int\int G(\boldsymbol{r}_1, \boldsymbol{r}'_{01})\delta\left(\boldsymbol{r}'_{01} - \boldsymbol{r}_{01}\right)\delta\left(\boldsymbol{r}'_{02} - \boldsymbol{r}_{02}\right) G^*\left(\boldsymbol{r}_2, \boldsymbol{r}'_{02}\right)\, d\boldsymbol{r}'_{01}\, d\boldsymbol{r}'_{02} \\
&+ e^{i(\phi_2-\phi_1)} \int\int G(\boldsymbol{r}_1, \boldsymbol{r}'_{01})\delta\left(\boldsymbol{r}'_{01} - \boldsymbol{r}_{02}\right)\delta\left(\boldsymbol{r}'_{02} - \boldsymbol{r}_{01}\right) G^*\left(\boldsymbol{r}_2, \boldsymbol{r}'_{02}\right)\, d\boldsymbol{r}'_{01}\, d\boldsymbol{r}'_{02}.
\end{aligned} \tag{4.2}$$

Solving the integrals over $\boldsymbol{r}'_{01}$ and $\boldsymbol{r}'_{02}$ then leaves

$$\begin{aligned}
\Gamma_0(\boldsymbol{r}_1, \boldsymbol{r}_2) = &\, G(\boldsymbol{r}_1, \boldsymbol{r}_{01})G^*(\boldsymbol{r}_2, \boldsymbol{r}_{01}) \\
&+ G(\boldsymbol{r}_1, \boldsymbol{r}_{02})G^*(\boldsymbol{r}_2, \boldsymbol{r}_{02}) \\
&+ e^{i(\phi_1-\phi_2)}G(\boldsymbol{r}_1, \boldsymbol{r}_{01})G^*(\boldsymbol{r}_2, \boldsymbol{r}_{02}) \\
&+ e^{i(\phi_2-\phi_1)}G(\boldsymbol{r}_1, \boldsymbol{r}_{02})G^*(\boldsymbol{r}_2, \boldsymbol{r}_{01}),
\end{aligned} \tag{4.3}$$

where, based upon the working of Section 2.2, each of these Green functions is given by

$$G(\boldsymbol{r}, \boldsymbol{r}_{0i}, \omega) \approx \frac{\varrho h}{8Dk^2}\sqrt{\frac{2}{\pi k\left|\boldsymbol{r} - \boldsymbol{r}_{0i}\right|}}e^{i\left(k|\boldsymbol{r}-\boldsymbol{r}_{0i}|-\frac{\pi}{4}\right)}. \tag{4.4}$$

By substituting the form of each Green function into equation (4.3), the overall vibrational response correlation function is given by

$$\begin{aligned}\Gamma_0(\boldsymbol{r}_1,\boldsymbol{r}_2,\omega) = \frac{\varrho^2 h^2}{32\pi D^2 k^5}\Bigg[&\frac{1}{\sqrt{|\boldsymbol{r}_1-\boldsymbol{r}_{01}|\,|\boldsymbol{r}_2-\boldsymbol{r}_{01}|}}e^{ik(|\boldsymbol{r}_1-\boldsymbol{r}_{01}|-|\boldsymbol{r}_2-\boldsymbol{r}_{01}|)}\\ &+\frac{1}{\sqrt{|\boldsymbol{r}_1-\boldsymbol{r}_{02}|\,|\boldsymbol{r}_2-\boldsymbol{r}_{02}|}}e^{ik(|\boldsymbol{r}_1-\boldsymbol{r}_{02}|-|\boldsymbol{r}_2-\boldsymbol{r}_{02}|)}\\ &+\frac{e^{i(\phi_1-\phi_2)}}{\sqrt{|\boldsymbol{r}_1-\boldsymbol{r}_{01}|\,|\boldsymbol{r}_2-\boldsymbol{r}_{02}|}}e^{ik(|\boldsymbol{r}_1-\boldsymbol{r}_{01}|-|\boldsymbol{r}_2-\boldsymbol{r}_{02}|)}\\ &+\frac{e^{i(\phi_2-\phi_1)}}{\sqrt{|\boldsymbol{r}_1-\boldsymbol{r}_{02}|\,|\boldsymbol{r}_2-\boldsymbol{r}_{01}|}}e^{ik(|\boldsymbol{r}_1-\boldsymbol{r}_{02}|-|\boldsymbol{r}_2-\boldsymbol{r}_{01}|)}\Bigg].\end{aligned} \tag{4.5}$$

The WDF of the vibrational response of the plate is then found by substituting this correlation function into equation (2.23), with $\boldsymbol{r}_1 = \boldsymbol{r} + \frac{\boldsymbol{\xi}}{2}$ and $\boldsymbol{r}_2 = \boldsymbol{r} - \frac{\boldsymbol{\xi}}{2}$, as follows

$$\begin{aligned}W_0(\boldsymbol{r},\boldsymbol{p}) = \frac{\varrho^2 h^2}{32\pi D^2 k^5}\Bigg[&\int \frac{e^{i\left(k\left(\left|\boldsymbol{r}+\frac{\boldsymbol{\xi}}{2}-\boldsymbol{r}_{01}\right|-\left|\boldsymbol{r}-\frac{\boldsymbol{\xi}}{2}-\boldsymbol{r}_{01}\right|\right)-\boldsymbol{p}\right)\cdot\boldsymbol{\xi}}}{\sqrt{\left|\boldsymbol{r}+\frac{\boldsymbol{\xi}}{2}-\boldsymbol{r}_{01}\right|\left|\boldsymbol{r}-\frac{\boldsymbol{\xi}}{2}-\boldsymbol{r}_{01}\right|}}\,d\boldsymbol{\xi}\\ &+\int \frac{e^{i\left(k\left(\left|\boldsymbol{r}+\frac{\boldsymbol{\xi}}{2}-\boldsymbol{r}_{02}\right|-\left|\boldsymbol{r}-\frac{\boldsymbol{\xi}}{2}-\boldsymbol{r}_{02}\right|\right)-\boldsymbol{p}\right)\cdot\boldsymbol{\xi}}}{\sqrt{\left|\boldsymbol{r}+\frac{\boldsymbol{\xi}}{2}-\boldsymbol{r}_{02}\right|\left|\boldsymbol{r}-\frac{\boldsymbol{\xi}}{2}-\boldsymbol{r}_{02}\right|}}\,d\boldsymbol{\xi}\\ &+e^{i(\phi_1-\phi_2)}\int \frac{e^{i\left(k\left(\left|\boldsymbol{r}+\frac{\boldsymbol{\xi}}{2}-\boldsymbol{r}_{01}\right|-\left|\boldsymbol{r}-\frac{\boldsymbol{\xi}}{2}-\boldsymbol{r}_{02}\right|\right)-\boldsymbol{p}\right)\cdot\boldsymbol{\xi}}}{\sqrt{\left|\boldsymbol{r}+\frac{\boldsymbol{\xi}}{2}-\boldsymbol{r}_{01}\right|\left|\boldsymbol{r}-\frac{\boldsymbol{\xi}}{2}-\boldsymbol{r}_{02}\right|}}\,d\boldsymbol{\xi}\\ &+e^{i(\phi_2-\phi_1)}\int \frac{e^{i\left(k\left(\left|\boldsymbol{r}+\frac{\boldsymbol{\xi}}{2}-\boldsymbol{r}_{02}\right|-\left|\boldsymbol{r}-\frac{\boldsymbol{\xi}}{2}-\boldsymbol{r}_{01}\right|\right)-\boldsymbol{p}\right)\cdot\boldsymbol{\xi}}}{\sqrt{\left|\boldsymbol{r}+\frac{\boldsymbol{\xi}}{2}-\boldsymbol{r}_{02}\right|\left|\boldsymbol{r}-\frac{\boldsymbol{\xi}}{2}-\boldsymbol{r}_{01}\right|}}\,d\boldsymbol{\xi}\Bigg].\end{aligned} \tag{4.6}$$

The first two integrals are equivalent to the intergral part of equation (2.27). These integrals may thus be simplified in the same manner as applied in Section 2.2, by approximating parts of the integrand using the leading terms of their corresponding Taylor expansions via equation (2.28). Whilst Taylor expansions may also be applied to these parts of the final two integrals, these integrals are dependent on contributions from both source locations simultaneously. To solve

this issue, we assume that the distance between the observer location $\boldsymbol{r}$ and the two source locations $\boldsymbol{r_{01}}$ and $\boldsymbol{r_{02}}$ is far larger than the separation of the sources, such that $|\boldsymbol{r}-\boldsymbol{r}_{01}| \approx |\boldsymbol{r}-\boldsymbol{r}_{02}|$. This approximation limits the accuracy of the result in the proximity of the source locations. However, in this study it is the flow of vibrational energy to locations far away from the sources which is of interest, where this approximation is far more suitable. Based upon equation (2.28) and this approximation, the terms in the final two integrals of equation (4.6) may be approximated by

$$\begin{aligned} \left|\boldsymbol{r}+\frac{\boldsymbol{\xi}}{2}-\boldsymbol{r}_{0i}\right|\left|\boldsymbol{r}-\frac{\boldsymbol{\xi}}{2}-\boldsymbol{r}_{0j}\right| &\approx |\boldsymbol{r}-\boldsymbol{r}_{0i}|\,|\boldsymbol{r}-\boldsymbol{r}_{0j}| \\ \left|\boldsymbol{r}+\frac{\boldsymbol{\xi}}{2}-\boldsymbol{r}_{0i}\right|-\left|\boldsymbol{r}-\frac{\boldsymbol{\xi}}{2}-\boldsymbol{r}_{0j}\right| &\approx \frac{1}{2}\left(\frac{\boldsymbol{r}-\boldsymbol{r}_{0i}}{|\boldsymbol{r}-\boldsymbol{r}_{0i}|}+\frac{\boldsymbol{r}-\boldsymbol{r}_{0j}}{|\boldsymbol{r}-\boldsymbol{r}_{0j}|}\right)\cdot\boldsymbol{\xi} \end{aligned} \tag{4.7}$$

Applying the substitutions of equations (2.28) and (4.7) then leaves

$$\begin{aligned} W_0(\boldsymbol{r},\boldsymbol{p}) = \frac{F_0^2}{32\pi D^2 k^5}\Bigg[& \int \frac{e^{-i\left(\boldsymbol{p}-k\frac{\boldsymbol{r}-\boldsymbol{r}_{01}}{|\boldsymbol{r}-\boldsymbol{r}_{01}|}\right)}}{|\boldsymbol{r}-\boldsymbol{r}_{01}|}\,d\boldsymbol{\xi} \\ & + \int \frac{e^{-i\left(\boldsymbol{p}-k\frac{\boldsymbol{r}-\boldsymbol{r}_{02}}{|\boldsymbol{r}-\boldsymbol{r}_{02}|}\right)}}{|\boldsymbol{r}-\boldsymbol{r}_{02}|}\,d\boldsymbol{\xi} \\ & + e^{ik(|\boldsymbol{r}-\boldsymbol{r}_{01}|-|\boldsymbol{r}-\boldsymbol{r}_{02}|)+\phi_1-\phi_2}\int \frac{e^{-i\left(\boldsymbol{p}-\frac{k}{2}\left(\frac{\boldsymbol{r}-\boldsymbol{r}_{01}}{|\boldsymbol{r}-\boldsymbol{r}_{01}|}+\frac{\boldsymbol{r}-\boldsymbol{r}_{02}}{|\boldsymbol{r}-\boldsymbol{r}_{02}|}\right)\right)}}{\sqrt{|\boldsymbol{r}-\boldsymbol{r}_{01}|\,|\boldsymbol{r}-\boldsymbol{r}_{02}|}}\,d\boldsymbol{\xi} \\ & + e^{ik(|\boldsymbol{r}-\boldsymbol{r}_{02}|-|\boldsymbol{r}-\boldsymbol{r}_{01}|)+\phi_2-\phi_1}\int \frac{e^{-i\left(\boldsymbol{p}-\frac{k}{2}\left(\frac{\boldsymbol{r}-\boldsymbol{r}_{01}}{|\boldsymbol{r}-\boldsymbol{r}_{01}|}+\frac{\boldsymbol{r}-\boldsymbol{r}_{02}}{|\boldsymbol{r}-\boldsymbol{r}_{02}|}\right)\right)}}{\sqrt{|\boldsymbol{r}-\boldsymbol{r}_{01}|\,|\boldsymbol{r}-\boldsymbol{r}_{02}|}}\,d\boldsymbol{\xi}\Bigg]. \end{aligned} \tag{4.8}$$

The solution of these integrals is then given by

$$
\begin{aligned}
W_0(\boldsymbol{r},\boldsymbol{p}) = \frac{\varrho^2 h^2}{32\pi D^2 k^5} \Bigg[& \frac{e^{-\mu|\boldsymbol{r}-\boldsymbol{r}_{01}|}\delta\left(\boldsymbol{p} - k\frac{\boldsymbol{r}-\boldsymbol{r}_{01}}{|\boldsymbol{r}-\boldsymbol{r}_{01}|}\right)}{|\boldsymbol{r}-\boldsymbol{r}_{01}|} \\
+ & \frac{e^{-\mu|\boldsymbol{r}-\boldsymbol{r}_{02}|}\delta\left(\boldsymbol{p} - k\frac{\boldsymbol{r}-\boldsymbol{r}_{02}}{|\boldsymbol{r}-\boldsymbol{r}_{02}|}\right)}{|\boldsymbol{r}-\boldsymbol{r}_{02}|} \\
+ & \frac{e^{-\mu\sqrt{|\boldsymbol{r}-\boldsymbol{r}_{01}||\boldsymbol{r}-\boldsymbol{r}_{02}|}}e^{ik(|\boldsymbol{r}-\boldsymbol{r}_{01}|-|\boldsymbol{r}-\boldsymbol{r}_{02}|)+\phi_1-\phi_2}\delta\left(\boldsymbol{p} - \frac{k}{2}\left(\frac{\boldsymbol{r}-\boldsymbol{r}_{01}}{|\boldsymbol{r}-\boldsymbol{r}_{01}|} + \frac{\boldsymbol{r}-\boldsymbol{r}_{02}}{|\boldsymbol{r}-\boldsymbol{r}_{02}|}\right)\right)}{\sqrt{|\boldsymbol{r}-\boldsymbol{r}_{01}|\,|\boldsymbol{r}-\boldsymbol{r}_{02}|}} \\
+ & \frac{e^{-\mu\sqrt{|\boldsymbol{r}-\boldsymbol{r}_{01}||\boldsymbol{r}-\boldsymbol{r}_{02}|}}e^{ik(|\boldsymbol{r}-\boldsymbol{r}_{02}|-|\boldsymbol{r}-\boldsymbol{r}_{01}|)+\phi_2-\phi_1}\delta\left(\boldsymbol{p} - \frac{k}{2}\left(\frac{\boldsymbol{r}-\boldsymbol{r}_{01}}{|\boldsymbol{r}-\boldsymbol{r}_{01}|} + \frac{\boldsymbol{r}-\boldsymbol{r}_{02}}{|\boldsymbol{r}-\boldsymbol{r}_{02}|}\right)\right)}{\sqrt{|\boldsymbol{r}-\boldsymbol{r}_{01}|\,|\boldsymbol{r}-\boldsymbol{r}_{02}|}} \Bigg].
\end{aligned}
\tag{4.9}
$$

Here, additional factors have been included to each to account for losses due to damping as the rays propagate across the domain. In this equation, the first two terms are identical to equation (2.33), which describes the resultant WDF due to an individual point-force. These terms thus account for the direct contributions to the overall vibrational response of the plate from each of the point-forces. The final two terms then account for the additional contributions caused by the interference effects between the vibrational waves generated by each source. These terms are very similar, varying only by the sign on the exponent of the complex exponential term. Using Euler's formula, these factors may thus be combined into a single term. Substituting the result into equation (2.34), then gives the direct contribution to the phase-space density distribution across a plate due to two correlated point-force excitations as

$$
\begin{aligned}
\rho_0(\boldsymbol{r},\boldsymbol{p}) = & \rho_{\boldsymbol{r}_{01}}(\boldsymbol{r},\boldsymbol{p}) + \rho_{\boldsymbol{r}_{02}}(\boldsymbol{r},\boldsymbol{p}) + \\
& \frac{e^{-\mu\sqrt{|\boldsymbol{r}-\boldsymbol{r}_{01}||\boldsymbol{r}-\boldsymbol{r}_{02}|}}}{32\pi}\frac{\varrho^2 h^2}{Dk}\frac{\cos\left(k\left(|\boldsymbol{r}-\boldsymbol{r}_{01}| - |\boldsymbol{r}-\boldsymbol{r}_{02}|\right) + \phi_1 - \phi_2\right)}{\sqrt{|\boldsymbol{r}-\boldsymbol{r}_{01}|\,|\boldsymbol{r}-\boldsymbol{r}_{02}|}} \\
& \delta\left(\boldsymbol{p} - \frac{k}{2}\left(\frac{\boldsymbol{r}-\boldsymbol{r}_{01}}{|\boldsymbol{r}-\boldsymbol{r}_{01}|} + \frac{\boldsymbol{r}-\boldsymbol{r}_{02}}{|\boldsymbol{r}-\boldsymbol{r}_{02}|}\right)\right).
\end{aligned}
\tag{4.10}
$$

As in Section 2.2, this solution may then be converted onto the boundary coordi-

nate scheme using equation (2.37), propagated across the domain using equation (2.40), and mapped back into the cell interiors to define the overall phase-space energy density distribution $\tilde{\rho}_\infty$. This result could then be visualised by substituting this value into equation (2.41). As discussed in subsection 2.4, interference effects between vibrational waves generated by correlated sources lead to highly directional energy flows. As such, when visualising the vibrational response of structures under correlated point-force excitations, it would also useful to define the energy flow $\boldsymbol{I}(\boldsymbol{r}, \omega)$, given by

$$\boldsymbol{I}(\boldsymbol{r}, \omega) = \int \boldsymbol{p} \rho_\infty(\boldsymbol{r}, \boldsymbol{p}, \omega) \, d\boldsymbol{p}. \tag{4.11}$$

This quantity describes the mean flow of the energy density at each location of the plate.

In the remainder of subsection , several plots

To demonstrate the vibrational response of structures to correlated point-force excitations, the vibrational response of a plate excited by two in-phase point-forces separated by $d = |\boldsymbol{r}_1 - \boldsymbol{r}_2| = \frac{\pi}{k} = \lambda/2$ is considered. In this, and all remaining cases in subsections 4.1 and 4.2, these excitations are applied to homogeneous square plates with absorbing boundary conditions. The energy density and energy flow distributions across the plate with absorbing boundary conditions by these two sources are displayed in in Figure 34.

In this plot, a large vibrational response can be observed in the region directly between the two point sources. This is unsurprising, as the energy density contributed independently by each source is proportional to $e^{-\mu|\boldsymbol{r}-\boldsymbol{r}_{0i}|}/\left|\boldsymbol{r}-\boldsymbol{r}_{0i}\right|$, meaning that large energy density values will be observed at locations in close proximity to both sources. Given the dependence of the interference term on the separation from each source, the interference effects between the sources are also likely to have a large impact on the energy density observed within this region. Close to the sources, the separation from each source is minimal, meaning that

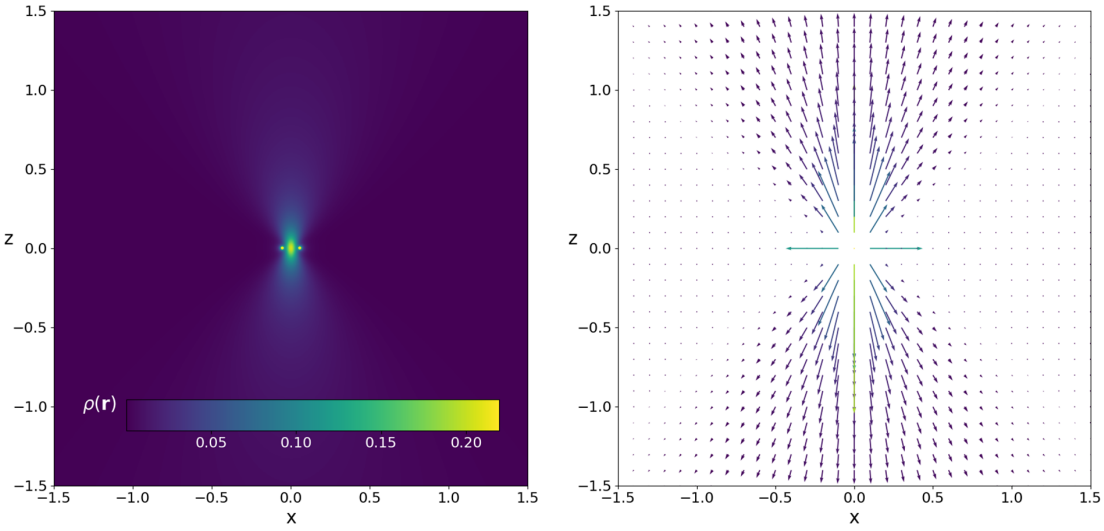

Figure 34: Energy density (left) and flow (right) across a plate with absorbing boundary conditions due to two point-forces with separation $d = 0.5\lambda$ and phases $\phi_1 - \phi_2 = 0$. The colour scale runs from low energy (dark blue) to high energy (yellow).

$|\boldsymbol{r} - \boldsymbol{r}_{01}| - |\boldsymbol{r} - \boldsymbol{r}_{02}| \approx 0$. Given that $\phi_1 = \phi_2 = 0$, the argument of the cosine term in equation (4.10) is thus be close to 0. As $\cos(0) = 1$, the vibrational waves generated by each source interfere constructively within this area, providing an additional strong positive contribution to the energy density directly between the two sources. Outside of this area, these interference effects further influence the observed vibrational behaviour, generating a highly directional energy flow away from the sources. As shown in Figure 34, the majority of the energy density flows in the $z-$axis away from the sources, with very little flow in the $z-$axis. The ability to generate such a highly directional energy flow using just two sources thus demonstrates the strong influence of these interference effects.

By adjusting ϕ_1 and ϕ_2, one can investigate the influence of the phase difference between the sources on the observed vibrational response. Setting $\phi_1 - \phi_2 = \pi$, the resultant vibrational response is displayed in Figure 35.

In this example the sources are in anti-phase, meaning that maxima in the force applied by one source occur simultaneously with minima in the force applied by the other. Focusing again on the region directly between the sources, once again

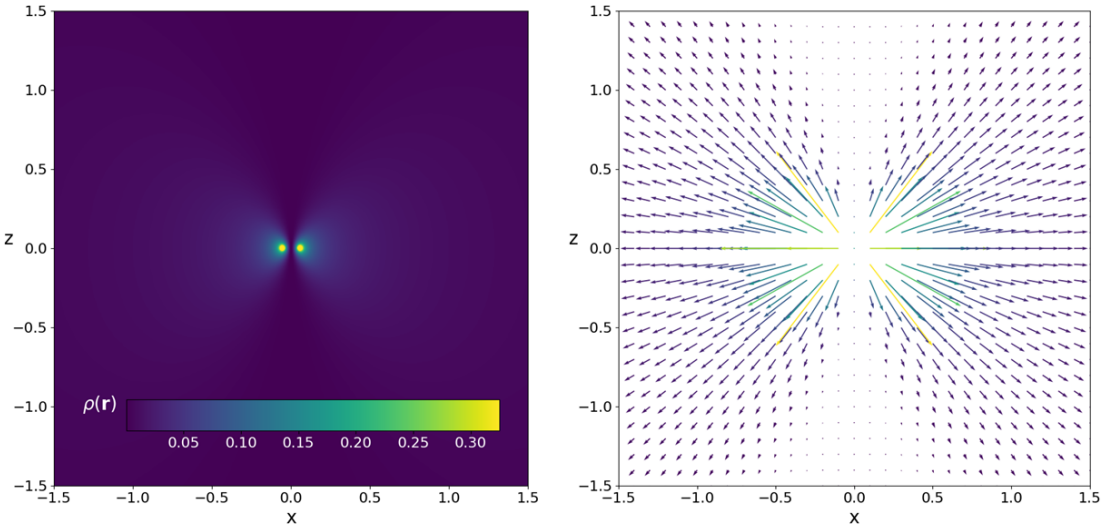

Figure 35: Energy density (left) and flow (right) across a plate with absorbing boundary conditions due to two point-forces separated by 0.5λ with phases $\phi_1 - \phi_2 = \pi$.

the separations from each source are minimal and rather similar. In this example however, the phase difference now ensures that the argument of the cosine term is given by $\phi_1 - \phi_2 = \pi$, with $\cos(\pi) = -1$. In this case, destructive interference now occurs between the vibrational waves generated by each source, providing a strong negative contribution to the energy density. This acts to cancel out the direct contributions from the sources, leading to the minima in the energy density between the sources as observed in Figure 35.

The phase difference also affects the flow of energy away from the sources, which is effectively the opposite to the in-phase result. Here, the majority of the energy now flows close to the $x-$axis, with minimal energy flowing in the $z-$axis. The stark contrast in the results observed for each phase-difference thus demonstrates the strong impact of this factor on the resultant vibrational behaviour of the plate. Similar results can be observed when considering sources which are more widely spaced, as shown in Figure 36.

In this plot, the increased separation of the sources further highlights the influence of the interference term in equation (4.10). When moving between the sources

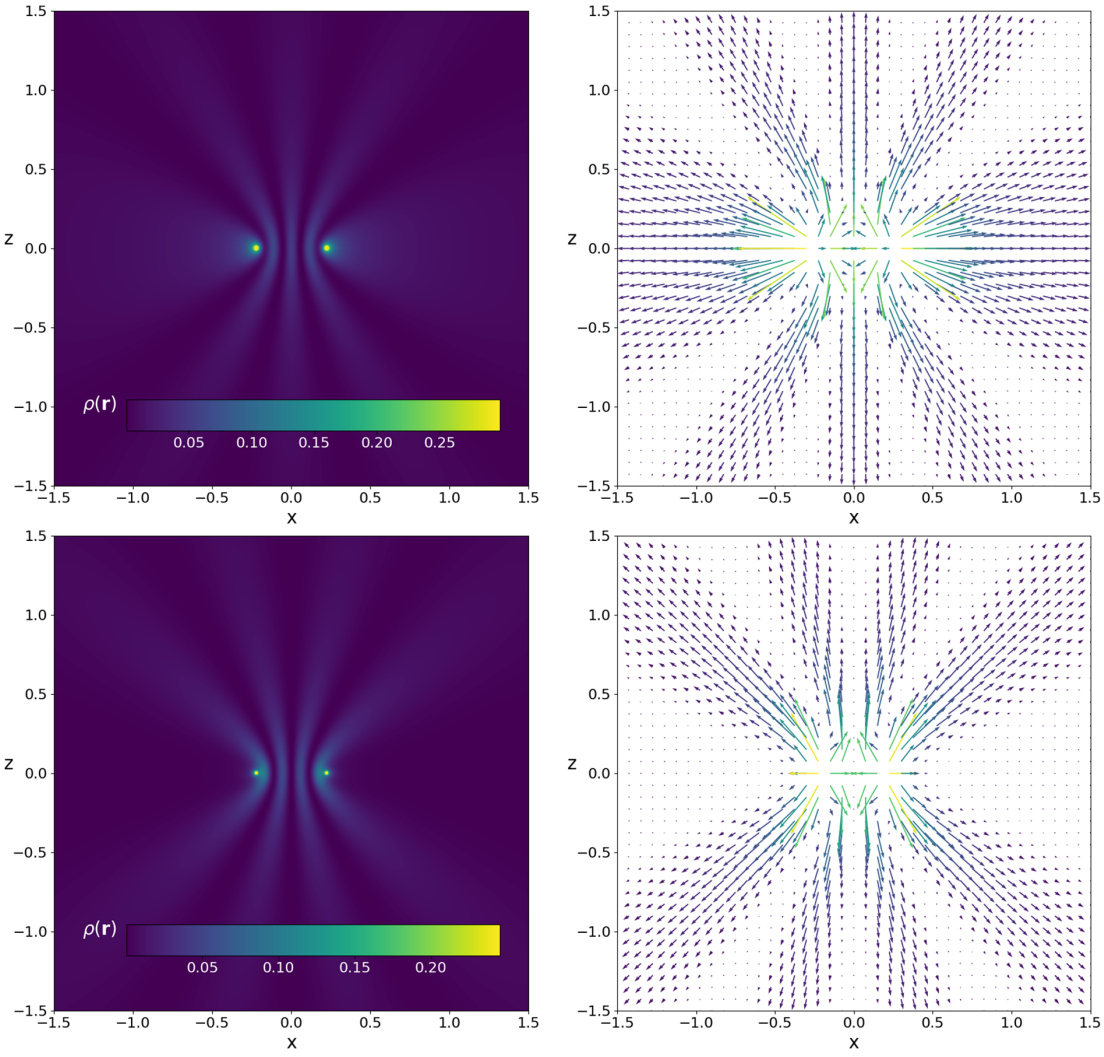

Figure 36: Energy density (left) and flow (right) across a plate with absorbing boundary conditions due to two point-forces with $d = 2\lambda$ and phase differences $\phi_1 - \phi_2 = 0$ (top) and $\phi_1 - \phi_2 = \pi$ (bottom).

$k(|\boldsymbol{r} - \boldsymbol{r}_{01}| - |\boldsymbol{r} - \boldsymbol{r}_{02}|)$ varies between $-\pi$ and $+\pi$, causing the cosine term to oscillate several times between -1 and $+1$, generating the observed sinusoidal oscillations in the energy density across this region. By comparing the energy density distributions between the sources for both phase differences, the influence of this factor on the observed vibrational behaviour is also clear. Within this region, changing the phase-difference of the sources produces a half-wavelength shift in the observed oscillation pattern, meaning that the locations of the peaks and troughs in the energy density in the anti-phase result are the direct oppo-

site of the in-phase results. Outside of this region, the interference effects once again generate strong directionality in the energy flow away from the sources. In both cases, energy density flows from the central region outwards through narrow cones, meaning that small regions experience a strong vibrational response whilst much of the plate displays minimal vibrational behaviour. As with the interior region, the energy flow results generated by each phase relationship appear to be the exact opposite of each-other.

By spacing the sources much further apart, the long range interactions between point-forces may be considered. The vibrational response of a plate to in-phase point-forces separated by $d = 100\lambda$ is demonstrated in Figure 37.

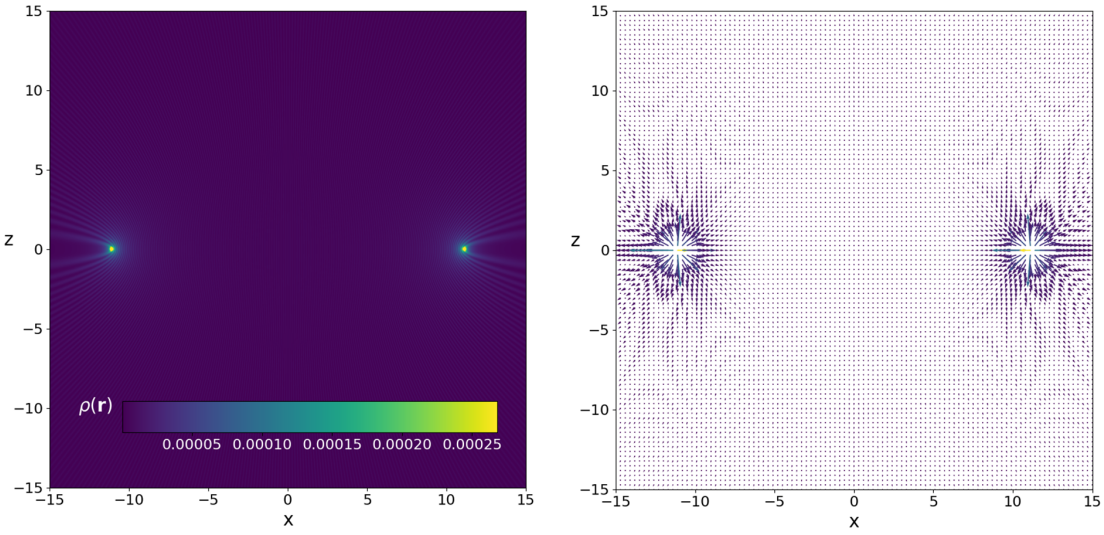

Figure 37: Energy density (left) and flow (right) across a plate with absorbing boundary conditions due to two point-forces separated by $d = 100\lambda$ with phase-difference $\phi_1 - \phi_2 = 0$.

In this plot, the interference patterns observed between the sources in prior examples cannot be seen, and the resultant vibrational energy distribution resembles the response of the plate to two non-interfering point-forces. To demonstrate this mathematically, the interference effects in the region directly between the two sources is again considered. In this region, although the cosine term still oscillates rapidly in space, the strength of the interference contribution is proportional

to $\frac{1}{\sqrt{|\boldsymbol{r}-\boldsymbol{r}_{01}||\boldsymbol{r}-\boldsymbol{r}_{02}|}}$. Given the separation of the sources, this term is extremely small across the majority of this region, thus providing minimal impact on the overall vibrational response of the plate. An exception to this is found close to either source, where one of the separation terms becomes sufficiently small that interference effects once again become important. This can be observed in Figure 37 through small oscillations in the energy density located close to each source. This also effects the energy flow within the system, causing a slight outward preference in the energy flow plot within this figure.

4.2 Excitation of a plate by N-phase shifted point-forces

Having considered the response of a plate to two point-force excitations, it is trivial to extend the approach to consider N sources applied at locations $\boldsymbol{r}_{0m}$. In this case, $\Gamma_f = \prod_{m=1}^{2}\sum_{n}^{N}\delta(\boldsymbol{r}'_m - \boldsymbol{r}_{0n})e^{i(-1)^{(m-1)}\phi_n}$. By substituting these terms into equation (2.21), the resultant phase space energy density distribution is given by

$$\begin{aligned}\rho_0(\boldsymbol{r},\boldsymbol{p}) = &\sum_{n=1}^{N}\rho_{\boldsymbol{r}_{0n}}(\boldsymbol{r},\boldsymbol{p}) + \frac{\varrho^2 h^2}{32\pi D k}\\ &\sum_{m=1}^{N}\sum_{l>m}^{N}\frac{e^{-\mu\sqrt{|\boldsymbol{r}-\boldsymbol{r}_{0m}||\boldsymbol{r}-\boldsymbol{r}_{0l}|}}\cos\left(k\left(|\boldsymbol{r}-\boldsymbol{r}_{0m}|-|\boldsymbol{r}-\boldsymbol{r}_{0l}|\right)+\phi_m-\phi_l\right)}{\sqrt{|\boldsymbol{r}-\boldsymbol{r}_{0m}|\,|\boldsymbol{r}-\boldsymbol{r}_{0l}|}}\\ &\delta\left(\boldsymbol{p}-\frac{k}{2}\left(\frac{\boldsymbol{r}-\boldsymbol{r}_{0m}}{|\boldsymbol{r}-\boldsymbol{r}_{0m}|}+\frac{\boldsymbol{r}-\boldsymbol{r}_{0l}}{|\boldsymbol{r}-\boldsymbol{r}_{0l}|}\right)\right).\end{aligned} \tag{4.12}$$

To demonstrate this result, the excitation of a plate by 9 in-phase point-forces is considered. The resulting energy density distribution is shown in Figure 38.
This result is similar to the energy density distribution observed in Figure 36 for two in-phase sources. This is especially true near the $x-$axis, where a strong energy flow is observed outwards from the line along which the sources are posi-

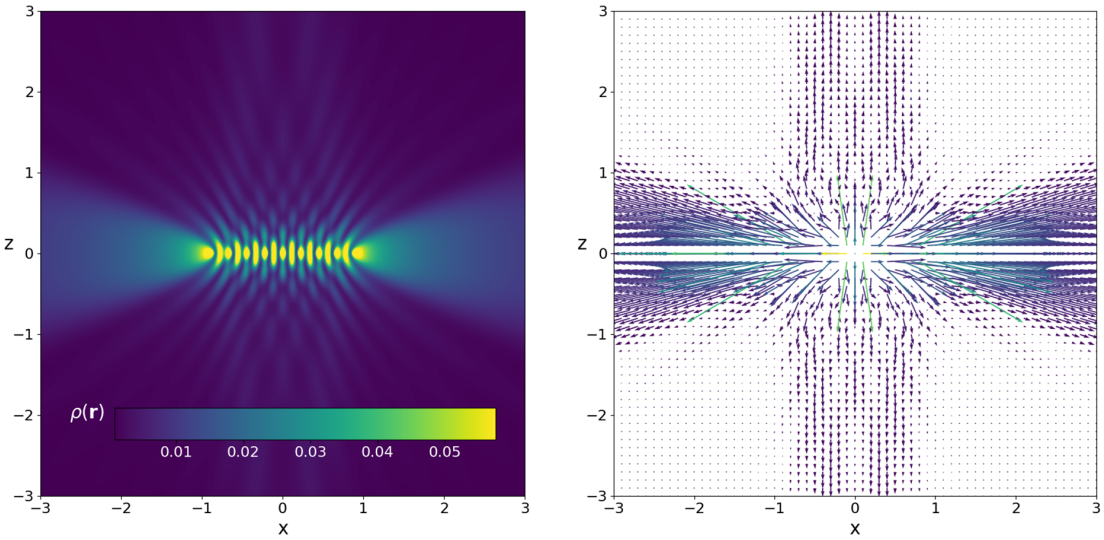

Figure 38: Energy density (left) and flow (right) across a plate with absorbing boundary conditions due to 9 in-phase point-forces with separations $d = \lambda$.

tioned, with minimal energy flow appearing elsewhere. The energy flow is however far more focused here than in the two-source case, producing a far narrower flow of energy away from the sources. Outside of this area, the large number of interactions between the vibrational waves generated by each source produces a complex interference pattern. As with the two source cases, the phases of the point-forces can be adjusted to achieve different vibrational responses. For N-sources, one approach for this is "phase-shifting" where the phase of the i^{th} source differs from its neighbour by some set margin. In Figure 39 the effect of setting this margin as $\phi_i - \phi_{i-1} = \pi$, which ensures that each source is in anti-phase with its direct neighbours, is considered.

As shown, the adjustment made to the phase distribution has a profound effect on the vibrational response of the plate. Here, a diamond shaped region of high vibrational energy can be observed around the sources, with width and height equal to the separation of the first and last sources. Throughout this shape, lines of minima can also be observed directly between each pair of sources, as demonstrated for pairs of anti-phase sources in Figure 35. As in the prior example, focused rays of vibrational energy can be observed flowing away from this diamond

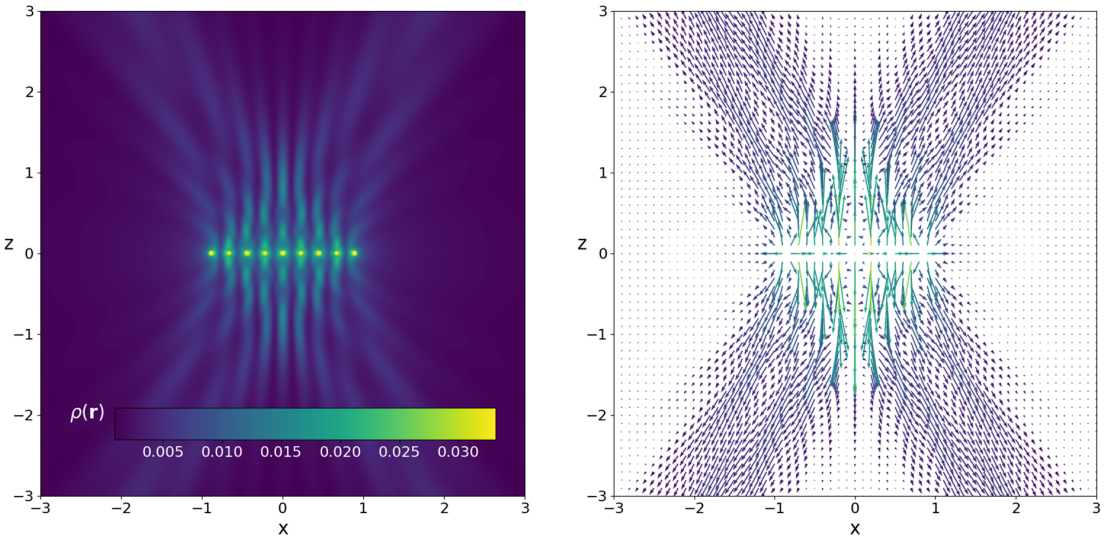

Figure 39: Energy density (left) and flow (right) across a plate with absorbing boundary conditions due to 9 point-forces with separations $d = \lambda$ and phase differences $\phi_i - \phi_{i-1} = \pi$.

shape, with minimal vibrational response found elsewhere. Through adjusting the phase-shift between each source, the influence of this effect on the vibrational response of the plate may be investigated. In Figure 40, the vibrational response of the plate under a phase-shift of $\phi_i - \phi_2 = 2\pi/3$ is considered.

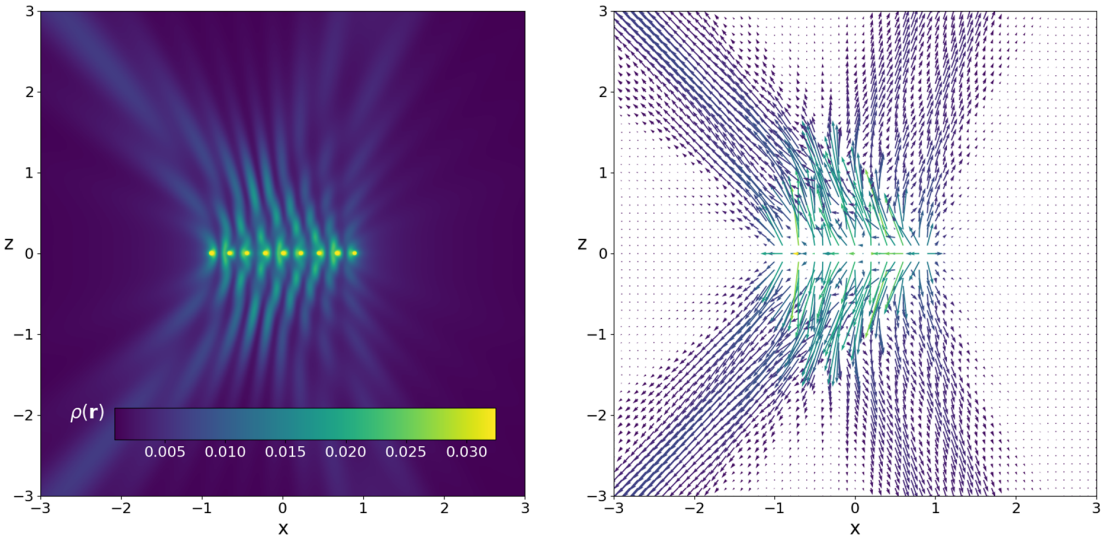

Figure 40: Energy density (left) and flow (right) across a plate with absorbing boundary conditions due to 9 point-forces with separations $d = \lambda$ and phase differences $\phi_i - \phi_{i-1} = 2\pi/3$.

This plot is rather similar to the π-shifted case, however the features of the energy distribution are no longer symmetric across the $z-$axis. Here, the lines of minimum energy density between the sources described previously are now off-centre, and curve towards the $-\hat{\boldsymbol{x}}$ direction further from the sources. This is because these minima are now found where $k\left(|\boldsymbol{r}-\boldsymbol{r}_{0i}|-\left|\boldsymbol{r}-\boldsymbol{r}_{0(i-1)}\right|\right)=-\frac{\pi}{3}$. Along with this shift, the beams of vibrational energy propagating from the sources are also skewed in this direction, and the leftmost beams demonstrate a greater energy density than those flowing in the $+\hat{\boldsymbol{x}}$ direction. This result thus demonstrates the strong influence of the applied phase-shift on the flow of vibrational energy within these systems.

Along with the phase-shift, the separation of the sources is another important factor in defining the vibrational response of the plate. The vibrational response of the plate to 9 in-phase point-forces with separation $d = 0.5\lambda$ is displayed in Figure 41.

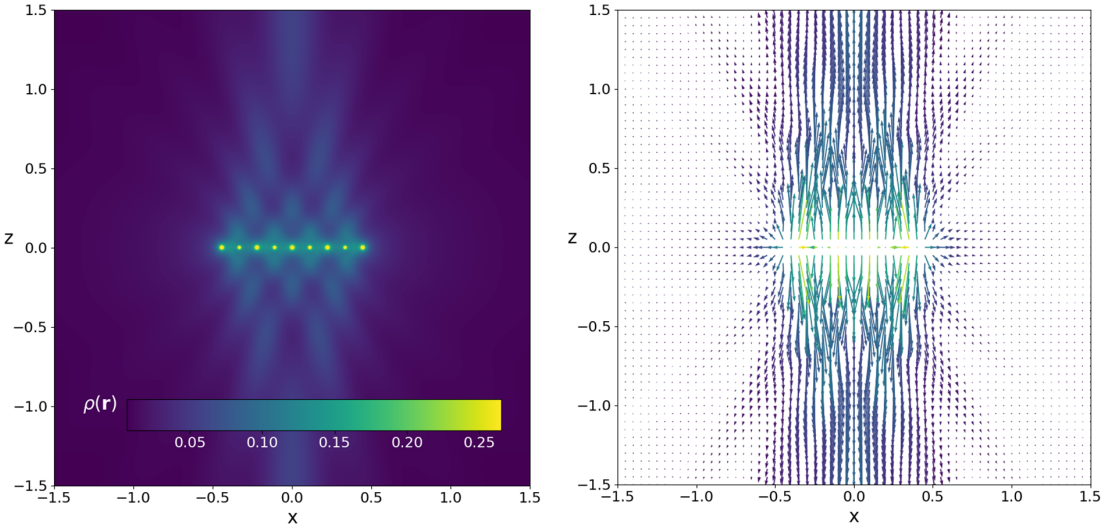

Figure 41: Energy density (left) and flow (right) across a plate with absorbing boundary conditions due to 9 point-forces each separated by 0.5λ with phase differences $\phi_i - \phi_{i-1} = 0$.

This result resembles the two-source case shown in Figure 34, with both plots demonstrating strong energy flow in the $z-$axis. In the two-source case however,

this energy flows outwards from the sources, becoming broader with increased distance from the sources. By contrast, in this case however, the energy flowing in this axis appears to become more focused with increased separation from the sources. Figure 4.2 then demonstrates the effect of applying phase-shifting to the observed vibrational response.

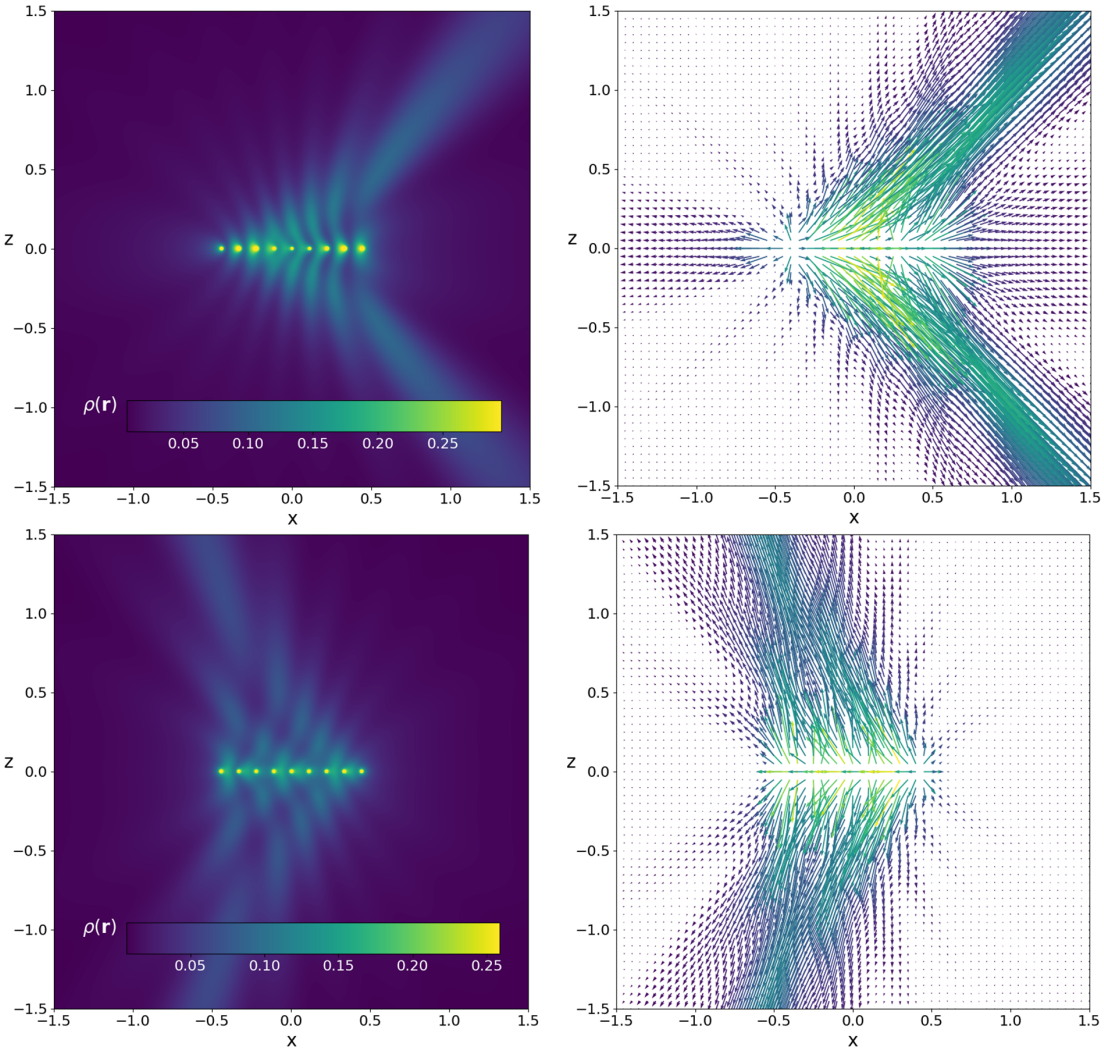

Figure 42: Energy density (left) and flow (right) across a plate with absorbing boundary conditions due to 9 point-forces each separated by 0.5λ with phase differences $\phi_i - \phi_{i-1} = 2\pi/3$ (top) and $\phi_i - \phi_{i-1} = -1\pi/3$ (bottom).

Figure 4.2 shows that the vibrational response of the plate is very similar in each case, displaying focused beams of vibrational energy propagating away from the sources, with minimal vibrational response elsewhere. It can also be observed that

the changes in phase difference lead to changes in the direction of propagation of the vibrational energy beams. This demonstrates that, with careful selection of this phase difference, it is possible to direct the beams of vibrational energy in any direction. This is the same technique applied in phased-array transducers, as discussed in subsection 2.4. In the context of DEP aircraft, the point-forces represent the interactions between the propellers and the passing air during flight. As the propellers rotate, these forces will thus oscillate based upon the current orientation of the propeller relative to the incoming flow. Phase differences could thus be implemented in these systems by adjusting the relative orientations of the propellers during flight. The results presented here then suggest that, with careful selection of this phase difference, along with the separation of the propulsors, it is possible to channel the vibrational energy produced by the propeller interactions in favourable directions. This could be applied to steer vibrational energy away from the fuselage to reduce the cabin noise experienced aboard the flight, or away from vital mechanisms to minimise mechanical wear.

This approach has already been implemented within distributed propulsion aircraft, to minimise the noise generated directly through the interactions between the propellers and the passing air. In these systems, passive noise reduction approaches involving adjustments to the shape or positioning of the propellers are avoided, due to the associated loss in aerodynamic performance of these methods [189–191]. Active control approaches, as discussed in subsection 2.4, are also ineffective in these systems, due to the large number of additional acoustic sources required to cancel out the noise from multi-propulsor configurations [190,192,193]. Instead phase-locking is employed, in which the rotation of the propellers is tuned to enable favourable interference effects between the sound waves generated by each source. These interference effects act to cancel out undesirable sounds or direct noise away from key locations such as the cabin [189–191]. In these systems, phase control can be maintained with simple devices, which add minimal complex-

ity, weight, or power requirements to the system [193, 194], and no modification is necessary to the shape of the propellers themselves [190]. The effectiveness of this approach has been demonstrated in numerous prior studies, producing wholesale noise reductions of $5 - 15\,dB$ [191, 193, 195, 196], and location targeted noise reductions of up to $30\,dB$ [190]. The electric motors applied by DEP aircraft are especially well suited to phase-locking systems, providing exceptional control and fast response to maintain synchronisation [191, 197]. These existing systems could then be adjusted to provide optimal reduction in both the air-bourne sound and structure-bourne vibrations generated by the multi-propulsor configurations used in DEP aircraft.

4.3 Implementation within DEA

The approach introduced in the prior subsections describes the free-space contribution to the vibrational response of structures under correlated point excitations. For a full description of the vibrational response, the homogeneous contribution from the energy density reflected at the structural boundary is also required, which necessitates the implementation of these sources within DEA. Each of the examples featured in this subsection considers the excitation of a flat plate of dimensions $3\,m \times 3\,m \times 3\,mm$, with material properties as described in subsection 3.3. The plate itself is represented computationally by a mesh of triangular elements as demonstrated in Figure 43.

To implement correlated point-force excitations within DEA, the boundary density across Γ_{src} must be defined. When considering the excitation of a plate by N sources of arbitrary phase, this is calculated by substituting equation (4.12) into equation (2.37), leaving

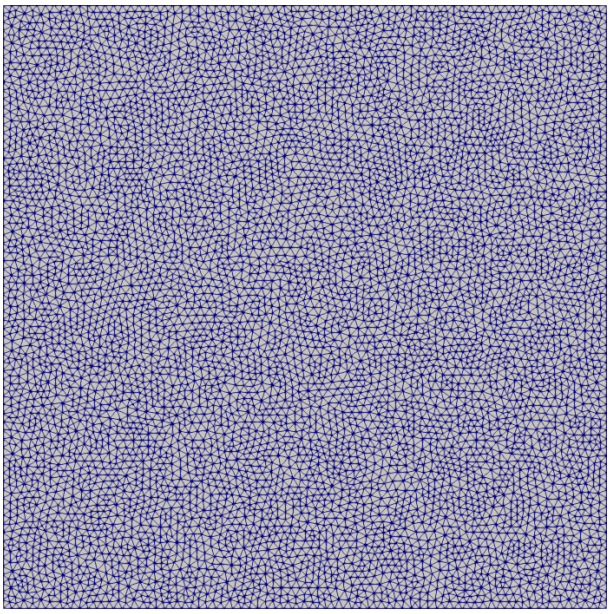

Figure 43: Mesh used to demonstrate the implementation of correlated point-forces in DEA.

$$\begin{aligned}\rho_0(s,p_s) = \frac{\varrho^2 h^2}{64\pi Dk}\Bigg[&\sum_{n=1}^{N}\frac{e^{-\mu|\boldsymbol{r}(s)-\boldsymbol{r}_{0n}|}}{|\boldsymbol{r}(s)-\boldsymbol{r}_{0n}|}\delta\left(\boldsymbol{p}(p_s)-k\frac{\boldsymbol{r}(s)-\boldsymbol{r}_{0n}}{|\boldsymbol{r}(s)-\boldsymbol{r}_{0n}|}\right)\\ &+2\sum_{m=1}^{N}\sum_{l>m}^{N}e^{-\mu\sqrt{|\boldsymbol{r}(s)-\boldsymbol{r}_{0m}||\boldsymbol{r}(s)-\boldsymbol{r}_{0l}|}}\\ &\frac{\cos\left(k\left(|\boldsymbol{r}(s)-\boldsymbol{r}_{0m}|-|\boldsymbol{r}(s)-\boldsymbol{r}_{0l}|\right)+\phi_m-\phi_l\right)}{\sqrt{|\boldsymbol{r}(s)-\boldsymbol{r}_{0m}|\,|\boldsymbol{r}(s)-\boldsymbol{r}_{0l}|}}\\ &\delta\left(\boldsymbol{p}(p_s)-\frac{k}{2}\left(\frac{\boldsymbol{r}(s)-\boldsymbol{r}_{0m}}{|\boldsymbol{r}(s)-\boldsymbol{r}_{0m}|}+\frac{\boldsymbol{r}(s)-\boldsymbol{r}_{0l}}{|\boldsymbol{r}(s)-\boldsymbol{r}_{0l}|}\right)\right)\Bigg]\cos\left(\theta(p_s)\right).\end{aligned} \tag{4.13}$$

The initial set of basis coefficients is then found by substituting this solution into equation (2.45) to give

$$
\begin{aligned}
f_{0,\boldsymbol{n}} = & \frac{2\beta+1}{2\sqrt{A_b k}} \frac{\varrho^2 h^2}{64\pi D k} \int_b \int_{-k}^{+k} \left[\sum_{n=1}^{N} \frac{e^{-\mu D(s,\boldsymbol{r}_{0n})}}{D(s,\boldsymbol{r}_{0n})} \delta\left(\boldsymbol{p}(p_s) - k \frac{\boldsymbol{r}(s) - \boldsymbol{r}_{0n}}{D(s,\boldsymbol{r}_{0n})} \right) + \right. \\
& 2 \sum_{m=1}^{N} \sum_{l>m}^{N} \frac{e^{-\mu\sqrt{D(s,\boldsymbol{r}_{0m}) D(s,\boldsymbol{r}_{0l})}} \cos\left(k \left(D(s,\boldsymbol{r}_{0m}) - D(s,\boldsymbol{r}_{0l}) \right) + \phi_m - \phi_l \right)}{\sqrt{D(s,\boldsymbol{r}_{0m}) D(s,\boldsymbol{r}_{0l})}} \\
& \left. \delta\left(\boldsymbol{p}(p_s) - \frac{k}{2} \left(\frac{\boldsymbol{r}(s) - \boldsymbol{r}_{0m}}{D(s,\boldsymbol{r}_{0m})} + \frac{\boldsymbol{r}(s) - \boldsymbol{r}_{0l}}{D(s,\boldsymbol{r}_{0l})} \right) \right) \right] \\
& \cos\left(\theta(p_s)\right) P_\beta(\sin\left(\theta(p_s)\right)) \, dp_s \, ds.
\end{aligned}
\tag{4.14}
$$

When implementing this result within DEA, an appropriate selection for Γ_{src}, the subsection of the boundary across which the initial boundary density is calculated, must be defined. In DEA, the rays which carry the energy density from Γ_{src} across the domain propagate independently, without interfering with other rays. As such, it is impossible to capture the interference effects between each source using the ray dynamics. Thus, if single cell boundaries were applied around each source, as is applied typically employed for point-force excitations in DEA, this result would capture only the direct contributions from the point-forces, without considering interference effects. The region within which the initial energy density is calculated must thus encompass all correlated point-forces within the system, along with their associated interference effects before being translated into a raytracing picture. For systems with several, widely-spaced, sources this initially excited region (IER) is likely to be large, spanning many mesh elements. Given the complex and spatially variable nature of the vibrational energy fields generated by correlated point-force excitations, it is inappropriate to compute the energy density across the boundary of all of the mesh elements within the excited region. Instead, the super-cell approach introduced in subsection 3.5 is applied to effectively merge the IER into a single, large, mesh element. The difficulty of this approach is then to define an appropriate choice for Γ_{src}.

As discussed, in terms of the accuracy of the generated solution it would be

preferable for Γ_{src} to be as large as possible, to ensure that it is able to properly encapsulate all of the interference effects between the point-forces. However, computing the initial boundary density distribution is far more computationally taxing than the subsequent propagation of rays across the domain. For computational reasons, it would thus be preferred that the IER is as small as possible. The ideal choice for the IER is thus the smallest possible region which is able to produce an accurate representation of the correlated point-forces and their associated interference effects. To introduce the approach chosen to define this region, the excitation of a plate by N point-forces applied at positions $\boldsymbol{r}_{0i} \in \Omega, i = 1, 2, ..., N$ is considered. The first stage of this calculation is to define the average position of all of the point sources $\bar{\boldsymbol{r}}$. The chosen boundary Γ_{src} is then a circle of radius $A \times max(\boldsymbol{r}_{0i} - \bar{\boldsymbol{r}})$, with A a parameter to be defined. This process is summarised in Figure 44.

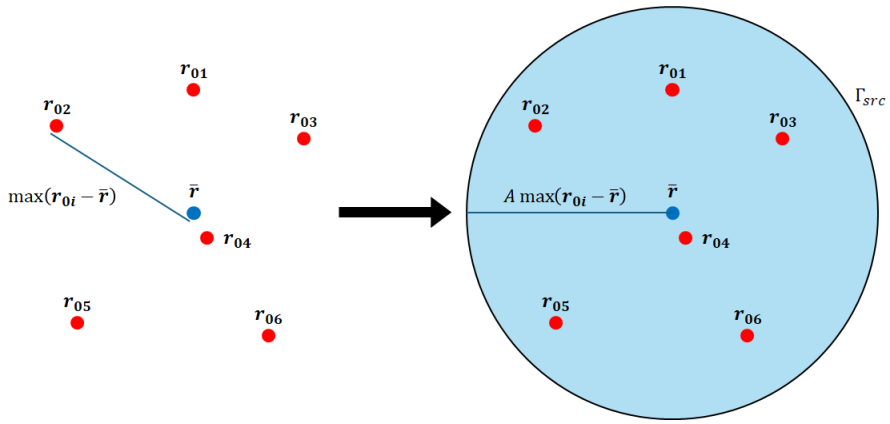

Figure 44: Process used to define the initial boundary Γ_{src} around a group of correlated point-forces in DEA.

When implementing this approach within DEA, the boundary density must be calculated across the outward-flowing boundary segments of the mesh elements at the edge of the circle. As such, it is impossible to define a perfectly circular excited region within a discretised mesh. Instead, one must define an approach to decide which mesh elements should be included to produce the best possible

representation of the circular excited region. In this approach, it is assumed that the mesh elements are sufficiently small that their locations may be represented by individual average positions. All elements with average locations within the defined radius of $\bar{\boldsymbol{r}}$ are then included within the IER, with all others left out. The IER for two point-force excitations applied to the plate described in Figure 43 is demonstrated in Figure 45.

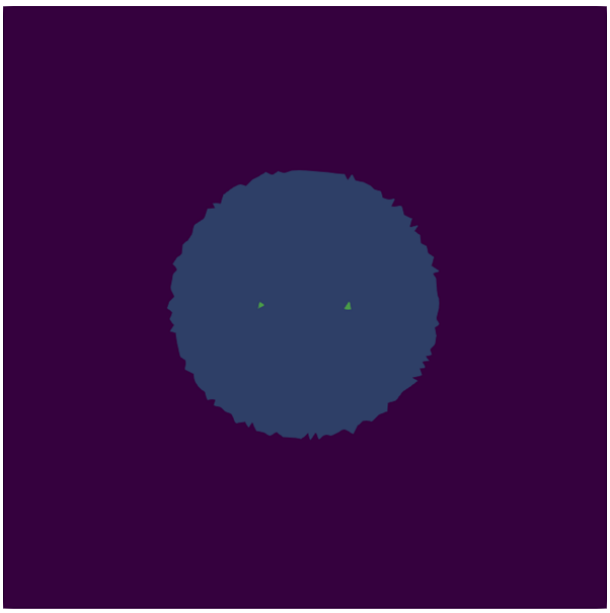

Figure 45: Example excited region within DEA for two point-force excitations. Here, green indicates the mesh elements containing the point-force excitations, with light blue indicating the remaining elements within the IER, which is defined with $A = 2$.

To complete the implementation of this approach within DEA, an appropriate value is needed for the radius parameter A. To identify an appropriate value for A, the energy density distribution across the plate for $N = 9$ sources phase-shifted by $\phi_i - \phi_{i-1} = 2\pi/3$ and separated by 0.5λ is plotted for different values of A. This result is demonstrated in Figure 46.

As shown, the close proximity of the boundary to the point-forces in the $A = 1.00$ leads to significant variance in the energy density flow. Although this case still displays a focused beam of vibrational energy away from the sources, the direction

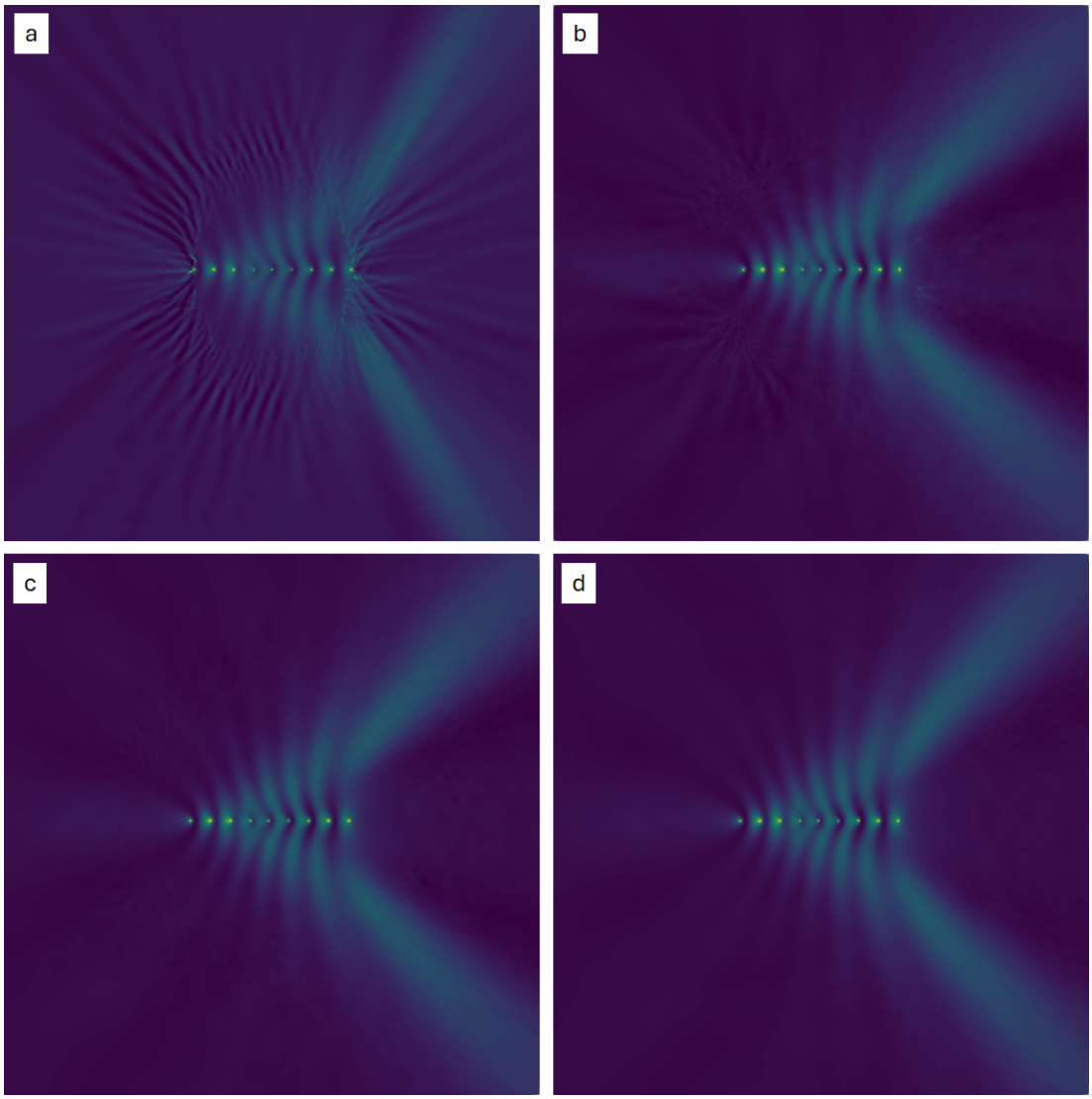

Figure 46: Energy density distribution across a plate with absorbing boundary conditions due to 9 point-forces, phase-shifted by $\phi_i - \phi_{i-1} = 2\pi/3$ and separated by 0.5λ calculated using DEA with A values of (a) $A = 1.00$, (b) $A = 1.25$, (c) $A = 1.50$, and (d) $A = 2.00$.

of this flow differs substantially from that found with a greater initial boundary. In addition, severe distortions in the energy density can be observed all across the boundary, once again highlighting the inability of the $A = 1.00$ boundary to properly capture the full interference field generated by the sources. The $A = 1.25$ case provides a significant improvement over this case, showing a strong resemblance to the analytical solution demonstrated in Figure 4.2. This suggests

that the $A = 1.25$ region is sufficient to properly capture all of the interference effects between the sources. However, some fringes in the energy density can still be observed in this example. The origin of these fringes is unknown, and could either be caused by deficiencies in the approach implemented to calculate the boundary density or in the applied mesh. These fringes are not observed in the $A = 1.50$ and $A = 2.00$ results, suggesting that these regions are sufficiently large to overcome the issues which generate these fringes. To minimise computational cost, $A = 1.50$ is preferred. This boundary is however not sufficient for all cases. For example, when considering the case of two in-phase point-forces separated by 2λ, fringes are observed in the $A = 1.50$ case and only disappear for $A = 3.00$. Similarly, for two in-phase point-forces separated by 0.5λ a value of $A = 12.00$ is required. These results are displayed in Figures 47 and 48.

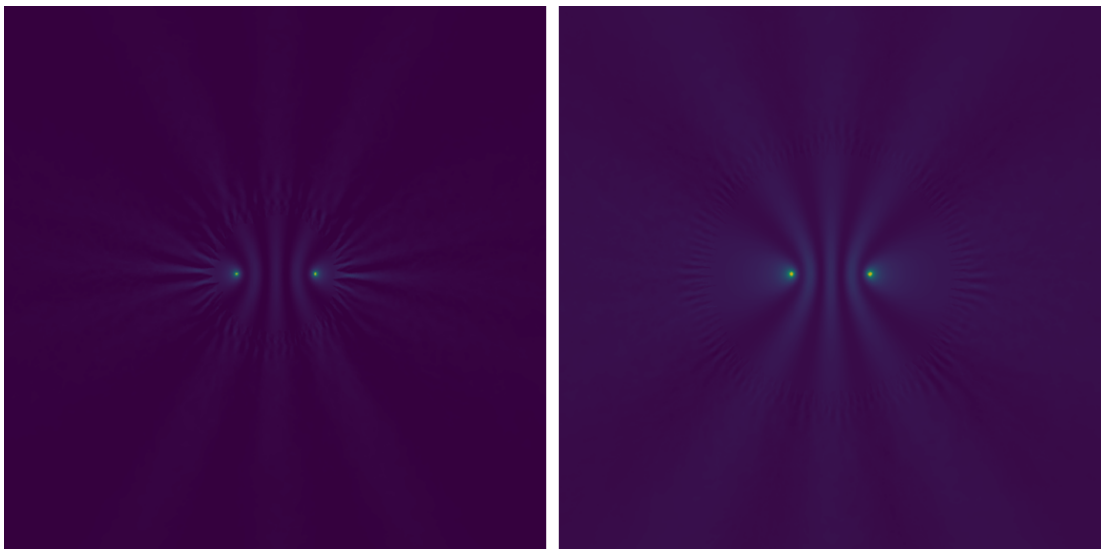

Figure 47: Energy density distribution across a plate with absorbing boundary conditions due to 2 in-phase point-forces, separated by 2λ calculated with $A = 2.00$ (left) and $A = 3.00$ (right).

The choice of an appropriate radius for the initial excited region is thus highly dependent on the number of sources applied and their separation. Interestingly, in each of the cases shown, the minimum appropriate radius has been found to be $Amax(|\boldsymbol{r}_{0i} - \boldsymbol{r}|) \approx 0.66$. Given the range of situations considered here

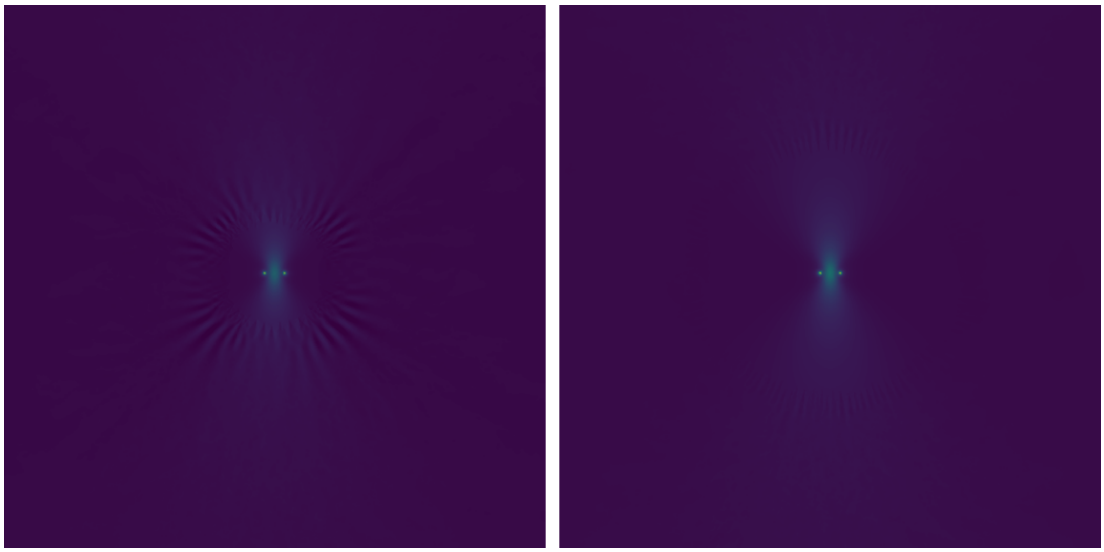

Figure 48: Energy density distribution across a plate with absorbing boundary conditions due to 2 in-phase point-forces, separated by 0.5λ calculated with $A = 2.00$ (left) and $A = 3.00$ (right).

this result may simply be coincidental. For example, the arrangement of mesh elements used to construct the IER in this case may happen to minimise this fringing effect. In any case, more work is required to develop meshes which are more suitable for implementing correlated point-force excitations, or to implement approaches for minimising this effect within DEA itself. In addition, a more thorough investigation into an approach to define appropriate IERs is necessary. The results demonstrated here are equivalent to the vibrational response of a plate under absorbing boundary conditions. The response of the plate with reflecting boundary conditions to 2 in-phase, correlated, point-forces separated by 2λ is demonstrated in Figure 49

Here, the flow of energy density away from the sources is sufficiently weak that the reflecting condition applied at the boundaries has little impact on the overall energy density distribution. The reflecting boundary result then closely resembles the absorbing boundary results demonstrated in Figure 47. The response of the plate with reflecting boundary conditions to 9 correlated point-forces phase shifted by $\phi_i - \phi_{i-1} = 2\pi/3$ and separated by 0.5λ is demonstrated in Figure 50.

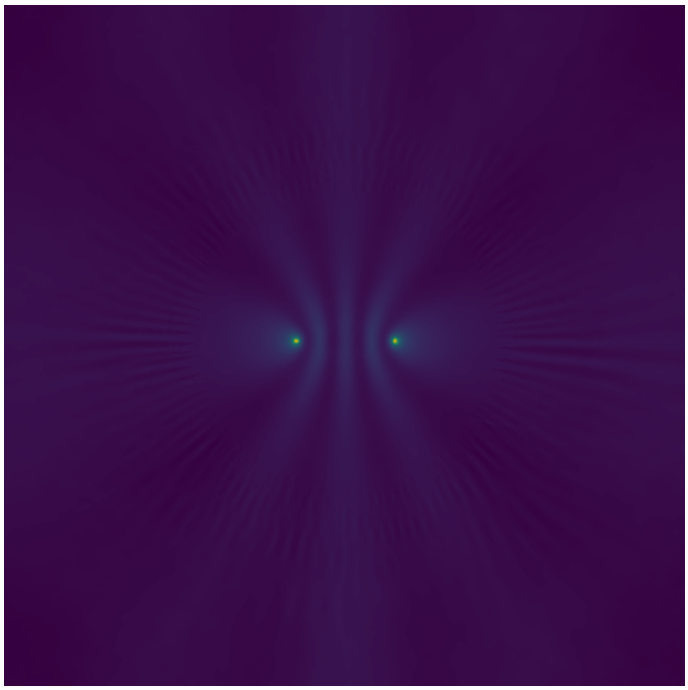

Figure 49: Energy density distribution across a plate with reflecting boundary conditions due to 2 in-phase point-forces separated by 2λ.

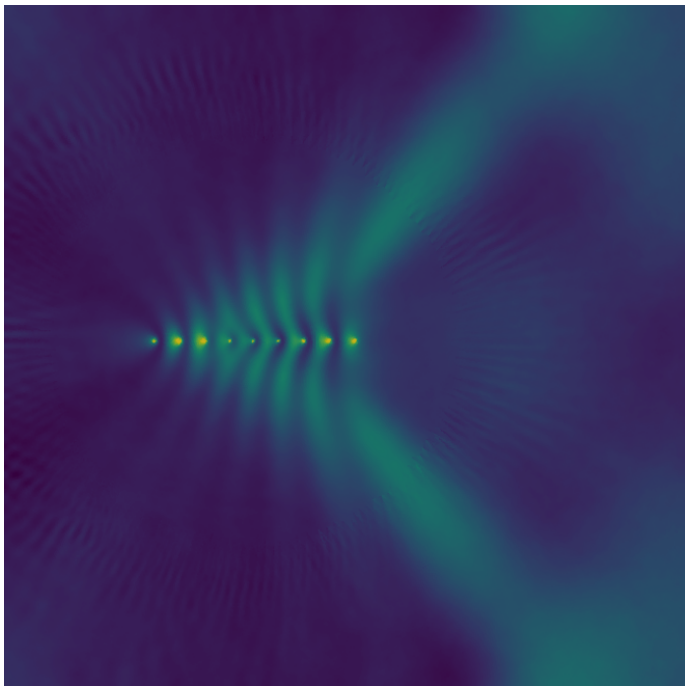

Figure 50: Energy density distribution across a plate with reflecting boundary conditions due to 9 point-forces each separated by 0.5λ with phase differences $\phi_i - \phi_{i-1} = 2\pi/3$.

Once again, this result is rather similar to the absorbing boundary case. However, the focused beams of energy density in this case are sufficiently strong that the influence of the reflecting boundary on the overall energy density distribution is clear. Upon encountering the edges of the plate, these beams are reflected towards the right-hand edge of the plate, leading to a buildup of energy density within these areas. These results then demonstrate the ability of DEA to effectively model the response of plates with varying boundary conditions to correlated point-force excitations.

4.4 Negative energy density and the HDF

As discussed in subsection 2.4, the interference between vibrational waves generated by different sources can be either constructive or destructive. When calculating the energy density due to correlated point-forces using equation (4.12), this effect is represented by the cosine term which oscillates between -1 and $+1$ across space. As the magnitude of this term depends on the product of the separation from each of the interfering points, this value will be at most equal to the sum of the contributions from each of the interfering point-forces. As such, the energy density $\rho(\boldsymbol{r}, \omega)$ will be non-negative for any number of point-forces at all locations on the plate. However, as shown in equation (4.12), the rays generated by this interference propagate with different momenta than those generated by the point-forces independently. The result is that many locations $(\boldsymbol{r}, \boldsymbol{p})$ across phase space will receive contributions only from rays generated through destructive interference, meaning that the phase-space density at these locations is negative. This is demonstrated in Figure 51.

This is important, as it is impossible for the energy to be negative at any location in space. When considering the vibrational response of plates to correlated point-force excitations, the approach involving the WDF phase-space representation of the system introduced in subsection 4.1 is unfeasible. As such, an alternate phase-

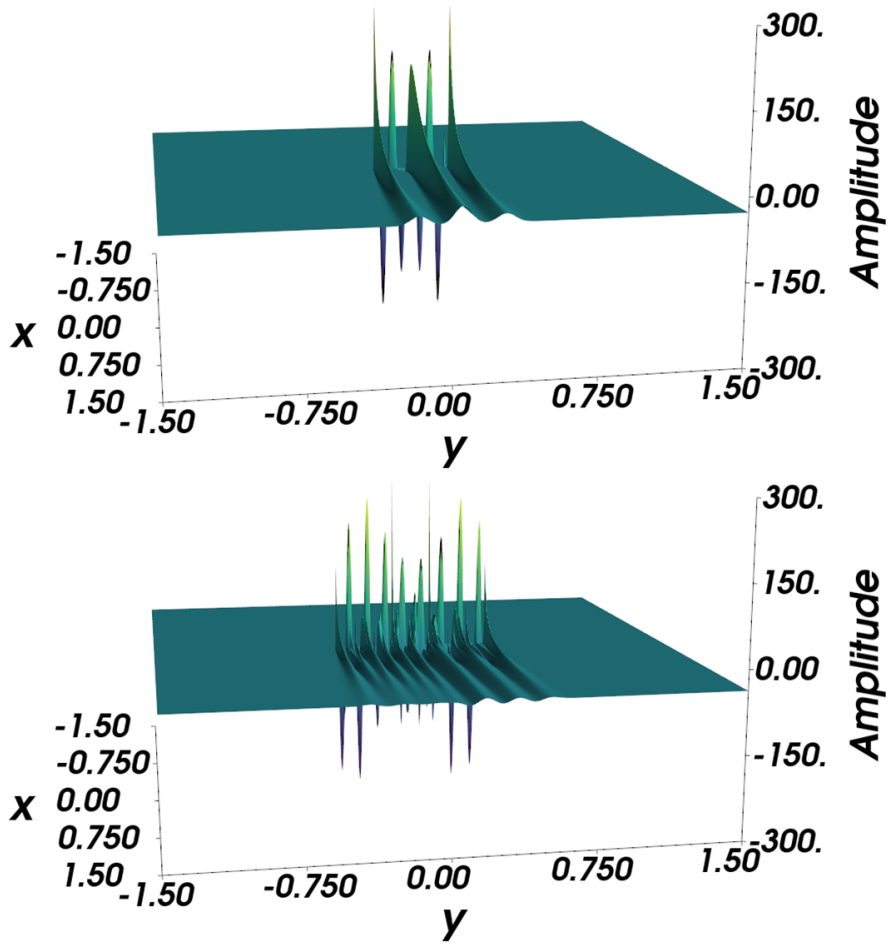

Figure 51: Phase-space density with $\boldsymbol{p} = k(1, 0)$ for two in-phase point-forces (top) and 9 point-forces with phase differences $\phi_i - \phi_{i-1} = 2\pi/3$ (bottom).

space representation of this system is required. For this, the Husimi Distribution Function (HDF) will be applied. To introduce this approach, the mathematical derivations of both the WDF and HDF are considered here.

The Wigner and Husimi functions were first developed to define the probability distributions of quantum systems in phase-space [198, 199]. Given a quantum state $|\psi\rangle$, the aim is to define the probability that each phase-space location $\boldsymbol{(r, p)}$ is occupied. In Wigner's approach, the WDF is given by [200]

$$W_\psi(\boldsymbol{r}, \boldsymbol{p}) = \int e^{-i\frac{1}{\hbar}\boldsymbol{p}\cdot\boldsymbol{\xi}} \left\langle \boldsymbol{r} + \frac{\boldsymbol{\xi}}{2} \middle| \hat{\rho} \middle| \boldsymbol{r} - \frac{\boldsymbol{\xi}}{2} \right\rangle d\boldsymbol{\xi}. \tag{4.15}$$

Where $\hat{\rho} = |\psi\rangle \langle\psi|$ is the density operator [199, 200], applying this substitution

then leaves

$$W_\psi(\boldsymbol{r},\boldsymbol{p}) = \int e^{-i\frac{1}{\hbar}\boldsymbol{p}\cdot\boldsymbol{\xi}} \left\langle \boldsymbol{r}+\frac{\boldsymbol{\xi}}{2}\middle|\psi\right\rangle \left\langle \psi\middle|\boldsymbol{r}-\frac{\boldsymbol{\xi}}{2}\right\rangle d\boldsymbol{\xi}. \tag{4.16}$$

In Dirac notation [199],

$$\langle \boldsymbol{x}|\psi\rangle = \psi(\boldsymbol{x}), \tag{4.17}$$

meaning that equation (4.16) can be rewritten as

$$W_\psi(\boldsymbol{r},\boldsymbol{p}) = \int e^{-i\frac{1}{\hbar}\boldsymbol{p}\cdot\boldsymbol{\xi}} \psi\left(\boldsymbol{r}+\frac{\boldsymbol{\xi}}{2}\right)\psi^*\left(\boldsymbol{r}-\frac{\boldsymbol{\xi}}{2}\right) d\boldsymbol{\xi}. \tag{4.18}$$

Defining a function $F\left(\boldsymbol{r}+\frac{\boldsymbol{\xi}}{2},\boldsymbol{r}-\frac{\boldsymbol{\xi}}{2}\right) = \psi\left(\boldsymbol{r}+\frac{\boldsymbol{\xi}}{2}\right)\psi^*\left(\boldsymbol{r}-\frac{\boldsymbol{\xi}}{2}\right)$, the resultant equation then closely resembles the Wigner transform applied to determine the WDF in equation (2.23).

The HDF is instead defined by

$$H_\psi(\boldsymbol{r},\boldsymbol{p}) = \langle\alpha|\hat{\rho}|\alpha\rangle\,. \tag{4.19}$$

where $|\alpha\rangle$ is the coherent state [198, 199]. Substituting once again for the density operator

$$H_\psi(\boldsymbol{r},\boldsymbol{p}) = \langle\alpha|\psi\rangle\,\langle\psi|\alpha\rangle\,. \tag{4.20}$$

In Dirac notation, $\langle a|b\rangle = (\langle b|a\rangle)^*$ and so

$$H_\psi(\boldsymbol{r},\boldsymbol{p}) = |\langle\alpha|\psi\rangle|^2\,. \tag{4.21}$$

Thus, the HDF is positive across all of phase space, as is required when computing the phase-space density. Returning to equation (4.20), these inner products can be evaluated by acting upon the kets with the identity operator $\hat{I}$. By definition,

$\hat{I}\,|\psi\rangle = |\psi\rangle$, and so this has no impact on the overall solution, thus

$$H_\psi(\boldsymbol{r},\boldsymbol{p}) = \left\langle \alpha \middle| \hat{I} \middle| \psi \right\rangle \left\langle \psi \middle| \hat{I} \middle| \alpha \right\rangle . \tag{4.22}$$

$\hat{I}$ can be expanded in terms of an arbitrary vector $|\boldsymbol{y}\rangle$, by $\hat{I} = \int |\boldsymbol{y}\rangle \langle \boldsymbol{y}|\, d\boldsymbol{y}$. Substituting into equation (4.22)

$$H_\psi(\boldsymbol{r},\boldsymbol{p}) = \left(\int \langle \alpha|\boldsymbol{y}\rangle \langle \boldsymbol{y}|\psi\rangle \, d\boldsymbol{y} \right) \left(\int \langle \psi|\boldsymbol{z}\rangle \langle \boldsymbol{z}|\alpha\rangle \, d\boldsymbol{z} \right). \tag{4.23}$$

By again exploiting equation (4.17), these integrals can be rewritten by

$$H_\psi(\boldsymbol{r},\boldsymbol{p}) = \left(\int \alpha^*(\boldsymbol{y})\psi(\boldsymbol{y})\, d\boldsymbol{y} \right) \left(\int \psi^*(\boldsymbol{z})\alpha(\boldsymbol{z})\, d\boldsymbol{z} \right). \tag{4.24}$$

where $\alpha(\boldsymbol{y})$ is the position representation of the coherent state, given by [201] as

$$\alpha(\boldsymbol{y}) = \frac{1}{(2\pi\sigma_r^2)^{1/4}} e^{-\frac{(\boldsymbol{y}-\boldsymbol{r})^2}{4\sigma_r^2} + \frac{i}{\hbar}\boldsymbol{p}\cdot\boldsymbol{y}}, \tag{4.25}$$

with σ_r a parameter to be determined. Substituting this into equation (4.24)

$$H_\psi(\boldsymbol{r},\boldsymbol{p}) = \frac{1}{\sqrt{2\pi}\sigma_r} \left(\int e^{-\frac{(\boldsymbol{y}-\boldsymbol{r})^2}{4\sigma_r^2} - \frac{i}{\hbar}\boldsymbol{p}\cdot\boldsymbol{y}} \psi(\boldsymbol{y})\, d\boldsymbol{y} \right) \left(\int \psi^*(\boldsymbol{z}) e^{-\frac{(\boldsymbol{z}-\boldsymbol{r})^2}{4\sigma_r^2} + \frac{i}{\hbar}\boldsymbol{p}\cdot\boldsymbol{z}}\, d\boldsymbol{z} \right) \tag{4.26}$$

which can be rewritten as

$$H_\psi(\boldsymbol{r},\boldsymbol{p}) = \frac{1}{\sqrt{2\pi}\sigma_r} \int\int e^{-\frac{(\boldsymbol{y}-\boldsymbol{r})^2}{4\sigma_r^2} - \frac{(\boldsymbol{z}-\boldsymbol{r})^2}{4\sigma_r^2} - \frac{i}{\hbar}\boldsymbol{p}\cdot(\boldsymbol{y}-\boldsymbol{x})} \psi(\boldsymbol{y})\psi^*(\boldsymbol{z})\, d\boldsymbol{y}\, d\boldsymbol{z}. \tag{4.27}$$

This problem may be rewritten using the following substitutions $\boldsymbol{y} = \boldsymbol{r}' + \frac{\boldsymbol{\xi}'}{2}, \boldsymbol{z} = \boldsymbol{r}' - \frac{\boldsymbol{\xi}'}{2}$ such that $\boldsymbol{r}' = \frac{1}{2}(\boldsymbol{y}+\boldsymbol{z})$ and $\boldsymbol{\xi}' = \boldsymbol{y} - \boldsymbol{z}$. Substituting these parameters into equation (4.27) leaves

$$H_\psi(\boldsymbol{r},\boldsymbol{p}) = \frac{1}{\sqrt{2\pi}\sigma_r}\int\int e^{-\frac{(\boldsymbol{\xi}')^2}{8\sigma_r^2}-\frac{i}{\hbar}\boldsymbol{p}\cdot\boldsymbol{\xi}'} e^{-\frac{(\boldsymbol{r}-\boldsymbol{r}')^2}{2\sigma_r^2}} \psi\left(\boldsymbol{r}'+\frac{\boldsymbol{\xi}'}{2}\right)\psi^*\left(\boldsymbol{r}'-\frac{\boldsymbol{\xi}'}{2}\right)\,d\boldsymbol{r}'\,d\boldsymbol{\xi}'. \tag{4.28}$$

To solve this, first the following integral solution is considered

$$\int_{-\infty}^{+\infty} e^{-\frac{(x-a)^2}{b^2}-2cx}\,dx = \sqrt{\pi}be^{-c^2b^2-2ac} \tag{4.29}$$

which can be proven by expanding the exponent of the integrand and then re-factorising the solution by completing the square and using the fact that $\int_{-\infty}^{+\infty} e^{-x^2}\,dx = \sqrt{\pi}$. Using this expression, the $\boldsymbol{\xi}'$ exponential term in equation (4.28) can be rewritten as

$$e^{-\frac{(\boldsymbol{\xi}')^2}{8\sigma_r^2}-\frac{i}{\hbar}\boldsymbol{p}\cdot\boldsymbol{\xi}'} = \frac{1}{\sqrt{2\pi}\sigma_p}\int e^{-\frac{1}{2\sigma_p^2}(\boldsymbol{p}-\boldsymbol{p}')^2} e^{-\frac{i}{\hbar}\boldsymbol{p}'\cdot\boldsymbol{\xi}'}\,d\boldsymbol{p}' \tag{4.30}$$

with $\sigma_p = \frac{\hbar}{2\sigma_r}$. Substituting this term into equation (4.28) then leaves

$$H_\psi(\boldsymbol{r},\boldsymbol{p}) = \frac{1}{2\pi\sigma_r\sigma_p}\int\int e^{-\frac{(\boldsymbol{p}-\boldsymbol{p}')^2}{2\sigma_p^2}} e^{-\frac{(\boldsymbol{r}-\boldsymbol{r}')^2}{2\sigma_r^2}} \left[\int e^{-\frac{i}{\hbar}\boldsymbol{p}'\cdot\boldsymbol{\xi}'}\psi\left(\boldsymbol{r}'+\frac{\boldsymbol{\xi}'}{2}\right)\psi^*\left(\boldsymbol{r}'-\frac{\boldsymbol{\xi}'}{2}\right)\,d\boldsymbol{\xi}'\right]\,d\boldsymbol{p}'\,d\boldsymbol{r}'. \tag{4.31}$$

The integral enclosed within the square brackets is the definition of the WDF, shown in equation (4.18). Hence

$$H_\psi(\boldsymbol{r},\boldsymbol{p}) = \frac{1}{2\pi\sigma_r\sigma_p}\int\int e^{-\frac{(\boldsymbol{p}-\boldsymbol{p}')^2}{2\sigma_p^2}} e^{-\frac{(\boldsymbol{r}-\boldsymbol{r}')^2}{2\sigma_r^2}} W_\psi(\boldsymbol{r}',\boldsymbol{p}')\,d\boldsymbol{p}'\,d\boldsymbol{r}'. \tag{4.32}$$

The HDF is then effectively the WDF smoothed by a Gaussian across phase-space [198, 199]. In quantum mechanics, the coherent state represents the minimum uncertainty state and so $\sigma_r\sigma_p = \frac{\hbar}{2}$ to ensure that the Heisenberg uncertainty

principle is maintained [199]. Through comparison of equations (4.18) and (2.23), it is apparent that in a vibrational modelling context $\sigma_r\sigma_p = \frac{1}{2}$. In this study, $\sigma_r = \frac{a}{\sqrt{2}}$ and $\sigma_p = \frac{1}{a\sqrt{2}}$ with $a = 0.4$ chosen for computational reasons.

To define the HDF version of the phase-space density for multiple correlated point-forces, equation (4.12) is substituted into equation (4.32), to give

$$\begin{aligned}\rho_{0,H}(\boldsymbol{r},\boldsymbol{p}) = \frac{1}{2\pi\sigma_r\sigma_p}\frac{\varrho^2h^2}{64\pi Dk\pi}\Bigg[&\sum_{n=1}^{N}\int\int\frac{e^{-\mu|\boldsymbol{r}'-\boldsymbol{r}_{0n}|}}{|\boldsymbol{r}'-\boldsymbol{r}_{0n}|}\delta\left(\boldsymbol{p}'-k\frac{\boldsymbol{r}'-\boldsymbol{r}_{0n}}{|\boldsymbol{r}'-\boldsymbol{r}_{0n}|}\right)\\ &e^{-\left(\frac{1}{2\sigma_r^2}|\boldsymbol{r}-\boldsymbol{r}'|^2+\frac{1}{2\sigma_p^2}|\boldsymbol{p}-\boldsymbol{p}'|^2\right)}\,d\boldsymbol{p}'\,d\boldsymbol{r}'\\ &+2\sum_{m=1}^{N}\sum_{l>m}\int\int\frac{\cos\left(k\left(|\boldsymbol{r}'-\boldsymbol{r}_{0m}|+|\boldsymbol{r}'-\boldsymbol{r}_{0l}|\right)+\phi_m-\phi_l\right)}{\sqrt{|\boldsymbol{r}'-\boldsymbol{r}_{0m}|\,|\boldsymbol{r}'-\boldsymbol{r}_{0l}|}}\\ &e^{-\mu\sqrt{|\boldsymbol{r}'-\boldsymbol{r}_{0m}||\boldsymbol{r}'-\boldsymbol{r}_{0l}|}}\delta\left(\boldsymbol{p}'-\frac{k}{2}\left(\frac{\boldsymbol{r}'-\boldsymbol{r}_{0m}}{|\boldsymbol{r}'-\boldsymbol{r}_{0m}|}+\frac{\boldsymbol{r}'-\boldsymbol{r}_{0l}}{|\boldsymbol{r}'-\boldsymbol{r}_{0l}|}\right)\right)\\ &e^{-\left(\frac{1}{2\sigma_r^2}|\boldsymbol{r}-\boldsymbol{r}'|^2+\frac{1}{2\sigma_p^2}|\boldsymbol{p}-\boldsymbol{p}'|^2\right)}\,d\boldsymbol{p}'\,d\boldsymbol{r}'\Bigg].\end{aligned} \tag{4.33}$$

In this equation, the integrals over $\boldsymbol{p}'$ can be solved using the corresponding delta functions, leaving

$$\begin{aligned}\rho_{0,H}(\boldsymbol{r},\boldsymbol{p}) = \frac{1}{2\pi\sigma_r\sigma_p}\frac{\varrho^2h^2}{64\pi Dk\pi}&\\ \Bigg[&\sum_{n=1}^{N}\int\frac{e^{-\mu|\boldsymbol{r}'-\boldsymbol{r}_{0n}|}}{|\boldsymbol{r}'-\boldsymbol{r}_{0n}|}e^{-\frac{1}{2\sigma_r^2}|\boldsymbol{r}-\boldsymbol{r}'|^2}e^{-\frac{1}{2\sigma_p^2}\left|\boldsymbol{p}-k\frac{\boldsymbol{r}'-\boldsymbol{r}_{0n}}{|\boldsymbol{r}'-\boldsymbol{r}_{0n}|}\right|^2}\,d\boldsymbol{r}'\\ &+2\sum_{m=1}^{N}\sum_{l>m}\int\frac{\cos\left(k\left(|\boldsymbol{r}'-\boldsymbol{r}_{0m}|+|\boldsymbol{r}'-\boldsymbol{r}_{0l}|\right)+\phi_m-\phi_l\right)}{\sqrt{|\boldsymbol{r}'-\boldsymbol{r}_{0m}|\,|\boldsymbol{r}'-\boldsymbol{r}_{0l}|}}\\ &e^{-\mu\sqrt{|\boldsymbol{r}'-\boldsymbol{r}_{0m}||\boldsymbol{r}'-\boldsymbol{r}_{0l}|}}e^{-\frac{1}{2\sigma_r^2}|\boldsymbol{r}-\boldsymbol{r}'|^2}e^{-\frac{1}{2\sigma_p^2}\left|\boldsymbol{p}-\frac{k}{2}\left(\frac{\boldsymbol{r}'-\boldsymbol{r}_{0m}}{|\boldsymbol{r}'-\boldsymbol{r}_{0m}|}+\frac{\boldsymbol{r}'-\boldsymbol{r}_{0l}}{|\boldsymbol{r}'-\boldsymbol{r}_{0l}|}\right)\right|^2}\,d\boldsymbol{r}'\Bigg].\end{aligned} \tag{4.34}$$

The equivalent HDF phase-space densities for the results presented in Figure 51 are shown in Figure 52.

As anticipated, in each case the HDF is positive across the entire plate, mean-

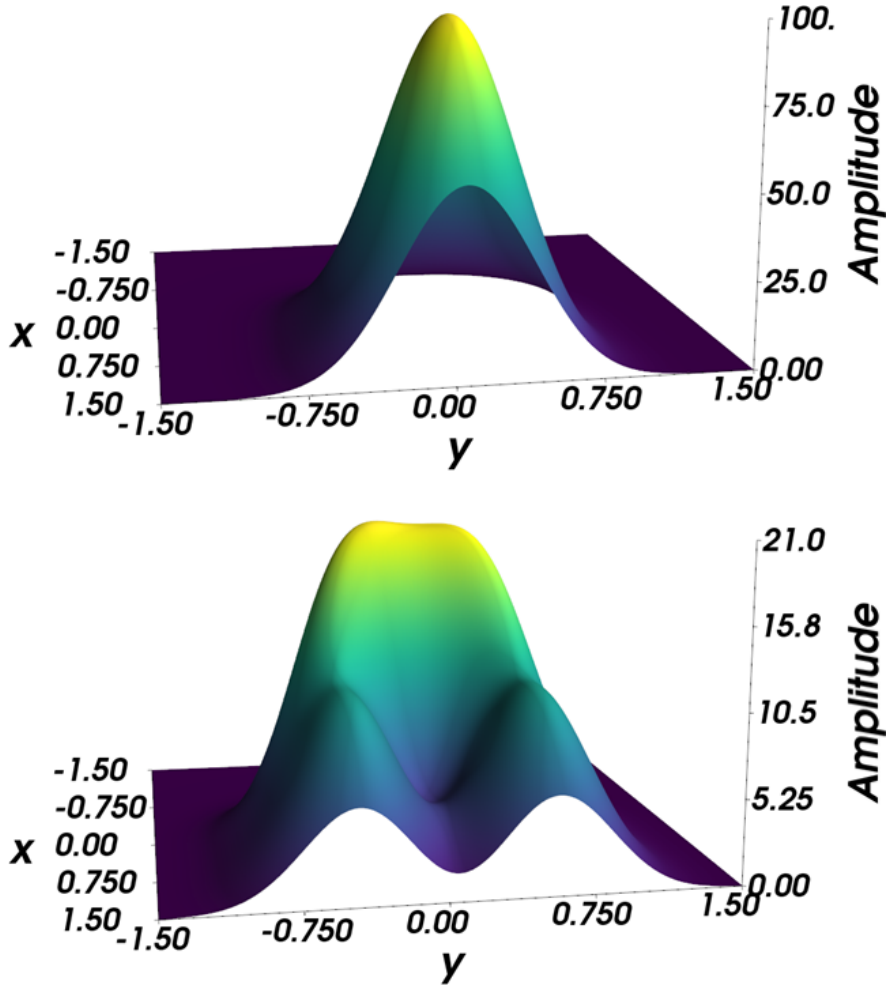

Figure 52: HDF with $\boldsymbol{p} = k(1, 0)$ for two in-phase point-forces (top) and 9 point-forces with phase differences $\phi_i - \phi_{i-1} = 2\pi/3$ (bottom).

ing that the resultant phase-space density will be valid across all of phase-space. The Gaussian smoothing applied to the WDF has however had a dramatic effect on the properties in the function. In Figure 51, each point-force is easily recognisable due to the sharp peaks in the WDF close to these locations. In the HDF, these details are replaced by a smooth distribution within which the original point-forces and their interference effects are impossible to distinguish. In each case however, the HDF still demonstrates a general flow of energy in the $+\hat{\boldsymbol{x}}$ direction, suggesting that not all of the detail from the WDF has been lost through the smoothing. As with the WDF, the energy density distribution is found by substituting equation (4.34) into equation (2.41). The energy density

distributions for the cases demonstrated in Figure 52 are shown in Figure 53.

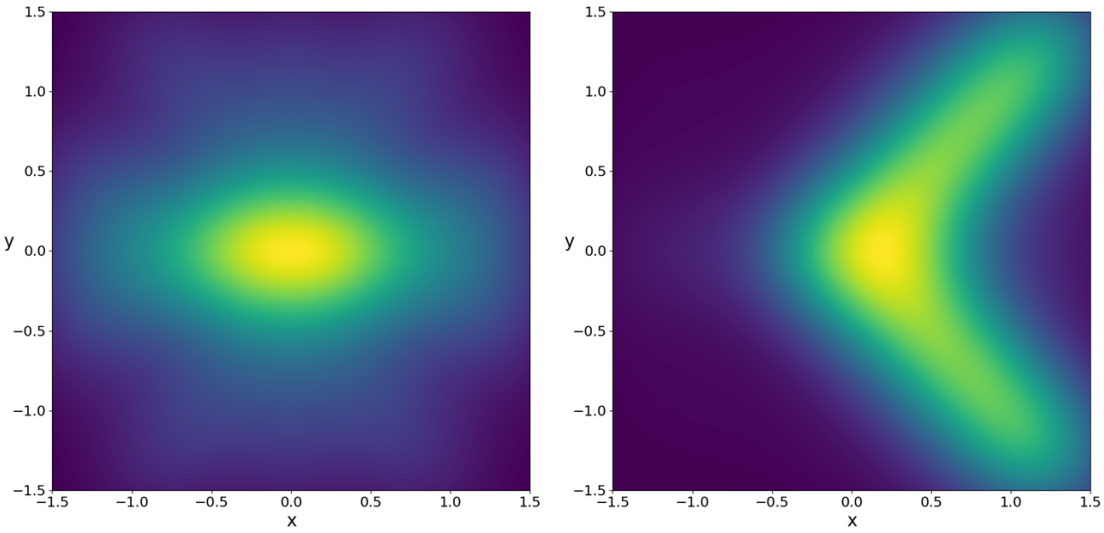

Figure 53: Energy density computed from the HDF for two in-phase point-forces (left) and 9 point-forces with phase differences $\phi_i - \phi_{i-1} = 2\pi/3$ (right).

As in the phase-space density case, the applied Gaussian smoothing has led to the loss of much of the detail of the original sources and their interactions. This is particularly prevalent in the two-source case, with the original sources now combined into a single Gaussian-like peak in the centre of the plate, with all details of the sources and their detailed local interference effects lost. Further from the sources however, some detail of the directional energy flow still remains. For example, the preference for the flow of energy outwards from the sources along the $y = 0$ line as shown in Figure 36 is still visible. In addition, both the WDF and HDF solutions demonstrate minimal flow of energy density towards the corners of the plate. The effects of computing the HDF solution are even more pronounced when discussing the 9-source case. Here, the smoothing applied has removed all detail of the point-forces and their local interactions, replacing these with a single wide peak in energy density found close to the centre of the plate. Outside of this area the HDF solution demonstrates focused beams of vibrational energy propagating out towards the corners of the plate, closely matching the WDF result in Figure 4.2.

These results thus demonstrate the capability of the HDF to product non-negative phase-space density distributions for correlated point-force excitations. This come at the cost of some of the detail in the solution, particularly in the region close to the sources. In the far-field however, the HDF results demonstrate very similar energy flow behaviour as found in the equivalent WDF results.

By following the approach discussed in subsection 4.3, the HDF approach can also be implemented within DEA. For this, the super-cell approach discussed in subsection 4.3 is again applied. The energy density distributions calculated using DEA for 2 in-phase point-forces and 9 point-forces phase shifted by $\phi_i - \phi_{i-1} = 2\pi/3$ are shown in Figure 54.

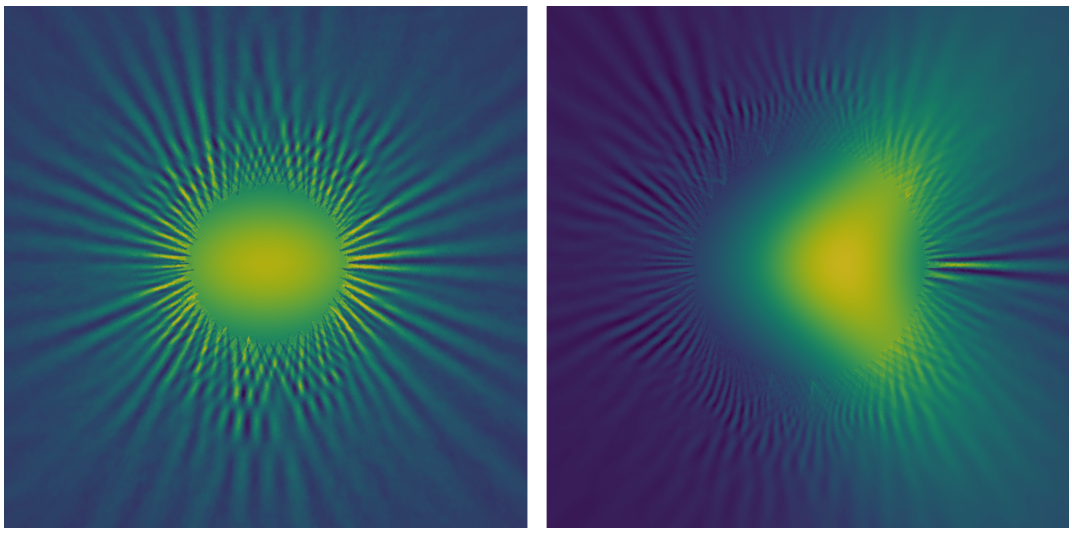

Figure 54: HDF energy density calculated using DEA for two in-phase point-forces (left) and 9 point-forces with phase differences $\phi_i - \phi_{i-1} = 2\pi/3$ (right).

When computed using DEA, the HDF approach demonstrates abrupt changes in the behaviour of the solution at the boundary of the IER. This is most prevalent in the 2 source case, with large fringes in the energy density found all across this boundary and minimal structure in the energy flow outside of this region. The 9 source case shows a somewhat more coherent result, demonstrating far smaller fringes in the energy density at the boundary and some continuation of the mean energy flow outside of this region. These results suggest that the

A values applied in subsection 4.3 for the WDF solution are insufficient when calculating the HDF solution. The resultant HDF energy density distributions when doubling the radius of the IER as compared to the WDF, using values of $A = 6.00$ and $A = 3.00$ for the 2- and 9-source cases respectfully, are shown in Figure 55.

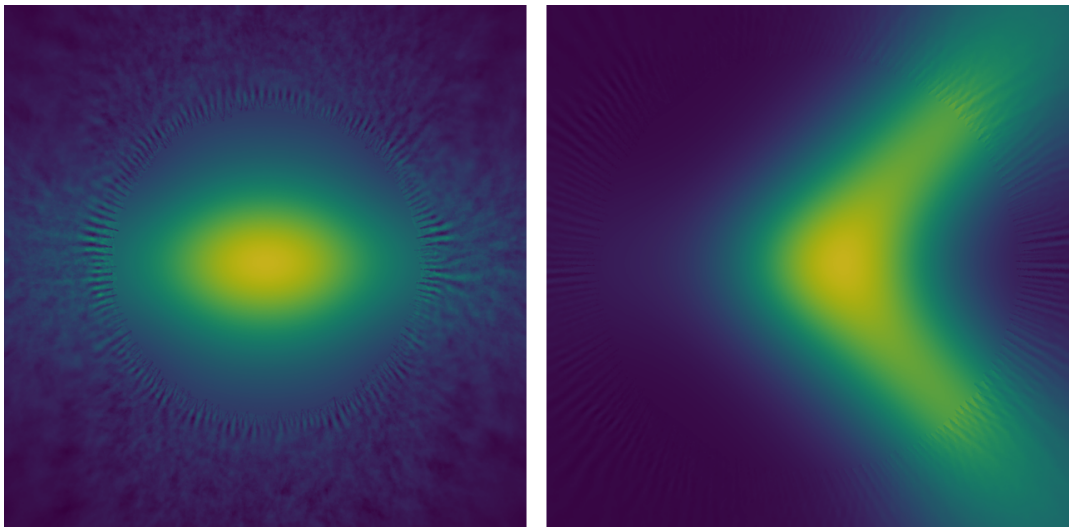

Figure 55: HDF energy densities for the 2- and 9-source cases shown in Figure 54 with $A = 6.00$ and $A = 3.00$ respectfully.

As shown, the increase in radius of the IER has produced improvements in the quality of the solutions shown. In each case, the fringes are far smaller and some detail of the flow outside of the IER can be shown. This is particularly true in the 9-source case, with continuation of the energy density beams propagating towards the corners of the plate achieved across the boundary of the IER. Even with this larger excited region, significant detail in the solution outside of this range is still lost. Given the extreme size of the IER in either case, this result then points to potential issues in the approach applied to define the initial boundary density using the HDF solution. As such, further work is required to ensure that the boundary representation of the HDF energy density calculated within DEA is accurate, along with defining an appropriate IER for these calculations.

4.5 Further work

In this study, an approach has been developed to calculate the vibrational response of flat plates to correlated point-force excitations using DEA. However, issues in the quality of the solutions produced mean that further work is required to achieve the ultimate goal of modelling the behaviour of DEP aircraft due to the correlated vibrations induced by the propeller array. As demonstrated in subsections 4.3 and 4.4, there are issues with fringes in the energy density at the boundary of the IER for the implementation of this approach within DEA. Although this issue can be somewhat rectified by increasing the radius of this region, the radius required to achieve this has been found to vary for each example and follows no clear pattern. As such, further work is required to attempt to identify the origin of these fringes and attempt to remove them. Otherwise, further attempts to define appropriate IERs are needed. Given the variety of results observed in subsections 4.3 and 4.4, this approach should take into consideration the number of sources and their separation, along with whether the result is computed using the WDF or HDF energy density distributions.

Once complete, this approach should be applied to model the vibrational response of real DEP aircraft structures to correlated point-forces representing the propeller structures. Figure 56 displays the NASA X-57 Maxwell, a DEP aircraft which could be used for such a calculation.

Given the separation of the wings, it seems sensible in this case to only consider the interference between vibrational waves produced by propellers positioned on the same wing. Even applying this assumption, the distribution of the propellers across the wing will mean that the IER will likely need to cover most of the wing structure. This is important, as the super-cell approach applied in this study requires initial excited region to be approximately flat, with constant material properties. As shown in this figure, the wing structure is curved at the leading and trailing edges, along with at the wing tip and on the extensions where the

Figure 56: NASA X-57 Maxwell, an example DEP aircraft [202].

propellers are placed. As such, the approach for defining the IER will need to be adjusted to account for curvature, which could be accomplished using geodesics [203], and changes in material properties

Once this study is completed, this approach could be combined with the correlated field approach discussed in Chapter 3, to calculate a spatially distributed description of the overall vibrational behaviour of DEP aircraft during flight.

4.6 Conclusion

In this chapter, an approach has been introduced to model the response of structures to correlated point-force excitations. To achieve this, the superposition principle has been applied, which states that the result of the interference of two impinging wavefields is the sum of the wavefields. Thus, the Green function of the vibrational response under N point-forces is given by the sum of the Green function for each individual source. The resultant energy density distribution was then found to be the sum of the individual contributions from each point-force, plus terms representing the interference effects between each pair of sources.

The resultant energy density distributions display detailed interference patterns which vary based upon the separation and phase-difference between the sources. By careful management of the phase-differences between each source, it has been demonstrated that these interference effects can be adjusted to generate narrow beams of vibrational energy that may be guided in different directions. This approach is already used in propeller aircraft to steer aerodynamic noise from the propellers away from the fuselage, thus demonstrating the validity of this result. The implementation of this approach within DEA has also been presented, demonstrating how an initial excited region which encapsulates the sources is necessary to capture all interference effects between the sources. Following this, the opportunity for the generation of non-physical negative phase-space density is also discussed and the HDF, the result of applying a Gaussian smoothing to the WDF, is introduced. Here it has been demonstrated that the HDF is able to fully positive phase-space density distribution, at the cost of solution detail particularly close to the point-forces. Finally, opportunities for potential future developments of this approach have been discussed, including the improvements required to apply this method to model the vibrational response of real DEP aircraft under correlated excitations originating from the propeller array.

Chapter 5

5 Conclusion

5.1 Summary

The aim of this project has been to develop an approach to model the vibrational behaviour of DEP aircraft during operation. Whilst in flight, these aircraft experience vibrational excitations from the TBL pressure field, along with through the interactions between the propellers and the passing air. Given the importance of the TBL pressure field for frequencies $> 500\,Hz$, the chosen approach had to be able to capture the vibrational behaviour of the system in the high-frequency range. In this range analytical approaches are unfeasible due to computational and methodological issues, and statistical approaches are preferred. In particular, the DEA approach was selected due to its excellent solution detail and minimal computational cost. The application of this approach to model the response of structures to individual point-force excitations was then introduced.

Within DEA, pressure sources are represented by appropriate correlation functions, which describe the level of coherence in the pressure applied by the source at different locations based upon their spatial separation. When modelling the vibrational behaviour of complex structures under TBLs, an effective correlation function representing the applied pressure field is required. Amongst the available models the Corcos and Mellen models were chosen, due to their mathematical simplicity and ability to easily transfer between spatial and wavenumber representations. The implementation of correlated pressure fields represented by

these models within DEA was then discussed in Chapter 3. There, the applied pressure field was assumed to be spatially homogeneous and was initially constrained to small regions of the structure. In this case, the vibrational response of the structure was found to depend on the geometry of the excited region and the properties of both the structure and the applied pressure field. The extension of the approach to full body pressure fields was then demonstrated by considering the excitation of flat plates by fully formed TBL pressure fields. The vibrational response of the plates demonstrated large spatial variability, with a strong dependence on the properties of the plate and the applied pressure field. These results demonstrate the need for a spatially distributed measure of the vibrational behaviour of structures under correlated pressure fields, which has found little attention in prior studies. In this section several limitations of the approach were also discussed. In particular, the applied homogeneous TBL pressure field is unlikely to reflect real DEP systems, due to structural complexities and non-idealised flow conditions. In addition, the implemented pressure fields fail to account for additional acoustic contributions to the applied pressure field, which would require updates to the source correlation function to be included.

With the TBL accounted for, the remainder of the thesis focused on the contribution of the propellers to vibrational behaviour of DEP aircraft. In subsection 2.4, it was discussed how interactions between the propellers and the surrounding air could induce vibrations within the structure. Due to the monochromatic nature of the propeller rotations within the system, this would lead to interference between the vibrational waves generated by each propeller. To model the vibrational response of structures to these effects, the propellers were modelled as correlated point-forces. The aim of Chapter 4 was thus to define the vibrational response of structures to correlated point-forces, including interference effects, using DEA. Based on the superposition theorem, it was assumed that the vibrational response of the plate was the sum of the responses to each individual

point-force. The resultant vibrational energy distribution is then the sum of the contributions from each point-force plus additional spatially oscillating terms capturing the interference effects. The vibrational behaviour of flat plates under correlated point-force excitations was then studied, demonstrating complicated energy distributions which vary greatly due to changes in the source separations and phase-differences. For large numbers of sources, it was found that certain combinations of these factors lead to the generation of focused beams of vibrational energy. With careful tuning, it was demonstrated that the direction of propagation of these beams could be guided in favourable directions. This could be applied to reduce cabin noise or minimise wear of vital mechanical components. The implementation of this approach within DEA was then discussed, including the requirement of a suitable IER within which the full interference effects must be computed. Following this, the issue of negative phase-space densities due to correlated point forces was highlighted. Here, the HDF, a Gaussian smoothed version of the WDF, was introduced as an alternative approach to compute the phase-space density. Although this solution is always positive, the applied smoothing removes much of the detail in the vibrational response, particularly close to the point-forces. In addition the implementation of this approach within DEA proved difficult, with discontinuities found across the boundary of the IER even for large boundaries. Finally, the future steps required to apply this approach to model the vibrational behaviour of DEP aircraft were discussed. Amongst these are the limitation of the IER to flat regions, which is a poor approximation of the complex three-dimensional structures that make up DEP aircraft.

5.2 Further Work

The presented work demonstrates a baseline for modelling the vibrational response of structures to TBL pressure fields and correlated point-force excitations.

To be able to apply this approach to compute the vibrational behaviour of DEP aircraft during flight, several extensions to the implemented approach must be developed. These include

- The assumed homogeneity of the TBL pressure field applied in Chapter 3 is unlikely to apply in real-world cases. Instead, the applied pressure field should vary dependent on local structural and TBL properties. This could be achieved by using the mesh-averaged approach suggested in subsection 3.6.5.

- The correlation function used to represent the TBL pressure field should be adjusted to include acoustic pressure contributions from within the TBL. This could be achieve by defining the WDF of the correlated pressure field in equation (3.10) using equation (3.40).

- The Corcos and Mellen correlation functions approximate the system as a flat plate positioned beneath a fully formed TBL flowing parallel to the plate surface. For more complex structures this must be adjusted to consider the formation of the TBL across the structure, along with the effect of structural complexities such as curvature and non-parallel components on the pressure applied.

- The current implementation of correlated point-force excitations within DEA generates fringes at the boundary of the IER. Further work is necessary to either remove these fringes, or to define appropriate IERs to minimise their effect.

- The requirement for the IER to be flat, with constant material properties, is problematic when applied to complex three-dimensional structures such as DEP aircraft. Further work is thus necessary to ensure that interference effects can be properly accounted for across such structures.

- The WDF produces negative phase-space densities, whilst the HDF guarantees positive results at the cost of solution detail. Further work is thus required to minimise the loss in detail in the solution whilst ensuring that the phase-space density is always positive.

- Once these prior issues have been solved, the correlated field and correlated point-force methodologies should be applied to compute the vibrational behaviour of DEP aircraft during flight. This method should then be combined with existing sound radiation techniques, to produce a detailed description of the noise experienced aboard DEP aircraft due to these vibrational sources.

Bibliography

[1] C. Friedrich and P.A. Robertson. Hybrid-electric propulsion for automotive and aviation applications. *CEAS Aeronautical Journal*, 6:279–290, 2015.

[2] AIRBUS. Global market forecast, 2021. Available at `https://www.airbus.com/en/products-services/commercial-aircraft/market/global-market-forecast`. Accessed [23.04.24].

[3] B.A. Adu-Gyamfi and C. Good. Electric aviation: A review of concepts and enabling technologies. *Transportation Engineering*, 9:100134, 2022.

[4] H.D. Kim, A.T. Perry, and P.J. Ansell. Progress in distributed electric propulsion vehicles and technologies. Technical report, AIAA, 2020.

[5] H.D. Kim, J.L. Felder, M. Tong, and M. Armstrong. Revolutionary aeropropulsion concept for sustainable aviation: turboelectric distributed propulsion. Technical report, NASA Glenn Research Center Cleveland, Ohio, U.S.A., 2013.

[6] J.T. Hwang and A. Ning. Large-scale multidisciplinary optimization of an electric aircraft for on-demand mobility. In *2018 AIAA/ASCE/AHS/ASC Structures, Structural Dynamics, and Materials Conference*, pages 1384–1401, 2018.

[7] N.K. Borer, M.D. Patterson, J.K. Viken, M.D. Moore, J. Bevirt, A.M. Stoll, and A.R. Gibson. Design and performance of the nasa sceptor distributed electric propulsion flight demonstrator. In *16th AIAA Aviation Technology, Integration, and Operations Conference*, page 3920, 2016.

[8] W. Kelei, Z. Zhou, F. Zhongyun, and G. Jiahao. Aerodynamic design of tractor propeller for high-performance distributed electric propulsion aircraft. *Chinese Journal of Aeronautics*, 34(10):20–35, 2021.

[9] S. Sahoo, X. Zhao, and K. Kyprianidis. A review of concepts, benefits, and challenges for future electrical propulsion-based aircraft. *Aerospace*, 7:100134, 2020.

[10] A.M Stoll. Comparison of cfd and experimental results of the leaptech distributed electric propulsion blown wing. In *15th AIAA aviation technology, integration, and operations conference*, page 3188, 2015.

[11] E. Greenwood, K.S. Brentner, R.F. Rau, and Z. Ted Gan. Challenges and opportunities for low noise electric aircraft. *International Journal of Aeroacoustics*, 21(5-7):315–81, 2022.

[12] E Wash. magnix continued flight testing reveals electric aircraft significantly reduce noise pollution, Apr 2021. Available at `https://www.prnewswire.com/news-releases/magnix-continued-flight-testing-reveals-electric-aircraft-significantly-reduce-noise-pollution-301264765.html`. Accessed [24.04.24].

[13] A. Caiazzo, N. Alujević, B. Pluymers, and W. Desmet. Active control of turbulent boundary layer sound transmission into a vehicle interior. *Journal of Physics: Conference Series*, 744:012026, 2016.

[14] W.R. Graham. Boundary layer induced noise in aircraft, Part I: The flat plate model. *Journal of Sound and Vibration*, 192(1):101–120, 1996.

[15] J.F. Wilby. Aircraft interior noise. *Journal of Sound and Vibration*, 190(3):545–564, 1996.

[16] F.J. Fahy. On simulating the transmission through structures of noise from turbulent boundary layer pressure fluctuations. *Journal of Sound and Vibration*, 3(1):57–81, 1966.

[17] H. Fathi, Z. El-Sayegh, J. Ren, and M. El-Gindy. Modelling and validation of a passenger car tire using finite element analysis. *Vehicles*, 6(1):384–402, 2024.

[18] S.M. Darwish, S.M. Elseufy, and A. Ahmad. Finite element analysis of an automobile engine hood. In *Proceedings of the 2013 International Conference on Industry, Engineering, and Management Systems*, volume 7, pages 62–69, 2013.

[19] T. McKelvey, T. Abrahamsson, and L. Ljung. Vibration data analysis for a commercial aircraft: Multivariable vibration data from an aircraft is analyzed using modern system identification tools. the identified linear vibrational model accurately describes the measured motion. *Automatica*, 32(12):1689–1700, 1996.

[20] R. Winter, M. Norambuena, J. Biedermann, and M. Böswald. Experimental characterization of vibro-acoustic properties of an aircraft fuselage. In *Proceedings of ISMA 2014 International Conference on Noise and Vibration Engineering*, volume 15, 2014.

[21] R. Winter, S. Heyen, and J. Biedermann. Experimental structure intensity analysis of an airbus a400m fuselage structure using high-resolution vibration measurements. In *Proceedings of the 23rd International Congress on Acoustics: Integrating 4th EAA Euroregio 2019*, pages 8118–8125, 2019.

[22] C. Maury, S.J. Elliott, and P. Gardonio. Turbulent boundary-layer simulation with an array of loudspeakers. *AIAA journal*, 42(4):706–713, 2004.

[23] C. Maury and T. Bravo. The experimental synthesis of random pressure fields: Practical feasibility. *The Journal of the Acoustical Society of America*, 120(5):2712–2723, 2006.

[24] A. Pouye, L. Maxit, C. Maury, and M. Pachebat. Reproduction of the vibroacoustic response of panels under stochastic excitations using the source scanning technique. *Journal of Sound and Vibration*, 510:116307, 2021.

[25] M. Aucejo, L. Maxit, and J.L. Guyader. Experimental simulation of turbulent boundary layer induced vibrations by using a synthetic array. *Journal of sound and vibration*, 331(16):3824–3843, 2012.

[26] C. Marchetto, L. Maxit, O. Robin, and A. Berry. Experimental prediction of the vibration response of panels under a turbulent boundary layer excitation from sensitivity functions. *The Journal of the Acoustical Society of America*, 143(5):2954–2964, 2018.

[27] S.A. Hambric, Y.F. Hwang, and W.K. Bonness. Vibrations of plates with clamped and free edges excited by low-speed turbulent boundary layer flow. *Journal of Fluids and Structures*, 19:93–110, 2004.

[28] F. Birgersson. *Prediction of random vibration using spectral methods*. PhD thesis, KTH, Stockholm, 2003.

[29] WR Graham. A comparison of models for the wavenumber-frequency spectrum of turbulent boundary layer pressures. *Journal of sound and vibration*, 206(4):541–565, 1997.

[30] C. Maury, P. Gardonio, and S.J. Elliott. A wavenumber approach to modelling the response of a randomly excited panel, part i: general theory. *Journal of Sound and Vibration*, 252(1):83–113, 2002.

[31] R.I. Wright and M.R.F. Kidner. Vibration absorbers: a review of applications in interior noise control of propeller aircraft. *Journal of Vibration and Control*, 10(8):1221–1237, 2004.

[32] K.D. Dunno. *Analysis of in-flight vibration for a turbo propeller aircraft.* PhD thesis, Clemson University, 2008.

[33] Z. Ilić, B. Rašuo, M. Jovanović, S. Jovičić, L. Tomić, M. Janković, and D. Petrašinović. The efficiency of passive vibration damping on the pilot seat of piston propeller aircraft. *Measurement*, 95:21–32, 2017.

[34] F. Liebers. Resonance vibrations of aircraft propellers, 1932.

[35] R.S. Sliff. Vibration evaluation of aircraft propellers, 1970.

[36] V. Wickramasinghe, D. Zimcik, and Y. Chen. A novel adaptive structural impedance control approach to suppress aircraft vibration and noise. In *RTO AVT Symposium on" Habitability of Combat and Transport Vehicles: Noise, Vibration and Motion", held in Prague, Czech Republic*, pages 16–1, 2004.

[37] H.D. Kim, A.T. Perry, and P.J. Ansell. A review of distributed electric propulsion concepts for air vehicle technology. In *2018 AIAA/IEEE Electric Aircraft Technologies Symposium (EATS)*, pages 1–21. IEEE, 2018.

[38] A. Hrennikoff. Solution of problems of elasticity by the framework method. *Journal of Applied Mechanics*, 8:169–175, 1941.

[39] C. Richard. Variational methods for the solution of problems of equilibrium and vibrations. *Bulletin of the American Mathematical Society*, 49:1–23, 1943.

[40] F. Fahy and P. Gardonio. Sound and structural vibration : Radiation, transmission and response. In Frank Fahy and Paolo Gardonio, editors,

Sound and Structural Vibration (Second Edition). Academic Press, Oxford, second edition edition, 2007.

[41] D.L. Logan. *A first course in the finite element method*, volume 4. Thomson, 2011.

[42] K.H. Huebner, D.L. Dewhirst, D.E. Smith, and T.G. Byrom. *The finite element method for engineers*. John Wiley & Sons, 2001.

[43] Arshad Mehmood. Using finite element method vibration analysis of frame structure subjected to moving loads. *International Journal of Mechanical Engineering and Robotics Research*, 4(1):50–65, 2015.

[44] C.A. Felippa. *Introduction to Finite Element Methods*. Department of Aerospace Engineering Sciences and Center for Aerospace Structures University of Colorado, 2003.

[45] K.J. Bathe. *Finite element procedures*. Klaus-Jurgen Bathe, 2006.

[46] X. Zhang, Y. Qiu, and M.J. Griffin. Developing a simplified finite element model of a car seat with occupant for predicting vibration transmissibility in the vertical direction. *Ergonomics*, 58(7):1220–1231, 2015.

[47] K. Charoensuk and T. Sethaput. The vibration analysis based on experimental and finite element modeling for investigating the effect of a multi-notch location of a steel plate. *Applied Sciences*, 13(21):12073, 2023.

[48] A.F. Seybert, X.F. Wu, and F.B. Oswald. Validation of finite element and boundary element methods for predicting structural vibration and radiated noise. In *Winter Annual Meeting of the ASME*, 1992.

[49] N. Vlahopoulos and N.H. Schiller. Energy finite element analysis developments for vibration analysis of composite aircraft structures. In *SAE 2011 Noise and Vibration Conference and Exhibition*, volume 4, 2011.

[50] E.A Patterson, I. Diamantakos, K. Dvurecenska, R.J. Greene, E. Hack, G. Lampeas, M. Lomnitz, and T. Siebert. Validation of a structural model of an aircraft cockpit panel: An industrial case study. *The Journal of Strain Analysis for Engineering Design*, 57(8):714–723, 2022.

[51] T. Kim and U. Lee. Vibration analysis of thin plate structures subjected to a moving force using frequency-domain spectral element method. *Shock and Vibration*, 2018:1–27, 2018.

[52] M. Richter, D. Chappell, N. Aimakov, and G. Tanner. Convergence of ray-density methods using transfer operators in different bases. *Forum Acusticum*, pages 231–237, 2020.

[53] T. Hartmann, S. Morita, G. Tanner, and D.J. Chappell. High-frequency structure-and air-borne sound transmission for a tractor model using dynamical energy analysis. *Wave Motion*, 87:132–150, 2019.

[54] S. Morita, T. Hartmann, and G. Tanner. Dynamical energy analysis modelling by using transfer path analysis. In *Proceedings of the ISMA 2018 International Conference on Noise and Vibration Engineering*, pages 229–241, 2018.

[55] F.J. Fahy. Statistical energy analysis: a critical overview. *Philosophical Transactions of the Royal Society of London. Series A: Physical and Engineering Sciences*, 346(1681):431–447, 1994.

[56] T. Hartmann, G. Tanner, G. Xie, D. Chappell, and J. Bajārs. Modelling of high-frequency structure-borne sound transmission on fem grids using the discrete flow mapping technique. *Journal of Physics Conference Series*, 744, 2016.

[57] J. Woodhouse. An introduction to statistical energy analysis of structural vibration. *Applied Acoustics*, 14(6):455–469, 1981.

[58] E. Hills, B.R. Mace, and N.S. Ferguson. Acoustic response variability in automotive vehicles. *Journal of Sound and Vibration*, 321(1):286–304, 2009.

[59] R.H. Lyon and G. Maidanik. Power flow between linearly coupled oscillators. *The journal of the Acoustical Society of America*, 34(5):623–639, 1962.

[60] P.W. Smith Jr. Response and radiation of structural modes excited by sound. *The Journal of the Acoustical Society of America*, 34(5):640–647, 1962.

[61] J.A. Steel. The prediction of structural vibration transmission through a motor vehicle using statistical energy analysis. *Journal of sound and vibration*, 193(3):691–703, 1996.

[62] S. Sohrabi, A. Segura Torres, E. Cierco Molins, A. Perazzolo, G. Bizzarro, and P.C. Rodríguez Sorribes. A comparative study of a hybrid experimental-statistical energy analysis model with advanced transfer path analysis for analyzing interior noise of a tiltrotor aircraft. *Applied Sciences*, 13(22):12128, 2023.

[63] G. Petrone, G. Melillo, A. Laudiero, and S. De Rosa. A statistical energy analysis (sea) model of a fuselage section for the prediction of the internal sound pressure level (spl) at cruise flight conditions. *Aerospace Science and Technology*, 88:340–349, 2019.

[64] Thibault Lafont, Francesca Ronzio, Théophane Courtois, and Davide Caprioli. Application of statistical energy analysis on a car: from the vehicle modeling to parts targeting. In *INTER-NOISE and NOISE-CON Congress and Conference Proceedings*, volume 253, pages 948–958. Institute of Noise Control Engineering, 2016.

[65] T. Koizumi, N. Tsujiuchi, H. Tanaka, M. Okubo, and M. Shinomiya. Prediction of the vibration in buildings using statistical energy analysis. In *Proceedings of the International Modal Analysis Conference (IMAC)*, pages 7–13, 2002.

[66] G. Tanner. Dynamical energy analysis—determining wave energy distributions in vibro-acoustical structures in the high-frequency regime. *Journal of Sound and Vibration*, 320(4):1023–1038, 2009.

[67] A. Le Bot and V. Cotoni. Validity diagrams of statistical energy analysis. *Journal of Sound and Vibration*, 329(2):221–235, 2010.

[68] T. Lafont, N. Totaro, and A. Le Bot. Review of statistical energy analysis hypotheses in vibroacoustics. *Proceedings of the Royal Society A: Mathematical, Physical and Engineering Science*, 470, 2014.

[69] D.J. Chappell, D. Löchel, N. Søndergaard, and G. Tanner. Dynamical energy analysis on mesh grids: A new tool for describing the vibro-acoustic response of complex mechanical structures. *Wave Motion*, 51(4):589–597, 2014.

[70] R.H. Lyon. *Theory and Application of Statistical Energy Analysis (Second Edition)*. Newnes, Boston, second edition edition, 1995.

[71] L. Maxit, M. Berton, C. Audoly, and D. Juvé. Discussion about different methods for introducing the turbulent boundary layer excitation in vibroacoustic models. *Flinovia-Flow Induced Noise and Vibration Issues and Aspects*, pages 249–278, 2015.

[72] K.S. Chae and J.G. Ih. Prediction of vibrational energy distribution in the thin plate at high-frequency bands by using the ray tracing method. *Journal of Sound and Vibration*, 240(2):263–292, 2001.

[73] F. Yan, R. Wilson, and P. Rutherford. Prediction of acoustic transmission in heavily damped system using hybrid ray-tracing-sea method. *Noise Control Engineering Journal*, 68:226–236, 2020.

[74] R.S. Langley and A.N. Bercin. Wave intensity analysis of high frequency vibrations. *Philosophical Transactions of the Royal Society of London. Series A: Physical and Engineering Sciences*, 346(1681):489–499, 1994.

[75] J.D. Palmer. *Vibrational energy flow in structures*. PhD thesis, University of Nottingham, 1994.

[76] X. Kong, H. Chen, D. Zhu, and W. Zhang. Study on the validity region of energy finite element analysis. *Journal of Sound and Vibration*, 333(9):2601–2616, 2014.

[77] R.S. Langley. On the vibrational conductivity approach to high frequency dynamics for two-dimensional structural components. *Journal of sound and vibration*, 182(4):637–657, 1995.

[78] O.M. Bouthier and R.J. Bernhard. Simple models of the energetics of transversely vibrating plates. *Journal of Sound and Vibration*, 182(1):149–164, 1995.

[79] P.E. Cho and R.J. Bernhard. Energy flow analysis of coupled beams. *Journal of Sound and Vibration*, 211(4):593–605, 1998.

[80] F. Han, R.J. Bernhard, and L.G. Mongeau. Prediction of flow-induced structural vibration and sound radiation using energy flow analysis. *Journal of Sound and Vibration*, 227(4):685–709, 1999.

[81] W.S. Choi, S.Y. Hong, H.W. Kwon, J.H. Seo, S. Rhee, and J.H. Song. Estimation of turbulent boundary layer induced noise using energy flow analysis for ship hull designs. *Proceedings of the Institution of Mechanical*

Engineers, Part M: Journal of Engineering for the Maritime Environment, 234:196–208, 2020.

[82] Y.H. Park and S.Y. Hong. Vibrational energy flow analysis of corrected flexural waves in timoshenko beam-part i: Theory of an energetic model. *Shock and Vibration*, 13(3):137–165, 2000.

[83] Miaoxia Xie, Feilong Yao, Ling Li, and Yueming Li. Research status and development trend of energy finite element analysis: a review. *Journal of Vibroengineering*, 25(2):247–268, 2023.

[84] A.S. Glassner, editor. *An introduction to ray tracing*. Academic Press Ltd., 1989.

[85] A. Krokstad, S. Strom, and S. Sørsdal. Calculating the acoustical room response by the use of a ray tracing technique. *Journal of Sound and Vibration*, 8(1):118–125, 1968.

[86] A. Appel. Some techniques for shading machine renderings of solids. In *Proceedings of the April 30-May 2, 1968, spring joint computer conference*, pages 37–45, 1968.

[87] B. Chouvion, A.A. Popov, S. Mcwilliam, and C.H.J. Fox. Vibration modelling of complex waveguide structures. *Computers & structures*, 89(11-12):1253–1263, 2011.

[88] V. Cervenỳ. *Seismic ray theory*, volume 110. Cambridge university press, 2001.

[89] D. Chappell, G. Tanner, D. Löchel, and N. Søndergaard. Discrete flow mapping: Transport of phase space densities on triangulated surfaces. *Royal Society of London Proceedings Series A*, 469, 2013.

[90] N. Aimakov. *Elastic wave energy scattering and propagation in composite structures*. PhD thesis, University of Nottingham, 2021.

[91] J.N. Reddy. *Theory and Analysis of Elastic Plates and Shells, Second Edition*. Taylor and Francis Group, 2006.

[92] R.C. HIBBELER. *Structural Analysis: 8th Edition*. Independently Published, 2020.

[93] N.M. Mohammed. *Vibroacoustics of complex structures-a wave chaos approach*. PhD thesis, University of Nottingham, 2021.

[94] D.J. Chappell and G. Tanner. Solving the stationary liouville equation via a boundary element method. *Journal of Computational Physics*, 234:487–498, 2013.

[95] M.J.A. Smith. *Wave propagation through periodic structures in thin plates*. PhD thesis, University of Auckland, 2013.

[96] C.M. Linton and P. McIver. *Handbook of mathematical techniques for wave/structure interactions*. Chapman and Hall/CRC, 2001.

[97] A. Sommerfeld. *Partial differential equations in physics*. Academic press, 1949.

[98] M. Abramowitz and I.A. Stegun. *Handbook of mathematical functions with formulas, graphs, and mathematical tables*, volume 55. US Government printing office, 1948.

[99] University of Waterloo. Bessel functions of the first and second kind. Available at `http://www.mhtlab.uwaterloo.ca/courses/me755/web_chap4.pdf`. Accessed [30.05.24].

[100] G. Tanner and N. Søndergaard. Wave chaos in acoustics and elasticity. *Journal of Physics A: Mathematical and Theoretical*, 40:R443, 2007.

[101] G. Gradoni, L.R. Arnaut, S.C. Creagh, G. Tanner, M.H. Baharuddin, C. Smartt, and D.W.P. Thomas. Wigner-function-based propagation of stochastic field emissions from planar electromagnetic sources. *IEEE Transactions on Electromagnetic Compatibility*, 60(3):580–588, 2017.

[102] D.M. Ramapriya, G. Gradoni, S.C. Creagh, E. Tanner, G.and Moers, and I.L. Arteaga. Nearfield acoustical holography-a wigner function approach. *Journal of Sound and Vibration*, 486:115593, 2020.

[103] R.G. Littlejohn and R. Winston. Corrections to classical radiometry. *JOSA A*, 10(9):2024–2037, 1993.

[104] E. Wigner. On the quantum correction for thermodynamic equilibrium. *Physical review*, 40(5):749, 1932.

[105] M.J. Bastiaans. Application of the wigner distribution function in optics. In W. Mecklenbräuker and F. Hlawatsch, editors, *The Wigner Distribution-Theory and Applications in Signal Processing*, pages 375–426. Elsevier, 1997.

[106] S. Creagh, G. Gradoni, T. Hartmann, and G. Tanner. Propagating wave correlations in complex systems. *Journal of Physics A: Mathematical and Theoretical*, 50:045101, 2016.

[107] G. Gradoni, S.C. Creagh, G. Tanner, C. Smartt, and D.W.P. Thomas. A phase-space approach for propagating field-field correlation functions. *New Journal of Physics*, 17(9):093027, 2015.

[108] H.J. Korsch and M.V. Berry. Evolution of wigner's phase-space density under a nonintegrable quantum map. *Physica D: Nonlinear Phenomena*, 3(3):627–636, 1981.

[109] R.S. Langley and K.H. Heron. Elastic wave transmission through plate/beam junctions. *Journal of Sound and Vibration*, 143(2):241–253, 1990.

[110] D.J. Chappell, G. Tanner, and S. Giani. Boundary element dynamical energy analysis: A versatile method for solving two or three dimensional wave problems in the high frequency limit. *Journal of Computational Physics*, 231(18):6181–6191, 2012.

[111] H. Schlichting and J. Kestin. *Boundary layer theory*, volume 121. Springer, 1961.

[112] K.P. Burr, T.R. Akylas, and C.C. Mei. School-wide program on fluid mechanics: Chapter two: two-dimensional laminar boundary layers, 2014. Available at: `https://web.mit.edu/fluids-modules/www/highspeed_flows/ver2/bl_Chap2/index.html`.

[113] B. Lautrup. *Physics of continuous matter: exotic and everyday phenomena in the macroscopic world*. CRC press, 2011.

[114] F.H. Abernathy. Film notes for fundamentals of boundary layers. *National Committee for Fluid Mechanics Film, Encyclopedia Britannica Educational Corporation*, 425, 1970.

[115] T. Benson. Boundary layer, 2021. Available at `https://www.grc.nasa.gov/www/k-12/BGP/boundlay.html`.

[116] K. Rued. Transitional boundary layers under the influence of high free stream turbulence, intensive wall cooling and high pressure gradients in hot gas circulation. Technical report, NASA, 1987.

[117] M. Alaoui. *Coherent structures and wall-pressure fluctuations modeling in turbulent boundary layers subjected to pressure gradients*. PhD thesis, Paris, ENSAM, 2016.

[118] K. Boldt. Aerodynamic measurements: Boundary layer components, 2022. Available at `https://www.grasacoustics.com/blog/aerodynamic-measurements-components-of-the-boundary-layer`. Accessed [21.05.24].

[119] Anna Caiazzo. *Modeling of turbulent boundary layer-induced noise and vibration: use of a Generalized Corcos model*. PhD thesis, KU Leuven, 2018.

[120] C. Guillon, L. Maxit, and E. Redon. Modelling vibrating panels excited by a non-homogeneous turbulent boundary layer. *Journal of Fluids and Structures*, 106:103378, 2021.

[121] A. Caiazzo, R. D'Amico, and W. Desmet. A generalized corcos model for modelling turbulent boundary layer wall pressure fluctuations. *Journal of Sound and Vibration*, 372:192–210, 2016.

[122] Y.F. Hwang, W.K. Bonness, and S.A. Hambric. On modeling structural excitations by low speed turbulent boundary layer flows. *Rapport technique, Applied Research Laboratory-Pennstate University*, 2003.

[123] GM Corcos. The structure of the turbulent pressure field in boundary-layer flows. *Journal of Fluid Mechanics*, 18(3):353–378, 1964.

[124] Y.F. Hwang, W.K. Bonness, and S.A Hambric. Comparison of semi-empirical models for turbulent boundary layer wall pressure spectra. *Journal of Sound and Vibration*, 319(1-2):199–217, 2009.

[125] T.S. Miller. *TURBULENT BOUNDARY LAYER MODELS FOR ACOUSTIC ANALYSIS*. PhD thesis, Wichita State University, 2011.

[126] W.K. Blake. *Mechanics of flow-induced sound and vibration, Volume 2: Complex flow-structure interactions*. Academic press, 2017.

[127] T.S. Miller, J.M. Gallman, and M.J. Moeller. Review of turbulent boundary layer models for acoustic analysis. *Journal of aircraft*, 49(6):1739–1754, 2012.

[128] A.O. Borisyuk and V.T. Grinchenko. Vibration and noise generation by elastic elements excited by a turbulent flow. *Journal of Sound and Vibration*, 204(2):213–237, 1997.

[129] W.K. Bonness, D.E. Capone, and S.A. Hambric. Low-wavenumber turbulent boundary layer wall-pressure measurements from vibration data on a cylinder in pipe flow. *Journal of Sound and Vibration*, 329(20):4166–4180, 2010.

[130] A.P. Dowling. Underwater flow noise. *Theoretical and Computational Fluid Dynamics*, 10(1):135–153, 1998.

[131] S. De Rosa, F. Franco, and D. Gaudino. Low frequency range response of a plate to different turbulent boundary layer excitation models. *Proceedings of ISMA 2010*, pages 625–638, 2010.

[132] A.V. Smol'Yakov, V.M. Tkachenko, and J.S. Wood. Model of a field of pseudosonic turbulent wall pressures and experimental data. *Soviet physics. Acoustics*, 37(6):627–631, 1991.

[133] R.H. Mellen. On modelling convective turbulence. *The journal of the Acoustical Society of America*, 88(6):2891–2893, 1990.

[134] D.M. Chase. Modelling the wavevector-frequency spectrum of turbulent boundary layer wall pressure. *Journal of sound and Vibration*, 70(1):29–67, 1980.

[135] S. Finnveden, F. Birgersson, U. Ross, and T. Kremer. A model of wall pressure correlation for prediction of turbulence-induced vibration. *Journal of Fluids and Structures*, 20(8):1127–1143, 2005.

[136] M.A. Josserand. *WAVEVECTOR-FREQUENCY SPECTRUM OF TRANSITION ZONE WALL PRESSURE FLUCTUATIONS (FLOW NOISE)*. The Pennsylvania State University, 1986.

[137] P. Tipler and G. Mosca. *Physics for Scientists and Engineers. 6th Edition*. W.H. Freeman and Company, 2008.

[138] T.B. Airimitoaie and I.D. Landau. Attenuation of vibrational interference—robust and adaptive approaches. In *2016 European Control Conference (ECC)*, pages 794–799, 2016.

[139] Anthony Gerig. *Introduction to Wave Physics*. Independently published, 03 2021.

[140] Inc Ducksters, Technological Solutions. Physics for kids: Wave behavior. Available at `www.ducksters.com/science/physics/wave_behavior.php`. Accessed [24.05.24].

[141] J. Sanny, S.J. Ling, and W. Moebs. *University Physics Volume 3*. Samurai Media Limited, 09 2016.

[142] S.J. Elliott. A review of active noise and vibration control in road vehicles, 2008.

[143] R. Alkhatib and M.F. Golnaraghi. Active structural vibration control: a review. *Shock and Vibration Digest*, 35(5):367, 2003.

[144] D. Miljković. Review of active vibration control. *32nd Information and Communication Technology, Electronics and Microelectronics*, pages 103–108, 2009.

[145] P. Konstanzer, B. Enenkl, P. Aubourg, and P. Cranga. Recent advances in eurocopter's passive and active vibration control. In *Annual Forum Proceedings-American Helicopter Society*, volume 64, pages 854–871. AMERICAN HELICOPTER SOCIETY, INC, 2008.

[146] A. Awada, R. Younes, and A. Ilinca. Review of vibration control methods for wind turbines. *Energies*, 14(11):3058, 2021.

[147] D. Xie, S. Yan, L. Zhu, H. Zhang, and X. Zhang. Review on vibration isolation method for atomic interference gravimeter. In *Journal of Physics: Conference Series*, volume 2125, page 012022, 2021.

[148] S.M. Kuo and D.R. Morgan. Active noise control: a tutorial review. *Proceedings of the IEEE*, 87(6):943–973, 1999.

[149] L.G. Morales. *Adaptive Filtering: Theories and Applications*. IntechOpen, 2013.

[150] H.M. Lee, Y. Hua, Z. Wang, K.M. Lim, and H.P. Lee. A review of the application of active noise control technologies on windows: Challenges and limitations. *Applied Acoustics*, 174:107753, 2021.

[151] R. Serizel, M. Moonen, J. Wouters, and S. H. Jensen. A zone of quiet based approach to integrated active noise control and noise reduction in hearing aids. In *2009 IEEE Workshop on Applications of Signal Processing to Audio and Acoustics*, pages 229–232. IEEE, 2009.

[152] J. Chambers, D. Bullock, Y. Kahana, A. Kots, and . Palmer. Developments in active noise control sound systems for magnetic resonance imaging. *Applied Acoustics*, 68(3):281–295, 2007.

[153] S.M. Kuo, S. Mitra, and W.S. Gan. Active noise control system for headphone applications. *IEEE Transactions on Control Systems Technology*, 14(2):331–335, 2006.

[154] R. Ahmad, T. Kundu, and D. Placko. Modelling of phased array transducers. *The Journal of the Acoustical Society of America*, 117(4):1762–1776, 2005.

[155] S.J. Song, H.J. Shin, and Y.H. Jang. Development of an ultra sonic phased array system for nondestructive tests of nuclear power plant components. *Nuclear engineering and design*, 214(1-2):151–161, 2002.

[156] V. Giurgiutiu. In-situ phased arrays with piezoelectric wafer active sensors. *Structural health monitoring with piezoelectric wafer active sensors*, pages 503–588, 2014.

[157] P. Kollias, R. Palmer, D. Bodine, T. Adachi, H. Bluestein, J.Y.N. Cho, C. Griffin, J. Houser, P.E. Kirstetter, and M.R. Kumjian. Science applications of phased array radars. *Bulletin of the American Meteorological Society*, 103(10):E2370–E2390, 2022.

[158] K. Yamagata, S. Tanaka, and K. Shogen. Broadcasting satellite system using onboard phased array antenna in 21-ghz band. In *2007 IEEE International Vacuum Electronics Conference*, pages 1–2, 2007.

[159] M.Q. Alolyania and K.M. Harb. Phased array antennas for satellite communications. In *2021 IEEE 12th Control and System Graduate Research Colloquium (ICSGRC)*, pages 150–153, 2021.

[160] R.E. Wallis and S. Cheng. Phased-array antenna system for the messenger deep space mission. In *2001 IEEE Aerospace Conference Proceedings (Cat. No. 01TH8542)*, volume 1, pages 41 – 49, 2001.

[161] O. Lorton, P.C. Guillemin, Y. M'Rad, A. Peloso, S. Boudabbous, C. Charbonnier, R. Holman, L.A. Crowe, L. Gui, and P.A. Poletti. A novel concept of a phased-array hifu transducer optimized for mr-guided hepatic ablation: embodiment and first in-vivo studies. *Frontiers in Oncology*, 12:899440, 2022.

[162] S. Rahimi, R.M. Jones, and K. Hynynen. A high-frequency phased array system for transcranial ultrasound delivery in small animals. *IEEE transactions on ultrasonics, ferroelectrics, and frequency control*, 68(1):127–135, 2020.

[163] K. Hynynen and R.M. Jones. Image-guided ultrasound phased arrays are a disruptive technology for non-invasive therapy. *Physics in Medicine & Biology*, 61(17):R206–48, 2016.

[164] S. Chatillon, G. Cattiaux, M. Serre, and O. Roy. Ultrasonic non-destructive testing of pieces of complex geometry with a flexible phased array transducer. *Ultrasonics*, 38(1-8):131–134, 2000.

[165] M.M. Woolfson and M.S. Woolfson. *Mathematics for Physics*. Oxford University Press, 2007.

[166] N. Schlömer. quadpy 0.17.19. Available at: `https://pypi.org/project/quadpy/` Accessed [30.05.24].

[167] C.M. Hogan and G.F. Magrave. Ray-tracing and eikonal solutions for low-frequency wavefields. *CREWES Research Report*, 19, 2007.

[168] L. Liu and K. Bhattacharya. Wave propagation in a sandwich structure. *International Journal of Solids and Structures*, 46(17):3290–3300, 2009.

[169] N. Bejjani, P. Margerit, K. Sab, J. Bodgi, and A. Lebee. The bending-gradient theory for flexural wave propagation in composite plates. *International Journal of Solids and Structures*, 191-192:99–109, 2020.

[170] AZO Materials. Aluminium / aluminum 6061 alloy (uns a96061). Available at: `https://www.azom.com/article.aspx?ArticleID=6636` Accessed [05.06.2024].

[171] R. Piessens and A.D. Poularikas. The hankel transform. *The transforms and applications handbook*, 2(9), 2000.

[172] T.M. Farabee and M.J. Casarella. Spectral features of wall pressure fluctuations beneath turbulent boundary layers. *Physics of Fluids A: Fluid Dynamics*, 3(10):2410–2420, 1991.

[173] É. Salze, C. Bailly, O. Marsden, E. Jondeau, and D. Juvé. An experimental characterisation of wall pressure wavevector-frequency spectra in the presence of pressure gradients. In *20th AIAA/CEAS Aeroacoustics Conference*, page 2909, 2014.

[174] Q. Leclere, A. Dinsenmeyer, E. Salze, and J. Antoni. A comparison between different wall pressure measurement devices for the separation and analysis of tbl and acoustic contributions. In *International Conference on Flow Induced Noise and Vibration Issues and Aspects*, pages 181–206, 2019.

[175] A.A. PINAR. *Aero and vibroacoustical prediction of the noise generated by turbulent boundary layers*. PhD thesis, KTH Royal Institute of Technology, 2019.

[176] S.P. Gravante, A.M. Naguib, C.E. Wark, and H.M. Nagib. Characterization of the pressure fluctuations under a fully developed turbulent boundary layer. *AIAA Journal*, 36(10):1808–1816, 1998.

[177] B. Gibeau and S. Ghaemi. Low- and mid-frequency wall-pressure sources in a turbulent boundary layer. *Journal of Fluid Mechanics*, 918, 2021.

[178] C. Marchetto, L. Maxit, O. Robin, and A. Berry. Predicting the vibration response of panels under a turbulent boundary layer excitation from their measured sensitivity functions. *NOVEM*, 2018.

[179] R.B. Shirts, S.R. Burt, and A.M. Johnson. Periodic boundary condition induced breakdown of the equipartition principle and other kinetic effects of finite sample size in classical hard-sphere molecular dynamics simulation. *The Journal of chemical physics*, 125(16), 2006.

[180] M. Cerrolaza, S. Shefelbine, and D. Garzón-Alvarado. *Numerical methods and advanced simulation in biomechanics and biological processes*. Academic Press, 2017.

[181] O. Sensoy, J.G. Almeida, J. Shabbir, I.S. Moreira, and G. Morra. Computational studies of g protein-coupled receptor complexes: Structure and dynamics. In *Methods in Cell Biology*, volume 142, pages 205–245, 2017.

[182] M.K. Bull. Wall-pressure fluctuations associated with subsonic turbulent boundary layer flow. *Journal of Fluid Mechanics*, 28(4):719–754, 1967.

[183] M. Goody. Empirical spectral model of surface pressure fluctuations. *AIAA journal*, 42(9):1788–1794, 2004.

[184] T.V. Kármán. Über laminare und turbulente reibung. *ZAMM-Journal of Applied Mathematics and Mechanics/Zeitschrift für Angewandte Mathematik und Mechanik*, 1(4):233–252, 1921.

[185] Heinrich Blasius. *Grenzschichten in Flüssigkeiten mit kleiner Reibung*. Druck von BG Teubner, 1907.

[186] B. Arguillat, D. Ricot, C. Bailly, and G. Robert. Measured wavenumber: Frequency spectrum associated with acoustic and aerodynamic wall pressure fluctuations. *The Journal of the Acoustical Society of America*, 128(4):1647–1655, 2010.

[187] P. Druault, A. Hekmati, and D. Ricot. Discrimination of acoustic and turbulent components from aeroacoustic wall pressure field. *Journal of Sound and Vibration*, 332(26):7257–7278, 2013.

[188] J.D. Chazot, O. Robin, J.L. Guyader, and N. Atalla. Diffuse acoustic field produced in reverberant rooms: A boundary diffuse field index. *Acta Acustica United With Acustica*, 102(3):503–516, 2016.

[189] A. Patterson, A. Gahlawat, and N. Hovakimyan. Propeller phase synchronization for small distributed electric vehicles. In *AIAA Scitech 2019 Forum*, page 1458, 2019.

[190] S. Guan, Y. Lu, T. Su, and X. Xu. Noise attenuation of quadrotor using phase synchronization method. *Aerospace Science and Technology*, 118:107018, 2021.

[191] B. Turhan, H.K. Jawahar, A. Gautam, S. Syed, G. Vakil, D. Rezgui, and M. Azarpeyvand. Acoustic characteristics of phase-synchronized adjacent propellers. *The Journal of the Acoustical Society of America*, 155(5):3242–3253, 2024.

[192] S. Johansson. *Active control of propeller-induced noise in aircraft: algorithms & methods*. PhD thesis, Blekinge Institute of Technology, 2000.

[193] X. Huang, L. Sheng, and Y. Wang. Propeller synchrophase angle optimization of turboprop-driven aircraft—an experimental investigation. *Journal of Engineering for Gas Turbines and Power*, 136(11):112606, 2014.

[194] G.C. Goodman, F.G. Pla, and S.B. Reddy. Phase locked loop control of turboprop aircraft engines for cancellation of interior or exterior noise. In *Proceedings of International Conference on Control Applications*, pages 1104–1107. IEEE, 1995.

[195] K.A. Pascioni, S.A. Rizzi, and N. Schiller. Noise reduction potential of phase control for distributed propulsion vehicles. In *AIAA Scitech 2019 Forum*, page 1069, 2019.

[196] O. Hertzman, S. Fligelman, and O. Stalnov. Abatement of a multi-rotor tonal noise component with phase control technology. In *28th AIAA/CEAS Aeroacoustics 2022 Conference*, page 2834, 2022.

[197] A. Patterson, N.H. Schiller, K.A. Ackerman, A. Gahlawat, I.M. Gregory, and N. Hovakimyan. Controller design for propeller phase synchronization with aeroacoustic performance metrics. In *AIAA Scitech 2020 Forum*, page 1494, 2020.

[198] L.E. Ballentine. *Quantum mechanics: a modern development: 2nd edition.* World Scientific Publishing Company, 2014.

[199] E. Colomés, Z. Zhan, and X. Oriols. Comparing wigner, husimi and bohmian distributions: which one is a true probability distribution in phase space? *Journal of Computational Electronics*, 14:894–906, 2015.

[200] W.B. Case. Wigner functions and weyl transforms for pedestrians. *American Journal of Physics*, 76(10):937–946, 2008.

[201] H.W. Lee. Theory and application of the quantum phase-space distribution functions. *Physics Reports*, 259(3):147–211, 1995.

[202] NASA. X-57 maxwell lithograph, 2018. Available at `https://www.nasa.gov/wp-content/uploads/2018/07/x-57-litho-print-v4.pdf?emrc=4275f8`. Accessed [18.07.24].

[203] Wenjuan Gong, Bin Zhang, Chaoqi Wang, Hanbing Yue, Chuantao Li, Linjie Xing, Yu Qiao, Weishan Zhang, and Faming Gong. A literature review: Geometric methods and their applications in human-related analysis. *Sensors*, 19(12), 2019.

Appendix A

Response of a flat plate to a correlated pressure field - Mellen model results

In subsection 3.4.3, it was demonstrated that the vibrational response of plates under small-patch TBL pressure fields modelled by the Corcos and Mellen models are almost identical. As a result, only the Corcos model was applied when computing the response of plates to the full TBL pressure field in Section 3.5. In this appendix this analysis is repeated to consider the vibrational energy distribution across plates excited by TBL pressure fields modelled using the Mellen model. As in the Corcos model case, the vibrational response of the plate will be considered for (i) absorbing boundary conditions (subsection A.1) (ii) reflecting boundary conditions (subsection A.2) (iii) periodic boundary conditions (subsection A.3). For this analysis, the system configurations applied are the same as

those described in subsection 3.6.1.

A.1 Absorbing boundary conditions

The vibrational response of the plate with absorbing boundary conditions to a TBL pressure field of various flow speeds represented by the Mellen model is shown in Figure 57.

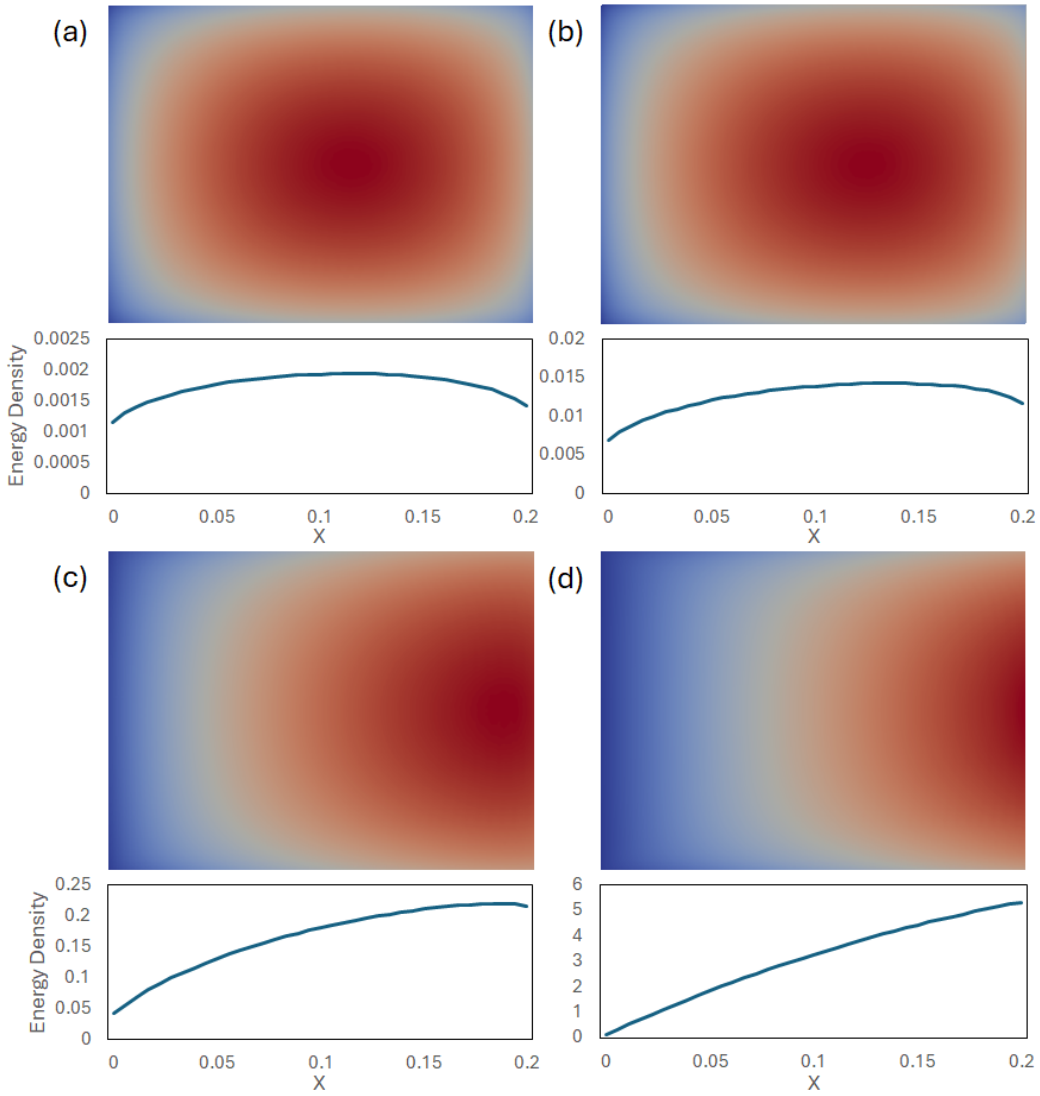

Figure 57: Vibrational response of a flat plate with absorbing boundary conditions and damping coefficient $\mu = 0.01$ under TBL pressure fields represented by the Mellen model with free-stream flow speeds (a) $19\,ms^{-1}$ (b) $50\,ms^{-1}$ (c) $150\,ms^{-1}$ (d) $300\,ms^{-1}$.

As expected, this plot demonstrates rather similar results to the Corcos model case, demonstrated in Figure 23. At $U_0 = 19\,ms^{-1}$, the near-isotropy of the Mellen CSD ensures that the peak in the energy density is again found close to the centre of the plate. This peak is however found slightly further downstream here compared to the Corcos model case. This is due to the slightly higher preference for the generation of rays which propagate in the flow direction for the Mellen model compared to the Corcos model, as discussed in subsection 3.4.2. This result is mirrored for the higher speed cases, with the Mellen model demonstrating the downstream shift in the energy density peak for increasing flow speed. In addition, in each case this peak is once again marginally further downstream than in the equivalent Corcos model case. At $U_0 = 300\,ms^{-1}$, the peak for both the Corcos and Mellen models is found at the trailing edge. In this case, the peak is marginally narrower for the Mellen model, again showing the increased preference for the propagation of energy in the mean flow direction when applying the Mellen model. As in the Corcos model case, this study can be repeated with various μ values to identify the effect of the damping on the vibrational behaviour of the plate under the Mellen TBL pressure field can be observed. This result is demonstrated in Figure 58.

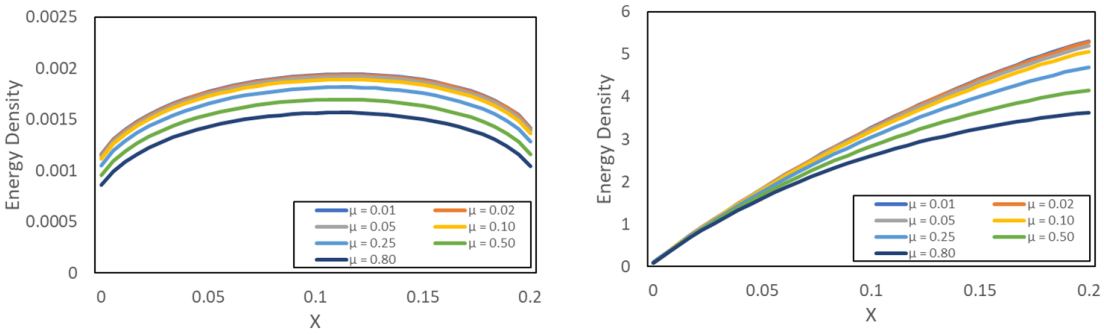

Figure 58: Energy density distribution in the $+\hat{\boldsymbol{x}}$ direction for flow speeds $U_0 = 50\,ms^{-1}$ (left) and $U_0 = 300\,ms^{-1}$ (right) when applying the Mellen model with absorbing boundary conditions.

As in the Corcos model case, changes in the damping coefficient have little effect

to the overall energy density distribution across the plate in the lower speed case, only influencing the magnitude of the energy density at each location. In the higher speed case, the effect of increasing the damping on the distribution of vibrational energy is again analogous to the Corcos model case. Here, the energy density is approximately constant for all μ at the leading edge, with an increasing "tailing off" of the energy density closer to the trailing edge for increasing μ values. As demonstrated by equations 3.13, 3.33, and 3.10, the damping of the plate has no influence on the energy density put into the plate by the TBL pressure field, and only impacts the magnitude of the initial boundary density at each location on Γ_{src}. It is thus unsurprising that changes to this value effect the response of the plate to each pressure field in the same manner, particularly when considering the similarity of the two models. One difference can be observed in the higher speed case however, as in Figure 24, the influence of the damping at the trailing edge causes the peak in the energy density to shift slightly upstream. In the Mellen model case, displayed in Figure 58, the slightly greater preference for the generation of rays which propagate in the flow direction ensures that the energy density peak remains at the trailing edge in this case. The full energy density distribution of the plate in the highest damping case, $\mu = 0.80$, for the Mellen model with different flow speeds is demonstrated by Figure 59.

As in the Corcos model case, the increased damping leads to a broadening of the energy density peak, along with a marginal upstream shift for all flow speeds besides $U_0 = 300\,ms^{-1}$.

A.2 Reflecting boundary conditions

The vibrational response of the plate with absorbing boundary conditions to a TBL pressure field of various flow speeds represented by the Mellen model is shown in Figure 60.

As in the Corcos model case, the preference for the generation of rays which

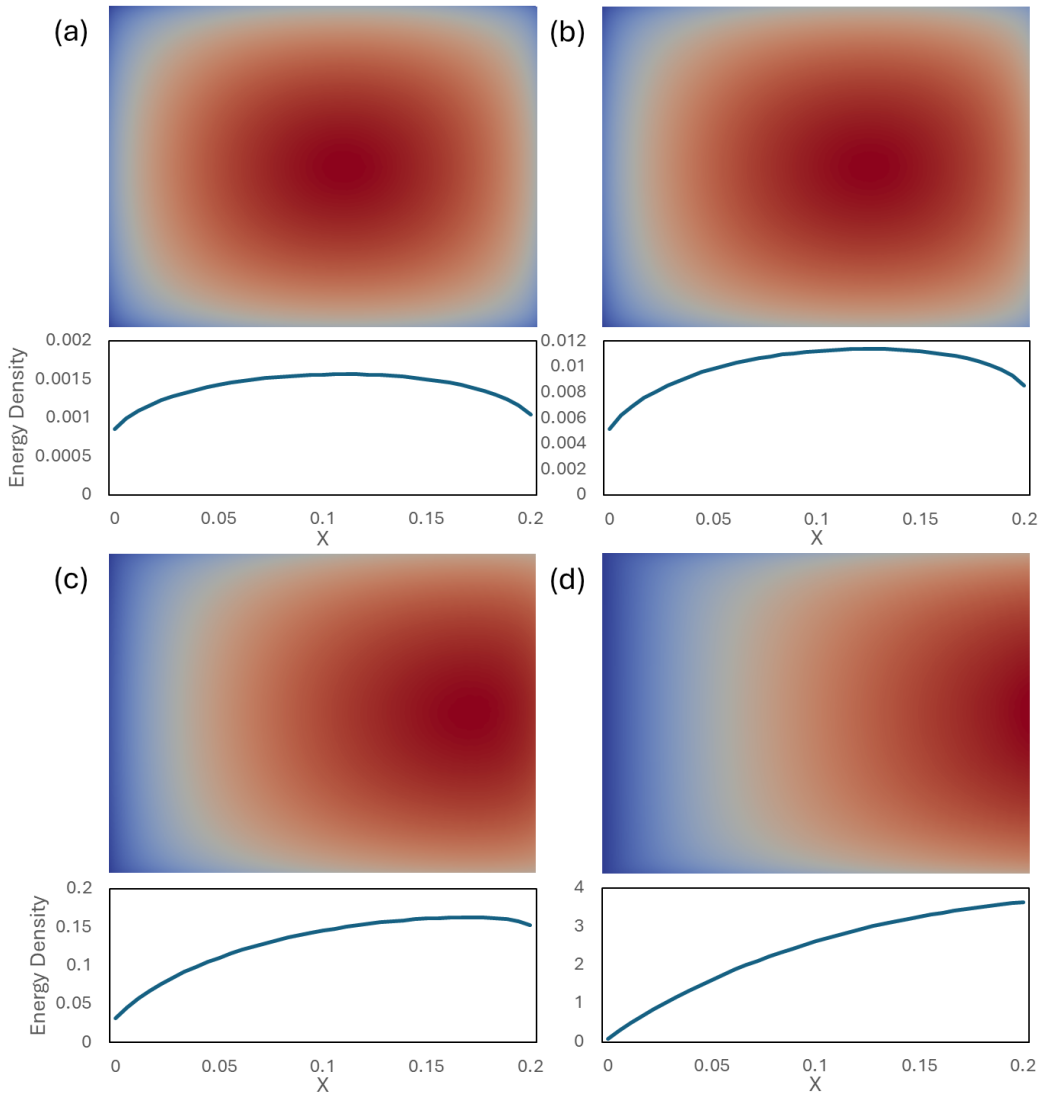

Figure 59: Vibrational response of a flat plate with absorbing boundary conditions and damping coefficient $\mu = 0.80$ under TBL pressure fields represented by the Mellen model with free-stream flow speeds (a) $19\,ms^{-1}$ (b) $50\,ms^{-1}$ (c) $150\,ms^{-1}$ (d) $300\,ms^{-1}$.

propagate in the mean stream flow direction ensures that the energy density increases linearly with increasing separation from the leading edge. Figure 61 then demonstrates the influence of the damping coefficient on the distribution of energy density across the plate.

As expected, the application of reflecting boundary conditions across the plate ensures that the damping coefficient has a large impact on the observed vibrational

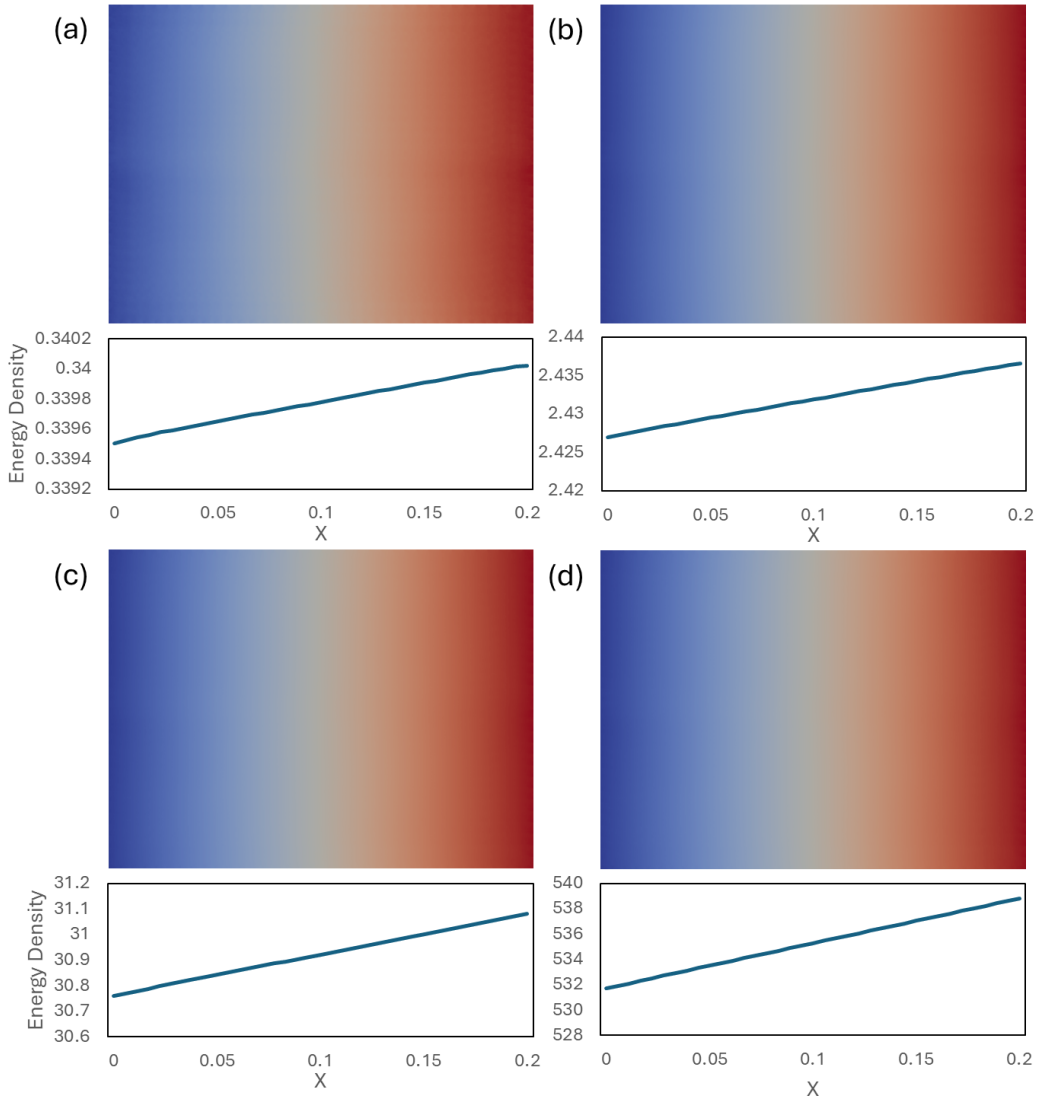

Figure 60: Vibrational response of a flat plate with reflecting boundary conditions and damping coefficient $\mu = 0.01$ under TBL pressure fields represented by the Mellen model with free-stream flow speeds (a) $19\,ms^{-1}$ (b) $50\,ms^{-1}$ (c) $150\,ms^{-1}$ (d) $300\,ms^{-1}$.

energy distribution. As in the Corcos model case, the difference in the energy density seems minimal compared to the magnitudes themselves, particularly for the lower damped cases, meaning that each line appears approximately flat for all damping coefficients. A clearer understanding of these energy distributions can be found by plotting the absolute and relative energy difference across the plate in each case. These results are displayed in Figure 62.

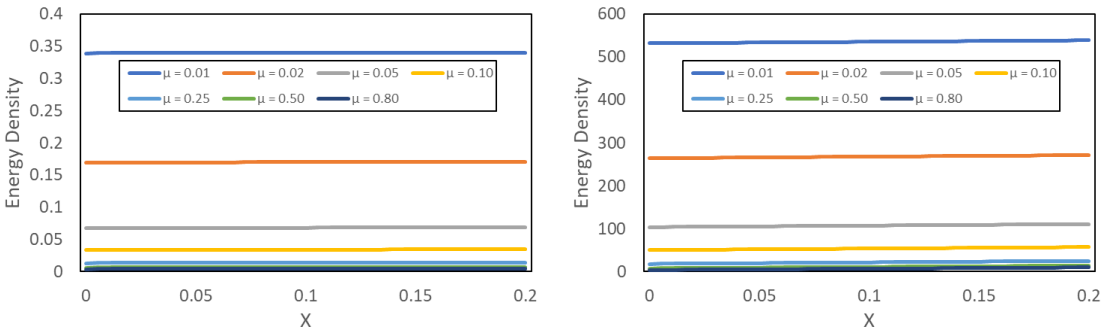

Figure 61: Energy density distribution in the $+\hat{\boldsymbol{x}}$ direction for flow speeds $U_0 = 50\,ms^{-1}$ (left) and $U_0 = 300\,ms^{-1}$ (right) when applying the Mellen model with reflecting boundary conditions.

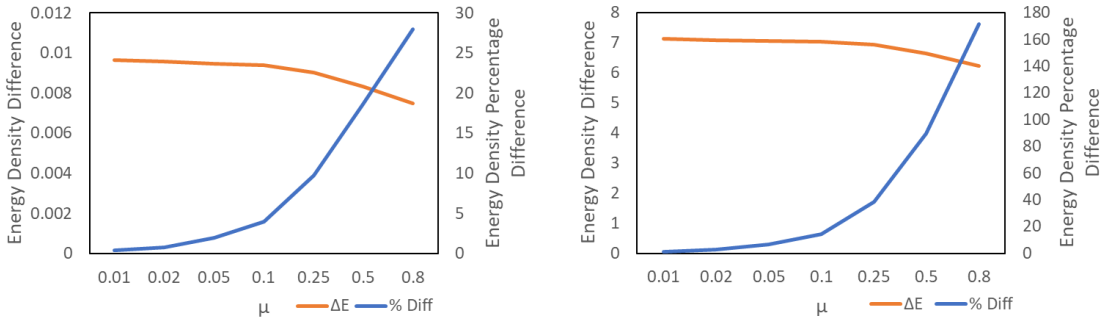

Figure 62: Absolute and relative energy difference in the energy between the leading and trailing edge of the plate for different μ values and flow speeds $U_0 = 50\,ms^{-1}$ (left) and $U_0 = 300\,ms^{-1}$ (right) with reflecting boundary conditions.

As in the Corcos model case, the energy difference across the plate is consistent in each case across most damping values, only beginning to fall in the highest damped cases. This is especially true in the higher speed case, with the energy difference found to be almost identical for $\mu \leq 0.25$ and falling only slightly after this point. This result is almost identical to that observed in Figure 29 for the Corcos model. In subsection 3.6.3, it was suggested that the reason for this is that the observed difference in the energy density across the plate is caused mainly by the initial propagation of the rays across the plate. The linear increase in the energy density downstream of the leading edge was then hypothesised to originate from the preference of the Corcos model to generate rays which propagate in the

mean-stream flow direction for all flow speeds. The results presented in this section then demonstrate that this result is also found when modelling the TBL pressure field using the Mellen model. By comparing the initial ray densities produced at each location by the Corcos and Mellen models for different flow speeds, as shown in Figures 17 and 18, one finds that in the flow direction the consistent detail across all of the plots is the preference for the generation of rays which propagate in the mean-stream flow direction. The fact that this linear energy distribution is observed for both models at all flow speeds, it is thus highly likely that this is the cause of the observed behaviour in this direction. Further evidence for this can be found by comparing the behaviour in the flow axis to that in the cross-flow direction. As shown by Figures 27 and 60, the energy density is constant in the cross-flow direction for both models across all flow speeds. By again considering the ray densities generated by both models from Figures 17 and 18, one finds that these distributions are also parallel across the $x-$axis for all flow speeds. Thus, the different properties of the initial ray density distribution in each direction correlate perfectly to the different energy distributions observed in each axis, regardless of the choice of model or flow conditions. It is thus highly likely that these results are a consequence of the initial ray density generated within the plate. As the difference in the energy density across the plate is constant for a wide range of damping values, it is then most likely that these effects are caused by the initial propagation of rays across the plate, which as shown by Figure 25 is effected minimally by the choice of damping coefficient.

In Figure 29, it was also demonstrated that the consistency of this energy difference for different damping coefficients, combined with the large influence of the damping coefficient on the overall vibrational energy density across the plate, generated a highly variable vibrational response across the plate in highly damped cases. For the Mellen model, this result is even more severe. For the $U_0 = 50\,ms^{-1}$ case, the energy difference across the plate is around 0.4% for $\mu = 0.01$, whilst

for the $\mu = 0.80$ case this difference is $\approx 28\%$. This is especially true for the $U_0 = 300\,ms^{-1}$ case, with the energy difference found to be $\approx 1.35\,\%$ in the $\mu = 0.01$ case, and $\approx 170\,\%$ in the $U_0 = 300\,ms^{-1}$ case. In each of these cases, the variance in the energy density across the plate is greater than in the Corcos model case. This result is unsurprising, given the increased preference in the initial ray density of the Mellen model for rays which propagate in the mean-stream flow direction compared to the Corcos model. Given that both models predict a large variation in the vibrational energy distribution across the plate it is likely that this result could also appear in experimental studies. By comparing the difference in the vibrational energy across the plate experimentally to the results generated by each model, one could then determine which of the Corcos or Mellen models provides a more accurate representation of the TBL pressure field.

A.3 Periodic boundary conditions

The vibrational response of the plate with periodic boundary conditions to a TBL pressure field represented by the Mellen model is shown in Figure 63.

The vibrational energy distributions under periodic boundary conditions for the Mellen model displayed here are again rather similar to the Corcos model results, shown in Figure 30. Much like the Corcos model, the parallel nature of the Mellen model in the cross-flow direction ensures that the energy density is constant in this direction. In the flow axis, the energy density distribution is also similar to the Corcos model result. At low speeds, the Mellen model produces a wide peak in the energy density close to the centre of the plate, which shifts increasingly downstream for increasing flow speeds. By comparing this result with Figure 57, one see the impact of the periodic boundary on the flow-parallel edges on the energy density distribution in this direction. As with the Corcos model case, this causes an increase in the contributions from rays which propagate in the cross-flow direction close to the centre of the plate. This increases the energy

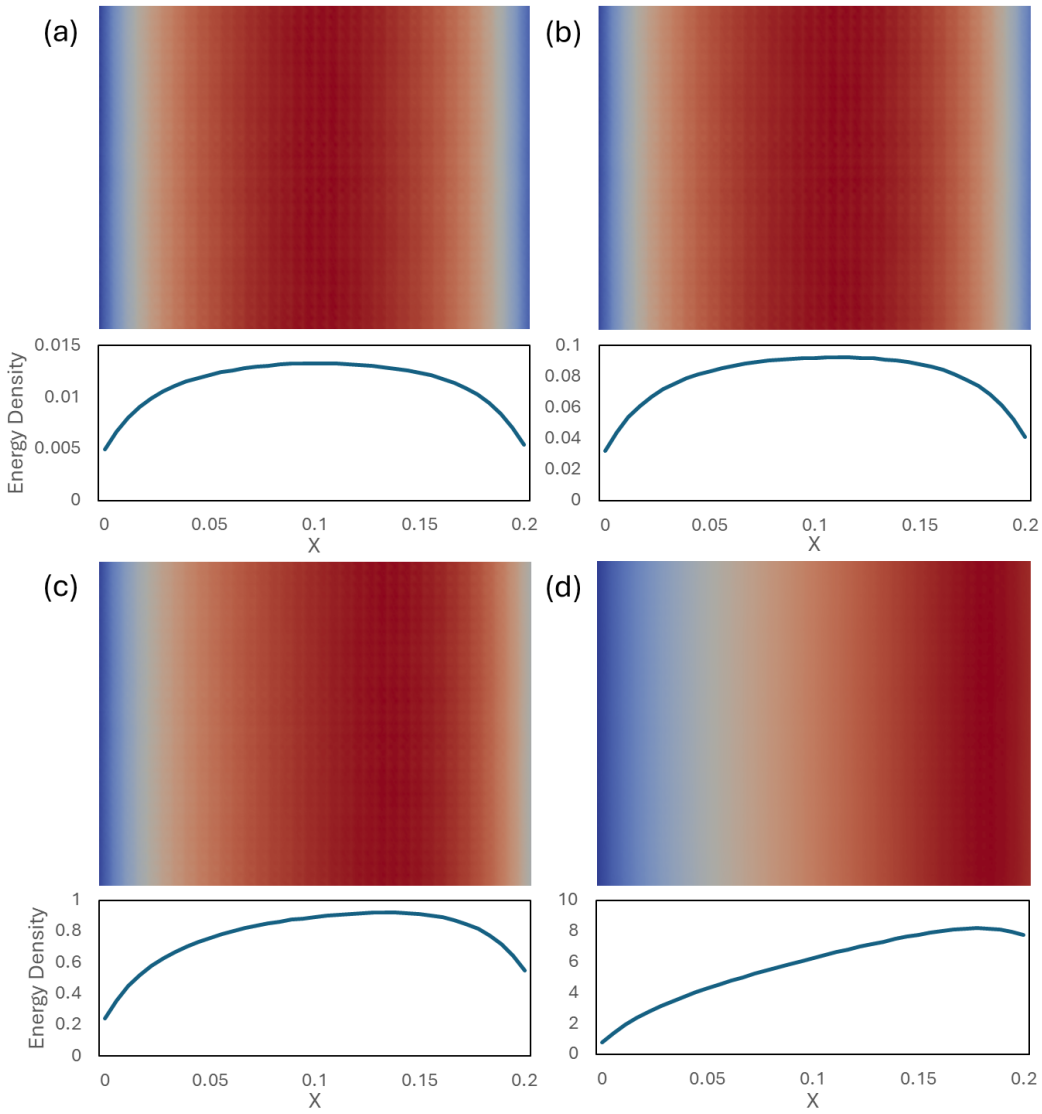

Figure 63: Vibrational response of a flat plate with periodic boundary conditions and damping coefficient $\mu = 0.01$ under TBL pressure fields represented by the Mellen model with free-stream flow speeds (a) $19\,ms^{-1}$ (b) $50\,ms^{-1}$ (c) $150\,ms^{-1}$ (d) $300\,ms^{-1}$.

density in the centre of the plate at all flow speeds, slowing the shift in the peak towards the trailing edge as compared to the absorbing boundary case. Given the increased directionality of the Mellen model compared to the Corcos model, in each case less of the overall ray density will be made up of rays which propagate in the cross-flow direction. This, combined with the greater preference for the generation of rays which propagate in the flow direction, ensure that these peaks

are closer to the trailing edge for all flow speeds for the Mellen model. This effect is most noticeable at higher flow speeds.

The influence of the damping on the results observed can be determined by plotting the streamwise energy distribution across the plate for different damping coefficients. This result is shown in Figure 31.

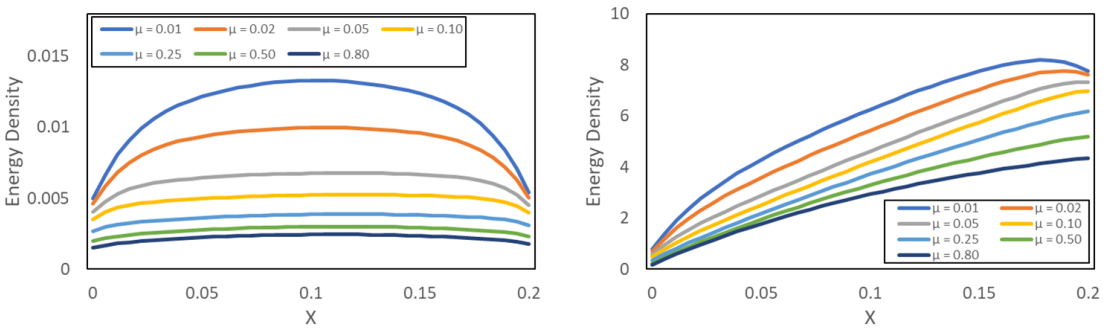

Figure 64: Energy density distribution in the $+\hat{\boldsymbol{x}}$ direction for flow speeds $U_0 = 50\,ms^{-1}$ (left) and $U_0 = 300\,ms^{-1}$ (right) when applying the Mellen model with periodic boundary conditions.

As in the Corcos model case, the damping of the plate has a large impact on the energy density distribution observed across the plate. As discussed in subsection 3.6.4, changes to the damping coefficient will have the largest impact on rays which propagate across the plate many times. These are chiefly the rays which propagate close to the centre of the plate in the cross-flow direction, and thus will contribute a large amount of energy density in this area. An increase in the damping coefficient will thus have a greater impact on the energy density at lower flow speeds, as in these cases a larger proportion of the initial ray density propagates in the cross-flow axis. This is demonstrated within this plot, as the peak in the energy density for the $U_0 = 50\,ms^{-1}$ case for $\mu = 0.01$ case is around $5.3\times$ greater than for $\mu = 0.80$. In the equivalent case for the Corcos model, discussed in subsection 3.6.4, the $\mu = 0.01$ result was around $4.3\times$ greater than the $\mu = 0.80$ result. This is interesting, as it would suggest that the cross-flowing rays have a larger influence on the energy density distribution for the Mellen

model than the Corcos model. One would expect that the greater directionality of the Mellen model as compared to the Corcos model would ensure that the cross-flowing rays have a smaller relative impact on the overall energy density distribution, meaning that the energy lost through increasing damping is reduced compared to the Corcos model. Further work is thus required to understand the reason for this. In the higher speed case, the effect of the higher damping on these cross-flowing rays is also apparent. As with the Corcos model, this causes a shift in the energy density peak in the downstream direction with increasing damping, with the peak in the energy density being found at the trailing edge of the plate for $\mu \geq 0.25$. The overall energy density distributions for $\mu = 0.80$ for the Mellen model under different flow speeds is shown in Figure 65.

As in the Corcos model case, the increased damping generates a broadening in the energy density peak at low flow speeds, along with a marginal downstream shift in the energy density peak. This shift of the energy density peak becomes more apparent at increasing flow speeds, reaching the trailing edge in the $U_0 = 300\,ms^{-1}$ case.

A.4 Conclusion

In this appendix, the vibrational response of a plate excited by a TBL pressure field represented by the Mellen model has been studied, as well as contrasted against the equivalent Corcos model results presented in Section 3.6. In each case, the similarity of the Corcos and Mellen models ensured that the results produced by the Mellen model show rather similar features to the equivalent Corcos model results. For absorbing boundary conditions, the marginally greater directionality of the Mellen model ensured that for all flow speeds the energy density peak was found slightly further downstream than in the equivalent Corcos case. In each case, the shape of the energy distributions were however rather similar to the Corcos model result, as was the influence of different damping coefficients

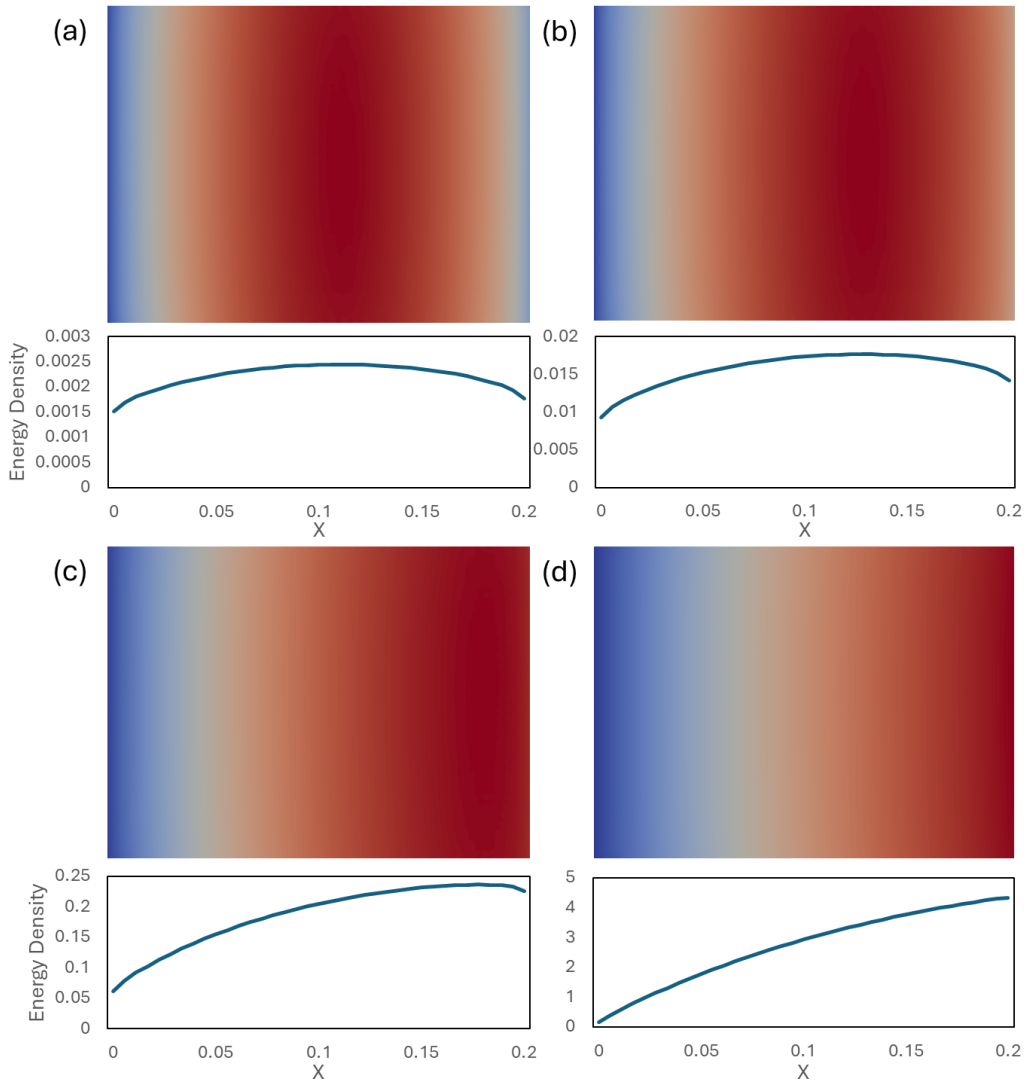

Figure 65: Vibrational response of a flat plate with periodic boundary conditions and damping coefficient $\mu = 0.80$ under TBL pressure fields represented by the Mellen model with free-stream flow speeds (a) $19\,ms^{-1}$ (b) $50\,ms^{-1}$ (c) $150\,ms^{-1}$ (d) $300\,ms^{-1}$.

on the distributions observed. In the reflecting boundary case the Mellen model displayed linearly increasing energy densities in the streamwise direction, in the same manner as the Corcos model. As with the Corcos model, the energy density difference across the plate was also found to be rather constant for different damping coefficients. This result then further supported the idea that this effect is caused by the initial propagation of the rays across the domain. In this case, the increased directionality of the Mellen model once again influenced the

energy distributions observed, causing a greater disparity in the energy density across the plate for all flow speeds and damping values. In the Periodic case, the Mellen model results once again closely resembled the Corcos model results, with constant energy density in the cross-flow direction and absorbing boundary-like distributions in the flow axis. In addition, an increase in the damping coefficient of the plate also showed a disproportionate reduction in the energy density across the centre of the plate, highlighting the influence of rays which are trapped within the plate by the periodic boundaries. However, this increase in damping demonstrated a larger impact on the energy density distribution for the Mellen model at low flow speeds than for the Corcos model. This is interesting, as it would be expected that the Mellen model should be influenced less by this action, due to the greater directionality of this model compared to the Corcos model. Further work is then required to properly investigate this outcome.